N° d’ordre NNT: 2017LYSEI046

THÈSE de DOCTORAT DE L’UNIVERSITÉ DE LYON

préparée au sein de
l’Institut National des Sciences Appliquées de Lyon

École Doctorale 162
Mécanique, Énergétique, Génie civil, Acoustique

Spécialité/ discipline de doctorat
MÉCANIQUE – GÉNIE MÉCANIQUE – GÉNIE CIVIL

Soutenue publiquement le 2 Juin, 2017, par:

Wenfeng YE

Numerical methods for the simulation of shear wave propagation in nearly incompressible medium — Application in elastography

---

Devant le jury composé de:

A S. BONNET-BENDHIA	Directeur de Recherche (ENSTA ParisTech)	Rapporteur
D. KOMATITSCH	Directeur de Recherche (Aix-Marseille Université)	Rapporteur
A. COMBESCURE	Professeur (INSA de Lyon)	Directeur de thèse
A. BEL-BRUNON	Maître de Conférences (INSA de Lyon)	Co-Directeur
S. CATHELINE	Directeur de Recherche (Université Lyon 1)	Examinateur
M. ROCHETTE	Ph.D. (ANSYS, France)	Examinateur
C. PRADA-JULIA	Directeur de Recherche (Institut Langevin)	Présidente du jury
R. KOLMAN	Ph.D. (Institute of thermomechanics, Czech)	Examinateur

LaMCoS - UMR CNRS 5514 - INSA de Lyon
20, avenue Albert Einstein, 69621 Villeurbanne Cedex (FRANCE)

Département FEDORA – INSA Lyon - Ecoles Doctorales – Quinquennal 2016-2020

SIGLE	ECOLE DOCTORALE	NOM ET COORDONNEES DU RESPONSABLE
CHIMIE	**CHIMIE DE LYON** **http://www.edchimie-lyon.fr** Sec : Renée EL MELHEM Bat Blaise Pascal 3e etage secretariat@edchimie-lyon.fr Insa : R. GOURDON	M. Stéphane DANIELE Institut de Recherches sur la Catalyse et l'Environnement de Lyon IRCELYON-UMR 5256 Équipe CDFA 2 avenue Albert Einstein 69626 Villeurbanne cedex directeur@edchimie-lyon.fr
E.E.A.	**ELECTRONIQUE, ELECTROTECHNIQUE, AUTOMATIQUE** **http://edeea.ec-lyon.fr** Sec : M.C. HAVGOUDOUKIAN Ecole-Doctorale.eea@ec-lyon.fr	M. Gérard SCORLETTI Ecole Centrale de Lyon 36 avenue Guy de Collongue 69134 ECULLY Tél : 04.72.18 60.97 Fax : 04 78 43 37 17 Gerard.scorletti@ec-lyon.fr
E2M2	**EVOLUTION, ECOSYSTEME, MICROBIOLOGIE, MODELISATION** **http://e2m2.universite-lyon.fr** Sec : Sylvie ROBERJOT Bât Atrium - UCB Lyon 1 04.72.44.83.62 Insa : H. CHARLES secretariat.e2m2@univ-lyon1.fr	M. Fabrice CORDEY CNRS UMR 5276 Lab. de géologie de Lyon Université Claude Bernard Lyon 1 Bât Géode 2 rue Raphaël Dubois 69622 VILLEURBANNE Cédex Tél : 06.07.53.89.13 cordey@univ-lyon1.fr
EDISS	**INTERDISCIPLINAIRE SCIENCES-SANTE** **http://www.ediss-lyon.fr** Sec : Sylvie ROBERJOT Bât Atrium - UCB Lyon 1 04.72.44.83.62 Insa : M. LAGARDE secretariat.ediss@univ-lyon1.fr	Mme Emmanuelle CANET-SOULAS INSERM U1060, CarMeN lab, Univ. Lyon 1 Bâtiment IMBL 11 avenue Jean Capelle INSA de Lyon 696621 Villeurbanne Tél : 04.72.68.49.09 Fax :04 72 68 49 16 Emmanuelle.canet@univ-lyon1.fr
INFOMATHS	**INFORMATIQUE ET MATHEMATIQUES** **http://infomaths.univ-lyon1.fr** Sec :Renée EL MELHEM Bat Blaise Pascal, 3e étage Tél : 04.72. 43. 80. 46 Fax : 04.72.43.16.87 infomaths@univ-lyon1.fr	M. Luca ZAMBONI Bâtiment Braconnier 43 Boulevard du 11 novembre 1918 69622 VILLEURBANNE Cedex Tél :04 26 23 45 52 zamboni@maths.univ-lyon1.fr
Matériaux	**MATERIAUX DE LYON** **http://ed34.universite-lyon.fr** Sec : Marion COMBE Tél:04-72-43-71-70 –Fax : 87.12 Bat. Direction ed.materiaux@insa-lyon.fr	M. Jean-Yves BUFFIERE INSA de Lyon MATEIS Bâtiment Saint Exupéry 7 avenue Jean Capelle 69621 VILLEURBANNE Cedex Tél : 04.72.43 71.70 Fax 04 72 43 85 28 Ed.materiaux@insa-lyon.fr
MEGA	**MECANIQUE, ENERGETIQUE, GENIE CIVIL, ACOUSTIQUE** **http://mega.universite-lyon.fr** Sec : Marion COMBE Tél:04-72-43-71-70 –Fax : 87.12 Bat. Direction mega@insa-lyon.fr	M. Philippe BOISSE INSA de Lyon Laboratoire LAMCOS Bâtiment Jacquard 25 bis avenue Jean Capelle 69621 VILLEURBANNE Cedex Tél : 04.72 .43.71.70 Fax : 04 72 43 72 37 Philippe.boisse@insa-lyon.fr
ScSo	**ScSo*** **http://recherche.univ-lyon2.fr/scso/** Sec : Viviane POLSINELLI Brigitte DUBOIS Insa : J.Y. TOUSSAINT Tél : 04 78 69 72 76 viviane.polsinelli@univ-lyon2.fr	M. Christian MONTES Université Lyon 2 86 rue Pasteur 69365 LYON Cedex 07 Christian.montes@univ-lyon2.fr

*ScSo : Histoire, Géographie, Aménagement, Urbanisme, Archéologie, Science politique, Sociologie, Anthropologie

Remerciements

Le travail présenté ici n'était jamais réalisable sans Alain COMBESCURE, directeur de thèse, à qui j'adresse mes sincères remerciements du fond du coeur pour m'avoir permis d'explorer le monde de la modélisation numérique avec une liberté complète de recherche. Je ne pourrai jamais oublier les discussions passionnantes que nous avons pu avoir sur les sens physiques des résultats obtenus dans cette thèse.

Je tiens à exprimer mes plus profonds remerciements à mes encadrants Aline BEL-BRUNON et Stefan CATHELINE, encadrants de thèse, pour leur patience, leur gentillesse et leur support sans limite. Leur grande expertise et sens de la rigueur ont apporté énormément de valeur de cette thèse. C'était aussi un très grand plaisir d'avoir travaillé avec eux. Leur encouragement et leur soutien à chaque conversation était ma source de motivation et d'inspiration. Je n'aurais pas pu aboutir ces travaux sans leur aide.

Ce travail n'aurait pas été possible sans le soutien de ANSYS et Michel ROCHETTE, qui m'ont permis, grâce à une allocation de recherches et diverses aides financières, de me consacrer sereinement à l'élaboration de ma thèse.

Je tiens également à remercier les membres de l'ancien équipe MSE (Mécanique des Solides et Endommagement). Le bon déroulement de la thèse est en grande partie due à la bonne ambiance dans le laboratoire. Je remercie sincèrement d'abord Jean-Claude BOYER, mon encadrant durant ma recherche de Master, pour m'avoir permis de découvrir la simulation par éléments finis, pour sa gentillesse et sa passion.

Par ailleurs, je remercie chaleureusement Anne-Sophie BONNET-BENDHIA et Dimitri KOMATITSCH pour avoir accepté de relire minutieusement ce manuscrit et m'avoir apporté des remarques et commentaires bénéfiques à travers leurs rapports détaillés. Je souhaite vivement remercier Claire PRADA-JULIA pour m'avoir fait l'honneur de présider le jury de thèse. J'exprime ma profonde reconnaissance à Radek KOLMAN pour m'avoir fait le plaisir de s'intéresser à mes travaux en acceptant de faire partie du jury.

J'adresse également mes vifs remerciements aux amis que j'ai rencontrés durant ma thèse : Jose Luis GOMEZ CHIRINOS, Guillaume SERGENT, Clément JARROUX, Clément GRENAT, Giovanna LACERRA, Alexandre BALAN, Lv ZHAO, Hu XIONG, Jorge Israel NUNEZ RAMIREZ, Claire DUPONT, Yancheng ZHANG, jerôme BLAIZOT, Damien CAMPELLO.

C'est avec une pensée à ma famille que je voudrais terminer ces remerciements. Merci à mes parents et ma soeur de m'avoir soutenu tout le temps dans ma vie. Le tout dernier merci pour Lihan, son soutien sans limite, sa patience, son encouragement et sa compréhension.

Résumé

L'élastographie transitoire est une technologie médicale de caractérisation qui permet d'estimer la rigidité des tissus mous biologiques. En visualisant la propagation de l'onde de cisaillement dans le tissu, on peut déduire le module de cisaillement μ. Au cours de la dernière décennie, cette technique a été utilisée avec succès pour étudier diverses pathologie, en particulier la fibrose, le cancer. Cependant, de nombreux facteurs, comme par exemple, la réflexion des ondes, les conditions aux limites et la précontrainte perturbent les mesures en élastographie, la qualité de la caractérisation mécanique du tissu peut alors être altérée. De plus, les tissus présentent des propriétés mécaniques plus complexes, dont la viscosité, la nonlinéarité et l'anisotropie, dont la caractérisation peut améliorer la valeur diagnostique de l'élastographie. Les simulations de propagation d'onde par Eléments Finis (EF) apparaissent alors prometteuses puisqu'elles permettent d'étudier l'influence des paramètres mécaniques intrinsèques et extrinsèques sur les vitesses de propagation et ainsi, de permettre l'identification de propriétés mécaniques complexes dans les cas de mesure réels.

Dans ce travail, nous développons un modèle d'éléments finis pour la propagation d'ondes non-linéaires dans les tissus mous. Les modèles numériques ont été validés à partir d'expériences d'élastographie issues de la littérature et ensuite utilisés pour évaluer l'identifiabilité des paramètres d'un modèle de comportement non-linéaire dans l'élastographie: la loi de Landau. En mesurant les ondes d'amplitude finie et les ondes de faible amplitude autour d'un état pré-déformé, une méthode pratique et robuste est proposée pour identifier la nonlinéarité des tissus homogènes en utilisant l'expérience d'élastographie.

La problématique du coût de calcul est également étudiée dans ce travail. En effet, la quasi-incompressibilité des tissus biologiques rend la vitesse de l'onde de pression extrêmement élevée, ce qui limite le pas de temps d'un calcul formulé en dynamique explicite.

Pour faire face à cette difficulté, différentes méthodes numériques sont présentées, dans lesquelles l'incrément de temps est limité par la vitesse d'onde de cisaillement au lieu de la vitesse d'onde de compression. Divers exemples numériques sont testés dans le cadre de l'élastographie dynamique, il a été montré que les méthodes sont précises pour ces problèmes et une réduction significative du temps CPU est obtenue.

MOTS CLÉS: Élastographie, Éléments finis, Onde de cisaillement, Incompressibilité, Hyperélasticité, Modèle de Landau, Identification des paramètres, Intégration temporelle, *Selective mass scaling*, Pas de temps fractionné.

Abstract

Transient elastography is a medical characterization technology that estimates the stiffness of biological soft tissues. By imaging the transient propagation of shear wave in tissues, one can deduce the shear modulus μ. In the last decade, this technique has been used successfully to study various pathologies, particularly fibrosis and cancers. However, numerous factors such as wave reflection, boundary conditions and pre-stress disturb elastography measurements, and the quality of the mechanical characterization of the tissue can be altered. Moreover, the tissues exhibit more complex mechanical properties, including viscosity, nonlinearity and anisotropy, the characterization of which can improve the diagnostic value of elastography. Simulations of wave propagation by finite element (FE) appear promising since they make it possible to study the influence of intrinsic and extrinsic mechanical parameters on the propagation speeds and thus to allow the identification of complex mechanical properties in the real measurement cases.

In this work, we develop a FE model for the propagation of nonlinear waves in soft tissues. The numerical models are validated from elastographic experiments taken from the literature, and then used to evaluate the identifiability of the parameters of a nonlinear model in elastography, *i.e.*, Landau's law. By measuring finite amplitude waves and low amplitude waves in pre-deformed states, a practical and robust method is proposed to identify the nonlinearity of homogeneous tissues using elastography experiment.

The problem of the cost of computation is also studied in this work. In fact, the quasi-incompressibility of biological tissues makes the compressional wave speed extremely high, which limits the time step of a simulation formulated in explicit dynamics.

To deal with this difficulty, different numerical methods are presented, in which the time step is controlled by the shear wave speed instead of the compressional wave speed. Various numerical examples are tested in the context of dynamic elastography, it has been shown that the methods are precise for these problems and a significant reduction of the CPU time is obtained.

KEYWORDS: Elastography, Finite element, Shear wave, Incompressibility, Hyperelasticity, Landau's model, Parameter identification, Time integration, Selective mass scaling, Fractional time step.

Contents

Contents i

List of Figures v

List of Tables xi

General introduction 1

1 State of the art 5

1.1 Elastography . . . 7
  1.1.1 Static elastography . . . 8
  1.1.2 Dynamic elastography . . . 8
  1.1.3 Nonlinear elastography . . . 12
1.2 Continuum mechanics . . . 16
  1.2.1 Linear elasticity . . . 17
  1.2.2 Nonlinear elasticity . . . 19
  1.2.3 Viscoelasticity . . . 25
1.3 Finite Element Method (FEM) . . . 26
  1.3.1 Problem description . . . 27
  1.3.2 Time integration methods . . . 28
  1.3.3 Critical time step . . . 30
1.4 Novelty of this work . . . 30

2 Nonlinear shear waves in soft tissues 33

2.1 Introduction . . . 35
2.2 Material modeling . . . 36
  2.2.1 Hyperelasticity . . . 36
  2.2.2 Comparison . . . 38
  2.2.3 Voigt viscoelasticity . . . 42
2.3 Simulations of nonlinear shear wave . . . 44
  2.3.1 Preliminary study: choose the compressible parameter . . . 44
  2.3.2 Plane wave . . . 44
  2.3.3 Nonplane wave . . . 49
  2.3.4 Wave interaction . . . 51

2.3.5 Discussion 51
2.4 Parametric study 53
2.4.1 Analytical formulation 53
2.4.2 Effect of amplitude 54
2.4.3 Effect of frequency 55
2.4.4 Effect of viscosity 55
2.4.5 Effect of the first nonlinear elastic parameter γ 56
2.4.6 Effect of the second nonlinear elastic parameter ζ 57
2.4.7 Discussion 58
2.4.8 Sign of the first nonlinear elastic parameter γ 59
2.5 Conclusion 61

3 Transverse isotropy in elastography 63
3.1 Introduction 65
3.2 Intrinsic transverse isotropy 66
3.2.1 Linear elastic ITI materials 66
3.2.2 Incompressibility 67
3.2.3 Shear wave propagation in incompressible ITI materials 67
3.2.4 Hyperelastic theory 68
3.2.5 Numerical validation 69
3.3 Extrinsic transversely isotropy: shear wave speeds under uniaxial pre-deformation 71
3.3.1 Analytical theory 73
3.3.2 Numerical validation 78
3.4 Extrinsic anisotropy: shear wave speeds under general pre-deformation . 80
3.4.1 Analytical theory 81
3.4.2 Numerical validation 82
3.5 Characterization of Landau's constitutive law by acoustoelastic effect . . 84
3.5.1 Solution property: accuracy 84
3.5.2 Solution property: stability 85
3.5.3 Solution property: uniqueness 88
3.5.4 Robust method to identify both A and D 88
3.6 Conclusion 90

4 Selective mass scaling method 93
4.1 Introduction 95
4.2 Separation of shear and volumetric eigenmodes 97
4.3 Selective mass scaling method 99
4.3.1 General form of SMS 99
4.3.2 The existing SMS method 100
4.3.3 The proposed SMS method 101
4.3.4 Validation 101
4.4 Numerical examples 105

4.4.1 Cantilever beam 106
4.4.2 Circular shear wave propagation 107
4.4.3 Planar shear wave propagation in heterogeneous media 109
4.4.4 Shear wave propagation in an anisotropic medium 112
4.4.5 Nonlinear shear wave propagation 115
4.4.6 Shear wave propagation in a pre-stressed medium 118
4.5 Conclusion 123

5 Fractional time-step method **125**
5.1 Introduction 127
5.2 Method 127
5.2.1 Mixed $\mathbf{u}-p$ formulation 128
5.2.2 Pressure stability 128
5.2.3 Fractional step time integration method 129
5.2.4 Discussion 131
5.3 Numerical examples 132
5.3.1 Spinning model 132
5.3.2 Heterogeneous model 134
5.3.3 Anisotropic model 136
5.3.4 Nonlinear shear wave model 136
5.4 Conclusion 137

General conclusions and perspectives **141**

Bibliography **145**

List of Figures

1.1 Scoring card for liver stiffness diagnosis. Source: www.echosens.com . . 7

1.2 Schematic representation of the experimental setup used in 1D transient elastography. Source:[SAN 02b] 9

1.3 Displacement field recorded by 1D transient elastography technique. Two types of wave with different speeds are observed: a compressional wave (P) and a shear wave (S). Due to its high speed the compressional wave propagates almost instantaneously throughout the sample while the shear wave propagation is clearly visible. Source: [CAT 98] 10

1.4 2D transient elastography: Shear waves are generated using a vibrator composed of two parallel rods. The linear array of transducers is placed between the rods. The shear wave front has a cylindrical shape in the out-of plane direction. Source: [SAN 02a] 11

1.5 Generation of the supersonic shear source: the source is sequentially moved along the axis, creating two quasi-plane and intense shear waves. Source: [BER 04] 12

1.6 Transverse wave attenuation measurement *v.s.* excitation frequency. Circles represent experimental results and solid lines represent theoretical solutions. (a) For gelatin phantoms; (b) For beef muscle. Source: [CAT 04] 13

1.7 An ultrafast transducer array is applied on the bottom of the phantom. A rigid plate is connected to a vibrator to generate plane wave 14

1.8 Source (left) and measured point (right) velocity history and their corresponding spectrum. The nonlinearity leads to the distortion on the wave shape and odd harmonic components in spectrum 15

1.9 Acoustoelastic experimental setup. An homogeneous load is applied on the top of the phantom, a low frequency pulse propagates in the medium and the displacements are tracked by a transducer set in the middle of the rod. Source: [CAT 03a] 15

1.10 Acoustoelastic experimental setup. The three possible configurations generating the propagation of polarized shear waves in the phantom under uniaxial stress (axis-2). The three resulting shear waves are designated as: (a) $S12$ or $S32$, (b) $S21$ or $S23$, (c) $S13$ or $S31$. Source: [CAT 03a] . . 16

1.11 Compressional and shear wave speed as a function of Poisson coefficient. $\rho = 1000\ kg/m^3, \mu = 1\ kPa$. 19

1.12 Deformation of a continuum body. 20
1.13 Two simplest viscoelastic models. (a) Maxwell; (b) Kelvin-Voigt 26

2.1 Uniaxial tension/compression test 39
2.2 Simple shear test. Fig.2.2(a) shows the relation between the shear strain and the shear stress; Fig.2.2(b) shows the pressure in simple shear which reflects Kelvin effect. 40
2.3 Preliminary model: the simulations are carried at different levels of the incompressibility 45
2.4 Nonlinear plane shear wave experiment presented in [JAC 07] 45
2.5 Geometry and FE model of plane shear wave propagation 46
2.6 Vertical displacement distributions in the refined zone. The wave front remains plane during the simulation, it confirms the hypothesis of plane shear wave propagation. 47
2.7 Vertical velocity history and its spectrum 47
2.8 Spectra of the vertical velocity versus propagation depth z 48
2.9 Plane wave: Evolution of the fundamental component and the third and fifth harmonics versus propagation depth. 48
2.10 Nonplane shear wave model. As both the gel and the vibrator are set to be enough large in the experiment, EF model can take advantage of plane strain hypothesis. 49
2.11 Nonplane wave with mono-excitation : displacement distribution at $t = 0.05\ s$ 50
2.12 Nonplane wave propagation: all harmonic generation 50
2.13 Global spectrum of nonplane wave propagation 51
2.14 plane wave propagation with interaction 52
2.15 Nonplane wave propagation with interaction 52
2.16 FEM simulations at different amplitudes: Evolution of the fundamental and odd harmonics components along the propagation distance. Note: circle marks in the Fig.(b) are the analytical results by Eq.2.28. 55
2.17 FEM simulations at different frequencies: Evolution of the fundamental and odd harmonics components along the propagation distance. Note: circle marks in the Fig.(b) are the analytical results by Eq.2.28. 56
2.18 FEM simulations with different viscosities: Evolution of the fundamental and odd harmonics components along the propagation distance. Note: circle marks in the Fig.(b) are the analytical results by Eq.2.28. 56
2.19 FEM simulations with different elastic parameters γ: Evolution of the fundamental and odd harmonics components along the propagation distance. Note: circle marks in the Fig.(b) are the analytical results by Eq.2.28. . . 57
2.20 FEM simulations with different elastic parameters ζ: Evolution of the fundamental and odd harmonics components along the propagation distance. Note: the analytical results are the same for three cases, presented by blue circle marks in Fig.(b). 58

2.21 Fit of the relationship between the odd harmonics amplitude and Goldberg number . . . 59
2.22 One element simple shear test for materials in Tab.2.5 . . . 60
2.23 Velocity history and its spectrum of three different materials, at depth $= 10\ mm$ . . . 61

3.1 Schematics of the TE technique for ITI materials. (a) The rod is perpendicular to the fibers axis, a shear wave propagates (k) perpendicularly to the fibers axis with a polarization (u) parallel to the fibers axis. (b) The rod is parallel to the fibers axis, a shear wave propagates (k) perpendicularly to the fibers axis with a polarization (u) perpendicular to the fibers axis. Such configurations give, respectively, access to the elastic constants μ_L and μ_T. Source: [ROY 11] . . . 65
3.2 Two modes of shear wave in ITI materials. For the same propagation direction ($k = [sin\theta\ 0\ cos\theta]^T$), PT mode (left) polarizes along the direction x_2; QT mode (right) polarizes in the (x_1,x_3) plan. . . . 68
3.3 The fiber direction from left to right: $\mathbf{a}_0 = [0\ 1\ 0]$, $\mathbf{a}_0 = [1\ 1\ 0]$, $\mathbf{a}_0 = [1\ 0\ 0]$ and $\mathbf{a}_0 = [0\ 0\ 1]$. The second configuration has been used twice to illustrate the influence of β, see Tab.3.1. . . . 70
3.4 The measurement of the shear wave speed based on the simulation results (Case 2 as example). . . . 71
3.5 Three typical configurations of linear polarized shear wave in a uniaxial pre-deformed medium. The propagation direction (k) and polarization direction (u) are either parallel or perpendicular to the elongation direction. 72
3.6 A practical *in vivo* measurement of acoustoelastic effect using the SSI technique [JIA 15a]. The wave type *iii* is measured based on this configuration. . . . 73
3.7 Shear wave speed in a uniaxially deformed (along the vertical direction) neo-Hookean solid. $\rho = 1000\ kg/m^3$, $\mu = 1\ kPa$ . . . 74
3.8 Shear wave speed in a uniaxially deformed Mooney-Rivlin solid. $\rho = 1000\ kg/m^3$, $c_1 = 0.286\ kPa$, $c_2 = 0.214\ kPa$ . . . 75
3.9 Shear wave speed in a uniaxially deformed Kirchhoff solid. $\rho = 1000\ kg/m^3$, $\mu = 1\ kPa$ . . . 76
3.10 Shear wave speed in a uniaxially deformed Landau's solid. $\rho = 1000\ kg/m^3$, $\mu = 1\ kPa, A = D = 10\ kPa.$ (Solid lines: Eq.3.23; Dashed lines: Eq.3.24; Dash- dot lines: Eq.3.25) . . . 78
3.11 Finite element models (half) of acoustoelastic analysis. The figures show the displacement introduced by the small dynamic load (along direction u) in the deformed configuration. . . . 79
3.12 Numerical simulations (circles) *v.s.* analytical solutions (Fig.3.8) of Mooney Rivlin solid. $\rho = 1000\ kg/m^3$, $c_1 = 0.286\ kPa$, $c_2 = 0.214\ kPa$. Error bars (2%) are estimated by the measurement at natural state. . . . 80

3.13 Numerical simulations (circles) *v.s.* analytical solutions of Landau's solid. $\rho = 1000\ kg/m^3$, $\mu = 1\ kPa$, $A = -5.71\ kPa$, $D = 4.55\ kPa$. Error bars: 2%. 81
3.14 New configurations of linear polarized shear wave in a generally pre-deformed medium. 82
3.15 2D FE model in Sec.2.3.2 after a certain pre-deformation, plane shear wave propagates from right to left. 83
3.16 Numerical simulations (circles) *v.s.* analytical solutions of Landau's solid in plane deformation. $\rho = 1000\ kg/m^3$, $\mu = 1\ kPa$, $A = -5.71\ kPa$, $D = 4.55\ kPa$. (Note: numerical results in Fig.(a) and Fig.(b) are from the same simulation.) 83
3.17 Comparison of different fitting results on the same experimental data (From [JIA 15b]). 84
3.18 Stability criterion of Landau's solid in uniaxially pre-deformation 86
3.19 Stability criterion of Landau's solid under plane deformation ($\xi = 1$) . . . 87
3.20 Stability criterion of Landau's solid when $\xi = 0.25$ (or $\xi = 0.75$) 87
3.21 Uniqueness issue, basic parameters: $\mu = 1\ kPa$, $A = -5.71\ kPa$, $D = 4.55\ kPa$. Three types of shear waves: type *i* (blue); type *ii* (red); type *iii* (green). 88
3.22 Wave speed of type *iii* in compression for materials in Tab.3.3. Symbols represent the numerical results. (Note: Mat.3 is unstable, the numerical simulation fails under large pre-deformation). 89

4.1 All eigenvectors of an ideal quadrilateral element (given by Tab.4.1) . . . 98
4.2 Test model: a square plate with distorted mesh of 50 degrees of freedom. . 102
4.3 Eigenvalues of test model, first three (rigid motion) modes absent 103
4.4 Eigenvectors distortion of test model (first three rigid body modes absent) 104
4.5 Deformations of eigenvectors for 3 shear eigenmode 105
4.6 Deformations of eigenvectors for 3 volumetric eigenmode 105
4.7 Cantilever beam model, dimension: $1 \times 1 \times 6\ mm$. 106
4.8 Cantilever Beam: displacement along A-A' for different cases. Lines: results by pure explicit simulation; Marks: results by proposed SMS method 107
4.9 Circular shear wave propagation model 108
4.10 Circular shear wave propagation: velocity distribution (left) and shear stress distribution (right) at $t = 0.03\ s$. Results are obtained by the proposed SMS method with $\alpha = 30$. 109
4.11 Circular shear wave propagation: vertical displacement at measuring points 109
4.12 Circular shear wave propagation: vertical velocity along O-O' at different time 110
4.13 Heterogeneous model: geometry and boundary conditions 110
4.14 Heterogeneous model: horizontal displacement along A-A' at different time 111
4.15 Heterogeneous model: horizontal velocity along A-A' at different time . . 111
4.16 Heterogeneous model: horizontal displacement at measuring points . . . 112
4.17 Heterogeneous model: horizontal velocity at measuring points 112

4.18 Heterogeneous model: shear stress distribution. Left: Pure explicit; Middle: Proposed SMS; Right: Existing SMS 113
4.19 Transversely isotropic linear elastic model, the vector of fibre direction is set along Y-direction. The source is applied at point O of the model. . . . 114
4.20 Anisotropic model: stress distribution at the end of simulation ($t = 0.04\ s$). 114
4.21 Anisotropic model: vertical displacement, velocity and acceleration at one point (A) near the load. 115
4.22 Anisotropic model: vertical displacement, velocity and acceleration at one point (C) far from the load. 115
4.23 Test of small amplitude wave. Shear stress distribution at time $t = 0.05\ s$. The mesh is deformed with the real displacement. 117
4.24 Test of small amplitude wave.Vertical displacement, velocity and acceleration at one point 30 *mm* far from the load 118
4.25 Test of large amplitude wave. Shear stress distribution at time $t = 0.05\ s$. The mesh is deformed with the real displacement. 119
4.26 Test of large amplitude wave. Vertical displacement, velocity and acceleration at one point 30 *mm* far from the load 120
4.27 Pres-stressed model: Geometry and static load distribution 121
4.28 Deformed configuration after static load, amplification factor = 1 121
4.29 Dynamic displacement distribution at $t = 0.05\ s$. Left: Explicit; Right: Proposed SMS. 122
4.30 Pre-stressed model: vertical displacement at measuring points 122
4.31 Pre-stressed model: vertical velocity at measuring points 122
4.32 Pre-stressed model: time history of energy evolution 123

5.1 Two type of mixed elements. (a) T3P3 element (b) Q4P1 element 129
5.2 Spinning model. (a) T3P3 element (b) Q4P1 element 132
5.3 Spinning model: pressure distribution at time $t = 0.03\ s$ 133
5.4 Spinning model: shear stress distribution at time $t = 0.03\ s$ 133
5.5 Heterogeneous model: Horizontal velocity along A-A' (see Fig.4.13) at different time 134
5.6 Heterogeneous model: Horizontal velocity at measuring points (see Fig.4.13) 134
5.7 Global shear stress distribution obtained by FTS method, the positions of heterogeneous blocks are shown. 135
5.8 Heterogeneous model: shear stress distribution at $t = 0.16\ s$ 135
5.9 Anisotropic model: Vertical displacement, velocity and acceleration at point A (see Fig.4.19). 136
5.10 Anisotropic model: Shear stress distribution at the end of simulation, $t = 0.04\ s$. 137
5.11 Test of large amplitude nonlinear wave.Vertical displacement, velocity and acceleration at one point 30 *mm* far from the load 138
5.12 Nonlinear wave model: At $t = 0.05\ s$ 139

5.13 Nonlinear wave model: Shear strain and stress distributions along dashed line . . . 139

List of Tables

2.1 Material parameters of Landau's visco-hyperelastic law. 46
2.2 Referenced model used in parametric study 54
2.3 Different materials in the parametric study of γ. Unity: kPa 57
2.4 Different combinations of elastic moduli in the parametric study of ζ. Unity: kPa 58
2.5 Different combinations of elastic moduli in the parametric study of the sign of γ. Unity: kPa 60

3.1 Five cases considered to validate the hyperelastic ITI model. $\mu_T = 1\ kPa$ and $\mu_L = 2\ kPa$ 71
3.2 Three types of linear polarized shear wave in an uniaxial pre-deformed medium, corresponding to Fig.3.5. Due to the uniaxial deformation in the direction 1, the direction 2 and 3 are exchangeable. 72
3.3 Three Landau's materials for testing the acoustoelastic behaviours. Unity: kPa 89
3.4 Comparison of different fitting methods by randomly disturbed the data in Fig.3.17. Initial condition: $\mu = 3.2\ kPa$, $A = -16.9\ kPa$ and $D = 5.1\ kPa$, so $\gamma = -0.15\ kPa$ 90

4.1 Eigenmodes of an ideal quadrilateral element with different integration strategies. (R.I.: reduced integration; S.I.: selective integration; F.I.: full integration;) 98
4.2 Cantilever beam model: summary of simulation parameters 107
4.3 Heterogeneous model: Material parameters 111

General introduction

Elastic properties of biological tissues are a typical indicator of several pathologies. Palpation has become widespread for hundreds even thousands years, and it is still considered as an effective method of detecting tumours and other pathologies. On the contrary, elastography is a modern, *in vivo* and quantitative imaging technology that evaluates tissue stiffness. In the last decade, it has been successfully used to investigate diseases in the liver, to detect breast cancer, thyroid and prostate cancers, and so on.

Current commercial elastography technique is based on the assumption of linear elasticity. For example, dynamic elastography, which is the core of in this work, estimates the shear modulus μ of tissues by measuring the propagation speed of infinitesimal (linear) shear waves. However, biological soft tissues exhibit more complex mechanical properties, including viscosity, nonlinearity and anisotropy. For diagnostic purposes, characterizing these properties may improve the value of elastography when they are studied separately or in combination with linear elasticity. For example, linear elasticity may not be specific in terms of tumour benignity and malignancy, while nonlinearity may be [KRO 98].

Considerable efforts have been made to improve the identification of complex constitutive laws for soft tissues. In dynamic elastography, characterizing the nonlinearity of biological tissues is based on two approaches: finite amplitude shear waves and acoustoelasticity. In the former case, considering biological tissues are very soft, shear waves can easily reach the nonlinear regime, where nonlinearity modifies the wave shape during propagation. Acoustoelasticity consists in measuring the speed of linear shear waves in a pre-stressed solid. For a nonlinear material, finite external load induces a change of wave speed, so a quantitative evaluation of this change corresponds to measuring the nonlinearity. However, although these nonlinear behaviours have been clearly observed in elastography experiments, they are still difficult to interpret, especially in terms of quantitative identification. The reason may be that elastography experiments have been so far post-treated using analytical models, which are based on simplifying assumption and therefore, cannot handle complex phenomena.

On the other side, elastography, even in the context of linear theory, is challenged by the complexity of human body. The practice of elastography is sometimes limited by conditions which are difficult to control *in vivo*. For example, fat tissues between liver and elastography probe could disturb the results easily while assessing of liver fibrosis. Studies have shown that internal pressure in organs also have an influence on measurements [MIL 10]. Moreover, spurious reflections by surrounding tissues could also make the examination meaningless.

In general, all these considerations point to the need of establishing accurate and efficient numerical models for elastography. As biological tissues are considered as soft solids, Finite Element Method (FEM), which is able to accurately and easily model detailed structure, is considered firstly. In the literature, FEM has been employed to study different factors which may influence elastography results. Heterogeneity and anisotropy have been taken into consideration in some work. Moreover, using experimental date, FEM has been used inside an inverse algorithm to reconstruct the stiffness map. However, in most of the applications, choosing the accurate material model for the tissue, and accounting for its constitutive complexity, is a key requirement to get high fidelity numerical simulations, therefore more complex constitutive models are necessary in elastography post-processing.

The first part of this work aims at choosing an appropriate material model for biological tissues and implementing it in FEM. In biomechanics, many models have been proposed for soft tissues and validated by different experiments. This work focuses on their nonlinear behaviour in dynamics in shear. For example, it will be shown that the famous neo-Hookean and Mooney-Rivlin models have an exactly linear behaviour in shear, so using these models for modeling nonlinear shear wave propagation does not make sense. In acoustical physic field, the weakly nonlinear theory (referred to as *Landau's law*) is widely used. Landau's law has two nonlinear parameters A and D and it exhibits a cubic nonlinear behaviour in shear, which leads to the generation of harmonics in nonlinear shear wave propagation. This has been clearly observed in soft tissues by elastography experiments.

In Chapter 2, nonlinear elastic Landau's law is introduced into a finite element formulation. In addition, viscosity is considered by Voigt model, which describes accurately the viscoelastic behaviour of soft tissues at the frequency range of elastography. The visco-hyperelastic Landau's model is employed in simulations based on elastography experiments, the numerical results show a good agreement with the experimental study. It is observed that a plane shear wave generates only odd harmonics and a nonplane wave generates both odd and even harmonics in the spectral domain. From these results, we propose a simple and forward method to identify one nonlinear parameter of Landau's law.

A second nonlinear elastography method is investigated in Chapter 3. Nonlinear parameters are determined by measuring wave speeds at different pre-deformed states, this is referred to as *acoustoelastic* experiments. Uniaxial pre-deformation makes tissue extrinsically transversely isotropic (TI). We show, by both theoretical analysis and numerical simulations, that an extrinsically TI material has three different shear wave speeds instead of two for intrinsically TI material (*e.g.* muscle). Moreover, the stability of the simulation as well as the uniqueness of the identified nonlinear parameters are discussed for Landau's law in various situations. A reliable method is proposed to deduce both nonlinear parameters (A and D) of Landau's law.

The second part of this work is a contribution to numerical methods in dynamics. Basically, dynamic elastography is a wave propagation problem, and it is well known that the explicit scheme is the most suited time integration method. However, incompressibility of tissues leads to a high value of the compressional wave speed which makes the time step extremely small in explicit method.

In Chapter 4, a new selective mass scaling (SMS) method is proposed to overcome this deficiency. The proposed SMS method selects the eigenfrequencies related to volumetric deformation modes to decrease them, while it keeps the shear eigenmodes unchanged. This makes the time step no longer limited by the compressional wave speed but by the shear wave speed. Thus, it allows for simulating shear wave propagation in soft tissue without compromising its incompressibility. In numerical examples, various situations which may be encountered in elastography simulations have been tested, a significant reduction of CPU time is always obtained with a good accuracy.

Finally, another numerical method referred to as *fractional time-step* (FTS) method is described in Chapter 5. FTS method treats the shear wave in explicit and the compressional wave in implicit, thus, the maximal time step depends on the shear wave speed like the SMS method. Numerical simulations are carried out to compare these two methods (SMS and FTS). Regarding efficiency, FTS is not better than SMS, but is still much faster than the pure explicit method. Besides, FTS method is more valuable for complex 3D models because it is available for tetrahedral elements without volumetric locking.

A general conclusion and perspectives of this work are given at the end of this manuscript.

Chapter 1

State of the art

This chapter contains three parts, it presents the elastography techniques, material models of biological tissue and the basis of finite element method.

Contents

1.1 Elastography **7**
1.1.1 Static elastography 8
1.1.2 Dynamic elastography 8
1.1.3 Nonlinear elastography 12
1.2 Continuum mechanics **16**
1.2.1 Linear elasticity 17
1.2.2 Nonlinear elasticity 19
1.2.3 Viscoelasticity 25
1.3 Finite Element Method (FEM) **26**
1.3.1 Problem description 27
1.3.2 Time integration methods 28
1.3.3 Critical time step 30
1.4 Novelty of this work **30**

1.1 Elastography

The tissue mechanical properties give diagnostic information about the presence or status of a disease. For example, cancerous tumours are often harder than the surrounding tissue, and diseased livers are stiffer than healthy ones. Fig.1.1 presents a scoring card for liver stiffness diagnosis which is provided by the company Echosens^{TM}. It compares the liver stiffness (in *kPa*) with the liver condition to diagnose the stage of fibrosis.

For this reason, the practice of palpation is a widespread method for detecting tumours and other pathologies. However, manual palpation has several important limitations: the examined tissue should be accessible by the clinician's hand; the result is easily distorted by surrounding tissue; palpation also relies on the experience of the examiner so no quantitative value can be provided. *Elastography* is a quantitative imaging technology that evaluates tissue stiffness by inducing a motion in tissues: it provides an elasticity-based image contrast, and allows clinicians to study non-invasively the mechanical properties of a tissue *in vivo*.

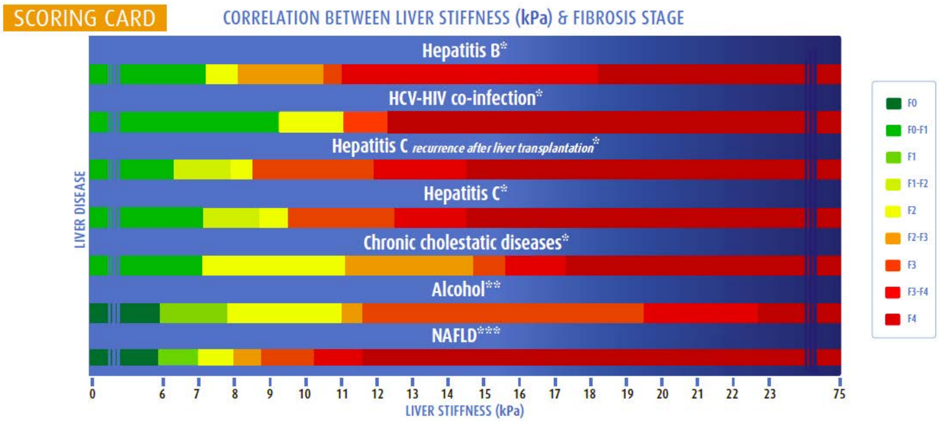

Figure 1.1: Scoring card for liver stiffness diagnosis. Source: www.echosens.com

Elastography can be used for the investigation of numerous disease conditions in organs. Firstly, it is used for organs or diseases where manual palpation is already widespread. For example, it has been considered the reference standard for fibrosis assessment, it is also useful in detecting and diagnosing breast, thyroid and prostate cancers. Moreover, it is also employed in some areas where manual palpation fails. For example, magnetic resonance elastography technique is desired to assess the brain stiffness [SAR 11].

In the last two decades, numerous elastographic techniques have been developed. These techniques could be distinguished by the type of mechanical excitations (static compression or dynamic vibration), the way excitation is generated (externally or internally), or the different imaging methods to measure the tissue motion (ultrasound transducer, magnetic resonance imaging or optical coherence tomography (OCT) [ADA 03]).

In the following, several existing active elastography techniques are briefly presented.

Their fundamental physics, as well as the advantages and limitations are discussed, this state of the art is intended to introduce the motivation of the PhD thesis.

1.1.1 Static elastography

Static elastography (SE) is a pioneer in this field which was firstly developed by Ophir *et al.* [OPH 91]. In this technique, an external compression is applied by pressing an probe on the tissue, and the ultrasound images are compared before and after the compression. Based on Hooke's Law, hard tissue will deform less than soft tissue within the same stress. Accordingly, the obtained strain image is proportional to the tissue stiffness.

This technique is capable of displaying the relative hardness of tissues with a high spatial resolution. However, it is limited by various complex boundary conditions for applications *in vivo*. Similar to manual palpation, static elastography provides only relative stiffness, the quantitative elastic parameter (Young's modulus, for example) is not available. Moreover, SE is also limited to tissues that can be compressed at their surface.

1.1.2 Dynamic elastography

In contrast to static elastography, another set of elastography techniques introduces dynamic vibrations into the tissue, they can be all referred to as *dynamic elastography*. In these techniques, elastic information is deduced by the shear wave propagation, and the same principal is used : shear wave travels faster through stiffer tissue than through softer tissue.

Dynamic elastography techniques have many variations, for instance, sonoelastography [PAR 92], shear wave elasticity imaging (SWE) [SAR 98], acoustic radiation force impulse imaging (ARFI) [NIG 01], passive elastography [GAL 11, KOO 14], *etc*. In what follows, the three most active techniques are described.

1.1.2.1 Transient Elastography (TE)

Transient elastography (TE) is one of the most prominent elastography techniques, which has become the reference tool for fibrosis assessment. This technique generates only one (or a few) cycle of low frequency excitation (from 50 Hz to 200 Hz) by a mechanical vibrator, the induced motion is then tracked by the ultrasonic transducer. Contrary to other techniques, only the first travel of the shear wave is used to deduce the stiffness of the examined tissue.

Fig.1.2(a) presents the first transient elastography experiment setup [CAT 99b]: the mechanical vibrator is placed at the top of an agar-gelatine phantom, which is widely used to mimic the viscoelastic behaviour of biological tissue. The ultrasonic transducer (called the *acquisition system* in the figure) is placed on the opposite side of the phantom and tracks the motion induced by the vibrator. This system has a shortcoming: it requires access to both sides of the medium, so the application *in vivo* is difficult. In 2002, Sadrin

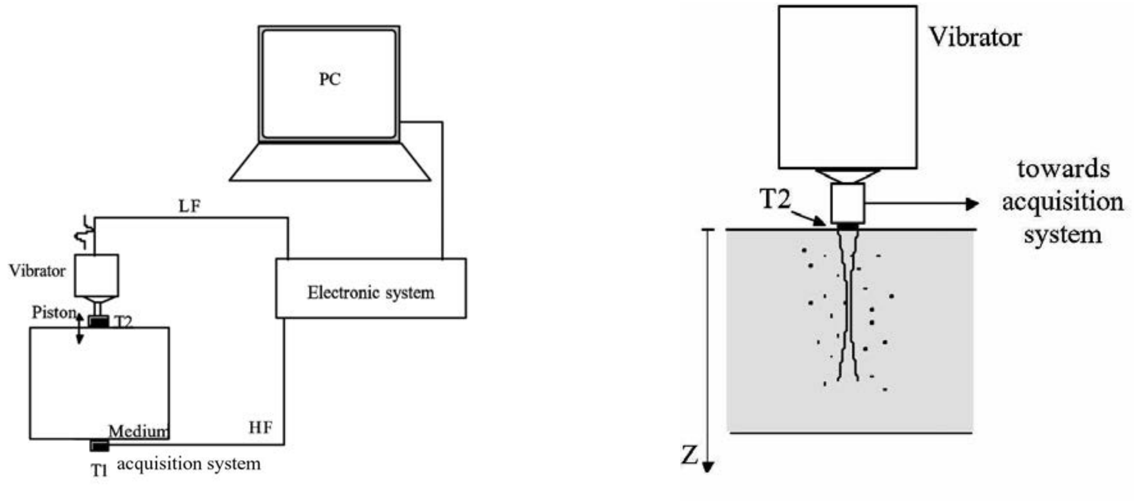

(a) First TE experiment setup: The acquisition system is placed on the opposite of the medium.

(b) Improved TE experiment setup: The acquisition system is fixed on the vibrator.

Figure 1.2: Schematic representation of the experimental setup used in 1D transient elastography. Source:[SAN 02b]

et al. [SAN 02b] proposed an improved system where the pulsed low frequency vibration is directly driven by the ultrasonic transducer itself, see Fig.1.2(b).

These two experiments are also called 1D transient elastography because the measurement locates along the axis of the vibrator. Fig.1.3 presents the typical results of the experiments using a seismogram-like representation: each horizontal curve represents the displacements (or strain) of the material point at a particular depth (z) as a function of time. So waves generated by the vibrator (P and S lines in the figure) propagate from the top to the bottom and reflect to the converse direction.

In Fig.1.3, S line represents the propagation of the shear wave front. Its slope can be used to compute the shear wave speed c_S. Assuming that the phantom is purely elastic, isotropic, homogeneous and nearly incompressible (the Poisson coefficient ν is close to 0.5), the Young's modulus E has a constant relationship with shear modulus μ, so it can be estimated by:

$$E = 2(1+\nu)\mu \simeq 3\mu = 3\rho c_S^2 \tag{1.1}$$

where ρ is the material specific mass.

Remark: Incompressibility

1. As water is the most abundant constituent of biological tissues, they are often considered as nearly-incompressible solids. Bulk modulus K is close to that of water, about 10 *GPa*, whereas shear modulus μ is typically in the order of *kPa*. This relationship leads Poisson coefficient ν to vary from 0.4999 99 to 0.4999 999 (see next section), so Eq.1.1 can be established.

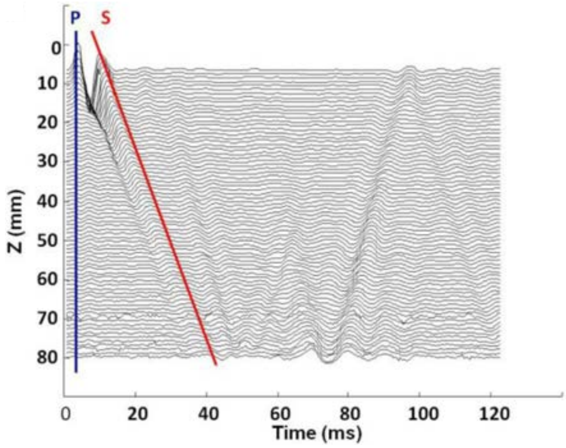

Figure 1.3: Displacement field recorded by 1D transient elastography technique. Two types of wave with different speeds are observed: a compressional wave (P) and a shear wave (S). Due to its high speed the compressional wave propagates almost instantaneously throughout the sample while the shear wave propagation is clearly visible. Source: [CAT 98]

2. In a dynamic aspect, quasi incompressibility indicates that compressional wave propagates much faster than shear wave. In fact, the compressional wave speed c_P is about $1000-1500\ m/s$ while the shear wave speed c_S is typically several meters per second. As shown in Fig.1.3, P line represents the compressional wave front generated by the vibrator, it crosses the whole medium almost instantaneously. Secondly, high incompressibility also means that the displacement due to compressional wave is small. Hence, only the shear component of the wave field can be measured by transducers, whereas the compression component (including reflected waves generated by it) is considered negligible or indistinguishable from noise. In fact, no matter which dynamic elastography technique is developed, incompressibility is a basic premise.

3. It will be seen, in the following, that the incompressibility is the key problem of this PhD work. It is the origin of the technique but also the challenge in its modeling. In most analytical models, in order to simplify the problem, tissue are treated as perfectly incompressible solids, so the compressional wave cannot propagate. For numerical methods, particularly, Finite Element Method (FEM), incompressibility causes difficulty both in spatial and temporal integrations. ■

The improved 1D TE setup (Fig.1.2(b)) is the basis of the product Fibroscan® developed by the company *EchoSens* France *(echosens.com)*. This product is designed to characterize the fibrotic state of liver by its elasticity, recall Fig.1.1. However, it has also been used to determine the mechanical parameters of other types of tissues, such as skin [GEN 04] and muscle [GEN 05].

On the other hand, 1D TE makes the measurement only along a line, so it is not a strict imaging technique. Afterwards, TE has been been introduced for a two-dimensional (2D) imaging in 2002 [SAN 02a]. Shear waves are generated by a vibrator composed of two parallel rods as shown in Fig.1.4. The linear array of transducers is placed between the rods and tracks the shear wave propagation in the image area. Then, an inversion algorithm is used to recover elasticity from the measured data, so the shear modulus distribution is mapped quantitatively. With this technique, experiments provide good results on both homogeneous and heterogeneous media.

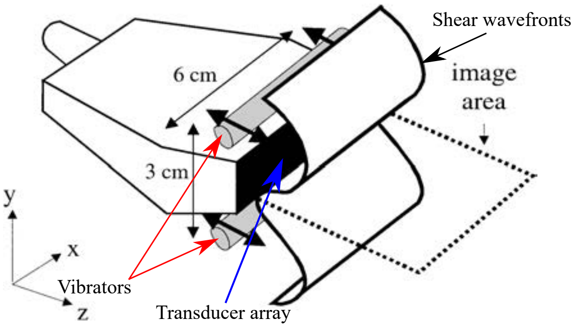

Figure 1.4: 2D transient elastography: Shear waves are generated using a vibrator composed of two parallel rods. The linear array of transducers is placed between the rods. The shear wave front has a cylindrical shape in the out-of plane direction. Source: [SAN 02a]

1.1.2.2 Supersonic Shear Imaging (SSI)

Supersonic Shear Imaging (SSI) is proposed in 2004 by Bercoff *et al.* [BER 04]. Instead of using a mechanical vibrator, SSI generates mechanical shear wave remotely by focusing ultrasound at a given location. As presented in Fig.1.5, the focal points move at a speed higher than the shear wave speed and 'push' inside the tissue successively (in this figure, 6 m/s versus 2 m/s). The resulting shear waves interfere constructively along a Mach cone creating two intense and quasi-plane shear waves propagating in opposite direction. The phenomenon is analogical with the 'sonic boom' created by a supersonic aircraft.

The shear wave propagation direction can be adjusted by the speed of the moving source. The ultrasound transducers are used to track the local tissue displacement and provide a full movie of the shear wave propagation through the tissue. After the measurement, a quantitative elasticity image is obtained by an inversion algorithm, which is similar to 2D transient elastography.

SSI allows generating shear wave remotely in tissue and avoids using heavy external vibrators. Based on SSI technique, the company SuperSonic Imagine *(supersonicimagine.com)* developed the product Aixplorer®, which is the only ultrasound scanner in the market able to quantitatively image elasticity in real time and in an operator-independent way [BRU 12].

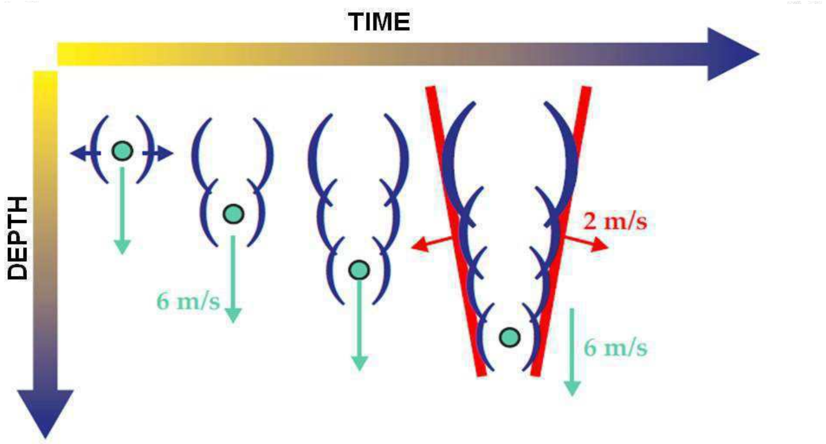

Figure 1.5: Generation of the supersonic shear source: the source is sequentially moved along the axis, creating two quasi-plane and intense shear waves. Source: [BER 04]

1.1.2.3 Magnetic Resonance Elastography (MRE)

In both TE and SSI techniques, the shear wave is measured by a ultra-fast ultrasonic scanning system which can generate images at a high-frame rate (up to 10000 images/s). Magnetic Resonance Elastography (MRE) is different: whether the shear wave is generated by a mechanical vibrator, or an acoustical radiation force, or even a cardiac motion [ZOR 15], the shear wave propagation is measured by a specially designed nuclear magnetic resonance sequence. Then, a similar inversion algorithm as in 2D TE is necessary to generate stiffness maps from the measured data.

One significant advantage of MRE is that it is capable to provide a 3D image of the tissue stiffness, which can cover an entire organ. Besides, contrary to ultrasound scanner, the tracking system is not limited by air or bone. As consequence, MRE is especially useful for brain examination. However, its disadvantage is the long acquisition time (about 20 minutes) which does not allow real time elasticity imaging.

1.1.3 Nonlinear elastography

All of the above mentioned techniques have been focused on measuring linear elastic property of tissue, *i.e.* Young's modulus. However, biological tissue exhibit a more complex mechanical behaviour, including viscosity, nonlinearity, anisotropy and heterogeneity, *etc*. Characterizing these properties may improve the diagnostic value of elastography when studied in combination with linear elastic modulus. It has been proved recently, that mechanical parameters, such as viscosity [SIN 05b] and anisotropy [SIN 05a], could help differentiating tissue. For example, clinicians could use elastic nonlinearity to discriminate benign and malignant breast tumors [KRO 98].

Dynamic elastography techniques give also particular contributions to this field, as presented in the following, a few nonlinear parameters have been assessed using shear waves. However, unlike linear elastic theory, countless nonlinear models have been proposed for biological tissues. Before characterizing the nonlinearity, the first step consists of choosing the most appropriate model for the examined tissue, secondly, the including parameters are identified by experimental data of elastography.

In the following, the second step *i.e.* the experiments of nonlinear elastography, is presented firstly, the choice of different material models will be presented in the next section (Chapter 1.2).

1.1.3.1 Measurement of viscosity

It is well known that soft tissues exhibit both elastic and viscous mechanical behaviours. Another main advantage of dynamic elastography methods is to potentially reveal the medium dynamic properties, such as viscosity.

Several investigators are actively developing methods to visualize viscoelasticity. For example, Asbach *et al.* [ASB 08] developed a multifrequency method to measure viscoelastic properties of normal liver tissue versus diseased liver tissue taken from patients with liver fibrosis. In the work of Catheline *et al.*[CAT 04], a plane monochromatic shear wave was generated, the dispersion curves of gelatin phantoms and *ex vivo* muscle were measured between 50 Hz and 500 Hz. It was demonstrated, for both tissues, that the attenuation coefficient increases with the frequency, see Fig.1.6. This result indicates that Voigt model (presented in section 1.2.3) seems to be more appropriate for the viscous property of tissues. Moreover, *In vivo*, Deffieux *et al.* [DEF 09] proposed to use SSI technique to conduct a shear wave spectroscopy experiment in the biceps brachii, abdominal muscle and liver of three healthy volunteers, showing important differences in the rheological behaviour for these different tissues.

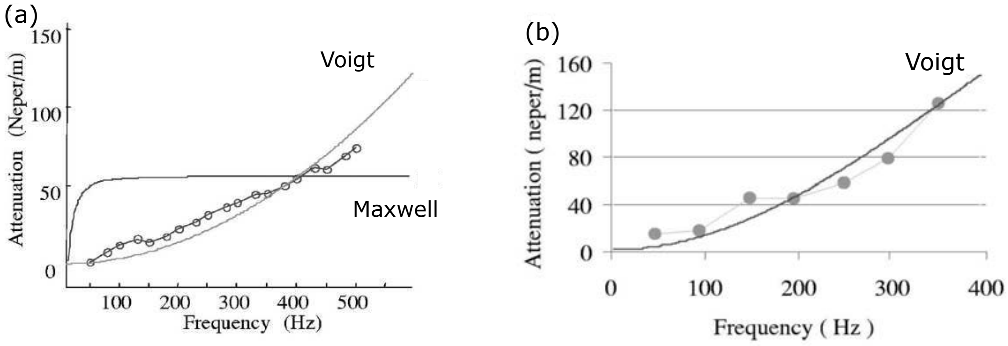

Figure 1.6: Transverse wave attenuation measurement *v.s.* excitation frequency. Circles represent experimental results and solid lines represent theoretical solutions. (a) For gelatin phantoms; (b) For beef muscle. Source: [CAT 04]

1.1.3.2 Measurement of nonlinearity

There are several possible ways to quantify nonlinearity in soft solids: propagation of shocked shear waves, nonlinear interaction between shear waves and acoustoelasticity.

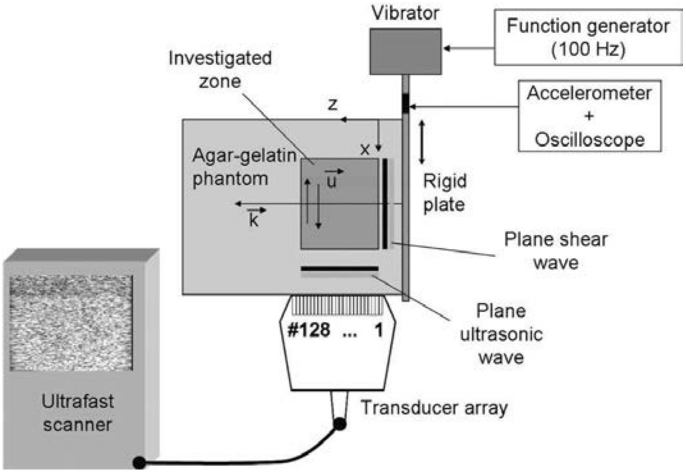

Figure 1.7: An ultrafast transducer array is applied on the bottom of the phantom. A rigid plate is connected to a vibrator to generate plane wave

In soft solids, due to very small shear wave speed c_S, the propagation of shear waves can easily reach nonlinear regime. This is characterized by Mach number defined as the ratio of the particle velocity to the wave speed. Dynamic elastography is able to generate waves with Mach number close to unity. With such a Mach number, nonlinearity has a big effect on the propagation of shear waves, which is observed by the modification of the shear waves shape.

Fig.1.7 represents a nonlinear elastography experiment [CAT 03b]. The low frequency shear wave is generated by shaking transversally a rigid plate applied on one side of the phantom with a vibrator. The transverse displacement field of the shear wave is measured in one dimension along the axis of the rigid plate. The source emitted by the vibrator is displayed in Fig.1.8 (left), it contains only the one fundamental frequency of 100 Hz. Then the particle velocity history measured at a point located 15 mm away from the source is displayed on the right, it is clear that the shape of the shear wave distorts during the propagation. Contrary to what is usually observed in 'hard solids', this distortion is dissymmetric. It is revealed by the presence of odd harmonics in the spectral domain, components at 300 Hz and 500 Hz. This observation is attributed to the cubic nonlinear effect in soft solids.

Based on this phenomenon, it is easy to design an experiment to characterize nonlinearity of soft solids: at the same level of amplitude, the more the shear wave distorts (*i.e.* the more harmonic waves are generated), the more nonlinear the medium is. Although the phenomenon is clearly observed, transferring this information into quantitative nonlinear parameters is still difficult, analytical nonlinear models are available only for very specific experimental conditions.

Up to now, the only contribution is reported by Rénier *et al.* [RÉN 08] on mimic phantoms. A nonlinear elastic coefficient is deduced by combining the nonlinear shear wave experiment with the results in acoustoelastic experiment presented in the following. However, it should be pointed out that the analytical model employed in this work has

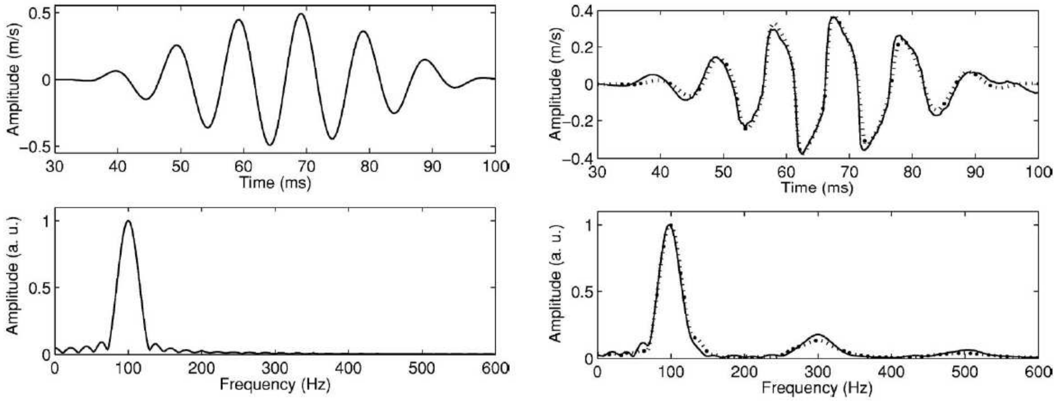

Figure 1.8: Source (left) and measured point (right) velocity history and their corresponding spectrum. The nonlinearity leads to the distortion on the wave shape and odd harmonic components in spectrum

limited applications, this will be deeply described in Chapter 2.

Acoustoelasticity is a different approach, it consists of measuring the speed of infinitesimal (linear) shear waves in pre-stressed solids. For a nonlinear material, the finite external load induces a change of the wave speed, so a quantitative evaluation of this change corresponds to measuring the nonlinearity. This theory has been established in solids since 1953 [HUG 53]. However, it was applied in soft solids (considered as nearly-incompressible solids) in recent years thanks to the development of dynamic elastography, where nonlinear elastic modulus is deduced from the change of the linear polarized shear wave speed as a function of the applied stress.

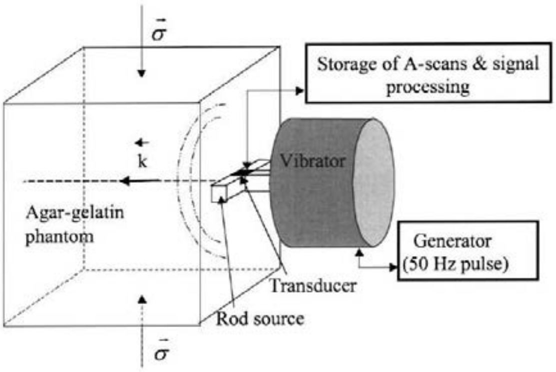

Figure 1.9: Acoustoelastic experimental setup. An homogeneous load is applied on the top of the phantom, a low frequency pulse propagates in the medium and the displacements are tracked by a transducer set in the middle of the rod. Source: [CAT 03a]

The first acoustoelastic analysis in soft solids was carried out by Catheline *et al.* [CAT 03a]. The experimental setup is presented in Fig.1.9. As in transient elastography, low frequency waves are generated by a mechanical vibrator and measured by an ultrasound transducer. An adjustable stress is applied by a water tank on the top of the phantoms. In the presented configuration, as the rod source is placed horizontally, it generates shear waves mainly polarized in the direction parallel to the load. By rotating the rod of 90°, a shear wave polarized perpendicularly to the stress direction is generated, and a different shear wave speed is obtained even the medium is naturally isotropic. This experiment was the first to quantitatively measure nonlinear elastic modulus of soft solids.

Afterwards, Gennisson *et al.* [GEN 07] extended this experiment by SSI technique, which is capable of generating quasi-plane shear waves. As described in Fig.1.10, SSI device is placed at three different positions surrounding the phantom, $\vec{k}$ represents the direction of shear wave propagation and $\vec{u}$ represents its polarization (vibration) direction. Using Sij for a shear wave propagating in i direction and polarizing in j direction, one can obtain shear waves: $S12$ or $S32$ in Fig.1.10(a), $S21$ or $S23$ in Fig.1.10(b) and $S13$ or $S31$ in Fig.1.10(c). This experiment setup contains all possible polarized shear waves in a uniaxially pre-stressed isotropic solid.

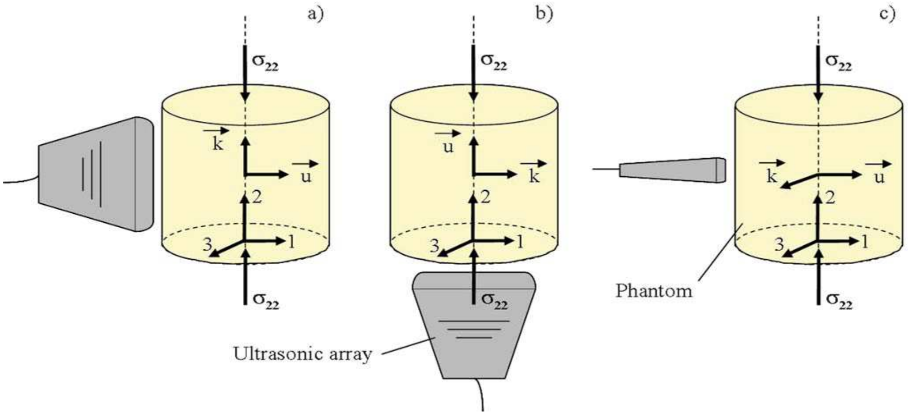

Figure 1.10: Acoustoelastic experimental setup. The three possible configurations generating the propagation of polarized shear waves in the phantom under uniaxial stress (axis-2). The three resulting shear waves are designated as: (a) $S12$ or $S32$, (b) $S21$ or $S23$, (c) $S13$ or $S31$. Source: [CAT 03a]

For real biological tissues, instead of measuring shear wave speeds with three different polarizations, one single polarization experiment under a varying uniaxial stress is sufficient to characterize the nonlinearity. Thus, *in vivo* assessment by this technique could be feasible. For example, Jiang *et al.* reported measurement of nonlinear elastic properties of *ex vivo* and *in vivo* tissue [JIA 15a, JIA 15b] very recently. The detail of acoustoelasticity will be presented in Chapter 3.

1.2 Continuum mechanics

Continuum mechanics plays an essential role in understanding and developing dynamic elastography. This section provides the mechanical background of elastography. Linear and nonlinear elastic theories[1] as well as viscoelasticity models are described. Some common material laws are listed, However, their development and implementation will be presented in the next chapter for the sake of clarity and illustration. More detailed description of continuous mechanics can be easily found in several books [BOW 11, BON 97, HOL 00].

1.2.1 Linear elasticity

When solids deform with a small amplitude, deformation can be described by engineering strain ε which is calculated from the displacement $\mathbf{u}$ and position $\mathbf{x}$:

$$\varepsilon_{ij} = \frac{1}{2}\left(\frac{\partial u_i}{\partial x_j} + \frac{\partial u_j}{\partial x_i}\right) \tag{1.2}$$

In classical linear elasticity, the behaviours of elastic materials can be described by a linear relationship between the stress $\boldsymbol{\sigma}$ and the engineering strain ε. This relationship is commonly known as the generalised Hooke's law:

$$\sigma_{ij} = C_{ijkl}\varepsilon_{kl} \tag{1.3}$$

where the elasticity tensor C_{ijkl} is a fourth order tensor. It contains 81 elastic coefficients, but due to symmetries, $C_{ijkl} = C_{klij} = C_{jikl} = C_{ijlk}$, so 21 are independent at most.

1.2.1.1 Isotropy

Isotropy is characterized by an identical behaviour in any material direction. Under the assumption of isotropic behaviour, only 2 independent constants are required in the elasticity tensor C_{ijkl}. There are various methods to define the two constants, they could be: the first and second Lamé constants (λ and μ); the bulk and shear modulus (K and μ) (so the shear modulus is indeed the second Lamé constant); Young's modulus and Poisson coefficient (E and ν).

Using Lamé constants, the relationship between stress and strain (Eq.1.3) for linear isotropic elastic materials is written by:

$$\sigma_{ij} = \lambda\varepsilon_{kk}\delta_{ij} + 2\mu\varepsilon_{ij} \tag{1.4}$$

---

[1] This chapter limits the discussion in the case of isotropy, anisotropic models will be described in Chapter 3.

where δ is the Kronecker symbol equal to 1 if $i = j$ and 0 otherwise. Lamé constants λ and μ can be expressed in terms of other constants which are more closely related to physical measurements by:

- Young's modulus $E = \frac{\mu(3\lambda+2\mu)}{\lambda+\mu}$
- Poisson coefficient $\nu = \frac{\lambda}{2(\lambda+\mu)}$
- Bulk modulus $K = \frac{3\lambda+2\mu}{3}$

1.2.1.2 Linear elastic waves

By combining Newton's second law and Hooke's law, the equation of motion is given by:

$$(\lambda + 2\mu)\nabla(\nabla \cdot \mathbf{u}) + \mu\nabla \times (\nabla \times \mathbf{u}) = \rho\frac{\partial^2 u}{\partial t^2} \tag{1.5}$$

In Eq.1.5, ∇ denotes the differential operator with respect to space. The first term $(\lambda + 2\mu)\nabla(\nabla \cdot \mathbf{u})$ accounts for the compressional/dilational part of the displacement field while the second term $\mu\nabla \times (\nabla \times \mathbf{u})$ accounts for the deviatoric part. From these two terms, the propagation speed of compressional wave c_P and shear wave c_S can be obtained:

$$c_P = \sqrt{\frac{\lambda + 2\mu}{\rho}} \tag{1.6}$$

$$c_S = \sqrt{\frac{\mu}{\rho}} \tag{1.7}$$

For plane waves, compressional wave is also called as *longitudinal* because the propagation direction is parallel to the polarization, and shear wave is called as *transversal* because the propagation direction is perpendicular to the polarization. For nonplane waves, this relation is not kept, compressional wave could be transversal and shear wave could also be longitudinal [CAT 15].

1.2.1.3 Incompressibility

It has been presented that biological tissues exhibit high incompressibility. In this sense, it is often useful to write the stress and strain measures as the sum of deviatoric and volumetric parts, the second part is also called the *spherical* part. The decompositions relationships are:

$$\begin{aligned} \boldsymbol{\sigma}^{vol} &= \frac{1}{3}tr(\boldsymbol{\sigma})\mathbf{I}, \quad \boldsymbol{\sigma}^{dev} = \boldsymbol{\sigma} - \boldsymbol{\sigma}^{vol} \\ \varepsilon^{vol} &= \frac{1}{3}tr(\varepsilon)\mathbf{I}, \quad \varepsilon^{dev} = \varepsilon - \varepsilon^{vol} \end{aligned} \tag{1.8}$$

where I is the second-order identity tensor and tr denotes the trace. Applying the decomposition of strain to Hooke's Law (Eq.1.3), it can also be obtained:

$$\sigma = 3K\varepsilon^{vol} + 2\mu\varepsilon^{dev} \tag{1.9}$$

The expression is separated to a part related to volume change and a part related to shape change. It can be seen that bulk modulus K characterizes only how the tissue volume changes in response to a compression, and the shear modulus μ quantifies how tissue responds to shear strain.

As above mentioned, quasi incompressibility is the basic condition of elastography. Fig.1.11 displays the relationship between the compressional wave speed and the level of compressibility (presented by Poisson coefficient), the shear wave speed c_S is set to unity. It can be seen that, in order to keep the compressional wave speed realistic in soft tissue, *i.e.* $c_P = 1000 - 1500\ m/s$ [PAL 05], the Poisson coefficient should be very close to 0.5. Namely, it includes five or six 9 after 0.4.

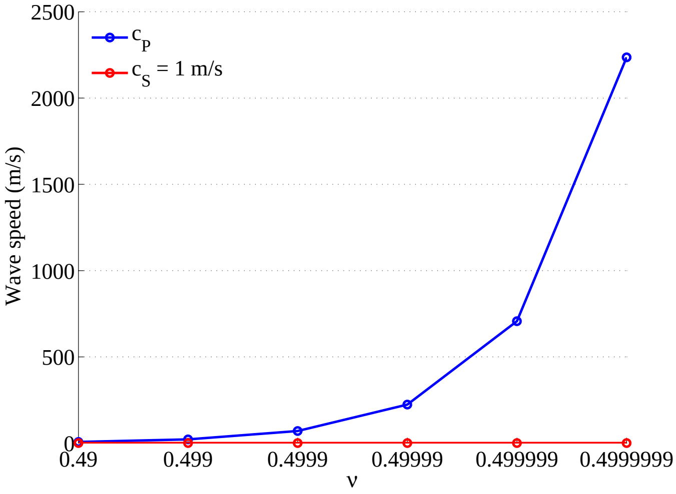

Figure 1.11: Compressional and shear wave speed as a function of Poisson coefficient. $\rho = 1000\ kg/m^3$, $\mu = 1\ kPa$.

1.2.2 Nonlinear elasticity

To characterize finite deformation, it is necessary to distinguish the undeformed configuration (Ω_0) and the deformed configuration (Ω) of the considered continuum (Fig.1.12). In contrast to linear elasticity, many different measures of strain and stress are used in nonlinear continuum mechanics to describe the same process. Some measures are in undeformed configuration and others are in deformed configuration. In the following, only measures in the undeformed configuration (Ω_0) are presented, they will be conjugate with the Total Lagrangian (TL) formulation in finite element method presented in the next section.

Suppose that a solid is subjected to a displacement field $\mathbf{u}$ at a material point of coordinate $\mathbf{X}$ in the reference configuration, as shown in Fig.1.12. The deformation gradient tensor $\mathbf{F}$ can be expressed as:

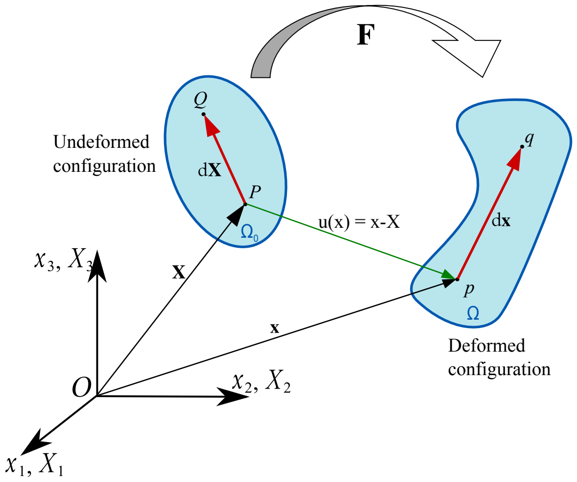

Figure 1.12: Deformation of a continuum body.

$$F_{ij} = \frac{\partial u_i}{\partial X_j} + \delta_{ij} \tag{1.10}$$

The Jacobian measures the volume change produced by a deformation, which is defined as:

$$J = det(\mathbf{F}) \tag{1.11}$$

If a material is fully incompressible, its volume remains constant. This corresponds to $J = 1$.

The Green (Green-Lagrange) strain **E** is a measure in the undeformed configuration, it is defined as:

$$\mathbf{E} = \frac{1}{2}(\mathbf{C} - \mathbf{I}) \tag{1.12}$$

where $\mathbf{C} = \mathbf{F}^T\mathbf{F}$ is the right Cauchy-Green deformation tensor. The Green strain tensor can also be expressed in terms of displacement gradient by:

$$E_{ij} = \frac{1}{2}(\frac{\partial u_i}{\partial X_j} + \frac{\partial u_j}{\partial X_i} + \frac{\partial u_k}{\partial X_i}\frac{\partial u_k}{\partial X_j}) \tag{1.13}$$

For small deformations and rotations, the Green strain tensor **E** can be approximated by the engineering strain ε in linear elastic theory.

Hyperelastic constitutive laws are used to model elastic behaviours when subjected to large strain. They account for material's nonlinear behaviour but also the nonlinearity from geometrical change. The initial application of hyperelastic laws is to model the rubber materials, but they can also be used for biological tissues.

Generally, hyperelastic models are constructed by specifying a strain energy W as a function of deformation. The stress-strain law is then deduced by differentiating the strain energy density:

$$\mathbf{S} = \frac{\partial W}{\partial \mathbf{E}} = 2\frac{\partial W}{\partial \mathbf{C}} \tag{1.14}$$

Where **S** is the second Piola-Kirchhoff (PK-2) stress which is conjugate to the Green strain tensor **E**. This definition ensures that the material is independent of the deformation path and is determined only by the value of the strain energy W.

The two following sections will describe the fundamental of the nonlinear elasticity, as they are usually presented in the continuum mechanics community (hyperelasticity) and the acoustics community (weakly nonlinear theory).

1.2.2.1 Hyperelasticity

In this section, some general features of isotropic hyperelastic materials are described and then examples of hyperelastic constitutive models which are widely used in biomechanical modeling are described.

For an isotropic hyperelastic material, the strain energy density W is defined as a function of the three principle invariants of the strain tensor **C**:

$$W = W(I_1, I_2, I_3) \tag{1.15}$$

Where the principle invariants are defined as

$$\begin{aligned} I_1 &= tr(\mathbf{C}) \\ I_2 &= \frac{1}{2}[(tr(\mathbf{C})^2 - tr(\mathbf{C}^2)] \\ I_3 &= det\mathbf{C} = J^2 \end{aligned} \tag{1.16}$$

Like in linear elasticity, it is useful to separate the effects associated to volumetric and deviatoric deformation for nearly incompressible materials. So the decoupled form of W is:

$$W = W^{dev}(\bar{I}_1, \bar{I}_2) + W^{vol}(J) \tag{1.17}$$

where $\bar{I}_1$ and $\bar{I}_2$ represent an alternative set of invariants of **C** and remain constant under a pure volume change.

$$\begin{aligned} \bar{I}_1 &= J^{-2/3} I_1 \\ \bar{I}_2 &= J^{-4/3} I_2 \end{aligned} \tag{1.18}$$

In Eq.1.17, the first term W^{dev} contains the strain energy associated to deviatoric deformation. It is the core of nearly incompressible hyperelastic model because it characterizes the nonlinear behaviour of the tissue. Normally, it contains more than one parameter.

The second term $W^{vol}(J)$ represents the strain energy associated to volumetric deformation. Because material hardly deforms this way, the corresponding nonlinear behaviour is neglected. Generally, it contains only one material parameter: the bulk modulus K. The value of K is much larger than other parameters. In FEM, it is used as a penalty function to enforce incompressibility. In the following, we use the simplest expression of W^{vol} which is:

$$W^{vol}(J) = \frac{1}{2}K(J-1)^2 \tag{1.19}$$

But alternative expressions could be:

$$\begin{aligned} W^{vol}(J) &= \frac{1}{2}K(lnJ)^2, \\ \text{or} \quad W^{vol}(J) &= K(JlnJ - J + 1) \end{aligned} \tag{1.20}$$

Now some specific models which are widely used in biomechanics modeling are presented:

neo-Hookean solid

$$W = \frac{\mu}{2}(\bar{I}_1 - 3) + \frac{K}{2}(J-1)^2 \tag{1.21}$$

where μ and K are material properties. As the simplest hyperelastic model, the involved parameters are the same as in linear elasticity. However, it still has a nonlinear behaviour because the strain is not linear.

Mooney-Rivlin solid

$$W = c_1(\bar{I}_1 - 3) + c_2(\bar{I}_2 - 3) + \frac{K}{2}(J-1)^2 \tag{1.22}$$

where c_1, c_2, and K are material properties. For small deformations, the shear modulus of the solid is $\mu = c_1 + c_2$.

Generalized polynomial solid

$$W = \sum_{i+j=1\ (i,j\geqslant 0)}^{N} c_{ij}(\bar{I}_1 - 3)^i(\bar{I}_2 - 3)^j + \frac{K}{2}(J-1)^2 \tag{1.23}$$

where c_{ij} and K are material properties. For small strains, the shear modulus can be written $\mu = 2(c_{01} + c_{10})$. Both neo-Hookean and Mooney-Rivlin solids are special cases of this law (with $N = 1$ and appropriate choices of c_{ij}). Values of $N > 2$ are rarely used, because it is difficult to fit such a large number of material properties to experimental data.

Fung-type solid
Fung-type model [FUN 90] is a famous model in biomechanics.

$$W = \frac{1}{2}[a(\bar{I}_1 - 3) + b(exp(c(\bar{I}_1 - 3)) - 1)] + \frac{K}{2}(J-1)^2 \tag{1.24}$$

where a, b, c and K are material parameters.

The above-mentioned models are available for almost all the FEM commercial software, such as ABAQUS, ANSYS, LS-DYNA.

1.2.2.2 Weakly nonlinear theory

Weakly nonlinear theory [LAN 86] is used to describe small, but not infinitesimal deformation of solids. As this description is well suited for finite amplitude waves, this model is widespread in acoustic. Assuming that the scalar strain energy density function W can be approximated by a Taylor series expansion in terms of Green strain $\mathbf{E}$, W can be expressed in index notation as:

$$W \simeq \frac{1}{2!}C_{ijkl}E_{ij}E_{kl} + \frac{1}{3!}C_{ijklmn}E_{ij}E_{kl}E_{mn} + \frac{1}{4!}C_{ijklmnpq}E_{ij}E_{kl}E_{mn}E_{pq} + O(E^5) \tag{1.25}$$

where the second, third and fourth order of elasticity tensors are defined as the partial derivatives of the internal energy with respect to the Green strain:

$$\begin{aligned} C_{ijkl} &= (\frac{\partial^2 W}{\partial E_{ij}E_{kl}})_{E=0} \\ C_{ijklmn} &= (\frac{\partial^3 W}{\partial E_{ij}E_{kl}E_{mn}})_{E=0} \\ C_{ijklmnpq} &= (\frac{\partial^4 W}{\partial E_{ij}E_{kl}E_{mn}E_{pq}})_{E=0} \end{aligned} \tag{1.26}$$

Note that Eq.1.25 is available for both isotropic and anisotropic materials. Due to symmetry, in the most general case, C_{ijkl} contains 21 independent constants as linear elastic theory, C_{ijklmn} and $C_{ijklmnpq}$ contain 56 and 126 independent constants respectively [GIA 16a].

For isotropic solids, another type of invariants defined by Landau and Lifshitz [LAN 86] are used:

$$\begin{aligned} I &= tr(\mathbf{E}) \\ II &= tr(\mathbf{E}^2) \\ III &= tr(\mathbf{E}^3) \end{aligned} \tag{1.27}$$

Destrade *et al.* [DES 10a] provides the general relationship between I_1, I_2 and I_3 of Eq.1.16 and I, II and III:

$$
\begin{aligned}
I_1 &= 3+2I \\
I_2 &= 3+4I-2II+2I^2 \\
I_3 &= 1+2I+2I^2-2II+\frac{4}{3}I^3-4I\cdot II+\frac{8}{3}III
\end{aligned}
\tag{1.28}
$$

It should be emphasized that, in these expressions, I_1, I_2, I_3 are the principal invariants of $\mathbf{C}$, but I, II and III are Landau invariants of $\mathbf{E}$.

The internal energy can therefore be developed as a function of Landau invariants. I, II and III are at first, second and third order. The development up to the fourth order appears as a linear combination of I^2 and II at the second order; III, $I\cdot II$ and I^3 at the third order; and I^4, II^2, $I\cdot III$ and $I^2\cdot II$ at the fourth order. It can be expressed in the form of:

$$
W=\frac{\lambda}{2}I^2+\mu II+\frac{A}{3}III+BI\cdot II+\frac{C}{3}I^3+EI\cdot III+FI^2\cdot II+GII^2+HI^4 \tag{1.29}
$$

The model contains two second-order elastic moduli λ and μ (still called Lamé coefficients), three third-order elastic constants A, B and C, and four forth-order elastic constants E, F, G and H.

Remark:

It is necessary to distinguish the second order Landau theory with the linear elastic theory. For isotropic linear elasticity, the internal energy could be expressed as

$$
W=\frac{\lambda}{2}tr(\varepsilon)^2+\mu tr(\varepsilon^2) \tag{1.30}
$$

The above expression is equivalent to the linear stress and strain relation in Eq.1.4. The second order Landau theory replaces the small strain tensor by the Green strain. It can be written by:

$$
W=\frac{\lambda}{2}tr(\mathbf{E})^2+\mu tr(\mathbf{E}^2) \tag{1.31}
$$

This model can be seen as a straightforward generalization of linear elasticity to large deformations. As a result, Eq.1.31 is not a fully linear material model, the geometrical nonlinearity contained in Green strain is kept in the model. This point will be reflected in nonlinear shear wave presented in the next chapter. In fact, the second order Landau model is equivalent to *Saint Venant-Kirchhoff material* in continuum mechanics [BON 97]. ■

1.2.2.3 Incompressible Landau model

Eq.1.29 contains the internal energy due to both the volumetric and deviatoric deformations. For soft solids considered as nearly incompressible, Catheline *et al.* [CAT 03a] identified the nonlinear elastic constants of mixed gel at the third order, so A, B and C. The value of A is in the order of kPa, whereas the values of B and C are in the order of GPa. The phenomenon is similar to the relationship between λ and μ. It is considered that, up to third order, shear effects in nearly incompressible solids are described entirely by the two small constants μ and A.

The huge difference of elastic constants poses difficulties when one attempts to model nonlinear effects associated with shear deformation in soft solids. Small errors in identified values of the large constants λ, B, and C easily alter the effect of shear deformation.

To avoid this difficulty, it is necessary to develop an uncoupled strain energy function as in continuum mechanics, where the constants accounting for shear effects are of comparable order. Hamilton *et al.* [HAM 04] developed such a function which is equivalent to the fourth order Landau law (Eq.1.29), but the volumetric and deviatoric components are separated. The deviatoric part W^{dev} is expressed by:

$$W^{dev} = \mu II + \frac{A'}{3} III + D II^2 \tag{1.32}$$

To obtain this expression, we recall the third relation in Eq.1.28, and assuming $I_3 = 1$ (fully incompressible), we can express the invariant I as combination of II and III:

$$I = -I^2 + 2II - \frac{2}{3} I^3 + 2I \cdot II - \frac{4}{3} III \tag{1.33}$$

By recursion, one obtains a development of I in the incompressible case until the fourth order in the form [HAM 04, JAC 07]:

$$I = II - \frac{4}{3} III + II^2 + O(\mathbf{E}^5) \tag{1.34}$$

By substituting this expression in the development of internal energy W (Eq.1.29), Eq.1.32 is recovered with the following relations:

$$\begin{aligned} A' &= A \\ D &= \frac{\lambda}{2} + B + G \end{aligned} \tag{1.35}$$

Contrary to the models in the previous section, Landau model has not been largely considered in the mechanical field. For example, it is not available in any commercial FEM code. The development and implementation of this model in FEM contest remains to be done.

1.2.3 Viscoelasticity

Elastic models described in the previous sections assume that the deformations are reversible. However, energy dissipation generates irreversible phenomena in biological tissues. The dissipation is particularly complex in solids, it can have various origins: viscosity, thermal conduction, molecular relaxation, *etc.*

For an isotropic, nearly-incompressible material, assuming the viscous stress is proportional to strain rate, their relationship can be written in terms of deviatoric and volumetric part as the elasticity, that is:

$$\boldsymbol{\sigma}^{visco} = 2\eta\dot{\varepsilon}^{dev} + \xi\dot{\varepsilon}^{vol} \tag{1.36}$$

where η and ξ are the coefficients of bulk and shear viscosity.

For studies on viscoelastic materials, authors linear empirical laws are generally used. In terms of modeling, the two simplest models are introduced (see Fig.1.13): Voigt (Kelvin-Voigt) model and Maxwell model.

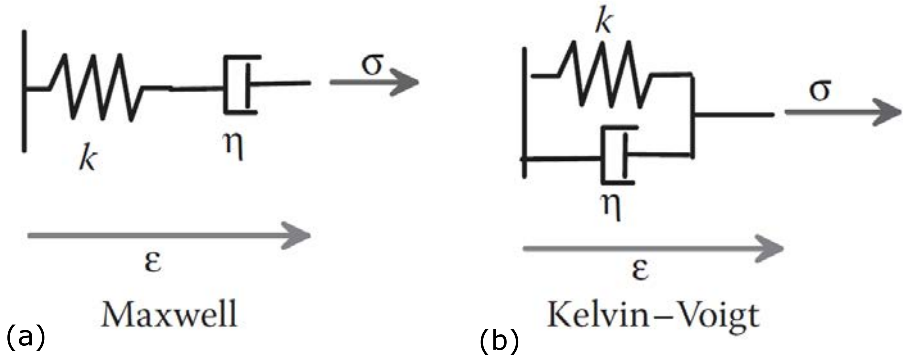

Figure 1.13: Two simplest viscoelastic models. (a) Maxwell; (b) Kelvin-Voigt

The Voigt model is composed of a spring, with spring constant *k*, and a dashpot, with viscosity coefficient η in parallel, while the Maxwell model is composed of a spring and a dashpot in series. Elements in series have the same stress, while their strain is different. On the other hand, elements in parallel feel the same strain, while the stresses differ. Based on these principles, the equilibrium equation for each model can be presented, for Maxwell model

$$k\sigma + \eta\frac{d\sigma}{dt} = k\eta\frac{d\varepsilon}{dt} \tag{1.37}$$

And for Voigt model

$$\sigma = k\varepsilon + \eta\frac{d\varepsilon}{dt} \tag{1.38}$$

Although the Maxwell model is more often used for solids, for liquid-like solids such as biological tissues, the Voigt model seems more convenient (see Sec.1.1.3.1). So for multidimensional cases, stress can be expressed as the sum of elastic part and the viscous part.

$$\boldsymbol{\sigma}^{total} = \boldsymbol{\sigma}^{elas} + \boldsymbol{\sigma}^{visco} \tag{1.39}$$

In this work, Voigt model is generalized into nonlinear strain domain and considered for nonlinear shear waves in soft solids, more details will be presented in Chapter 2.

1.3 Finite Element Method (FEM)

Apart from some very simple situations, the partial differential equations resulting from a continuum mechanical boundary value problem can only be solved with numerical methods. The complex geometry of the studied object and the employed constitutive equations additionally complicate the solution of the problem.

Numerical method used for biomechanical models are dominated by (displacement based) finite element because they can accurately and easily model detailed structure. For elastography, FEM is capable of modeling complicated geometries, material behaviours, heterogeneities, pre-stress, and boundary conditions of soft tissue. In the literature, Chen *et al.* [CHE 05, CHE 06] investigated the effects of boundary conditions, excitation frequency using simple FEM models. To take into account the heterogeneity (*i.e.* tumours in healthy tissue), 2D [PAL 05] and 3D [LEE 12] finite element models have been proposed.

On the other hand, FEM is also a common method for solving an inverse problem to reconstruct the stiffness map from measured displacements in dynamic elastography [PAR 09, ZHA 15]. This problem has been solved with both direct and iterative FEM schemes, each of these methods has its own advantages and disadvantages which are examined by Honarvar *et al.* [HON 16].

Meanwhile, it is necessary to mention other numerical methods on the contribution of elastodynamics modeling, especially for nearly incompressible materials. For example, focused shock shear waves in brain have been investigated with finite difference method [GIA 16b]; Bruel *et al.* [BUR 12] have proposed a potential based finite element method in which the compressional and shear waves are totally decoupled. Moreover, spectral element method has been studied for nearly incompressible materials in [PEE 14].

In this section, only forward displacement based FEM problems are considered, a brief introduction is given to a dynamic finite element code. The theory presented in this section is covered in a more comprehensive manner by [ZIE 00]

1.3.1 Problem description

For the sake of simplicity, the problem is described under the assumption of infinitesimal strain. Let the region of interest be defined as Ω ($\Omega \equiv \Omega_0$). The displacement field be defined as $\mathbf{u}(\mathbf{x},t)$, which depends on position $\mathbf{x} \in \Omega$ ($\mathbf{x} \equiv \mathbf{X}$) for any given time $t \in [0,T]$.

$$\begin{array}{ll} \rho\ddot{\mathbf{u}} = div(\boldsymbol{\sigma}) + \mathbf{f}_V & \text{in } \Omega \times [0,T] \\ \mathbf{u} = \bar{\mathbf{u}} & \text{over } \partial\Omega_u \times [0,T] \\ \boldsymbol{\sigma} \cdot \mathbf{n} = \mathbf{f}_S & \text{over } \partial\Omega_f \times [0,T] \\ \{\mathbf{u}, \dot{\mathbf{u}}\} = \{\mathbf{u}_0, \mathbf{v}_0\} & \text{in } \Omega|_{t=0} \end{array} \tag{1.40}$$

where $\mathbf{f}_V$ indicates the body force, $\mathbf{f}_S$ is the surface load, $\mathbf{n}$ is the unit normal to the boundary $\partial\Omega_f$, $\mathbf{u}_0$ and $\mathbf{v}_0$ are the initial displacement and velocity, respectively.

The first equation of System(1.40) represents the momentum balance. The second and the third ones denote essential and natural boundary conditions, respectively. The fourth one denotes initial conditions. The prescribed boundary displacements are applied to the boundary $\partial\Omega_u$ and the prescribed tractions are applied to the boundary $\partial\Omega_f$. The union between $\partial\Omega_u$ and $\partial\Omega_f$ constitutes the entire boundary of the problem $\partial\Omega$, so that $\partial\Omega_u \cup \partial\Omega_f = \partial\Omega$ and $\partial\Omega_u \cap \partial\Omega_f = \emptyset$.

The problem introduced in System1.40 is rewritten in the weak formulation as find $\mathbf{u}(\mathbf{x},t)$ such that:

$$\begin{aligned} \int_{\Omega} (\rho\ddot{\mathbf{u}} \cdot \delta\mathbf{u} + \boldsymbol{\sigma}(\mathbf{u}) : \varepsilon(\delta\mathbf{u}))d\Omega = \int_{\Omega} \mathbf{f}_V \cdot \delta\mathbf{u} d\Omega + \int_{\partial\Omega_f} \mathbf{f}_S \cdot \delta\mathbf{u} d\Gamma \\ \forall\delta\mathbf{u} = \mathbf{0} \text{ over } \partial\Omega_u \times [0,T] \end{aligned} \tag{1.41}$$

where the symbol : indicates a scalar product between two tensors of order 2.

A displacement-based finite element method [ZIE 00] is employed in order to numerically integrate in space the weak formulation of the problem in Eq.1.41 via mesh Ω^h, so that:

$$\mathbf{u}(\mathbf{x},t) = \phi(\mathbf{x})\mathbf{U}(t) \tag{1.42}$$

where $\phi(\mathbf{x})$ denotes the finite elements space discretization and $\mathbf{U}(t)$ indicates the displacements variables.

For simplicity and without loss of generality, we consider a linear elastic system with damping, the well-known transient FEM model can be obtained as follows:

$$\begin{aligned} &\mathbf{M}\ddot{\mathbf{U}}(t) + \mathbf{C}\dot{\mathbf{U}}(t) + \mathbf{K}\mathbf{U}(t) = \mathbf{F}^{ext}(t) && \text{in } \Omega^h \times [0,T] \\ &\mathbf{U} = \bar{\mathbf{U}} && \text{over } \partial\Omega_u^h \times [0,T] \\ &\{\mathbf{U}, \dot{\mathbf{U}}\} = \{\mathbf{U}_0, \dot{\mathbf{V}}_0\} && \text{in } \Omega|_{t=0} \end{aligned} \tag{1.43}$$

where $\mathbf{K}$ is the linear stiffness matrix (nonlinear cases will be detailed further), $\mathbf{M}$ is the mass matrix, the damping matrix $\mathbf{C}$ is included for generality. $\mathbf{F}^{ext}$ is the external force vector. $\mathbf{U}_0$ and $\mathbf{V}_0$ are the initial nodal displacements and velocities, respectively.

1.3.2 Time integration methods

Time integration methods for semi-discretised finite element equation (Eq.1.43) may be separated in implicit methods and explicit methods. In implicit methods, the solution at time $t + \Delta t$ is based on the equilibrium conditions at time $t + \Delta t$ whereas explicit integration is based on equilibrium at time t. Implicit integration schemes are unconditionally stable whereas explicit time integration schemes are subjected to mostly strict stability conditions.

Examples of both implicit and explicit integration methods can be derived from the *Newmark family*, which is based on a key assumption for the calculation of displacement and velocity, expressed as:

$$\begin{aligned}\mathbf{U}_{t+\Delta t} &= \mathbf{U}_t + \Delta t\dot{\mathbf{U}}_t + \frac{\Delta t^2}{2}[(1-2\beta)\ddot{\mathbf{U}}_t + 2\beta\ddot{\mathbf{U}}_{t+\Delta t}] \\ \dot{\mathbf{U}}_{t+\Delta t} &= \dot{\mathbf{U}}_t + \Delta t[(1-\gamma)\ddot{\mathbf{U}}_t + \gamma\ddot{\mathbf{U}}_{t+\Delta t}]\end{aligned} \tag{1.44}$$

where $\mathbf{U}_{t+\Delta t}$, $\dot{\mathbf{U}}_{t+\Delta t}$ and $\ddot{\mathbf{U}}_{t+\Delta t}$ are the time discretised approximation of the displacement, velocity and acceleration at time $t+\Delta t$. The Newmark parameters β and γ dictate the scheme properties, such as stability, accuracy and efficiency.

Consider the classical implicit method, also refered to as constant average acceleration method: it takes $\beta = 1/4$ and $\gamma = 1/2$. Introducing these parameters in the above expression and combining with the semi-discretised Equation 1.43, we obtain

$$(\frac{4}{\Delta t^2}\mathbf{M} + \frac{2}{\Delta t}\mathbf{C} + \mathbf{K})\mathbf{U}_{t+\Delta t} = \mathbf{F}^{ext}_{t+\Delta t} + \mathbf{M}(\frac{4}{\Delta t^2}\mathbf{U}_t + \frac{4}{\Delta t^2}\dot{\mathbf{U}}_t + \ddot{\mathbf{U}}_t) + \mathbf{C}(\frac{2}{\Delta t}\mathbf{U}_t + \dot{\mathbf{U}}_t) \tag{1.45}$$

which may be solved for the unknown displacements $\mathbf{U}_{t+\Delta t}$. Clearly, this requires the solution of a set of simultaneous equations due to the presence of the non-diagonal stiffness matrix $\mathbf{K}$ on the left hand side of the equation. For nonlinear problems, $\mathbf{K}$ is a function of $\mathbf{U}_{t+\Delta t}$, so an iterative algorithm (for example, Newton-Raphson) is required. Hence, linearized systems should be solved several times until equilibrium (Eq.1.45) is reached. The main advantage of the implicit method is the unconditional stability, FE simulations in implicit are meaningful for any choice of time step Δt. However, it should be mentioned that accuracy and convergence requirements also limit the time step.

The central difference method is the most commonly used explicit scheme in FEM. It can be derived from the Newmark family by setting $\beta = 0$ and $\gamma = 1/2$, expressions for acceleration and velocity are:

$$\begin{aligned}\ddot{\mathbf{U}}_t &= \frac{1}{\Delta t^2}(\mathbf{U}_{t-\Delta t} - 2\mathbf{U}_t + \mathbf{U}_{t+\Delta t}) \\ \dot{\mathbf{U}}_t &= \frac{1}{2\Delta t}(\mathbf{U}_{t+\Delta t} - \mathbf{U}_{t-\Delta t})\end{aligned} \tag{1.46}$$

Substituting these expressions into the semi-discretised Equation 1.43 at time t, we obtain

$$(\frac{1}{\Delta t^2}\mathbf{M} + \frac{1}{2\Delta t}\mathbf{C})\mathbf{U}_{t+\Delta t} = \mathbf{F}^{ext}_t - (\mathbf{K} - \frac{2}{\Delta t^2}\mathbf{M})\mathbf{U}_t - (\frac{1}{\Delta t^2}\mathbf{M} - \frac{1}{2\Delta t}\mathbf{C})\mathbf{U}_{t-\Delta t} \tag{1.47}$$

which can be solved for $\mathbf{U}_{t+\Delta t}$. In FE codes, $\mathbf{K}\mathbf{U}_t$ is replaced by internal nodal force $\mathbf{F}^{int}_t$, it is calculated at element level and then assembled as a vector. Hence, there is not necessary to construct and save a heavy global stiffness matrix, this is even more valuable for nonlinear problems because the stiffness matrix $\mathbf{K}$ changes at every time step.

For short, fast dynamic (for example, wave propagation) problems, it is appropriate to neglect structural damping (not material damping), then the equations simplify to give

$$\mathbf{U}_{t+\Delta t} = \Delta t^2 \mathbf{M}^{-1}(\mathbf{F}_t^{ext} - \mathbf{F}_t^{int}) + 2\mathbf{U}_t - \mathbf{U}_{t-\Delta t} \tag{1.48}$$

If the mass matrix $\mathbf{M}$ is diagonal, *i.e*, using a lumped mass matrix, the matrix inversion is trivial. Moreover, note that the nonlinearity ($\mathbf{F}_t^{int}$) present on the right-hand side only, there is no iterative procedure to achieve the equilibrium. Finally, the explicit method tends to be very efficient at each time step.

Generally, due to different numerical properties, the explicit method is regarded as the most appropriate time integration method for wave propagation problems, especially when the nonlinearity is introduced.

1.3.3 Critical time step

The conditional stability of the algorithm is the major drawback of the central difference explicit method. That is, if the time step Δt is set larger than critical value Δt_{crit}, the solution will exhibit instability, rendering the results meaningless. This critical time step is given by [HUG 12]

$$\Delta t_{crit} \leq \frac{2}{\omega_{max}} \tag{1.49}$$

where ω_{max} is the maximum eigenfrequency of the system. The eigenfrequencies of a linear system are solutions of the generalised eigenvalue problem

$$(\mathbf{K} - \omega_i^2 \mathbf{M})\mathbf{u}_i = \mathbf{0} \tag{1.50}$$

where the eigenvectors $\mathbf{u}_i$ and corresponding eigenfrequencies ω_i form the n eigensolutions $(\mathbf{u}_i, \omega_i)$. These eigensolutions are assumed to be ordered such that $\omega_1 \leq \omega_2 \leq \ldots \leq \omega_n$, so that $\omega_{max} = \omega_n$. The eigenvalues of the system λ_i are related to the eigenfrequencies by $\lambda_i = \omega_i^2$.

The time step limit (Eq.1.49) is referred to as *Courant-Friedrich-Lewy* (CFL) condition. For a solid mechanics FE problem, the maximum eigenfrequency is dependent on the material properties and the FE mesh. In practice, the maximum eigenfrequency ω_{max} of an complete FE system can only be obtained numerically and it could be expensive for large systems. Hence, Eq.1.49 is usually replaced by the following simplified expression for engineering applications:

$$\Delta t_{crit} \leq \frac{L_{min}^e}{c_P} \tag{1.51}$$

where L_{min}^e is the characteristic length of the smallest element, c_P the compressional wave speed of the solid. This equation means that the time step must be smaller than the time required by a compressional stress wave to cross the smallest element of the mesh. Hence the time step is controlled by the compressional wave speed. For nearly incompressible materials, the stable time step is extremely small, this will be the key problem in Chapter 4 and 5.

1.4 Novelty of this work

Elastography applications require the use of accurate and efficient FEM models to simulate the propagation of shear waves in soft media. These models are necessary to improve post-processing of experimental results, to reconstruct viscoelasticity of heterogeneous tissues, to analyse influencing factors such as boundary conditions, internal pressure in organs, *etc.* Furthermore, FEM simulations can be of considerable value to test the reconstruction algorithm used to process elastography images, and ensure that those do not alter speed measurement and therefore, elasticity estimation.

The objective of this PD work is to provide an accurate and efficient simulation for dynamic elastography. The two main points addressed in this thesis are:

1. The development of an accurate material model for investigating the propagation of shear waves in soft tissues, that can be viscous, nonlinear elastic, heterogeneous, anisotropic and pre-stressed;

2. The development of efficient numerical methods to overcome the excessively small time step in explicit FEM simulations due to incompressibility.

Point 1 will be addressed in Chapter 2 and 3. Chapter 2 presents the development of the weakly nonlinear theory in the FEM formulation. The corresponding simulations provide a reliable guideline to characterize the nonlinear elastic parameters of soft tissue by finite amplitude wave; Chapter 3 focuses on nonlinear elastography by acoustoelastic effect. In this case, isotropic materials are considered extrinsically transversely isotropic after a uniaxial pre-stress. In order to fully understand this phenomenon, intrinsically transversely isotropic materials, *e.g.* muscles, are also introduced.

Point 2 will be addressed in Chapter 4 and 5. In Chapter 4, we propose a new selective mass scaling method in which the time step of the explicit scheme is no longer limited by the compressional wave speed but by the shear wave speed. A significant reduction of CPU time is obtained with a good accuracy for elastography simulations which is classified into transient dynamic problem of nearly incompressible materials. Chapter 5 describes an alternative numerical method for the same problem. This methods treats shear wave in the explicit method but compressional wave in the implicit method. Finally, it has similar performance with the selective mass scaling method. The method was initially proposed by Lahiri *et. al* [LAH 05], in our work, it is generalized into quadrilateral/hexahedral elements. Its applications in elastography simulations are also discussed.

The manuscript ends with a conclusion and perspectives for this work.

Chapter 2

Nonlinear shear waves in soft tissues

Most of the work presented in this chapter is included in the paper submitted to *International Journal for Numerical Methods in Biomedical Engineering [YE ew] (under review).*

Contents

2.1 Introduction 35

2.2 Material modeling 36

2.2.1 Hyperelasticity 36

2.2.2 Comparison 38

2.2.3 Voigt viscoelasticity 42

2.3 Simulations of nonlinear shear wave 44

2.3.1 Preliminary study: choose the compressible parameter 44

2.3.2 Plane wave 44

2.3.3 Nonplane wave 49

2.3.4 Wave interaction 51

2.3.5 Discussion 51

2.4 Parametric study 53

2.4.1 Analytical formulation 53

2.4.2 Effect of amplitude 54

2.4.3 Effect of frequency 55

2.4.4 Effect of viscosity 55

2.4.5 Effect of the first nonlinear elastic parameter γ 56

2.4.6 Effect of the second nonlinear elastic parameter ζ 57

2.4.7 Discussion 58

2.4.8 Sign of the first nonlinear elastic parameter γ 59

2.5 Conclusion 61

2.1 Introduction

As pointed out in Chapter 1, FEM is able to provide the approximate solution of nonlinear partial differential equations on complex domains, and thus, can be also used to analyze nonlinear shear wave propagation in elastography. In the literature, Chen *et al.* [CHE 05, CHE 06] investigated the effects of boundary conditions, excitation frequency using simple FEM models. To take into account the heterogeneity (tumours in healthy tissues), 2D [PAL 05] and 3D [LEE 12] finite element models have been proposed. In addition, inverse algorithm based on FEM is also considered to reconstruct the stiffness map [PAR 09, ZHA 15]. To our knowledge, most of the above-mentioned models use linear elastic materials (Hooke's law) with or without viscosity, very few consider hyperelastic laws [JIA 15a].

The objective of this chapter is to accurately model the nonlinear shear wave propagation in soft solids by FEM. FEM models may indeed be valuable to find a simple method to identify nonlinear parameters of tissues. To achieve this, a reliable material model is necessary: visco-hyperelastic Landau's model in the case of incompressibility is a potential choice because it has been largely used in the above-mentioned experimental and theoretical work [CAT 03b, JAC 07, GEN 07, CAT 03a, ZAB 04, WOC 08, DES 10b, MIC 10] . However, to our knowledge, the numerical study of this model is rare. Most recently, Giammarinaro *et al.* [GIA 16b] reported the numerical analysis of shock waves in brain with Landau's model. However, the work was carried out by Finite Difference method (FDM), a FEM model is still lacking. Moreover, nonlinear wave propagation occurs widely in many systems. In addition to elastography, it has been investigated in the field of medical ultrasound [KHE 12], geophysics [SAE 04], vibration [ALS 01], seismology [MOC 05] and so on. In either field, FEM is considered as a generalized tool, and the development of material models is always essential.

This chapter is structured as follow. Section 2.2 presents nonlinear models of nearly incompressible soft solids. The weakly nonlinear elastic theory of the forth-order Landau's law is firstly developed in the finite element formulation, simple numerical tests are carried out to compare its behaviour with common hyperelastic laws. Furthermore, in order to model nonlinear shear waves in soft solids, the visco-elastic property is considered by Voigt model.

In section 2.3, the FE simulations are carried out to model the nonlinear shear wave propagation in soft solids. The models are based on the experimental work of Jacob *et al.* reported in [JAC 07], in which both plane and noneplane shear wave experiments are carried out. To our knowledge, this is the first time that nonlinear shear wave of nearly incompressible Landau's law is analysed by FEM.

In section 2.4, the FE model of plane shear wave is considered with different simulation parameters, which include the frequency and amplitude of excitation, the viscosity and nonlinearity of Landau's material. These parameters contains all the factors that may affect the nonlinear behaviour of plane waves in homogeneous solids. The numerical results are compared with the analytical solution, and a practical method is proposed to identify the nonlinear parameter of a homogeneous tissue. A conclusion is given at the end.

2.2 Material modeling

2.2.1 Hyperelasticity

In Chapter 1, we have presented that biological materials are generally modeled by hyperelastic models, so the constitutive law is described by a strain energy function W. For an isotropic hyperelastic model, W can be written as a function of $W(I_1, I_2, I_3)$ (the principle invariants of strain tensor $\mathbf{C}$) in the field of solids mechanics, or as a function of $W(I, II, III)$ (other invariants of Green strain $\mathbf{E}$) in the field of acoustic.

Based on these two concepts, countless models are generated. In this section, we present the connection and difference between the most used laws in these two different fields. A comparison between related models is given using FEM simulations. It is shown that, in biomechanics, choosing the accurate material model is a key requirement to get high-fidelity numerical simulations.

2.2.1.1 Continuum mechanics model: Rivlin model

For mechanical models, we refer to Rivlin model [RIV 48] which is mostly used to model rubber-like materials. It is presented here because of its close relation with the acoustic model presented in the following. Rivlin model can be seen as the special case of the generalized polynomial form (Eq.1.23) by setting $N = 2$ and $c_{11} = c_{02} = 0$. The potential is:

$$W_{Rivlin} = c_{10}(\bar{I}_1 - 3) + c_{01}(\bar{I}_2 - 3) + c_{20}(\bar{I}_1 - 3)^2 + \frac{K}{2}(J - 1)^2 \tag{2.1}$$

where c_{10}, c_{01} and c_{20} are the three material constants related to shear behaviour, and K is the bulk modulus. Furthermore, by setting $c_{20} = 0$, we obtain the Mooney-Rivlin model; by setting both c_{01} and c_{20} to 0, we obtain the neo-Hookean model, which is the simplest hyperelastic model.

This model is largely used in solid mechanics for many years, it is also inherently included in the most FEM software. The process of implementation is omitted in this manuscript but detailed description can be found in [BON 97, HOL 00].

2.2.1.2 Nonlinear acoustic model: Landau's law

In seismology and physic acoustics, incompressible Landau's model (Eq.1.32) is widely used. This model is employed in a number of theoretical works [ZAB 04, MIC 10, DES 10b], experimental works [JIA 15b, JIA 15a] and numerical works [GIA 16b] in elastography. For the sake of simplification, all of them considered the model as fully incompressible (supposing $W^{vol} = 0$). This assumption is practically right because compressional waves provide no relevant information in the experiments.

In FEM formulation, it is convenient to introduce a slight compressibility in constitutive laws. Especially for the explicit time integration method, compressibility is indispensable to keep the compressional wave propagate at a finite speed. To achieve that, Eq.1.32 and Eq.1.19 are combined and fourth order nearly incompressible Landau's model (called by Landau's model in the following) is written by

$$\begin{aligned} W =& W^{dev} + W^{vol} \\ =& \mu II + \frac{A}{3} III + D II^2 + \frac{1}{2} K (J-1)^2 \end{aligned} \tag{2.2}$$

Again, μ, A and D represent the second, third, and fourth order shear moduli. They all have the same order of magnitude (*kPa*) in soft solids, and they play a key role in nonlinear shear wave propagation. K is the bulk modulus which is several orders larger than the shear modulus, generally, in the order of *GPa*. This model allows both compressional wave and shear wave propagating in the medium with the realistic speed .

2.2.1.3 Implementation

As it is the first time that Landau's model is introduced in FEM, we provide full expressions used in the code implementation.

For any decoupled hyperelastic model, the PK-2 stress **S** can be derived from the strain energy by

$$\begin{aligned} \mathbf{S} =& \frac{\partial W^{vol}}{\partial \mathbf{E}} + \frac{\partial W^{dev}}{\partial \mathbf{E}} \\ =& \mathbf{S}^{vol} + \mathbf{S}^{dev} \end{aligned} \tag{2.3}$$

With the following relations:

$$\frac{\partial J}{\partial \mathbf{C}} = \frac{1}{2} J \mathbf{C}^{-1}, \ \frac{\partial tr(\mathbf{E})}{\partial \mathbf{E}} = \mathbf{1} \tag{2.4}$$

and making use of the chain rule in Eq.2.2 leads to:

$$\begin{aligned} \mathbf{S} =& 2\frac{\partial W^{vol}}{\partial \mathbf{C}} + \frac{\partial W^{dev}}{\partial \mathbf{E}} \\ =& pJ\mathbf{C}^{-1} + 2\mu \mathbf{E} + A\mathbf{E}^2 + 4D tr(\mathbf{E}^2)\mathbf{E} \end{aligned} \tag{2.5}$$

Where p indicates the hydrostatic pressure, and is obtained by $p = K(J-1)$.

Some FEM codes (*e.g.* ABAQUS) are based on the current configuration, so the Cauchy stress tensor $\boldsymbol{\sigma}$ is necessary (note that Cauchy stress shares the same symbol with the engineering stress in linear theory.). It can be obtained by the transformation relation as:

$$\sigma = \frac{1}{J}\mathbf{F}\mathbf{S}\mathbf{F}^T \tag{2.6}$$

In order to use a hyperelastic model in an implicit finite element solver (*e.g.* ABAQUS/Standard [HIB 02]), the fourth order elasticity tensor has to be derived. In the reference configuration, the elasticity tensor is defined as

$$\mathbb{C} = \frac{\partial^2 W}{\partial \mathbf{E}^2} = \frac{\partial \mathbf{S}}{\partial \mathbf{E}} \tag{2.7}$$

Substituting the Eq.2.5 into Eq.2.7 gives:

$$\begin{aligned} \mathbb{C} = {} & KJ(J-1)(\mathbf{C}^{-1}\otimes\mathbf{C}^{-1} - 2\mathbb{I}_{\mathbf{C}^{-1}}) + KJ^2\mathbf{C}^{-1}\otimes\mathbf{C}^{-1} \\ & + 2\mu\mathbb{I} + 2A\mathbf{E}:\mathbb{I} + 8D\mathbf{E}\otimes\mathbf{E} + 4Dtr(\mathbf{E}^2)\mathbb{I} \end{aligned} \tag{2.8}$$

where $\mathbb{I} = \frac{1}{2}(\delta_{ik}\delta_{jl} + \delta_{il}\delta_{jk})$ stands for the fourth-order identity tensor, and $(\mathbb{I}_{\mathbf{C}^{-1}})_{ijkl} = -\frac{1}{2}(\mathbf{C}^{-1}_{ik}\mathbf{C}^{-1}_{jl} + \mathbf{C}^{-1}_{il}\mathbf{C}^{-1}_{jk})$.

The spatial elasticity tensor can be obtained by the push-forward operation defined as:

$$\mathbb{c}_{ijkl} = \frac{1}{J}\mathbf{F}_{iI}\mathbf{F}_{jJ}\mathbf{F}_{kK}\mathbf{F}_{lL}\mathbb{C}_{IJKL} \tag{2.9}$$

Particularly, ABAQUS/Standard uses the elasticity tensor associated to the Jaumann objective rate of the Cauchy stress, which can be obtained by:

$$\mathbb{c}^{\sigma J} = \mathbb{c} + \frac{1}{2}(\delta_{ik}\sigma_{jl} + \sigma_{ik}\delta_{jl} + \delta_{il}\sigma_{jk} + \sigma_{il}\delta_{jk})\mathbf{e}_i\otimes\mathbf{e}_j\otimes\mathbf{e}_k\otimes\mathbf{e}_l \tag{2.10}$$

2.2.2 Comparison

In the last chapter, one can see that continuum mechanics models and nonlinear acoustic models use different invariants definitions of finite deformation tensors. It is of interest to illustrate the relationship between these models. Especially, it has been shown in [DES 10a, JIA 15a], that Rivlin and Landau's energy functions are equivalent to fourth order with the following relationships between the parameters:

$$\mu = 2(c_{10} + c_{01}),\ A = -8(c_{10} + 2c_{01}),\ D = 2(c_{10} + 3c_{01} + 2c_{20}) \tag{2.11}$$

Rivlin model is inherently included in ABAQUS package, Landau's model is implemented by a user subroutine (UMAT) written in Fortran. In order to verify these relations, FEM simulations are carried out. We use a single hybrid hexahedral element ($C3D8H$ in ABAQUS) of $1 \times 1 \times 1mm^3$. The material parameters are chosen to be the measured value in mixed gel [RÉN 08]. So $\mu = 6.6\ kPa$, $A = -37.7\ kPa$ and $D = 30\ kPa$. Accordingly, the equivalent Rivlin model parameters are: $c_{10} = 1.8875\ kPa$, $c_{01} = 1.4125\ kPa$

and $c_{20} = 4.4375\ kPa$. Moreover, to illustrate the difference, the neo-Hookean model is also presented with $c_{10} = \frac{\mu}{2} = 3.3\ kPa$. To ensure the relative incompressibility, the bulk modulus K is set to 1 GPa in all the models.

2.2.2.1 Uniaxial tension/compression

The first test consists in a uniaxial compression/tension for stretches λ of 0.5 to 1.5. The deformation gradient $\mathbf{F}$ is:

$$\mathbf{F} = \begin{bmatrix} \lambda & 0 & 0 \\ 0 & \frac{1}{\sqrt{\lambda}} & 0 \\ 0 & 0 & \frac{1}{\sqrt{\lambda}} \end{bmatrix} \tag{2.12}$$

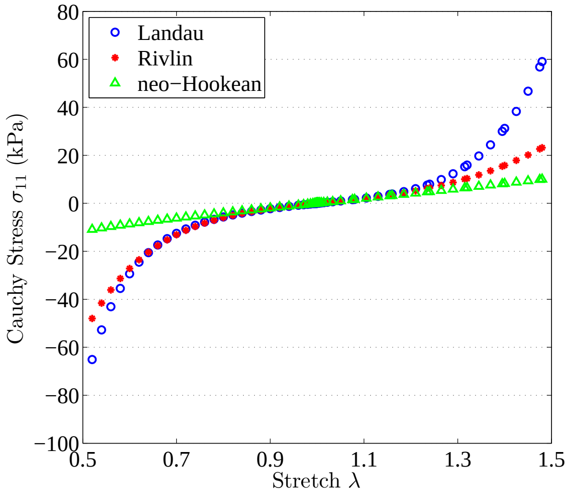

Figure 2.1: Uniaxial tension/compression test

Fig.2.1 represents the Cauchy stress along the stretch direction during the deformation. All three models have the same behaviour at small deformation range. However, Landau's and Rivlin models harden strongly in large deformation, both in tension and in compression, whereas neo-Hookean shows almost a linear property in the whole range of deformation. In large deformation, Landau's model exhibits a larger nonlinearity, especially in tension, than Rivlin model. Moreover, both models have different behaviours between tension and compression, which is particularly clear for Rivlin model. A similar phenomenon has been reported in the experiment of swine brain tissue [SUS 09].

2.2.2.2 Simple shear

Now we consider an elastic cube sheared by two plates, the deformation gradient is given by:

$$\mathbf{F} = \begin{bmatrix} 1 & 0 & 0 \\ 0 & 1 & \kappa \\ 0 & 0 & 1 \end{bmatrix} \tag{2.13}$$

with κ is the amplitude of shear strain which varies from 0 to 0.5.

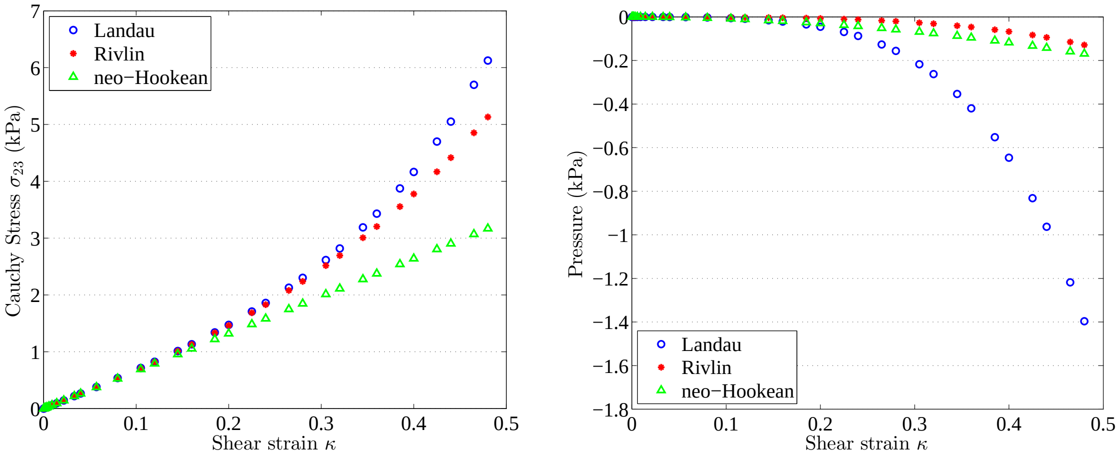

(a) Shear stress (b) Pressure

Figure 2.2: Simple shear test. Fig.2.2(a) shows the relation between the shear strain and the shear stress; Fig.2.2(b) shows the pressure in simple shear which reflects Kelvin effect.

Fig.2.2(a) displays the shear strain-stress curves. For the three models, the behaviour is similar at the beginning of load. Then, Landau's and Rivlin models show moderate stiffening at large strains. However, there is still an obvious difference in large shear, up to 20% when κ equals 0.5. On the other hand, neo-Hookean law is linear. This property being essential for the nonlinear shear wave propagation study in the following, the analytical expression of shear stress as a function of strain κ is given in the following box. It can be seen both neo-Hookean and Mooney-Rivlin models have an exactly linear behaviour.

Here we give the analytic expressions of Cauchy shear stress for the shear deformation described by Eq.2.13. These expressions are directly related to the generation of harmonics in nonlinear shear wave propagation presented in the next section. Neo-Hookean and Mooney-Rivlin models have a purely linear relationship, they can be written as

$$\sigma_{23} = 2c_{10}\kappa \tag{2.14}$$

and

$$\sigma_{23} = 2(c_{10} + c_{01})\kappa \tag{2.15}$$

respectively.

For Rivlin model which includes a higher order term, we have:

$$\sigma_{23} = 2(c_{10} + c_{01})\kappa + 4c_{20}\kappa^3 \tag{2.16}$$

And for Landau's material, the shear stress is expressed by:

$$\sigma_{23} = \mu\kappa + (\mu + \frac{A}{2} + D)\kappa^3 + (\frac{A}{4} + \frac{3}{2}D)\kappa^5 + D\kappa^7 \tag{2.17}$$

In Eq.2.17, the last two terms have a slight effect at the level of nonlinear strain considered here. In a number of works [ZAB 04, WOC 08, MIC 10, JAC 07], these terms are neglected, so Landau's model clearly coincides with Rivlin model, and the relationships in Eq.2.11 are recovered. Besides, the coefficient of the cubic term is defined as the nonlinear coefficient in plane shear wave γ:

$$\gamma = \mu + \frac{A}{2} + D \tag{2.18}$$

In this work , we define a second nonlinear coefficient denote ζ which is the coefficient at the fifth term in Eq.2.17, so

$$\zeta = \frac{A}{4} + \frac{3}{2}D \tag{2.19}$$

This coefficient has a very small effect at the typical level of nonlinear wave propagation considered in this work, its utility is discussed latter.

Fig.2.2(b) represents the pressure evolution during shear deformation. Although there is no volume change in this case, pressure is generated, this is known as Kelvin effect [OGD 97] . It can be seen that this effect is much stronger in Landau's model than in the other two models, nevertheless, pressure is much smaller than shear stress at a given deformation.

To sum up, the behaviours of different hyperelastic models are compared in simple cases. Importantly, the similarity and difference between Rivlin and Landau's model have been shown. This comparison highlights the need for developing accurate material models for numerical modeling. For our purpose, simulating nonlinear shear wave propagation in soft solids, the material model should be carefully considered. In a limited shear deformation, say $\kappa \leq 0.2$, Rivlin and Landau's model have almost the same behaviour. In large deformations, Rivlin model is less nonlinear than Landau's model. However, this may be out of the range where weakly nonlinear theory (Landau's law) should be applied. Finally, models such as neo-Hookean do not have nonlinear behaviour in shear.

2.2.3 Voigt viscoelasticity

In finite amplitude wave propagation, nonlinear elasticity generates higher harmonics of the fundamental frequency. On the other hand, the absorption of the medium decreases the amplitude of deformation which limits the generation of these harmonics. As a result, nonlinear wave propagation cannot be modeled without considering viscosity. In nonlinear acoustic, viscoelasticity of soft solids is often described by Voigt model (see Chapter 1.2.3). We describe here its implementation in both infinitesimal and finite strains.

Voigt material can be represented by a purely viscous damper and purely elastic spring connected in parallel (Fig.1.13), consequently, the total stress is the sum of the elastic stress and viscous stress, see Eq.1.39. This relation is valid for both infinitesimal strain and finite strain models. But for finite strains, it should be emphasized that the two components of stress should be homologous.

2.2.3.1 Infinitesimal strain

At small-strain, there is only one strain tensor ε and one stress tensor $\boldsymbol{\sigma}$. For an isotropic, nearly-incompressible material, the viscous stress can be written in terms of deviatoric and volumetric parts as in elasticity, that is,

$$\boldsymbol{\sigma}^{visco} = 2\eta\dot{\varepsilon}^{dev} + \xi\dot{\varepsilon}^{vol} \tag{2.20}$$

With the relation of the separation of strain rates:

$$\dot{\varepsilon}^{vol} = \frac{1}{3}tr(\dot{\varepsilon})\mathbf{1}, \;\; \dot{\varepsilon}^{dev} = \dot{\varepsilon} - \dot{\varepsilon}^{vol} \tag{2.21}$$

In Eq.2.20, the superposed dot denotes the time derivative, η and ξ are the shear and bulk viscosity coefficients, respectively. It is reported that ξ is 2 orders smaller than η in gels [JAC 07]. Moreover, Voigt model leads to a quadratic dependency of the shear absorption coefficient with frequency, this assumption has also been validated by experiments in [RÉN 08].

2.2.3.2 Large strain

The generalization of small-strain viscoelastic constitutive relations to finite strain is carried out directly [ZAB 04]. It writes:

$$\mathbf{S}^{visco} = 2\eta\dot{\mathbf{E}}^{dev} + \xi\dot{\mathbf{E}}^{vol} \tag{2.22}$$

However, it is essential that the correct work conjugate stress and strain measures be used when considering finite strain [DES 13b]. There are numerous examples in the literature that violate this, *e.g.* [ZAB 04, JAC 07].

$\dot{\mathbf{E}}$ is the Lagrangian variable, its spherical (trace) part does not vanish in isochoric motion. Hence it can not be split into deviatoric and volumetric components directly as in Eq.2.21.

To split Lagrangian strain (stress) properly, the following principle should be used: the deviatoric and volumetric components of a tensor are orthogonal in the sense that $\mathbf{S}^{dev} : \dot{\mathbf{E}}^{vol} = \mathbf{S}^{vol} : \dot{\mathbf{E}}^{dev} = 0$. We omit here cumbersome calculations, the expression of separation has been given in the book of [BEL 13a]. For PK-2 stress $\mathbf{S}$:

$$\mathbf{S}^{vol} = \frac{1}{3}(\mathbf{S} : \mathbf{C})\mathbf{C}^{-1}, \;\; \mathbf{S}^{dev} = \mathbf{S} - \mathbf{S}^{vol} \tag{2.23}$$

And for Green strain rate $\dot{\mathbf{E}}$:

$$\dot{\mathbf{E}}^{vol} = \frac{1}{3}(\dot{\mathbf{E}} : \mathbf{C}^{-1})\mathbf{C}, \;\; \dot{\mathbf{E}}^{dev} = \dot{\mathbf{E}} - \dot{\mathbf{E}}^{vol} \tag{2.24}$$

2.2.3.3 Implementation in the explicit method

In the explicit method, assuming time interval is Δt from step n to $n+1$, the strain rate is calculated as

$$\dot{\varepsilon}_{n+1/2} = \frac{\varepsilon_{n+1} - \varepsilon_n}{\Delta t} \tag{2.25}$$

For nonlinear problems, ε is replaced by $\mathbf{E}$. Then, the viscous stress at $n+1$ is evaluated by the abovc strain rate at $n+1/2$. It can be seen that the viscosity lags by a half time step, this time lag is unavoidable for any full explicit time integration method. Generally, because of small time step used in the method, this viscous lag is negligible. On the other hand, the viscosity also decreases the stable time step for the explicit method (see Chapter 6 of [BEL 13b]).

In the following, a flowchart for evaluating visco-elastic stress is given. It takes infinitesimal strain as example, but the extension to nonlinear strain is straightforward.

0. At time step $n+1$, known $\mathbf{U}_n$ and $\mathbf{U}_{n+1}$;

1. Compute elastic stress $\boldsymbol{\sigma}_{n+1}^{elas}$ by elastic constitutive equation;

2. Compute strain rate $\dot{\varepsilon}_{n+1/2}$ by Eq.2.25;

3. Split strain rate into deviatoric part and volumetric part by Eq.2.21; (for nonlinear strain, using Eq.2.24)

4. Compute viscous stress $\boldsymbol{\sigma}_{n+1/2}^{visco}$ with Eq.2.20;

5. Compute total stress with $\boldsymbol{\sigma}_{n+1}^{tot} = \boldsymbol{\sigma}_{n+1}^{elas} + \boldsymbol{\sigma}_{n+1/2}^{visco}$;

6. Compute internal force $\mathbf{F}_{n+1}^{int}$ with $\boldsymbol{\sigma}_{n+1}^{tot}$.

2.3 Simulations of nonlinear shear wave

In this section, nonlinear shear wave propagation in soft solids is analyzed using FEM simulations. Two models are considered, one for plane shear wave and the other for nonplane shear wave, they are both based on experiments of artificial gels in [JAC 07] . In this experiment, it has been observed that plane wave generates only the odd harmonics at $3f, 5f$, ... (f is the fundamental frequency), and nonplane shear wave generates all harmonic components, *i.e.* $2f, 3f$, ... For plane wave, the phenomenon can be explained as the cubic term in the shear stress expression (Eq.2.17) contains only the odd frequencies after the Fourier transform [CAT 03b]. However, there is still no analytical model for nonplane wave. The objective of this section is to illustrate that FEM is able to simulate both plane and nonplane waves and to provide very similar results as both the analytical model and the experiments.

In the following, simulations are carried out by our in-house FE code, Landau's visco-hyperelastic model presented above is employed. In numerical aspect, bi-linear quadrangular elements combined with selective integration strategy are used to handle volumetric locking and hourglass effect at the same time. On the other side, the explicit scheme is employed because it is the most suited time integration method for wave propagation problems, even though its efficiency is decreased by the high incompressibility of soft solids.

2.3.1 Preliminary study: choose the compressible parameter

For nonlinear wave propagation simulations, the explicit scheme is employed because it is the most suited time integration method for wave propagation problems. However, its efficiency is decreased by the high incompressibility of soft solids, the time step should be extremely small to satisfy the stability condition (Eq.1.51).

To keep a reasonable time step without loss of reliability, a preliminary model is proposed in Fig.2.3. A simple model is carried out with different Poisson coefficients. It can be seen, in this homogeneous model, that the simulations tend to converge at the high level of the incompressibility. To ensure the accuracy, the Poisson coefficient $\mu = 0.4999$ is used in the following, this parameter indicates that the compressional wave speed is hundreds meters per second, or the bulk modulus is in the order of 10^4 kPa.

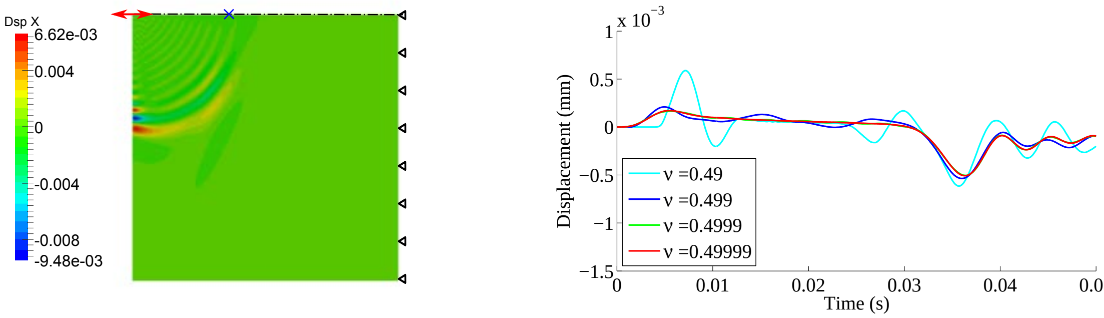

(a) A plane strain, homogeneous square with a dynamic oscillation at the top-left corner. $\mu = 1$ kPa, $\rho = 1000$ kg/m^3

(b) The horizontal displacement history at the fork point (see left)

Figure 2.3: Preliminary model: the simulations are carried at different levels of the incompressibility

2.3.2 Plane wave

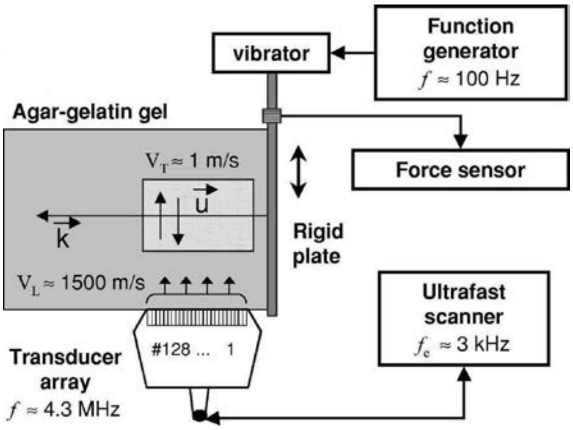

Figure 2.4: Nonlinear plane shear wave experiment presented in [JAC 07]

The propagation of plane shear wave is considered firstly. In the experiment, the artifical solid is composed of agar and gelatin mixed with hot water and solidified. A rigid plate is placed on the right side of the solid and generates a low frequency shear wave, see Fig.2.4. The shear wave propagates transversely at a very low speed (several meters per second), and this particle motion is measured by a transducer array placed at the bottom. For a more detailed description, the reader is invited to consult the original paper [JAC 07].

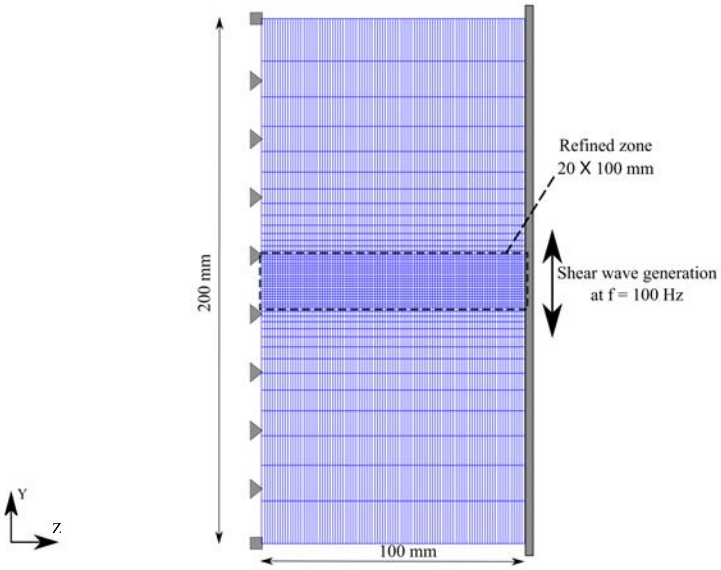

Figure 2.5: Geometry and FE model of plane shear wave propagation

The geometry and the FE model for the plane shear wave experiment are shown in Fig.2.5. The plane strain hypothesis can be used, which allows an enormous reduction of the computation cost. The size of the model is chosen to be large enough to avoid reflections, hence the model contains 4949 nodes and 4800 elements. The measurement is only located in the zone where the mesh has been refined by 2000 square elements. The length of each element is 1 *mm* which ensures more than 20 elements per wavelength (c_s/f).

The material parameters of Landau's visco-hyperelastic law are summarized in Tab.2.1, they are chosen from the values reported in the experiments. In order to keep the time step reasonable in numerical simulations, the bulk modulus K is set to 10^4 *kPa*. Besides, it should be emphasized that only a relation of the third and fourth order shear moduli A and D is given in [JAC 07], there is no effective way to discriminate them separately. Herein, we set $D = 0$ to determine the value of A. In the next section, it will be shown that this approximation has minor effect in the results.

The boundary conditions are set to prevent the rigid motion, see Fig.2.5. To generate plane wave, vertical displacements are applied on the right side of the model, the dynamic excitation is described by the following function:

$$U_y(t) = A_0\, sin(2\pi f t)(1 - cos(\frac{2\pi f}{N} t)), \;\; 0 \leqslant t \leqslant \frac{N}{f} \tag{2.26}$$

Material parameters	
$\rho\ (kg/m^3)$	1000
$\mu\ (kPa)$	4.4
$A\ (kPa)$	41.1
$D\ (kPa)$	0
$K\ (kPa)$	10^4
$\eta\ (kPa\ s)$	0.6×10^{-3}
$\xi\ (kPa\ s)$	0.5×10^{-5}

Tableau 2.1: Material parameters of Landau's visco-hyperelastic law.

where $A_0 = 0.8\ mm$, $N = 5$ and the frequency $f = 100\ Hz$.

This simulation lasts for $0.075\ s$, the time step is set to $0.5 \times 10^{-6}\ s$ to keep the stability of the explicit scheme.

Fig.2.6 shows the vertical displacement distributions in the refined zone at three times. It can be observed that the wave front remains plane until the end of the simulation, which indicates that the assumption of plane wave propagation is hold.

The resulting velocity of the source and the corresponding spectrum are displayed in Fig.2.7 with blue lines. The source contains only the component of $100\ Hz$, which is the fundamental component. The maximal velocity reaches to $500\ mm/s$, it is about 24% of the linear shear wave speed in this model ($c_s = 2.1\ m/s$). This ratio ensures that the nonlinear behaviour can be clearly observed.

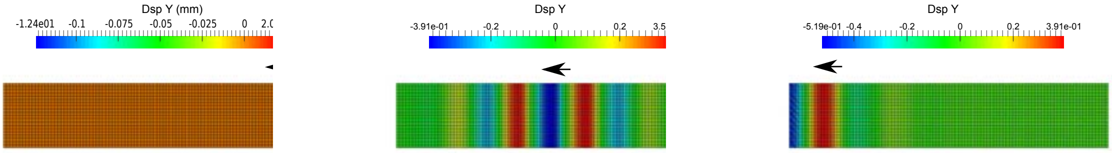

(a) $t = 0.0075\ s$

(b) $t = 0.0525\ s$

(c) $t = 0.075\ s$, end of simulation

Figure 2.6: Vertical displacement distributions in the refined zone. The wave front remains plane during the simulation, it confirms the hypothesis of plane shear wave propagation.

In the numerical results, the vertical velocity history and its spectrum are measured $20\ mm$ away from the source, see the red lines in Fig.2.7. In the time domain, the wave form is clearly different from the source signal, the distortion is in a dis-symmetrical way which is reflected by the odd harmonic components (300, 500 Hz, ...) in the spectral domain.

A comparison with the experimental results of [JAC 07] is displayed in Fig.2.8. The figure represents the global spectrum along the distance of propagation from 5 to 50 mm. It can be seen that two results are very close, both the fundamental and the first odd

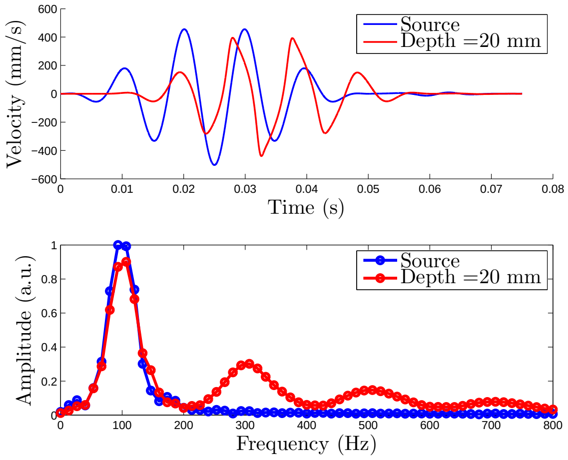

Figure 2.7: Vertical velocity history and its spectrum

harmonic ($3f$) cross the whole model with similar amplitudes. The experimental results looks more accurate in spectrum (narrow frequency band), this is because that the experiment has a longer duration which leads to a better Fourier transform.

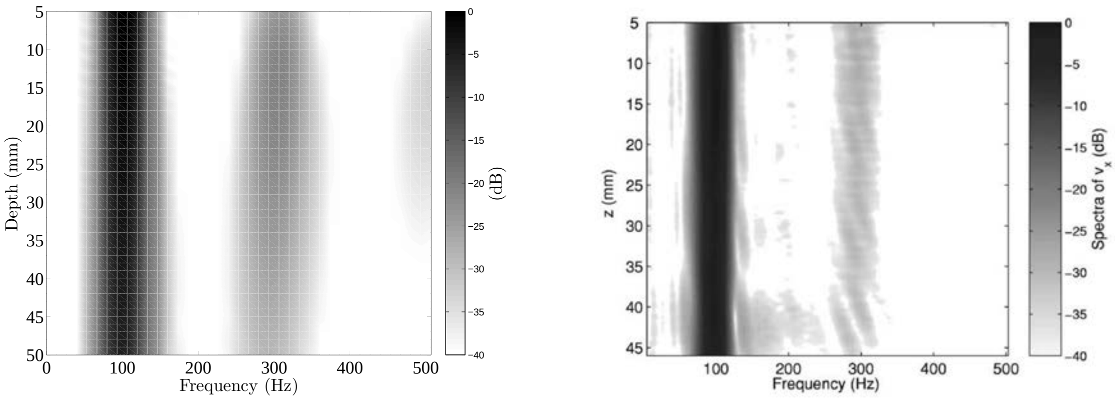

(a) Simulation results

(b) Experimental results in [JAC 07]

Figure 2.8: Spectra of the vertical velocity versus propagation depth z

The evolutions of these amplitudes are presented as a function of the depth, and displayed in Fig.2.9. In the numerical results (Fig.2.9(a)), the fundamental component (100 Hz) decreases linearly because of the viscosity. The two harmonic components reach 10% and 3% of the fundamental component respectively. The maximal amplitudes locate at the depth of 12 mm, it reflects the fact that a part of the energy is transmitted to higher frequencies because of the elastic nonlinearity. Moreover, one can see that the harmonics amplitude grows until 12 mm and then decreases, the tendency is caused by the fact that the viscous dissipation becomes the dominant effect with respect to the nonlinearity. The experimental results are shown in Fig.2.9(b), the harmonic components seem slightly larger, however, the two results are still very similar.

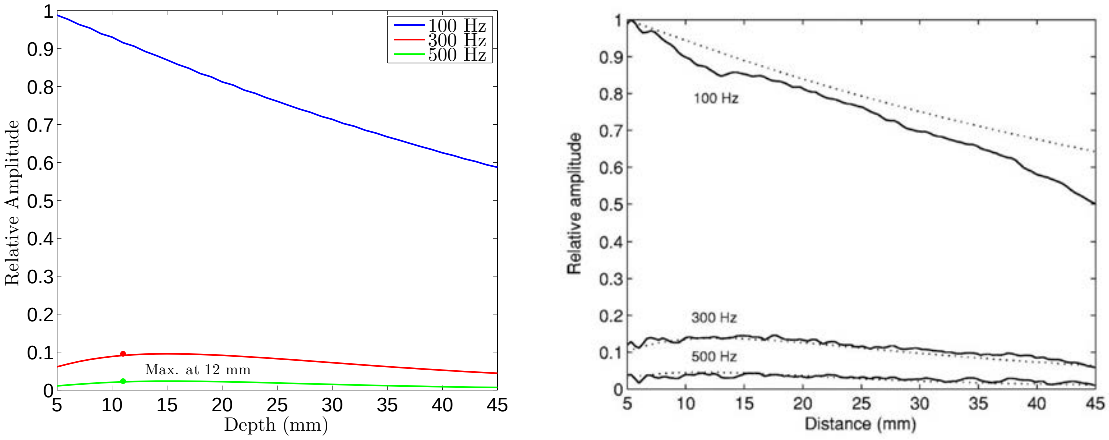

(a) Numerical simulation results

(b) Experimental results (solid lines) in [JAC 07] (The dotted lines present the analytical solution)

Figure 2.9: Plane wave: Evolution of the fundamental component and the third and fifth harmonics versus propagation depth.

2.3.3 Nonplane wave

In this part, nonplane shear wave propagation is investigated for the same material. The corresponding experiment setup is presented in Fig.2.10(a). In this model, the propagation direction ($\vec{k}$) coincides with the polarization direction ($\vec{u}$), the wave is refered to longitudinal-like polarized shear wave, and it has been theoretically predicted in the linear domain [CAT 15].

The experiment shows that this shear wave generates all harmonics components (at $2f$,$3f$,...). To our knowledge, an analytical method is still missing to predict this phenomenon, so the numerical model could be a valuable tool to validate this experiment.

In this experiment, both the solid and the vibrator bar are large enough to avoid reflections from two lateral sides, so plane strain hypothesis can be used again. The finite element model is described in Fig.2.10(b), it has 4900 nodes and 4761 elements, the refined zone contains 2500 squares with a length of 1 mm. The vibration bar is modelled by prescribing the displacement at the top-left corner in the width of 2 mm. The measurement locates along the symmetric axis of the refined zone, the nodal velocity in the z direction is recorded at every time step.

The material parameters have been summarized in Tab.2.1. The excitation is also described by Eq.2.26, with $A_0 = 0.8\ mm$, $N = 7$ and $f = 100\ Hz$. Fig.2.11 shows the displacement contour at time $t = 0.05\ s$, both the shear wave front and the surface wave front (at the left side) emitted by the source can be observed. The foregoing wave front does not reach the edge of the model, so the measurement can not disturbed by reflections.

In Fig.2.12, the particles velocity and the corresponding spectrum of the source and at two different points are compared. Unlike the plane waves, the wave form remains symmetric along the propagation depth, and all (odd and even) harmonics components

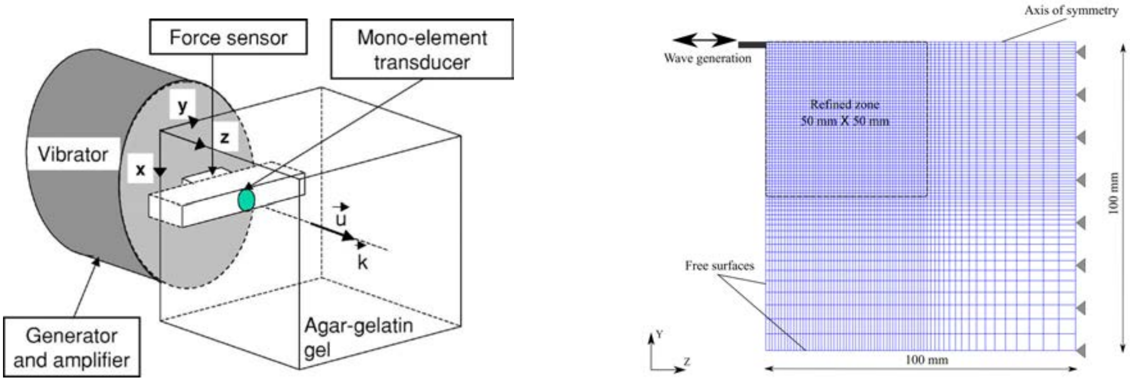

(a) Experiment setup in [JAC 07]   (b) FE model

Figure 2.10: Nonplane shear wave model. As both the gel and the vibrator are set to be enough large in the experiment, EF model can take advantage of plane strain hypothesis.

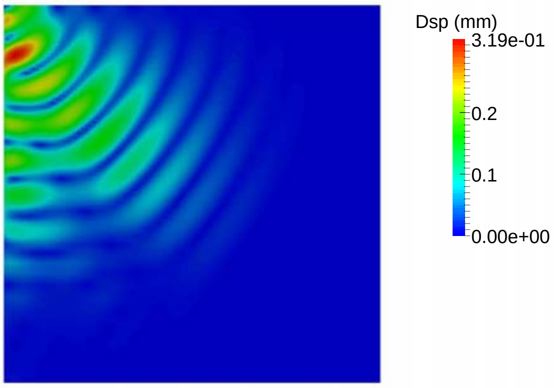

Figure 2.11: Nonplane wave with mono-excitation : displacement distribution at $t = 0.05\ s$

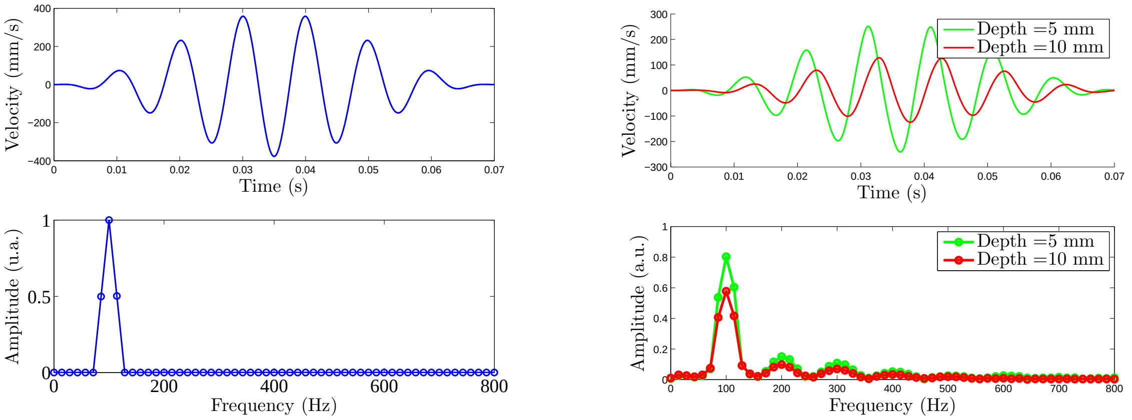

(a) Source velocity and spectrum

(b) Particle velocity and its spectrum at different depth

Figure 2.12: Nonplane wave propagation: all harmonic generation

($2f$, $3f$, ...) appear in the spectrum. Then, the global spectrum is displayed in Fig.2.13, the harmonic components are still observable, however, we can see that the amplitude decreases quickly as long as the wave propagates, which reflects the diffraction caused by the finite size of the source. These results validate the experimental observation in [JAC 07].

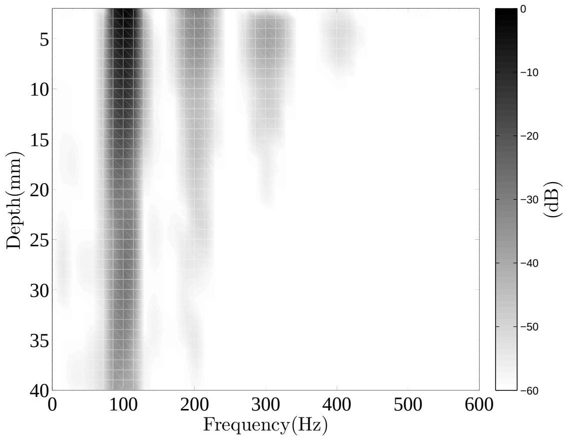

Figure 2.13: Global spectrum of nonplane wave propagation

2.3.4 Wave interaction

In addition, the experiments with two superimposed excitation have also been reported in [JAC 07]. The vibrator is then excited by a superposition of two sinusoidal components:

$$U_y(t) = 0.6\ (sin(2\pi f_1 t) + sin(2\pi f_2 t)) \tag{2.27}$$

The two frequencies $f_1 = 100\,Hz$ and $f_2 = 140\,Hz$ are chosen to be the same as in the experiment. For the plane wave model, the global spectrum is presented in Fig.2.14(b). Except for the fundamental components, the odd harmonics ($3f_1$, $3f_2$ and $5f_1$) are observed similarly as above. Moreover, the odd sum frequencies ($2f_1 \pm f_2$ and $f_1 \pm 2f_2$) are observed which is very similar to the experimental work.

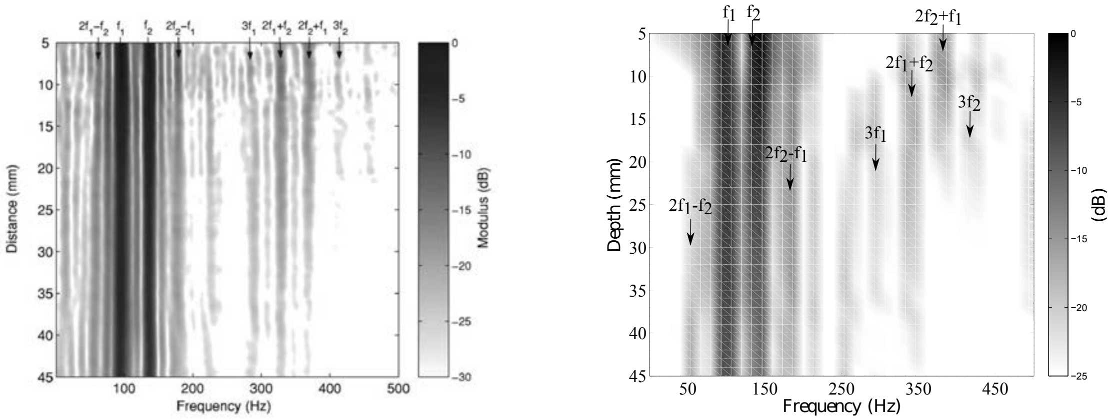

(a) Experimental results (Fig.6(a) in [JAC 07])

(b) Simulation results

Figure 2.14: plane wave propagation with interaction

Secondly, the wave interaction in nonplane case is tested by the same function of Eq.2.27. The global spectrum is presented in Fig.2.15(b). As predicted, all possible combinations of harmonic components are observed ($2f_{1,2}$, $3f_{1,2}$,$f_1 \pm f_2$, ...), but this effect is quickly damped because of diffraction. The comparison to experimental results in the literature is shown, Fig.2.15(a). For clarity of each, the scale bar is not the same, this is caused by different time of acquisition between the experiment and the simulation. However, the purpose is to show that the harmonic generation locate at the same frequencies.

2.3.5 Discussion

In this section, FEM simulations of nonlinear shear wave propagation in soft solids are presented. Plane and nonplane shear waves are generated by a harmonic excitation and a superimposed excitation, the numerical results show a good agreement with the experimental work.

In addition, the same models have been carried out for neo-Hookean and Rivlin models, the viscosity is considered the same way (Voigt model). As predicted, neo-Hookean produces no harmonics because of its linear behaviour in shear, and Rivlin models produce the same harmonics as Landau's law because the two models are identical at the range of deformation produced by nonlinear waves.

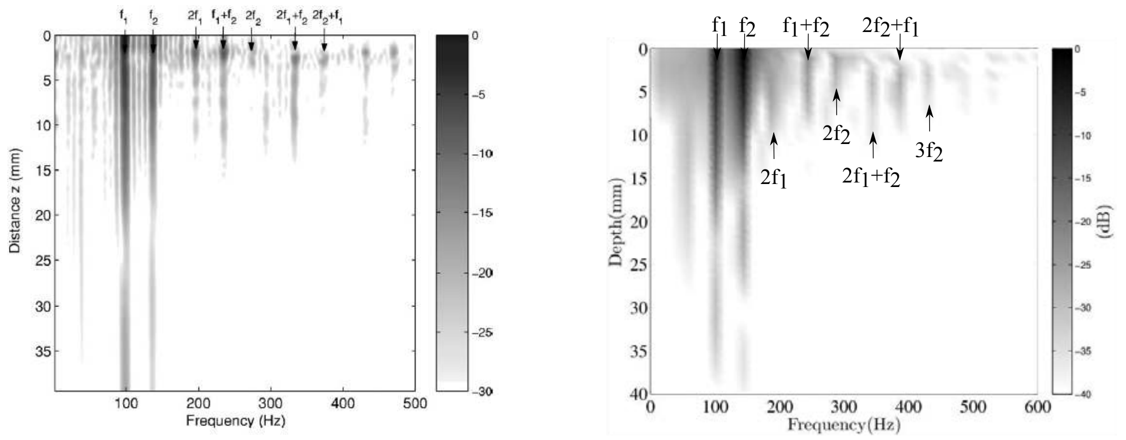

(a) Experimental results (Fig.10 in [JAC 07])

(b) Simulation results

Figure 2.15: Nonplane wave propagation with interaction

2.4 Parametric study

In the above, we have shown that nonlinear elasticity generates higher harmonics. At the same time, viscosity has two effects: firstly, it decreases the amplitude of wave which limits the continuing generation of the harmonics. Secondly, the absorption coefficient increases with frequency, so the higher harmonics attenuate quickly which leads to another energy loss.

This special phenomenon provides a guideline to identify the nonlinearity of soft solids by transient elastography technique. In this section, a parametric study is carried out for the plane wave model, the objective is to find a practical method to identify the nonlinear elastic parameters (A or D, or both) of homogeneous tissues.

2.4.1 Analytical formulation

Before performing the parametric study by FEM, we recall the analytical formulation given by Zabolotskaya *et al.* [ZAB 04] for fundamental and first odd harmonic amplitude. Given a harmonic source excitation, by supposing the harmonic component remains small, the fundamental and first odd harmonic amplitude (of particular velocity) as a function of propagation distance z can be expressed as follow:

$$\begin{aligned} \bar{A_1}(z) &= v_0 e^{-\alpha z} \\ \bar{A_3}(z) &= -\frac{\beta \omega v_0^3}{24 c_s^3 \alpha}\left(e^{-3\alpha z} - e^{-9\alpha z}\right) \end{aligned} \tag{2.28}$$

These equation involve: the shear absorption coefficient $\alpha = \frac{\eta \omega^2}{2\rho c_s^3}$, the dimensionless nonlinear elastic coefficient $\beta = \frac{3\gamma}{2\mu}$, the angular frequency $\omega = 2\pi f$ and the source velocity $v_0 = A_0 \omega$.

Material parameters	
ρ (kg/m^3)	1000
μ (kPa)	4
A (kPa)	40
D (kPa)	0
K (kPa)	10^4
η $(kPa\ s)$	0.3×10^{-3}
ξ $(kPa\ s)$	0.5×10^{-5}
Load parameters (Eq.2.26)	
f (Hz)	100
A_0 (mm)	0.6
N	5

Tableau 2.2: Referenced model used in parametric study

It should be emphasized that this analytical result is obtained under the assumption of weak nonlinearity, which assumes that Goldberg number Γ is small. Goldberg number is a dimensionless coefficient to characterize the relative importance of the nonlinearity and the viscosity. For a harmonic excitation, it can be written as:

$$\Gamma = \frac{2\rho\beta v_0^2}{\eta\omega} \tag{2.29}$$

The relative amplitudes are used in the following for comparison convenience. They are defined by:

$$\begin{aligned} A_1(z) &= \bar{A}_1(z)/max(\bar{A}_1) \\ A_3(z) &= \bar{A}_3(z)/max(\bar{A}_1) \end{aligned} \tag{2.30}$$

This analytical model has been used in [RÉN 08] to measure the nonlinear elastic coefficient of mixed gel phantoms. However, the model has two limits. Firstly, the second harmonic component at $5f$ has not been considered. Secondly, Eq.2.28 is only valid for small Goldberg number which limits its application in real elastography experiments.

These limits can be mended by the numerical simulations. In the following, the plane wave model presented in Sect.2.3.2 is employed again, all parameters involved in Goldberg number (Eq.2.29), *i.e.* amplitude, frequency, viscosity, nonlinearity, are studied separately. In each analysis, without an opposite statement, the simulation parameters (summarized in Tab.2.2) remain the same as in Sect.2.3.2.

2.4.2 Effect of amplitude

Firstly, the effect of the load amplitude A_0 is investigated. At the same frequency, the higher the amplitude, the more nonlinearity is observed. We choose for the amplitude of the source A_0 in Eq.2.26 the values of 0.4 mm, 0.6 mm and 0.8 mm, other simulation parameters are kept constant. So the Goldberg numbers are 6.03, 13.57, 24.13 respectively by Eq.2.29.

The relative amplitude at the fundamental frequency and two harmonics are presented in Fig.2.16. At the fundamental frequency, as seen in Fig.2.16(a), dissipation is linear and increases with increasing amplitude. Nonlinearity effect is higher so more energy is transmitted into higher frequencies domain.

The first odd harmonic component is displayed in Fig.2.16(b), and the analytical results by Eq.2.28 is also presented. In the case of small Goldberg number (blue), the analytical solution shows a good agreement with the simulation result. As the Goldberg number grows, the analytical solution quality decreases. In Fig.2.16(c), the second harmonic amplitude is shown, notice that the maximum amplitude locations change slightly with influence of the load amplitude.

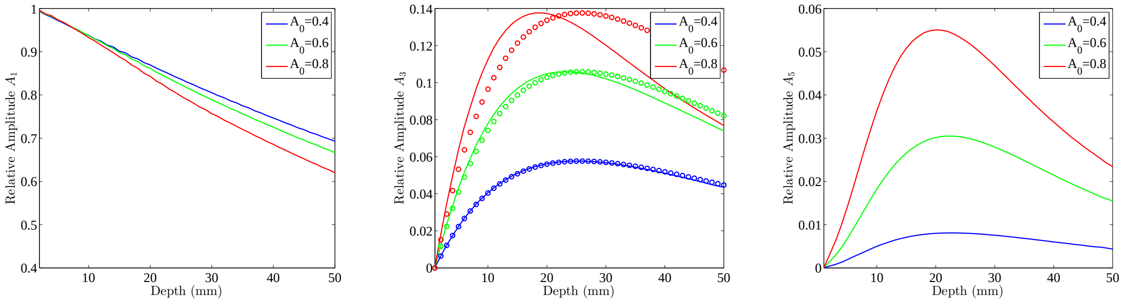

(a) At fundamental frequency f (b) At first odd harmonic $3f$ (c) Second odd harmonic: $5f$

Figure 2.16: FEM simulations at different amplitudes: Evolution of the fundamental and odd harmonics components along the propagation distance. Note: circle marks in the Fig.(b) are the analytical results by Eq.2.28.

2.4.3 Effect of frequency

The second test consists in using different excitation frequencies but the same load amplitude. In this case, the nonlinear wave is generated at the frequency of 80 Hz, 100 Hz and 120 Hz, they lead to Goldberg numbers of 10.86, 13.57, 16.29 respectively. Note that different frequencies change the source velocity, and also the dissipation character.

The results are shown in Fig.2.17. In Fig.(a), the dissipation effect increases very fast with the frequency. The first harmonic amplitudes are shown in Fig.(b). Again, the analytical solution leads to a good agreement with the numerical solution when Goldberg number is small. Then, it can be seen that high frequency excitation generates also high harmonic amplitudes. But contrary to the effect of amplitude, the frequency of excitation changes largely the location of the maximal amplitude. At high frequency, the harmonics build up earlier.

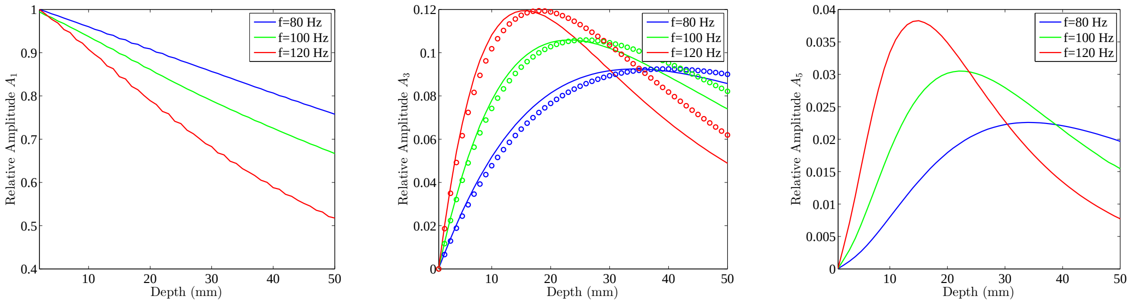

(a) At fundamental frequency (b) At first odd harmonic: $3f$ (c) At second odd harmonic: $5f$

Figure 2.17: FEM simulations at different frequencies: Evolution of the fundamental and odd harmonics components along the propagation distance. Note: circle marks in the Fig.(b) are the analytical results by Eq.2.28.

2.4.4 Effect of viscosity

The effect of the viscosity is now considered. Three shear viscous coefficients η are chosen, they are 0.2, 0.3 and 0.4 *Pa s*. Consequently, the Goldberg numbers are 20.36, 13.57, 10.18.

As shown in Fig.2.18, a small viscous coefficient leads to less loss of the fundamental component, but creates higher harmonic amplitudes. Also, it makes the maximal harmonics amplitude set up later. As expected, the analytical solution is valid when Goldberg number is small. Furthermore, in Fig.2.18(c), it can be seen the second harmonic amplitude with less viscosity (blue curve) is much more outstanding. It can be explained by that the viscosity coefficient has more effect at high frequency domain than at low frequency.

2.4.5 Effect of the first nonlinear elastic parameter γ

Now, we verify the influence of the first nonlinear elastic parameter $\gamma = \mu + \frac{A}{2} + D$ (Eq.2.18). Three materials summarized in Tab.2.3 are tested, it can be seen the fourth-order shear modulus D is set to be 0. As other parameters remain the same, Goldberg numbers are 2.26, 7.92,13.57 respectively.

Fig.2.19 shows the simulation results. The following conclusions can be obtained within expectations. Firstly, in Fig.(a), the red line decreases more than others because more energy is transmitted to generate harmonics components. Secondly, in Fig.(b)(c), it is clearly observed that the high nonlinear material generates larger harmonic amplitude. But even when both A and D are 0 (Material No.1), the Landau's material is still nonlinear

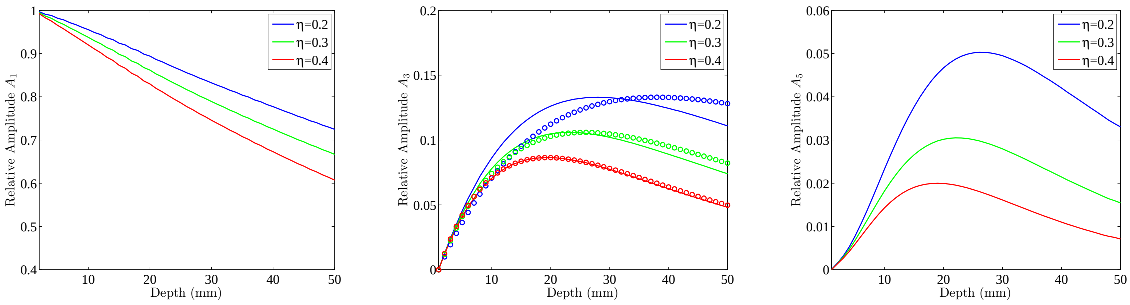

(a) At fundamental frequency (b) At first odd harmonic: $3f$ (c) At second odd harmonic: $5f$

Figure 2.18: FEM simulations with different viscosities: Evolution of the fundamental and odd harmonics components along the propagation distance. Note: circle marks in the Fig.(b) are the analytical results by Eq.2.28.

Material	μ	A	D	γ (Eq.2.18)
No. 1	4	0	0	4
No. 2	4	20	0	14
No. 3	4	40	0	24

Tableau 2.3: Different materials in the parametric study of γ. Unity: *kPa*

and small amplitude harmonics exist. Lastly, the analytical model gives the accurate results only in weak nonlinearity.

2.4.6 Effect of the second nonlinear elastic parameter ζ

Finally, different combinations of A and D are employed but the nonlinear elastic coefficient γ is kept the same. The materials are summarized in Tab.2.4, it can be seen that, even if γ is the same, varying the combinations between A and D still lead the second nonlinear coefficient ζ ($\zeta = \frac{A}{4} + \frac{3}{2}D$, see Eq.2.19) to be different.

In the results, the Fig.2.20(a) shows the same dissipation behaviour at the fundamental frequency. For the analytical model in which ζ is not involved, the three materials lead to the same Goldberg number which equals 13.57, so only one analytical result is shown in

Material	μ	A	D	γ	ζ (Eq.2.19)
No. 4	4	40	0	24	10
No. 5	4	0	20	24	30
No. 6	4	60	−10	24	0

Tableau 2.4: Different combinations of elastic moduli in the parametric study of ζ. Unity: *kPa*

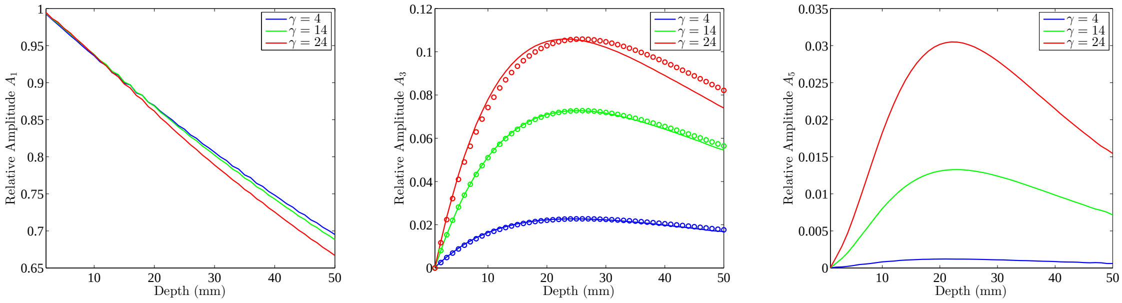

(a) At fundamental frequency f (b) At first odd harmonic $3f$ (c) At Second odd harmonic $5f$

Figure 2.19: FEM simulations with different elastic parameters γ: Evolution of the fundamental and odd harmonics components along the propagation distance. Note: circle marks in the Fig.(b) are the analytical results by Eq.2.28.

Fig.2.20(b). In this figure, the three simulation results overlap with no much difference, but they are all slightly different from the analytical solution.

Then, for the second odd harmonic $5f$ in Fig.(c), the difference among three materials can be observed at the maximal amplitude. The gap is attributed to the difference of the second nonlinear coefficient ζ. For instance, ζ in material No.5 is the most important, so it has the largest harmonic amplitude (green curve). However, at typical level of strain of elastography, this effect is too small to be accurately estimated with a plane wave approach, *i.e.*, the maximal difference is only 0.2% compared to the load amplitude. So the second nonlinear elastic parameter ζ is difficult to be determined only by plane wave experiments.

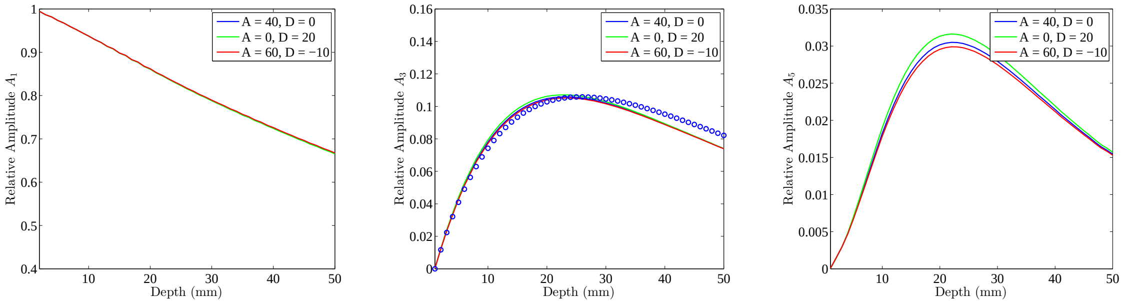

(a) At fundamental frequency f (b) At first odd harmonic $3f$ (c) At Second odd harmonic $5f$

Figure 2.20: FEM simulations with different elastic parameters ζ: Evolution of the fundamental and odd harmonics components along the propagation distance. Note: the analytical results are the same for three cases, presented by blue circle marks in Fig.(b).

2.4.7 Discussion

In this section, the generation of odd harmonics of nonlinear plane shear wave is studied with different parameters. The simulation results are compared to the existing analytical model, a good agreement is achieved at small Goldberg numbers. The comparison indicates that the analytical solution is accurate when the Goldberg number is smaller than about 10.

The simulations results are now displayed by the maximal amplitudes as a function of Goldberg number Γ, see Fig.2.21. For the first odd harmonic at $3f$ (Fig.2.21(a)), the amplitude does not increase linearly with the Goldberg number, thus a quadratic term is involved in the fitting. Meanwhile, the second harmonic at $5f$ (Fig.2.21(b)) shows a linear growth with the Goldberg number.

Finally, two equations respectively for the first and second harmonic are fitted in Eq.2.31. The fitting curves are also presented in Fig.2.21, a good agreement can be observed.

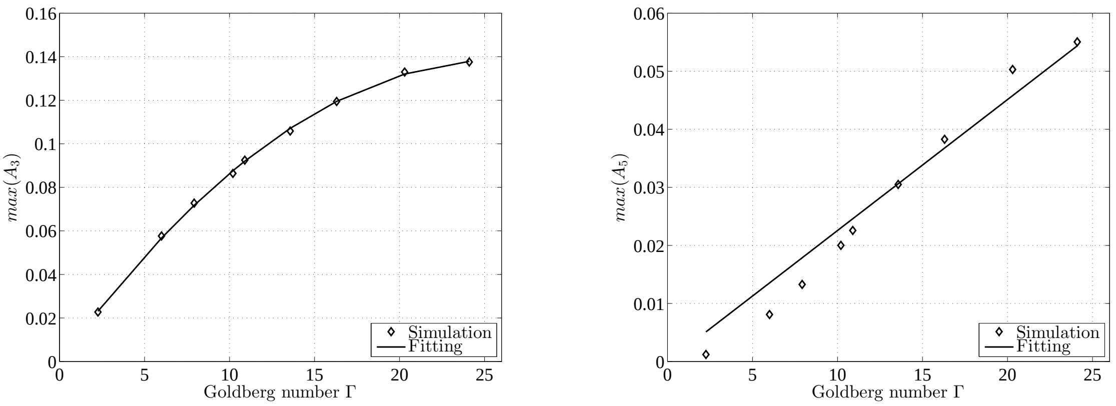

(a) The first odd harmonic: A_3

(b) The second odd harmonic: A_5

Figure 2.21: Fit of the relationship between the odd harmonics amplitude and Goldberg number

$$
\begin{aligned}
max(A_3) &= -0.206e^{-3} \times \Gamma^2 + 10.7e^{-3} \times \Gamma \\
max(A_5) &= 2.26e^{-3} \times \Gamma
\end{aligned}
\tag{2.31}
$$

These relationships indicate that, the Goldberg number Γ can be deduced for a homogeneous soft solid by measuring the harmonic components. In real life condition, plane wave in biological tissues can easily be generated by Supersonic Shear Imaging (SSI) technique [BER 04]. The linear parameters such as the shear modulus μ and the coefficient of viscosity η are not difficult to determine [CAT 04]. Therefore, the nonlinear coefficient γ can be deduced by Eq.2.29.

Theoretically, both relations in Eq.2.31 can be used to determine the nonlinear parameter γ, but the second odd harmonic amplitude is too small so that the application in real

Material	μ	A	D	γ	ζ (Eq.2.19)
No. 7	4	40	0	24	10
No. 8	4	-8	0	0	-2
No. 9	4	-56	0	-24	-16

Tableau 2.5: Different combinations of elastic moduli in the parametric study of the sign of γ. Unity: *kPa*

life leads to large errors. So the equation of the first odd harmonic should be considered firstly.

At last, these relationships are valid for a large domain (Goldberg number Γ from 0 to 25) which extends the analytical model to highly nonlinear response. However, the discrimination of the two elastic moduli A and D still can not be performed.

2.4.8 Sign of the first nonlinear elastic parameter γ

The above result allows deducing the magnitude of the first nonlinear elastic parameter γ, here we consider its sign. Assuming $\mu = 4$ *kPa* and $D = 0$, the nonlinear coefficient γ depends only on A, three different values of A are in Tab.2.5. From the table, material No.8 is almost linear in shear because $\gamma = 0$, and materials No.7 and No.9 have strong but opposite nonlinear property in shear.

This can be easily verified by the elementary test presented in Sec.2.2.2. Fig.2.22 shows the simple shear test for the three materials. No.8 (blue) remains linear. For the two nonlinear materials, No.7 exhibits hardening while No.9 exhibits softening. Note also that material No.9 (red) becomes unstable after $\kappa = 0.2$, stress decreases while strain grows. The stability of Landau's model will be discussed in Chapter 3.

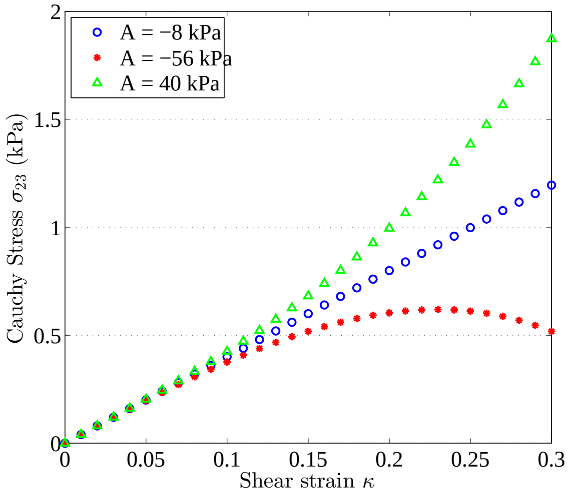

Figure 2.22: One element simple shear test for materials in Tab.2.5

Then the plane wave model presented in Sect.2.3.2 is employed again. Fig.2.23 shows the velocity curve and the corresponding spectrum for the three materials 10 *mm* away from the source. As expected, for the linear material (blue lines), there is no distortion on the wave form (time domain) and only the fundamental components exists in the spectral domain. Both nonlinear materials produce odd harmonic components, it can bee remarked that the harmonic components have the same amplitude level for two different materials, no difference can be found in the spectral domain to distinguish them. However, the velocity history curves clearly show the different distortions, which indicates the sign of the nonlinear parameter.

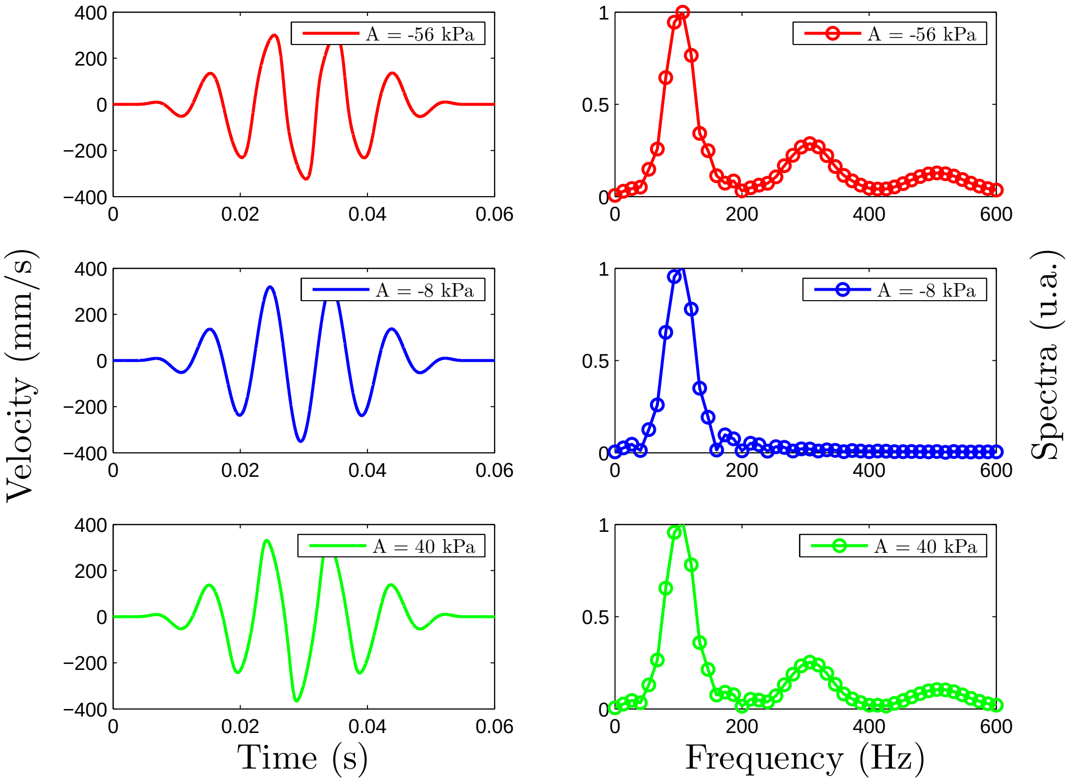

Figure 2.23: Velocity history and its spectrum of three different materials, at depth = 10 *mm*

2.5 Conclusion

In this chapter, nearly incompressible hyperelastic Landau's law is introduced into a FE formulation. It is compared to classical laws in the field of continuum mechanics, the model is close to Rivlin model in a limited range of deformation. However, neo-Hookean and Mooney-Rivlin model have an exactly linear behaviour in shear, so it can not be used to model nonlinear shear waves.

The viscosity of soft solids is also considered for dynamic applications. Voigt model is employed because it describes accurately the viscoelastic behaviour of soft solids at low frequency range. Numerical simulations show a good agreement with the experiments in the literature. However, it is necessary to point out that Voigt model is not considered to be validated at high frequency range.

In the parametric study, we propose a simple, forward method to identify the nonlinear parameter of homogeneous soft solids. This is achieved by measuring the amplitudes of first odd harmonics of nonlinear plane waves. However, Landau's law contains two nonlinear parameters A and D, and only the sum of them can be deduced by this method. In order to fully characterize Landau's material, *i.e.*, identify A and D separately, an other experiment should be involved, this will be discussed in the next chapter.

The visco-hyperelastic Landau's model has a broad perspective in numerical simulations of complex nonlinear wave phenomena, such as real geometry, heterogeneity [SAN 02a], diffraction [CAT 99a] and focalisation [GIA 16b] effect.

Moreover, Landau's FE model is potentially valuable for inverse problems. For example, characterizing tumours surrounded by healthy tissues is an important issue and it is often considered as an inverse problem. In the last decade, substantial progress has been made in linear elasticity [MCL 06a, MCL 06b] and viscosity [MCL 11]. Further effort is necessary in the nonlinear domain.

Chapter 3

Transverse isotropy in elastography

Contents

3.1 Introduction 65

3.2 Intrinsic transverse isotropy 66

3.2.1 Linear elastic ITI materials 66

3.2.2 Incompressibility 67

3.2.3 Shear wave propagation in incompressible ITI materials 67

3.2.4 Hyperelastic theory 68

3.2.5 Numerical validation 69

3.3 Extrinsic transversely isotropy: shear wave speeds under uniaxial pre-deformation 71

3.3.1 Analytical theory 73

3.3.2 Numerical validation 78

3.4 Extrinsic anisotropy: shear wave speeds under general pre-deformation 80

3.4.1 Analytical theory 81

3.4.2 Numerical validation 82

3.5 Characterization of Landau's constitutive law by acoustoelastic effect . 84

3.5.1 Solution property: accuracy 84

3.5.2 Solution property: stability 85

3.5.3 Solution property: uniqueness 88

3.5.4 Robust method to identify both A and D 88

3.6 Conclusion 90

3.1 Introduction

The objective of this chapter is to characterize the nonlinear elastic parameters of soft tissues in elastography using the acoustoelastic effect: finite pre-deformation changes the shear wave speed in nonlinear materials. Pre-deformation is often applied uni-axially, as shown in Fig.1.9 and Fig.1.10. As the speeds of wave propagation would be different depending on the propagation and polarization directions, tissues are consequently considered as transversely isotropic (TI) in the deformed configuration. From now, these materials are referred to as *extrinsic transversely isotropic* (ETI) materials.

Contrary to ETI materials, *intrinsic transversely isotropic* (ITI) represents materials which naturally have different mechanical properties in one direction with respect to the other two. This phenomenon is quite common in biological media such as muscles, tendon or bones. It is necessary to fully understand the shear wave behaviour in ITI materials before analysing ETI materials.

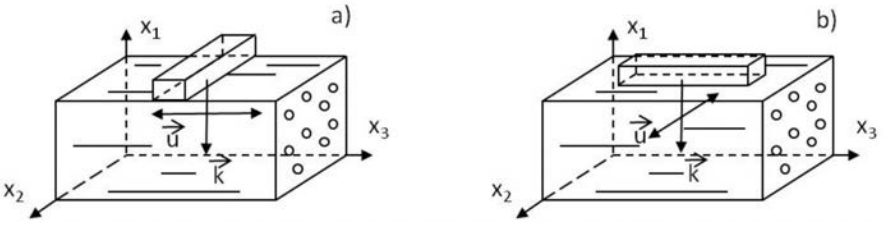

Figure 3.1: Schematics of the TE technique for ITI materials. (a) The rod is perpendicular to the fibers axis, a shear wave propagates (k) perpendicularly to the fibers axis with a polarization (u) parallel to the fibers axis. (b) The rod is parallel to the fibers axis, a shear wave propagates (k) perpendicularly to the fibers axis with a polarization (u) perpendicular to the fibers axis. Such configurations give, respectively, access to the elastic constants μ_L and μ_T. Source: [ROY 11]

Another reason to investigate ITI and ETI together is that they require almost the same experimental setup, as shown in Fig.3.1. Using this technique, local elasticity of muscles was obtained from shear wave measurements and a strong difference was found for shear waves propagating perpendicular or parallel to the muscle fibers [ROY 11]. Nevertheless, compared to the acoustoelastic experiments (see in Fig.1.9), the setup is very similar.

However, anisotropy can make the wave propagation phenomenon very complicated. For nonplane waves, the group velocity and phase velocity should be distinguished along different propagation directions [ROU 13, PAP 06, TWE 15]. For the sake of simplicity, only plane wave is considered in this chapter. This simplification follows the convention of the SSI technique (see Chapter1.1.2.2) and makes that there is only one wave speed in the shear wave propagation.

In this chapter, linear and nonlinear ITI materials are firstly investigated. Secondly, the work is focused on the ETI materials induced by uniaxial pre-deformation, several common material models are considered, and especially for Landau's solid. Then, uniaxial pre-deformation is generated for more general cases, and the analytical theory is validated by numerical models. In the end, a practical and reliable method is proposed to identify the nonlinear parameters of Landau's solid by acoustoelastic elastography.

3.2 Intrinsic transverse isotropy

In this section, linear and nonlinear elastic theory of ITI materials are presented. ITI models have a large application for tissues such as ligaments, tendons and cardiac muscle [WEI 96]. Some numerical simulations follow to validate the implementation of these models in FEM.

3.2.1 Linear elastic ITI materials

Linear elastic theory is considered firstly. Using Voigt's notation, the elasticity tensor C_{ijkl} in Eq.1.3 can be represented by a 6×6 symmetric matrix. Given Cartesian coordinates (x_1, x_2, x_3) with the axis of symmetry (fiber direction) $\hat{A} = x_3$, ITI materials are isotropic in the (x_1, x_2) plane. Finally, the elasticity tensor contains five independent elastic constants, and it takes the form of

$$C = \begin{bmatrix} C_{11} & C_{12} & C_{13} & & & \\ C_{12} & C_{11} & C_{13} & & & \\ C_{13} & C_{13} & C_{33} & & & \\ & & & C_{55} & & \\ & & & & C_{55} & \\ & & & & & C_{66} \end{bmatrix} \tag{3.1}$$

with the relationship $C_{66} = \frac{C_{11} - C_{12}}{2}$.

In engineering, ITI materials are usually described by Young's moduli (E_T, E_L), Poisson's coefficients (ν_{LT}, ν_{TT}) and shear moduli (μ_T, μ_L) where longitudinal (L) and transverse (T) directions are defined with respect to the material symmetry. These parameters can be included into the compliance matrix (inverse of the elasticity tensor) in an explicit form,

$$S = C^{-1} = \begin{bmatrix} 1/E_T & -\nu_{TT}/E_T & -\nu_{LT}/E_L & & & \\ -\nu_{TT}/E_T & 1/E_T & -\nu_{LT}/E_L & & & \\ -\nu_{LT}/E_L & -\nu_{LT}/E_L & 1/E_L & & & \\ & & & 1/\mu_L & & \\ & & & & 1/\mu_L & \\ & & & & & 1/\mu_T \end{bmatrix} \tag{3.2}$$

with the relationship

$$\mu_T = \frac{E_T}{2(1 + \nu_{TT})} \tag{3.3}$$

3.2.2 Incompressibility

Considering incompressibility, it is necessary to keep the volumetric part of deformation (trace of the strain tensor) null. This is given by using Eq.1.3 and Eq.3.2,

$$\varepsilon_{vol} = \frac{1}{E_T}(1-\nu_{TT}-\nu_{LT}\frac{E_T}{E_L})(\sigma_{11}+\sigma_{22})+\frac{1}{E_L}(1-2\nu_{LT})\sigma_{33} \equiv 0 \tag{3.4}$$

By the above expression, it can be seen that Poisson's coefficients must satisfy the following conditions:

$$\nu_{TT} = 1-\frac{E_T}{2E_L} \tag{3.5}$$

and

$$\nu_{LT} = 0.5 \tag{3.6}$$

Therefore, there are three independent elastic constants for an incompressible ITI material: μ_T, μ_L and the ratio between the Young's modulus defined as $\beta = E_T/E_L$. Sometimes, the third parameter is represented by the expression of $E_L+\mu_T-4\mu_L$.

As fibers bring strength in ITI materials, in general, we have $E_L \geqslant E_T$. Considering the two extreme cases, $E_L = E_T$ and $E_L \gg E_T$, into Eq.3.5 and Eq.3.3, it is easy to find the lower and upper limit of Young's modulus in the transverse direction,

$$3\mu_T \leqslant E_T \leqslant 4\mu_T \tag{3.7}$$

It is worth to note that this relationship has been derived in [ROY 11] through the stability approach.

Finally, we point out, in numerical simulations, that quasi-incompressibility is ensured by setting ν_{LT} near to 0.5.

3.2.3 Shear wave propagation in incompressible ITI materials

In this work, we focus on shear wave propagation. It has been established that two shear (the word of *transverse* would be more accurate) wave may propagate in incompressible ITI materials [ROU 13, PAP 06, TWE 15, QIA 15], with speeds (phase velocities) given by

$$\rho c_{PT}^2 = \mu_T sin^2\theta + \mu_L cos^2\theta \tag{3.8}$$

$$\rho c_{QT}^2 = \mu_L + 4(\frac{\mu_T}{\beta}-\mu_L)sin^2\theta cos^2\theta \tag{3.9}$$

where the two modes are described in Fig.3.2. The first wave with the subscript 'PT' indicates purely transverse mode, polarized along x_2 direction. In some works, it is also named as *slow transverse wave* [PAP 06, TWE 15] or *shear horizontal wave* [QIA 15].

The second wave with ‘QT’ indicates quasi-transverse mode, polarized in (x_1,x_2) plan. Correspondingly, it is named as *fast transverse wave* or *quasi-shear vertical wave*.

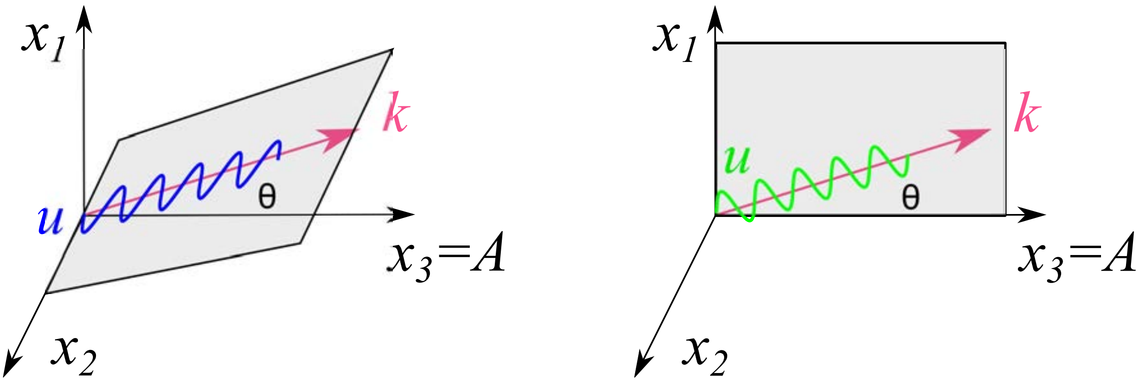

Figure 3.2: Two modes of shear wave in ITI materials. For the same propagation direction ($k = [sin\theta\ 0\ cos\theta]^T$), PT mode (left) polarizes along the direction x_2; QT mode (right) polarizes in the (x_1,x_3) plan.

Eq.3.8 shows that the speed of the PT mode depends only on the two shear moduli, μ_T and μ_L. They have been measured in early elastography experiments [GEN 03, SIN 05a]. Very recently, the third parameter β is considered by measuring QT mode at $\theta = 45°$ [QIA 15].

3.2.4 Hyperelastic theory

For completeness, the nonlinear ITI models are presented in this section. Within the general framework of ITI hyperelasticity, the strain energy can be written as

$$W = W_{iso}(I_1, I_2, I_3) + W_{aniso}(I_4, I_5) \tag{3.10}$$

The anisotropic invariants I_4 and I_5 arise directly from the anisotropy introduced by fibers. They are defined by

$$\begin{aligned} I_4 &= \mathbf{a}_0 \cdot \mathbf{C}\mathbf{a}_0 \\ I_5 &= \mathbf{a}_0 \cdot \mathbf{C}^2\mathbf{a}_0 \end{aligned} \tag{3.11}$$

where $\mathbf{a}_0$ represents the fiber direction in the undeformed configuration.

In Eq.3.10, the first term represents the mechanical response of the isotropic ground substance matrix, the second term represents the contribution of mainly collagen fibers. In most cases, the interaction fiber-matrix is omitted. The dependency on I_5 is also often omitted because many effects can be introduced into the function of I_4.

For example, the standard reinforcing model, which is a popular model in biomechanics literature, combines neo-Hookean model (Eq.1.21) with a quadratic function of I_4:

$$W = c_1(\bar{I}_1 - 3) + \frac{K}{2}(J-1)^2 + c_2(I_4 - 1)^2 \tag{3.12}$$

Remark:

For Eq.3.12 or similar ITI nearly incompressible hyperelastic models, there is a discussion on whether using the full invariant of I_4 or just its deviatoric part $\bar{I}_4 = J^{-2/3}I_4$. The latter case comes from the tradition of decoupling the strain energy for isotropic materials. The problem has been addressed recently in [NOL 14], the use of I_4 is more realistic because the volumetric anisotropic contribution is represented. However, if the bulk modulus K is every high, there is almost no difference. ■

A necessary condition for all hyperelastic models is that the (initial) elastic modulus should be recovered from these models at infinitesimal deformation [MUR 13, DES 13a]. Apparently, Eq.3.12 includes only two parameters (excluding the bulk modulus K), it is not possible to be compatible with the linear theory (Eq.3.3). Indeed, the standard reinforcing model implies that the two shear moduli are equal, $\mu_L = \mu_T$. This is incorrect for soft tissues, because a number of experiments (see in [QIA 15]) have shown that the shear moduli are different along and across the muscle fibers.

To capture the full mechanical response of ITI soft tissue, and at the same time, to ensure the compatibility condition between the linear theory and hyperelastic models, the following conditions have to be satisfied [MER 05],

$$\begin{cases} W_1 + W_2 = \mu_T/2 \\ W_1 + W_2 + W_5 = \mu_L/2 \\ W_{44} + 4W_{45} + 4W_{55} = (E_L + \mu_T - 4\mu_L)/4 \end{cases} \tag{3.13}$$

where $W_i = \partial W/\partial I_i$ and $W_{ij} = \partial^2 W/\partial I_i \partial I_j$ for $i, j \in 1,2,4,5$. It can be noted that both anisotropic invariants I_4 and I_5 should be included. Murphy [MUR 13] has shown that the standard models (*e.g.* Eq.3.12) can be 'fixed' by adding a new term. For instance, the standard reinforcing model may be rewritten in form of

$$W = \frac{c_1}{2}(\bar{I}_1 - 3) + \frac{c_2}{8}(I_4 - 1)^2 + \frac{c_3}{2}(2I_4 - I_5 - 1) + \frac{K}{2}(J-1)^2 \tag{3.14}$$

To be in accordance with the linear elastic theory, the parameters are calculated by

$$c_1 = \mu_T, \quad c_2 = E_L + \mu_T - 4\mu_L, \quad c_3 = \mu_T - \mu_L \tag{3.15}$$

Using the above expressions, Eq.3.12 is recovered when $\mu_L = \mu_T$. What is more, if $\mu_L = \mu_T$ and $E_L = E_T$, both c_2 and c_3 vanish, and the model is reduced to isotropic.

Note that Eq.3.14 is only an idealized model, it ensures that the model coincides with the linear theory at small deformation, but there is no nonlinear parameter involved.

3.2.5 Numerical validation

In the following, numerical examples are considered for the two following purposes. Firstly, they demonstrate Eq.3.8 and Eq.3.9 numerically. It is especially necessary to illustrate how the third parameter β affects the wave speed. Secondly, they validate the hyperelastic ITI model in Eq.3.14 based on the fact that, for small amplitude waves, the propagation speed should be identical to the linear elastic theory.

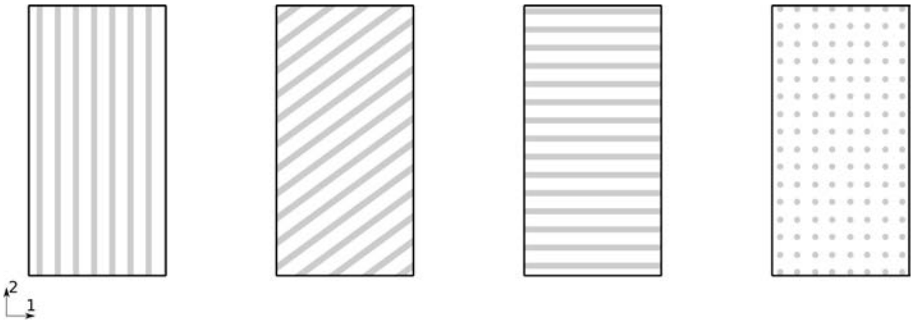

Figure 3.3: The fiber direction from left to right: $\mathbf{a}_0 = [0\ 1\ 0]$, $\mathbf{a}_0 = [1\ 1\ 0]$, $\mathbf{a}_0 = [1\ 0\ 0]$ and $\mathbf{a}_0 = [0\ 0\ 1]$. The second configuration has been used twice to illustrate the influence of β, see Tab.3.1.

With this intention, five cases (see Tab.3.1) and four configurations (see Fig.3.3) are considered. All the cases are under the assumption of plane strain and plane wave propagation, the geometry of the FE model is the same as in Sec.2.3.2, so the details are omitted here.

In cases 1, 4 and 5, the fiber directions coincides with the coordinate directions x_1, x_2 and x_3 respectively, the shear wave speed is only driven by μ_L or μ_T. In cases 2 and 3, the fibers are aligned on 45° in the (x_1,x_2) plan, so the third parameter β has the largest effect on the shear wave speed ($\sqrt{\mu_T/(\beta\rho)}$ by Eq.3.9) . Subsequently, two values of β, 0.25 and 0.11, are tested to illustrate the corresponding effect. Hence, all parameters involved in ITI incompressible material are tested.

After the numerical simulations, the shear wave speeds are measured from the displacement history at different depths (x_1 direction). This is the same process as in 1D transient elastography (see Chapter1.1.2.1). Taking case 2 as an example, Fig.3.4(a) is a typical presentation of elastography experiments, the progression of the shear wave fronts can be clearly distinguished, and it can be sure that the results are not polluted by reflected waves. Fig.3.4(b) presents the same results but clearer, each curve represents the displacements at one depth. For clarity, the displacements are amplified by a factor of 10^3. The maximal values of each displacement are marked by red points, the corresponding shear wave speed is then deduced by the linear regression of these points.

Finally, all measured speeds are summarized in Tab.3.1. By comparing with the analytical results, it can be observed that the measured values have a very good accuracy. The incompressible ITI hyperelastic model is therefore validated.

Case	fiber direction	β	c_S (m/s) theory (Eq.3.8 or Eq.3.9)	c_S (m/s) measure
1	$\mathbf{a}_0 = [0\ 1\ 0]$	0.25	1.41	1.40
2	$\mathbf{a}_0 = [1\ 1\ 0]$	0.25	2	1.99
3	$\mathbf{a}_0 = [1\ 1\ 0]$	0.11	3	3.01
4	$\mathbf{a}_0 = [1\ 0\ 0]$	0.25	1.41	1.40
5	$\mathbf{a}_0 = [0\ 0\ 1]$	0.25	1	0.98

Tableau 3.1: Five cases considered to validate the hyperelastic ITI model. $\mu_T = 1\ kPa$ and $\mu_L = 2\ kPa$

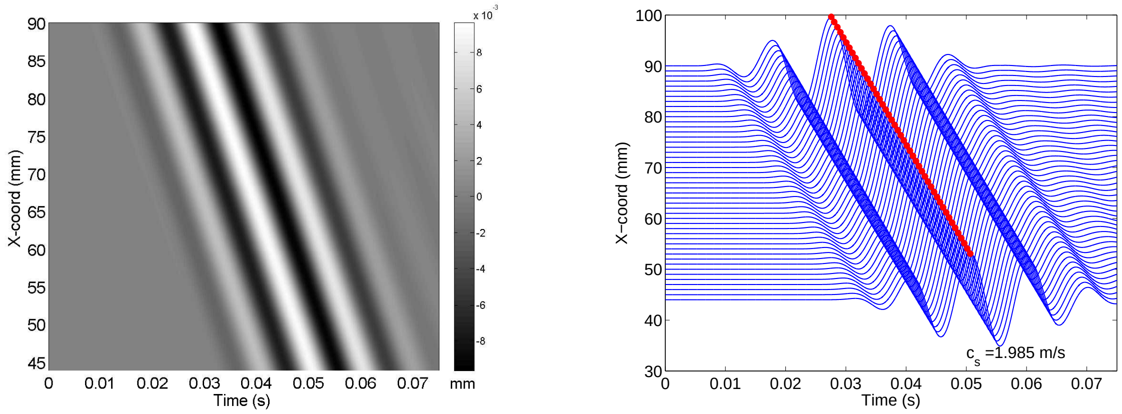

(a) Typical figure of 1D transient elastography

(b) Displacement is amplified by 10^3. Shear wave speed is deduced by the linear regression of maximal points.

Figure 3.4: The measurement of the shear wave speed based on the simulation results (Case 2 as example).

3.3 Extrinsic transversely isotropy: shear wave speeds under uniaxial pre-deformation

In this section, transversely isotropy is caused by a uniaxial finite pre-deformation. When small amplitude waves propagate in this pre-deformed configuration, the propagation speed is different to the natural state. This is known as acoustoelastic effect and can be used for characterizing the nonlinear parameters of soft tissues.

Assume that an isotropic, incompressible [1] solid is subjected to a uniaxial tension or compression in direction x_1. The gradient of deformation can be expressed by the stretch λ in the principal direction,

---

[1] Analytical analysis is always carried out by fully incompressible hypothesis, $W_{vol} = 0$.

Wave type	Polarization u	Propagation k
i	2 or 3	1
ii	2 (3)	3 (2)
iii	1	2 or 3

Tableau 3.2: Three types of linear polarized shear wave in an uniaxial pre-deformed medium, corresponding to Fig.3.5. Due to the uniaxial deformation in the direction 1, the direction 2 and 3 are exchangeable.

$$\mathbf{F} = \begin{bmatrix} \lambda & 0 & 0 \\ 0 & 1/\sqrt{\lambda} & 0 \\ 0 & 0 & 1/\sqrt{\lambda} \end{bmatrix} = \begin{bmatrix} e+1 & 0 & 0 \\ 0 & \frac{1}{\sqrt{e+1}} & 0 \\ 0 & 0 & \frac{1}{\sqrt{e+1}} \end{bmatrix} \tag{3.16}$$

where the elongation parameter $e = \lambda - 1$ ($e > 0$ for tension) can be directly measured from experiments.

Like the analysis for ITI materials, only special configurations of plane shear waves are considered, three types of wave are described in an ETI material (see Fig.3.5) and are also summarized in Tab.3.2.

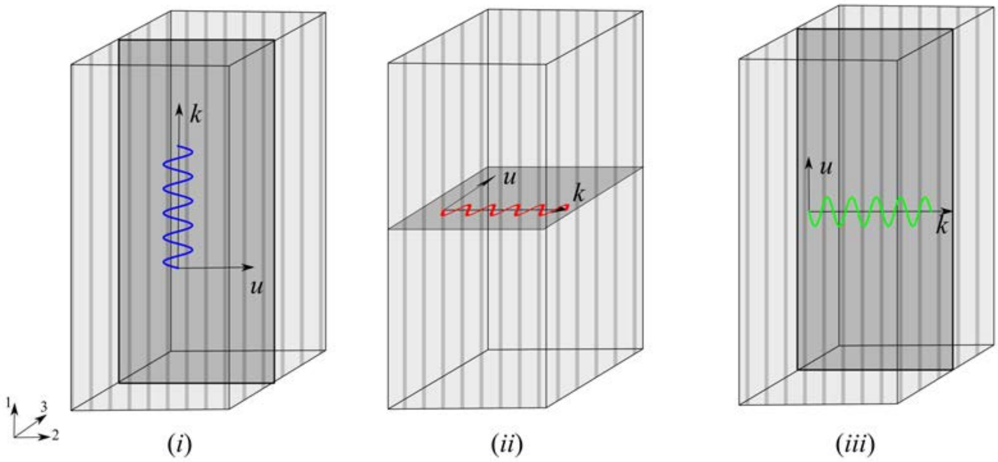

Figure 3.5: Three typical configurations of linear polarized shear wave in a uniaxial pre-deformed medium. The propagation direction (k) and polarization direction (u) are either parallel or perpendicular to the elongation direction.

Remark:

- For ITI materials, we have shown that wave types *i* and *iii* have the same propagation speed (they correspond to the QT mode with $\theta = 90°$ and $\theta = 0°$). However, this is no longer true for ETI materials, it will be shown that these two waves have very different behaviours once a pre-deformation is applied.

- From a practical point of view, wave type *iii*, which propagates normal to the direction of the elongation and polarizes along that direction, is the easiest configuration to achieve in an *in vivo* measurement. As shown in Fig.3.6 from [JIA 15a], pre-deformation can be applied by pressing the SSI device, the plane wave generated by it propagates normally to the loading direction and polarizes along this direction. ■

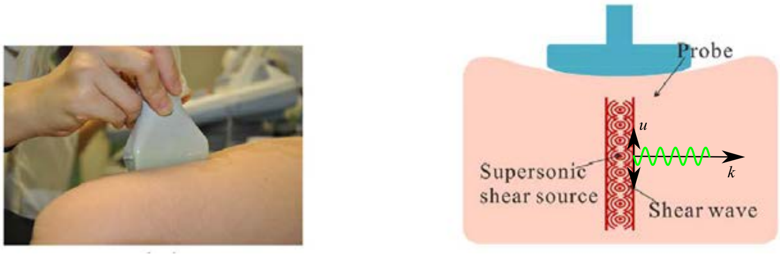

Figure 3.6: A practical *in vivo* measurement of acoustoelastic effect using the SSI technique [JIA 15a]. The wave type *iii* is measured based on this configuration.

3.3.1 Analytical theory

The theory describing the small amplitude shear wave propagation in a pre-deformed hyperelastic solids is briefly presented here, more details can be found in [OGD 07, DOW 90, DES 05].

Suppose that the material is subjected to a homogeneous pre-deformation F_{ij} (same as Eq.3.16, it is convenient to use the component form in the following). In the deformed configuration, the incremental motion equation is the key governing equation, it can be expressed as

$$C_{0piqj}u_{j,pq} - \dot{p}_{,i} = \rho u_{i,tt} \tag{3.17}$$

where p is a Lagrange multiplier to hold the incompressibility constraint, note that the density ρ does not change before and after pre-deformation. C_{0piqj} is the push forward of the elasticity tensor C_{piqj} (see its definition in Eq.2.7), defined as

$$C_{0piqj} = \frac{1}{J}F_{pk}F_{ql}C_{kilj} \tag{3.18}$$

Our first interest is to analyze how the shear wave speed depends on the different models and deformation state of a soft tissue. For the three special configurations, the shear wave speeds can be written as [DES 10b]:

$$\begin{aligned}
\rho c_{i}^{2} &= C_{01212} = (\lambda_1 W_1 - \lambda_2 W_2)\lambda_1^2/(\lambda_1^2 - \lambda_2^2) \\
\rho c_{ii}^{2} &= C_{02323} = (\lambda_2 W_2 - \lambda_3 W_3)\lambda_2^2/(\lambda_2^2 - \lambda_3^2) \\
\rho c_{iii}^{2} &= C_{02121} = (\lambda_2 W_2 - \lambda_1 W_1)\lambda_2^2/(\lambda_2^2 - \lambda_1^2)
\end{aligned} \tag{3.19}$$

where W is the strain energy function and $W_i = \partial W/\partial\lambda_i$, the three shear wave speeds are presented by c_i, c_{ii} and c_{iii} respectively. It is emphasized that the speeds are expressed in the deformed configuration, which is consistent with the measurement in experiments. Moreover, Eqs.3.19 are true for both isotropic and anisotropic hyperelastic materials depending on the choice of energy function W.

In the following, we apply the analytical theory into several common isotropic material models.

3.3.1.1 Neo-Hookean solid

For a start, neo-Hookean solid (Eq.1.21) is considered. By applying Eqs.3.19, we obtain

$$\rho c_i^2 = (e+1)^2\mu \tag{3.20a}$$

$$\rho c_{ii}^2 = \frac{\mu}{e+1} \tag{3.20b}$$

$$\rho c_{iii}^2 = \frac{\mu}{e+1} \tag{3.20c}$$

The same results have been shown in [SHE 12] through a different approach. These expressions are plotted in Fig.3.7 by setting both the density ρ and the (initial) shear modulus μ to unity.

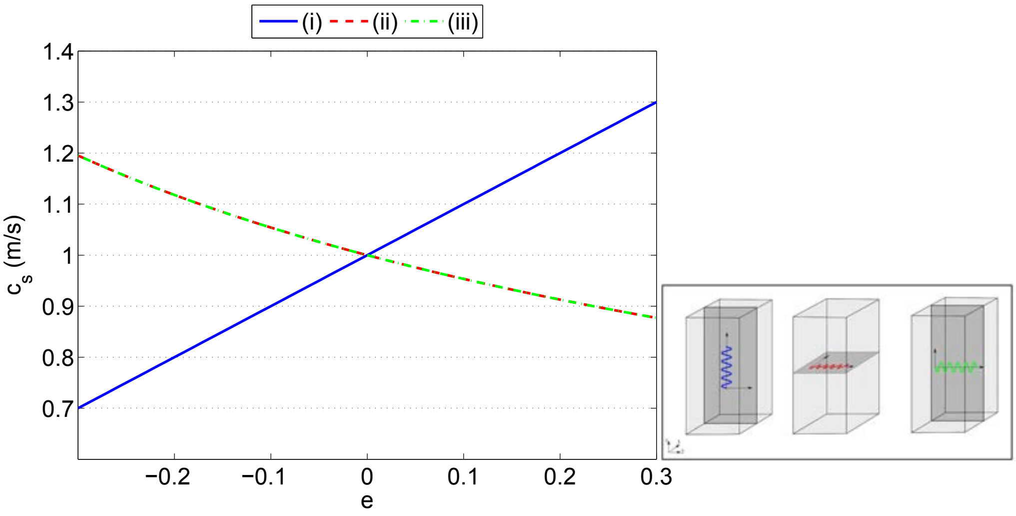

Figure 3.7: Shear wave speed in a uniaxially deformed (along the vertical direction) neo-Hookean solid. $\rho = 1000\ kg/m^3$, $\mu = 1\ kPa$

An interesting phenomenon is remarked for neo-Hookean solids: the wave type *ii* and *iii* have the same propagation speed. Particularly, the time necessary for the three types of waves to cross a neo-Hookean material is constant at any state of pre-deformation. In other words, the wave speeds do not change if they are expressed in the initial configuration. This is consistent with the linear elastic theory.

3.3.1.2 Mooney-Rivlin solid

Secondly, Mooney-Rivlin model (Eq.1.22) is adopted into Eqs.3.19, we obtain

$$\rho c_i^2 = 2c_1 e^2 + (4c_1 + 2c_2)e + 2(c_1 + c_2) \tag{3.21a}$$

$$\rho c_{ii}^2 = \frac{2c_1 + 2c_2(e+1)^2}{e+1} \tag{3.21b}$$

$$\rho c_{iii}^2 = \frac{2c_1(e+1) + 2c_2}{(e+1)^2} \tag{3.21c}$$

In Fig.3.8, the same test is shown using the above expressions. The results are clearly different than in neo-Hookean solid, the pre-deformation leads to three different wave speeds, and their variations along the pre-deformation are also different. It can be seen that the wave type *i* increases with the elongation *e*, the type *iii* decreases and the type *ii* remains almost constant.

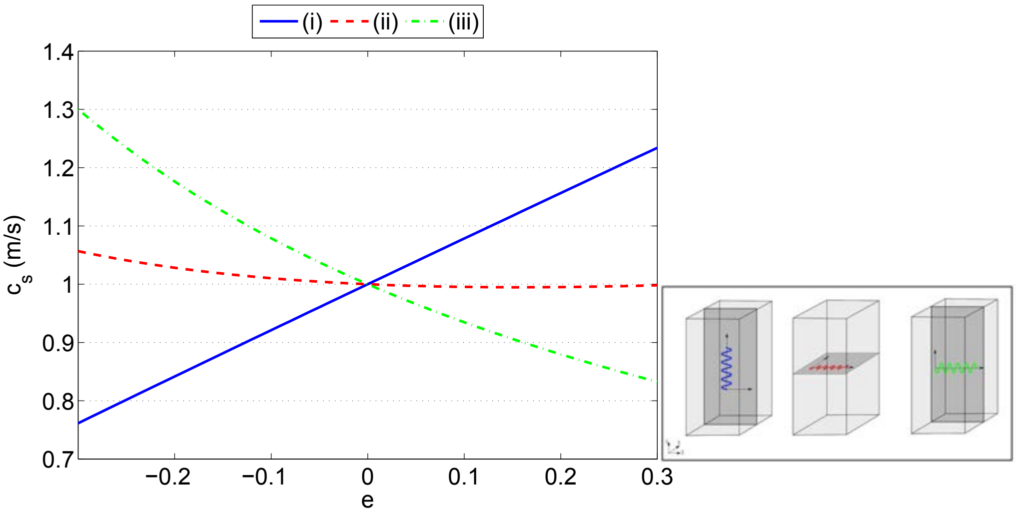

Figure 3.8: Shear wave speed in a uniaxially deformed Mooney-Rivlin solid. $\rho = 1000\ kg/m^3$, $c_1 = 0.286\ kPa$, $c_2 = 0.214\ kPa$

3.3.1.3 Kirchhoff solid

As aforementioned in Chapter 1, Kirchhoff solid is a special case of Landau's model where $A = D = 0$. However, as it shares the same material parameter with neo-Hookean solid, it is thus interesting to show its acoustoelastic behaviour. Applying Eq.3.19 for

Kirchhoff solid (Eq.1.31), we obtain

$$\rho c_i^2 = \mu(e^4 + 4e^3 + 5e^2 + 3e + 1) \tag{3.22a}$$

$$\rho c_{ii}^2 = \mu \frac{1-e}{(e+1)^2} \tag{3.22b}$$

$$\rho c_{iii}^2 = \mu \frac{e^3 + 3e^2 + 2e + 1}{(e+1)^2} \tag{3.22c}$$

The corresponding results are plotted in Fig.3.9. With the same material parameters as given in neo-Hookean solid, Kirchhoff solid is clearly different, the speeds of the three waves are all different. Compared to Mooney-Rivlin solid (Fig.3.8), the waves of type *i* have similar variation, but the waves type *ii* and *iii* change the variation directions.

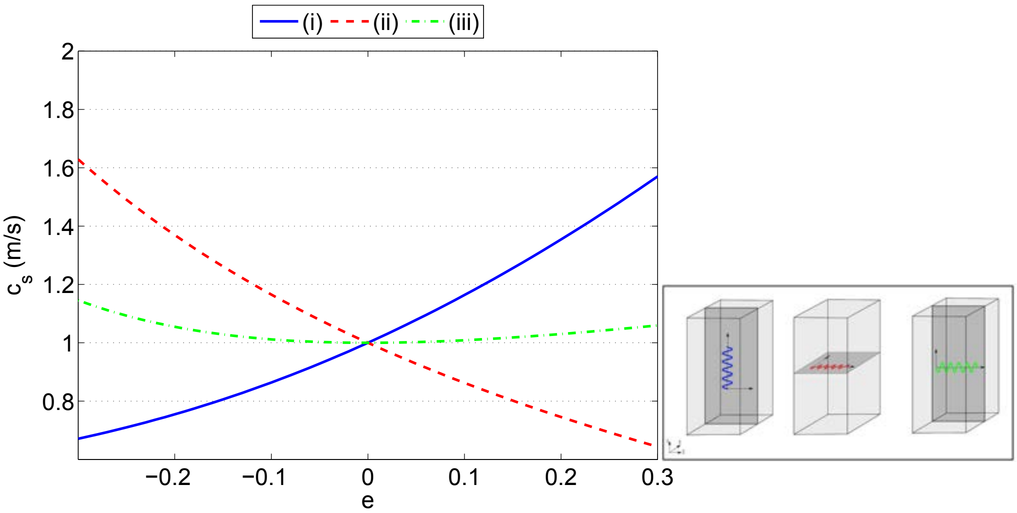

Figure 3.9: Shear wave speed in a uniaxially deformed Kirchhoff solid. $\rho = 1000\ kg/m^3$, $\mu = 1\ kPa$

3.3.1.4 Landau's solid

Finally, the incompressible Landau's model (Eq.1.32) is considered into Eqs.3.19, the resulting expressions are cumbersome but straightforward. They are written in form of

$$\begin{aligned}
\rho c_i^2 &= \mu(e^4+4e^3+5e^2+3e+1)+\frac{A}{4}(e^6+6e^5+13e^4+13e^3+7e^2+e) && \text{(3.23a)}\\
&+\frac{D}{2}e^2\frac{e^7+9e^6+33e^5+64e^4+74e^3+55e^2+24e+6}{e+1} &&\\
\rho c_{ii}^2 &= \mu\frac{1-e}{(e+1)^2}+\frac{A}{4}\frac{e(e-2)}{(1+e)^3}+\frac{D}{2}e^2\frac{-e^5-5e^4-7e^3+e^2+6e+6}{(e+1)^4} && \text{(3.23b)}\\
\rho c_{iii}^2 &= \mu\frac{e^3+3e^2+2e+1}{(e+1)^2}+\frac{A}{4}e\frac{e^5+6e^4+13e^3+13e^2+7e+1}{(e+1)^3} && \text{(3.23c)}\\
&+\frac{D}{2}e^2\frac{e^7+9e^6+33e^5+64e^4+74e^3+55e^2+24e+6}{(e+1)^4} &&
\end{aligned}$$

For limited pre-deformations, the high order terms are negligible. Destrade *et al.* [DES 10b] have given the simplified expressions up to the second order,

$$\rho c_i^2 \simeq \mu+(3\mu+\frac{A}{4})e+(5\mu+\frac{7A}{4}+3D)e^2 \tag{3.24a}$$

$$\rho c_{ii}^2 \simeq \mu-(3\mu+\frac{A}{2})e+(5\mu+\frac{7A}{4}+3D)e^2 \tag{3.24b}$$

$$\rho c_{iii}^2 \simeq \mu+\frac{A}{4}e+(2\mu+A+3D)e^2 \tag{3.24c}$$

It can be observed that, contrary to the nonlinear shear wave propagation presented in the previous chapter, the parameter D has a one order smaller influence on the wave speed. In this sense, it is reasonable to keep the statement that A is the third order and D is the fourth order elastic parameters.

For small pre-deformation, $|e| \ll 1$, the second order terms can be further neglected. Recalling that the pre-deformation can be calculated by $e \simeq -\sigma/(3\mu)$ for incompressible solids, the expressions derived in [GEN 07] are recovered,

$$\rho c_i^2 \simeq \mu-\sigma(1+\frac{A}{12}) \tag{3.25a}$$

$$\rho c_{ii}^2 \simeq \mu+\sigma(1+\frac{A}{6}) \tag{3.25b}$$

$$\rho c_{iii}^2 \simeq \mu-\sigma(\frac{A}{12}) \tag{3.25c}$$

In Fig.3.10, a comparison of these approximations is made for the material with $\mu = 1$ *kPa*, $A = D = 10$ *kPa*. It can be concluded that, the first order approximation (Eq.3.25) is no longer valid for pre-deformation larger than 3%. Below 10%, the second order approximation (Eq.3.24) introduces about 5% error (except for the wave type *iii* in compression). It is emphasized that this is only a general observation based on specific material parameters. With different combinations of nonlinear parameters A and D, the conclusion may change. Nevertheless, knowing that the pre-deformation can easily reach 0.3 for most soft tissues [JIA 15a], it is suggested to keep high order approximations to model experiments on soft tissues. This point will be clearly illustrated in the following (Sec.3.5.1).

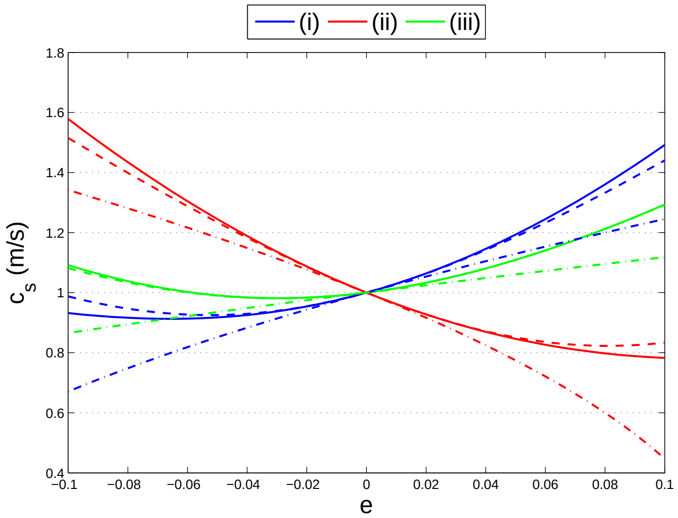

Figure 3.10: Shear wave speed in a uniaxially deformed Landau's solid. $\rho = 1000\ kg/m^3$, $\mu = 1\ kPa$, $A = D = 10\ kPa$. (Solid lines: Eq.3.23; Dashed lines: Eq.3.24; Dash- dot lines: Eq.3.25)

3.3.2 Numerical validation

In order to validate these analytical results, a FE numerical model is presented. Firstly, the static simulations are carried out by the classical Newton-Raphson algorithm, then the pre-deformed geometry is imported into the dynamic simulation with explicit time integration method.

The model considered here is a cuboid with a size of $60 \times 30 \times 30\ mm$, see Fig.3.11. It is meshed by 54000 cubic elements with a side length of $l_e = 1\ mm$. A homogeneous static load is applied at its surface and a small dynamic load is applied at the edge to generate a plane shear wave. As shown in Fig.3.11, two configurations are used to simulate the three types of wave. From Fig.3.11(a), the waves types i and ii are measured following the two directions, it can be seen that the wave type i (blue) is slightly faster than the type ii (red). In Fig.3.11(b), shear wave propagates in the symmetric plane, the wave of type iii (green) is measured.

For all numerical simulations, quasi incompressibility is ensured by setting the bulk modulus $K = 10\ MPa$.

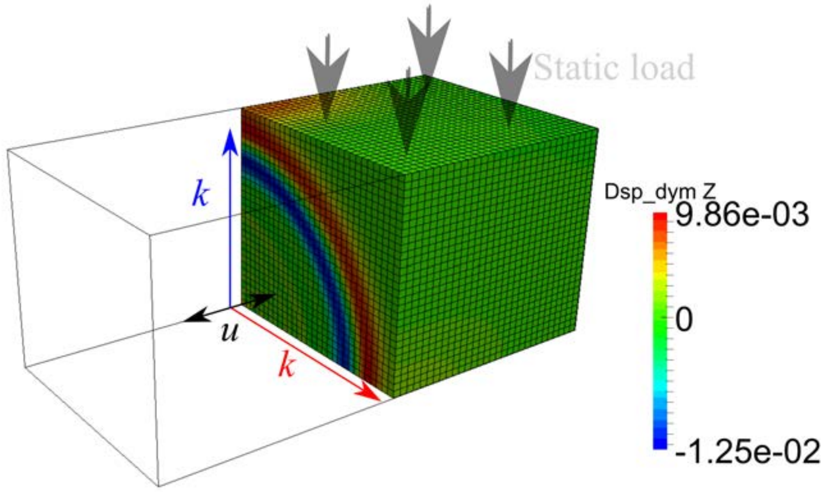

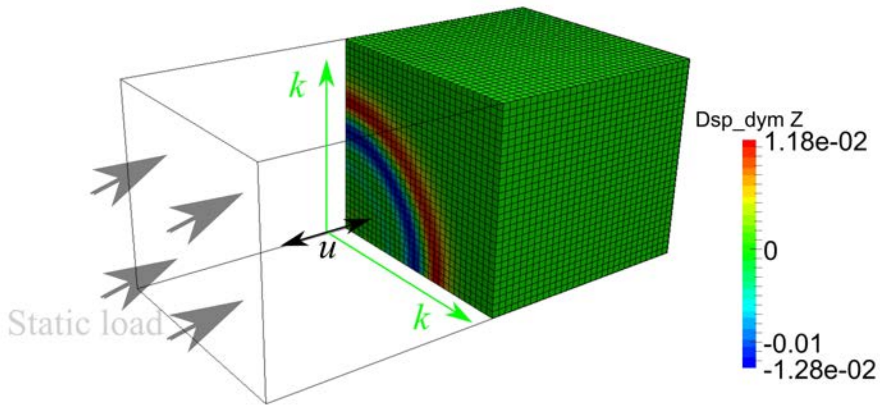

(b) In this configuration, wave type *iii* is measured

Figure 3.11: Finite element models (half) of acoustoelastic analysis. The figures show the displacement introduced by the small dynamic load (along direction *u*) in the deformed configuration.

3.3.2.1 Mooney-Rivlin solid

The given Mooney Rivlin solid is tested firstly, a comparison is made in Fig.3.12 with the analytical solutions mentioned above. Due to the high computational cost, both the size and mesh density of the 3D model are limited. As a result, more errors exist for the wave speeds measured by the simulations, this can be confirmed by the error for the natural state (no pre-deformation, $e = 0$). Always, the numerical results predict correctly the change of wave speed at all pre-deformed states.

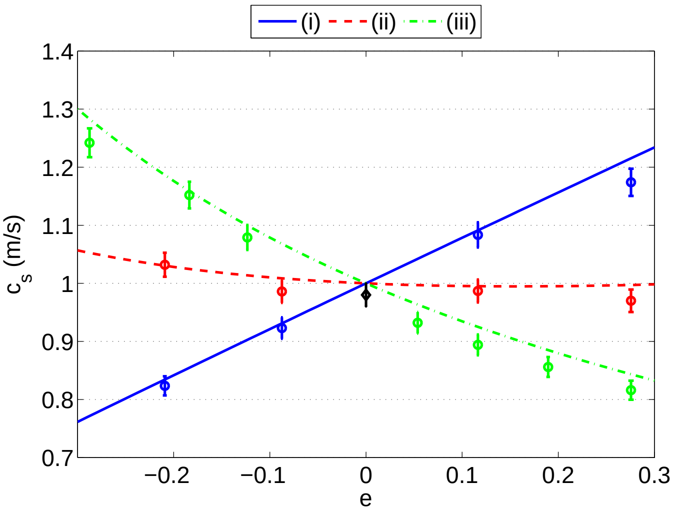

Figure 3.12: Numerical simulations (circles) *v.s.* analytical solutions (Fig.3.8) of Mooney Rivlin solid. $\rho = 1000\ kg/m^3$, $c_1 = 0.286\ kPa$, $c_2 = 0.214\ kPa$. Error bars (2%) are estimated by the measurement at natural state.

3.3.2.2 Landau's solid

Secondly, Landau's solid is tested with the normalized parameters from [RÉN 08]: $\mu = 1\ kPa$, $A = -5.71\ kPa$, $D = 4.55\ kPa$. In the following (Sec.3.5.2), we will show that this combination satisfies the stability condition, so it can be subjected to large pre-deformation. In Fig.3.13, the numerical results are in a good agreement with the analytical expressions in Eq.3.23. The most significant difference with Mooney-Rivlin solid is that wave speeds increase for both pre-compression and pre-tension.

3.4 Extrinsic anisotropy: shear wave speeds under general pre-deformation

In the previous section, we show the acoustoelastic behaviour for different hyperelastic models in a uniaxially pre-deformed configuration, the numerical simulations are consistent with the analytical theory. In real life conditions, the uniaxial pre-deformation is not

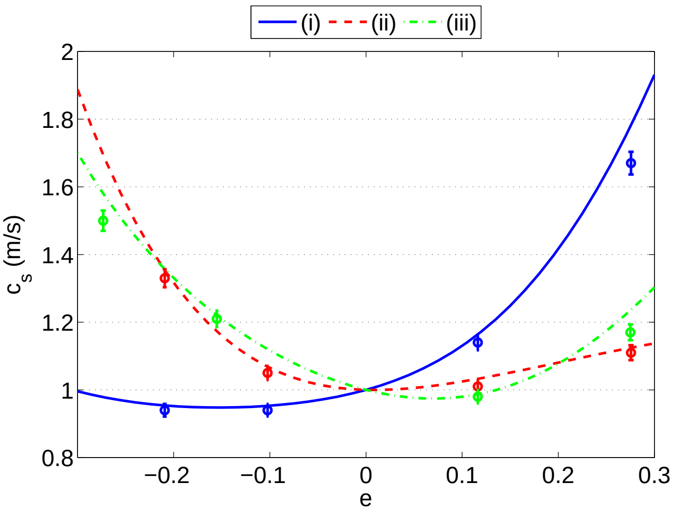

Figure 3.13: Numerical simulations (circles) *v.s.* analytical solutions of Landau's solid. $\rho = 1000\ kg/m^3$, $\mu = 1\ kPa$, $A = -5.71\ kPa$, $D = 4.55\ kPa$. Error bars: 2%.

always easy to achieve. Considering the assumption of (locally) homogeneous strain and incompressibility, the pre-deformation in the region of interest can be described as

$$\mathbf{F} = \begin{bmatrix} \lambda & 0 & 0 \\ 0 & \lambda^{-\xi} & 0 \\ 0 & 0 & \lambda^{\xi-1} \end{bmatrix} \tag{3.26}$$

where ξ is a parameter which is in the range of $0-1$. $\xi = 1$ and $\xi = 0$ represent the plane strain deformation case and $\xi = 0.5$ represents a uniaxial strain.

Remark:

On this topic, a new method has been proposed by Jiang *et al.* [JIA 15a] to determine both ξ and λ for a given experiment. For the first time, nonlinear elastography by acoutoelastic effect has been carried out *in vivo* in this paper. ■

3.4.1 Analytical theory

A remarkable difference should be emphasized for general pre-deformation. As the deformation in direction 3 is not necessarily the same as in direction 2, the pre-deformed material is no longer transversely isotropic, but orthogonally isotropic. Thus another three types of shear wave appear, as illustrated in Fig.3.14. Consequently, their wave speeds are summarized in Eq.3.27.

$$\begin{aligned} \rho c_{iv}^2 &= C_{01313} = (\lambda_1 W_1 - \lambda_3 W_3)\lambda_1^2/(\lambda_1^2 - \lambda_3^2) \\ \rho c_{v}^2 &= C_{03232} = (\lambda_3 W_3 - \lambda_2 W_2)\lambda_3^2/(\lambda_3^2 - \lambda_2^2) \\ \rho c_{vi}^2 &= C_{01212} = (\lambda_1 W_1 - \lambda_2 W_2)\lambda_1^2/(\lambda_1^2 - \lambda_2^2) \end{aligned} \tag{3.27}$$

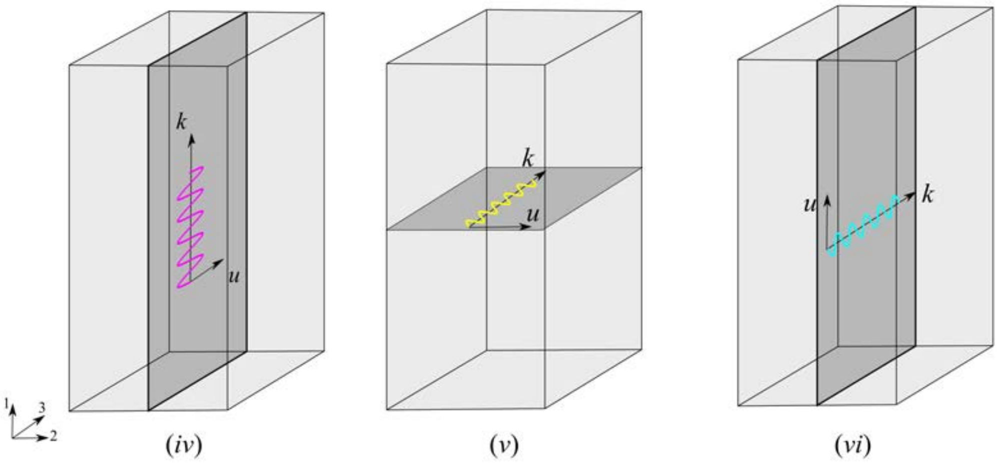

(iv) (v) (vi)

Figure 3.14: New configurations of linear polarized shear wave in a generally pre-deformed medium.

Six different shear waves could make the problem very complicated, however, the analytical model is still available and there is no need to discuss all the situations. In the following, a special case in plane strain hypothesis is discussed by both analytical and numerical methods.

3.4.2 Numerical validation

By setting $\xi = 1$, the deformation in direction 3 is constrained. Holding this hypothesis for static and dynamic load, only two shear waves (type *i* and *iii*) exist, thus the analytical expressions can be easily validated by 2D numerical models.

The FE model from Sec.2.3.2 is employed again. Moreover, considering the shear wave speeds depend on the pre-deformation and not the pre-stress (as it can be seen from Eq.3.18), the pre-deformed state can be considered either by compression or by tension, as shown in Fig.3.15. Consequently, for a same configuration or simulation, the shear wave can be regarded as either type *iii* or type *i*.

In Fig.3.15, the numerical simulations are compared to the analytical solutions. The same simulation results are used for the wave type *iii* and type *i*. Because the FE mesh is refined enough in this 2D model, the numerical results are very close to the analytical curves. Moreover, the numerical results also prove that the wave speed indeed depends only on the pre-deformation (the reason of using the word ‘pre-deformation’ instead of ‘pre-stress’).

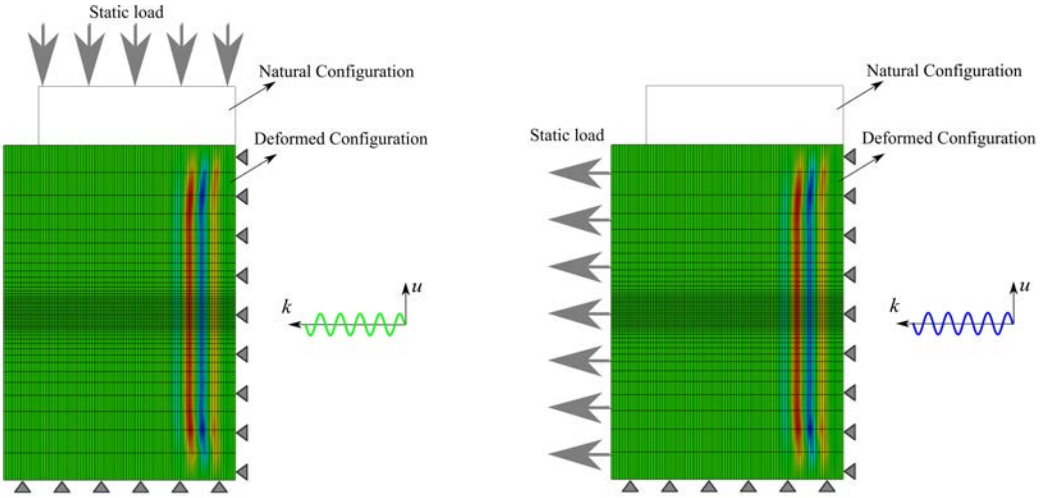

(a) Pre-deformation induced by compression, wave speed of type *iii* is measured

(b) Pre-deformation induced by tension, wave speed of type *i* is measured

Figure 3.15: 2D FE model in Sec.2.3.2 after a certain pre-deformation, plane shear wave propagates from right to left.

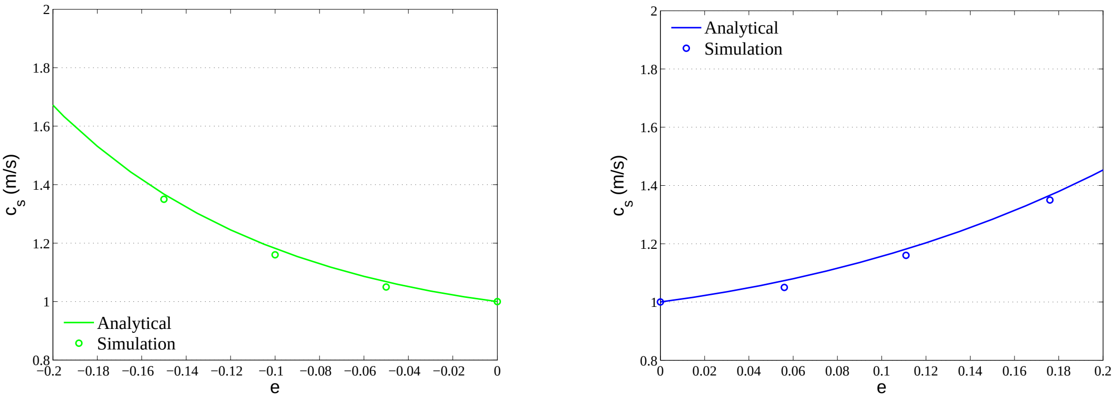

(a) Considered as compression, see Fig.3.15(a)

(b) Considered as tension, see Fig.3.15(b)

Figure 3.16: Numerical simulations (circles) *v.s.* analytical solutions of Landau's solid in plane deformation. $\rho = 1000\ kg/m^3$, $\mu = 1\ kPa$, $A = -5.71\ kPa$, $D = 4.55\ kPa$. (Note: numerical results in Fig.(a) and Fig.(b) are from the same simulation.)

3.5 Characterization of Landau's constitutive law by acoustoelastic effect

In the above, the influence of pre-deformation on the shear wave speed of nonlinear materials has been presented. However, determining the nonlinear parameters of a soft tissue is an inverse problem. Many inverse problems are ill-posed, small errors in the input data can make the identified solution meaningless.

Thus, it is necessary and important to consider the properties of inverse solutions, *i.e.* the accuracy, stability, uniqueness. For example, in [JIA 15a, LI 16], a condition number has been proposed to ensure that the wave speed has a large enough variation to be measured under different states.

In the following, the solution properties are considered and a robust fitting method is proposed for Landau's solid.

3.5.1 Solution property: accuracy

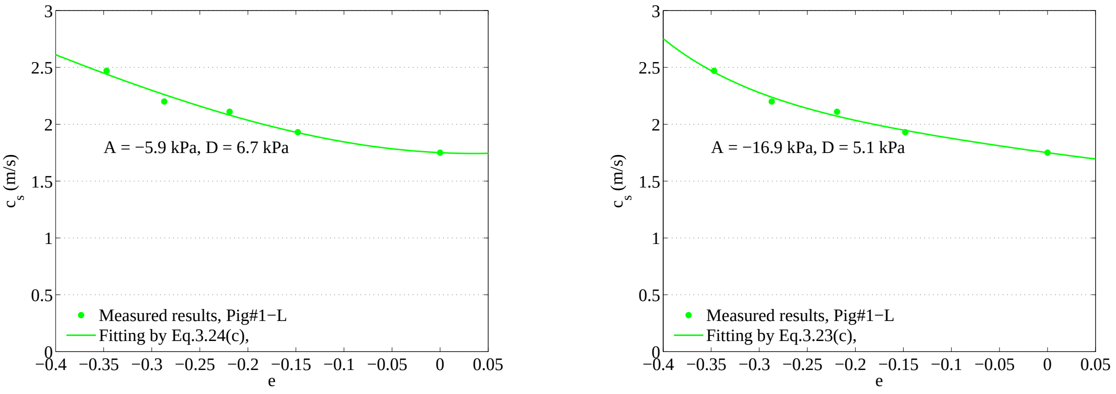

(a) Fitted by the second order approximation, Eq.3.24(c). Note: in the original paper, $A = -5.6$, $D = 6.8$, errors come from the re-pickup of data

(b) Fitted by the accurate expression, Eq.3.23(c)

Figure 3.17: Comparison of different fitting results on the same experimental data (From [JIA 15b]).

Firstly, as mentioned above, wave speeds in biological tissues are measured under large pre-deformations. To keep the accuracy in fitting, it is better to keep the accurate analytical expression of wave speed.

In [JIA 15b], Jiang *et al.* accessed the nonlinear parameters of pig brains *ex-vivo*, this is known as the only work in which both nonlinear parameters of Landau's solid are identified by acoustoelastic elastography. In this work, the shear wave speed of type *iii* have been measured by SSI technique under different pre-compression state, up to

$e = -0.4$. Then, the second order approximated expression, Eq.3.24(c), is used to fit the parameters A and D, as shown in Fig.3.17(a). However, if the same data is fitted by the accurate expression (Eq.3.23(c)), as shown in Fig.3.17(b), a very different result is obtained, especially for the parameter A.

3.5.2 Solution property: stability

The stability criterion is another important issue. At least, the materials identified by acoustoelastic effect should satisfy the stability criterion (the second law of thermodynamics). On the other hand, the stability criterion give a guideline in identifications. Moreover, materials which satisfy the stability condition ensure the solvability of numerical models in large deformation, the material which violates the stability criterion is not suggested to be used [BEL 13a].

In general, the stability criterion can be examined by verifying that the elasticity tensor C_{piqj} is positive definite. In this work, the stability is considered by a small perturbation under finite pre-deformation [ZHO 96]: it is necessary to ensure that the shear wave speeds are positive and finite under the corresponding pre-deformation state[2], *i.e*, the right terms of Eq.3.19 and Eq.3.27 should always be positive.

For example, for neo-Hookean and Mooney-Rivlin models, considering that the elongation parameter e varies from -1 to $+\infty$, it is sufficient to set $\mu > 0$ or $c_1, c_2 > 0$ to ensure stability in any deformation. Moreover, Kirchhoff solid is always unstable in large tension, because Eq.3.22a(b) is negative when $e > 1$.

However, the stability criterion of Landau's solid changes under different pre-deformation states. To handle this variation, the following method is proposed: firstly, the (initial) shear modulus μ should always be positive, so the objective is to find appropriate values of A and D to make sure that the material is stable under the given pre-deformation; secondly, the stable zone is searched in the domain of $-10 \leq \frac{A}{\mu} \leq 10$ and $-10 \leq \frac{D}{\mu} \leq 10$, which follows the experimental observations that μ, A and D are in the same order of magnitude; finally, Eqs.3.23 are calculated at different levels of pre-deformation, and the zone which satisfies the right term being positive are plotted.

3.5.2.1 Uniaxial pre-deformation ($\xi = 0.5$)

Fig.3.18(a) and (b) display the stable zone of Landau's solid in uniaxial compression and tension respectively. Both figures show that the stable zone reduces when the pre-deformation level ($|e|$) grows. The lines correspond to the upper limit of the stability area for different values of e; for instance, the pink area at the top is the stability area for $|e| < 0.55$. With $|e| < 0.15$, all the values of A and D in the searching range satisfy the stability criterion. Generally, when $|e|$ is about 0.5, the parameter A could be both positive and negative, but D should be positive, the stability criterion in tension is slightly stricter than in compression.

---

[2] The compressional wave speed in nearly incompressible models can be ensured by large positive value of the bulk modulus K.

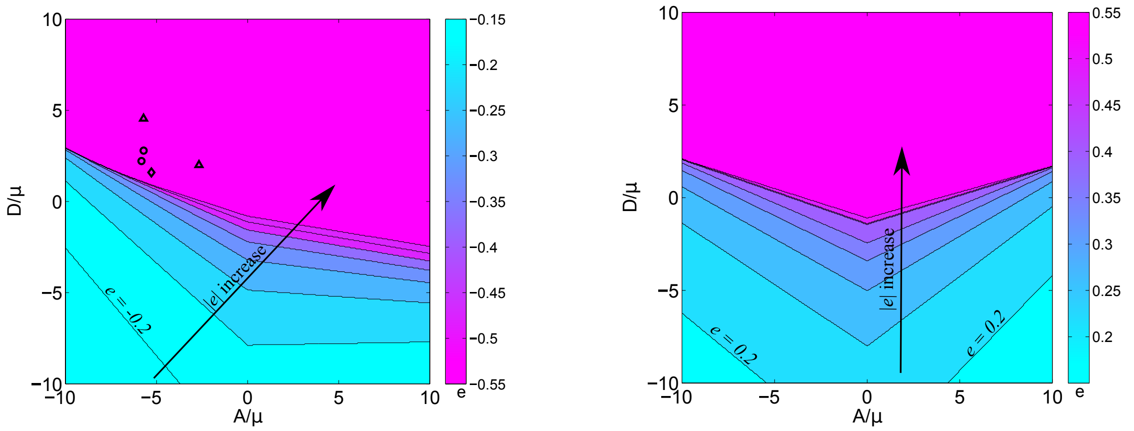

(a) In compression. △ from [RÉN 08]; ○ from [JIA 15b]; ◇ from Fig.3.17(b).

(b) In tension.

Figure 3.18: Stability criterion of Landau's solid in uniaxially pre-deformation

Particularly, experimental characterizations of A and D in uniaxial pre-compression have been carried out for mixed gels in [RÉN 08] and pig brains in [JIA 15b], their results are also plotted in Fig.3.18(a). In the above, we have mentioned the fitting method in [JIA 15b] may induce errors, a new point from the accurate fitting expression (see Fig.3.17(b)) is added. Nevertheless, all the points locate in the stable zone, this information provides a necessary condition for the identified solution.

3.5.2.2 Plane strain ($\xi = 1$)

The stability criterion is analyzed in plane strain by setting $\xi = 1$. In this case, the material is regarded as extrinsic orthogonal isotropic, it is necessary to ensure that all six wave speeds (Eq.3.19 and Eq.3.27) are positive to fully satisfy the stability condition.

The corresponding figures are shown in Fig.3.19, compared to the uniaxial pre-deformation (Fig.3.18), the most significant difference is that the pre-tension limits a large stable zone of the positive values of A. This may explains why the measured value of A is always negative.

3.5.2.3 General cases ($\xi = 0.25$)

The stability criterion is now considered for a general case, $\xi = 0.25$ (equivalent to $\xi = 0.75$). The results are displayed in Fig.3.20, not much difference is found compared to the uniaxial cases.

To ensure that Landau's solid is stable for any deformation state, the analysis with arbitrary ξ is carried out, however, the results are similar to the special cases presented above. In general, the parameter A should be negative and D should be positive, this observation is consistent with most experiment results [GEN 03, JIA 15b].

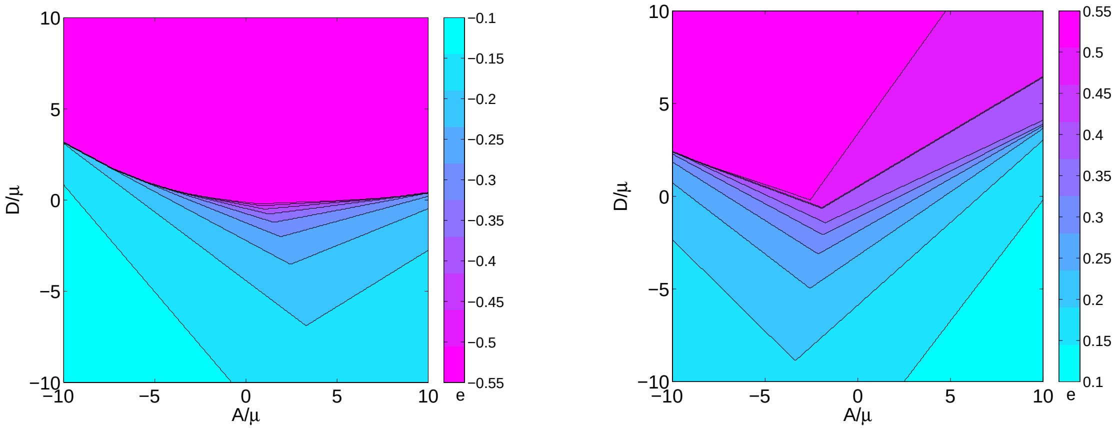

(a) In compression (b) In tension

Figure 3.19: Stability criterion of Landau’s solid under plane deformation ($\xi = 1$)

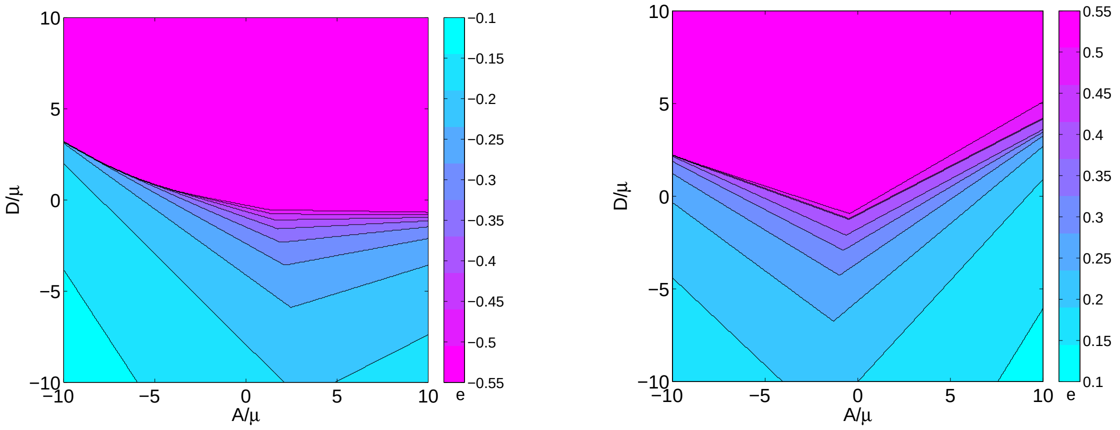

(a) In compression (b) In tension

Figure 3.20: Stability criterion of Landau’s solid when $\xi = 0.25$ (or $\xi = 0.75$)

3.5.3 Solution property: uniqueness

It has been clearly shown that the nonlinearity can be identified by acoustoelastic effect in elastography experiments. Theoretically, choosing any type of shear waves, by measuring its speed at several states of pre-deformation, the parameters A and D can be fitted from the analytical expressions. However, as two parameters are fitted from the same experimental data, it is important to consider the uniqueness issue, *i.e.* consider the influence of the two parameters on the wave speed separately.

For illustration purpose, a simple problem is considered. Let us consider the basic parameters of Landau's solid $\mu = 1\ kPa$, $A = -5.71\ kPa$, $D = 4.55\ kPa$. By increasing by 50% and decreasing by 50% the parameters A and D separately, Fig.3.21 shows the wave speeds of Landau's solid as a function of the state of compression. In Fig.3.21(a), the parameter A has not much influence on the wave of type *iii*, which means that A is difficult to be accurately identified even if D is known. Fig.3.21(b) shows that parameter D has a significant influence on the wave of type *iii*. In general, both parameters have important influence on the wave type *ii*, but this type is difficult to achieve in experimental condition.

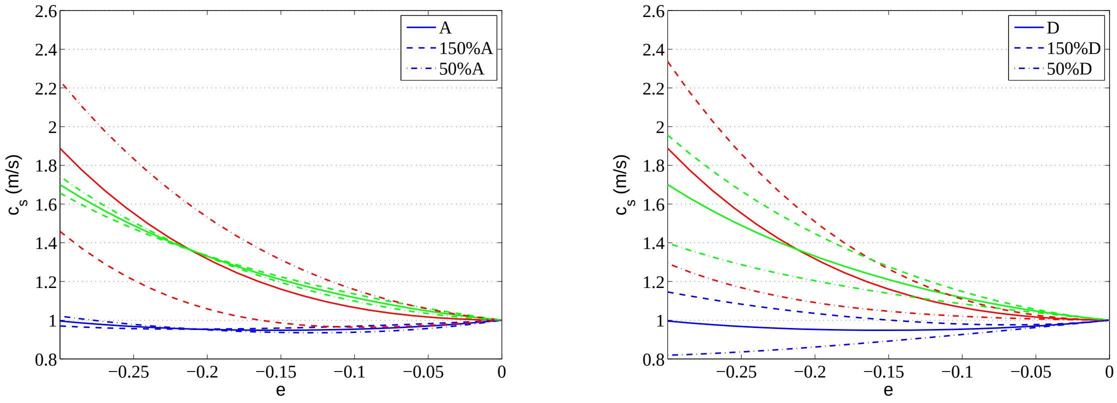

(a) Influence of the parameter A

(b) Influence of the parameter D

Figure 3.21: Uniqueness issue, basic parameters: $\mu = 1\ kPa$, $A = -5.71\ kPa$, $D = 4.55\ kPa$. Three types of shear waves: type *i* (blue); type *ii* (red); type *iii* (green).

3.5.4 Robust method to identify both A and D

It is worth reminding the major conclusion of the previous chapter, the parameter $\gamma = \mu + \frac{A}{2} + D$ can be deduced by nonlinear shear wave experiments. Our idea is to bring this information into acoustoelastic experiments, so only one parameter is unknown for the fitting. To make this possible, it is necessary to make sure that materials have different acoustoelastic behaviours even when they have the same γ.

Without the consideration of the stability criterion, three materials are given in Tab.3.3, they are set to have the same γ so that they cannot be differentiated by the nonlinear shear

Material	μ	A	D	γ (Eq.2.18)
No.1	1	10	0	5
No.2	1	0	5	5
No.3	1	15	-2.5	5

Tableau 3.3: Three Landau's materials for testing the acoustoelastic behaviours. Unity: *kPa*

wave experiment, and their speeds of wave type of *iii* under pre-compression are displayed in Fig.3.22. A numerical solution is also given for each case. The wave speeds are very different under the same pre-deformation state, so once the parameter γ is measured from nonlinear shear wave, the parameters A and D can be separated from the acoustoelastic experiments.

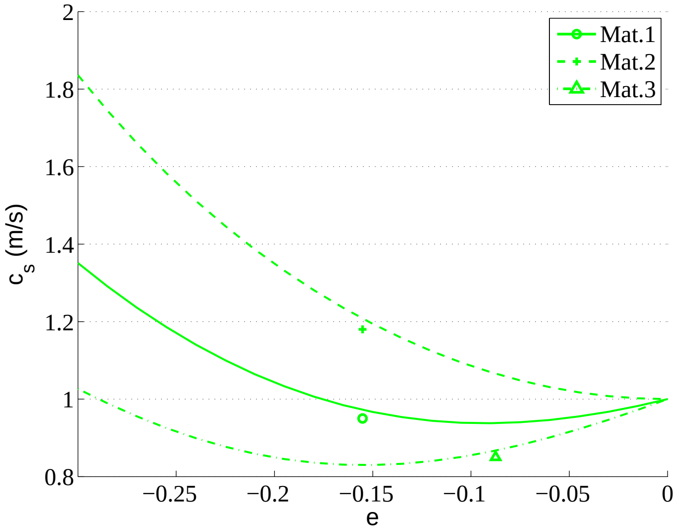

Figure 3.22: Wave speed of type *iii* in compression for materials in Tab.3.3. Symbols represent the numerical results. (Note: Mat.3 is unstable, the numerical simulation fails under large pre-deformation).

By combining the two nonlinear elastography techniques, it is believed that the characterization of Landau's solid is more reliable and robust. To illustrate this point, the following experiment is considered: the experimental data from Fig.3.17 are disturbed randomly at the level of 5% five times. In each case, the fitting results with and without the information of γ are summarized in Tab.3.4. It can be seen that the two parameters fitting method (identifying A and D at the same time) give very different values of A. Only 5% of experimental errors will lead to the very unfaithful fitting results. On the contrary, the fitting results with γ identified firstly is much more stable, the standard deviation is only 0.7 (4%) for A and 0.3 (6%) for D, which indicates that the identified parameters are much more reliable.

case	Two parameters fitting		Fitting with γ	
	$A\ (kPa)$	$D\ (kPa)$	$A\ (kPa)$	$D\ (kPa)$
#1	-23.5	5.7	-16.2	4.8
#2	-6.3	3.9	-17.2	5.2
#3	-10.0	4.6	-17.9	5.6
#4	-26.1	6.4	-17.3	5.3
#5	-17.2	4.9	-16.4	4.8
Avg.	-16.6 ± 8.5	5.1 ± 1.0	-17.0 ± 0.7	5.2 ± 0.3

Tableau 3.4: Comparison of different fitting methods by randomly disturbed the data in Fig.3.17. Initial condition: $\mu = 3.2\ kPa$, $A = -16.9\ kPa$ and $D = 5.1\ kPa$, so $\gamma = -0.15\ kPa$

At last, it should be emphasized that this analysis is based on particular parameters, the conclusion might change for different combinations of A and D. However, this methodology is adapted for all the parameters and all the models, and it is always important to explore the properties of the solution in inverse procedure.

3.6 Conclusion

In this chapter, the plane shear wave behaviour of both intrinsic and extrinsic TI materials is presented. Linear incompressible ITI materials contain three independents parameters: the two shear moduli μ_T and μ_L and the third parameter β, which can be also measured by elastography. Accordingly, to ensure the consistency with linear theory, hyperelastic ITI models should contain both anisotropic invariants I_4 and I_5. The implementation of these models in our FEM code is validated by several simple numerical simulations.

Afterwards, extrinsic anisotropic materials are investigated by analytical and numerical methods and good agreements are achieved. For uniaxial pre-deformation, we find that ETI materials have three different shear wave speeds (depending on models) instead of two speeds in ITI materials. The analysis is focused on Landau's solid, a number of solution properties (stability criterion, fitting methods, uniqueness) are discussed. Different from hyperelastic models, the stability of Landau's solid depends on state of the deformation. At last, a reliable method is proposed to measure the two nonlinear parameters of Landau's solid with the help of the conclusion of Chapter 2. It is worth to mention that the analysis presented is carried out for Landau's solid, but it is necessary and important for all models identified from acoustoelastic experiments.

However, it should be noted that the method is based on the fact that a homogeneous loading is applied along one principal direction. This hypothesis can be easily disrupted by the presence of inclusions in the neighbourhood of the applied pre-deformation.

For complex cases that cannot be treated using analytical models, for example, non-plane shear wave, not homogeneous pre-deformation, *etc.*, the only solution might be evaluating numerically the shear wave speed by importing the pre-deformation state into FEM simulations. Further effort is needed, especially on the development of more efficient FEM tools.

Chapter 4

Selective mass scaling method

Most of the work presented in this chapter is included in the paper submitted to *International Journal for Numerical Methods in Engineering [YE 17].*

Contents

4.1 Introduction **95**

4.2 Separation of shear and volumetric eigenmodes **97**

4.3 Selective mass scaling method **99**

4.3.1 General form of SMS 99

4.3.2 The existing SMS method 100

4.3.3 The proposed SMS method 101

4.3.4 Validation 101

4.4 Numerical examples **105**

4.4.1 Cantilever beam 106

4.4.2 Circular shear wave propagation 107

4.4.3 Planar shear wave propagation in heterogeneous media 109

4.4.4 Shear wave propagation in an anisotropic medium 112

4.4.5 Nonlinear shear wave propagation 115

4.4.6 Shear wave propagation in a pre-stressed medium 118

4.5 Conclusion **123**

4.1 Introduction

In the last two chapters, we have shown that explicit time integration is interesting for simulations of transient elastography. The explicit method has particular advantages in treating complex nonlinear problems, whereas the implicit method requires iterative process, and sometime convergence is difficult to achieve. However, all simulations presented before have a common shortcoming: the simulation time is relatively long even if the incompressibility parameter has been largely compromised, and this would be even more problematic in 3D models.

For the following reasons, it is valuable to find an efficient numerical method that provides a much larger stable time step in fast dynamic simulations of highly incompressible material:

- Even when the incompressibility parameter is largely decreased, the time step is small compared to the shear wave speed, it is desirable to reduce CPU time in the above simulations.

- For simulations of heterogeneous model, such as a hard inclusion surrounded by soft medium, the compressional wave creates numerous reflected compressional waves, but also shear waves. The compromise on the compressional wave speed could therefore lead to errors on the reflected wave speeds and alter tissue characterization.

- In order to analyse the coupling effect between the compressional and the shear waves in elastography experiments, the real compressibility parameter will be indispensable.

One approach used to amplify the critical time step for explicit time integration is the selective mass scaling (SMS) method. The basic idea is to add mass to reduce eigenfrequencies in high frequency range while changing the lower ones as little as possible [OLO 05].

Some SMS methods focus on thin wall structures, see in [OLO 04, COC 13, COC 15]. In this case, the time step is limited by the small thickness, the selective mass scaling consists in increasing the masses associated with the local rotations. Olovsson *et al.*[OLO 04] propose an acceleration filter for solid elements in order to reduce the relative motion among the nodes in thickness direction. Cocchetti *et al.*[COC 13, COC 15] consider solid-shell elements, the displacements of nodes are represented by a linear transformation on the middle plane, then mass is added on the “deformation” of middle plane to decrease the high frequencies. These methods keep the scaled mass matrix in lumped form. They have a good performance for finite rotation and deformation problems. However, these methods can not be used directly for general 3D structures.

Frías *et al.*[FRÍ 14] propose a method to choose global high eigenfrequencies range by the proper orthogonal decomposition (POD) method, the mass scaling is applied only on the high eigenfrequencies. This method also keeps the lumped mass matrix but a pre-calculation with normal time steps is required at the beginning of simulations to create the POD space.

A number of SMS methods are proposed for general utilization for which no pre-calculation is required. For example, stiffness proportional method is described in [OLO 05, MAC 95]. This method is accurate in numerous applications and it preserves the eigenmodes: this can be analytically proven. This method is referred to as *existing SMS method* in this work. Tkachuk and Bischoff [TKA 14] present different strategies to construct the scaled mass matrix, and they prove mathematically that accurate SMS methods should not distort the eigenmodes of the original systems, which are related to the eigenspace of stiffness matrix.

For the above mentioned methods [OLO 05, MAC 95, TKA 14], the scaled mass matrix can not be lumped. This leads to a larger CPU time to get the accelerations, especially for nonlinear problems. One way to avoid this time consuming step is to directly construct the inverse mass matrix as presented in [TKA 15, LOM 13]. Tkachuk and Bischoff [TKA 15] propose a general method based on Hamilton's principle: the method shows its accuracy for many problems, but the reduction of computational cost is limited (typically 50%).

To our knowledge, all these SMS methods are developed for inertia dominant problems, but not for transient dynamic problems. One reason is that the optimal SMS requires the knowledge of mode distributions in the spectrum [TKA 14]. For transient dynamic problems, the response mode distribution depends on the loading type which may change a lot for each problem. On the other hand, the amplification of time step is normally not desired for these problems, because the simulation duration is always short and the number of output requests is not far from the number of time step.

However, wave propagation in incompressible material is specific. Incompressibility makes the compressional wave speed much faster than the shear wave speed (typically 3 orders of magnitude larger for the biological tissues), but hardly any energy is transmitted by compressional wave. In other words, almost all strain energy is contained in shear wave propagation. So the time step required to accurately integrate the global system is much larger than the stable time step which is limited by the compressional wave.

In this chapter, we present a new SMS method which is applied in such a way that the stable time step is driven by the shear wave speed and no more by the compressional wave speed. The shear eigenmodes and the volumetric eigenmodes are separated, the mass scaling is then applied only on the volumetric modes. Selective integration is used to control *locking* for simple elements. This method results in a mass matrix which can not be lumped. For geometrically linear problems, the resulting scaled mass matrix is inverted only once during the whole simulations. Unlike the implicit time integration methods, no iteration is needed to deal with the material nonlinearity. Finally, a significant reduction of computational costs is obtained with a good accuracy.

This chapter is organized as follow. Section 4.2 describes the separation between the shear eigenmodes and volumetric eigenmode as well as the reduced/selective integration for quadrilateral and hexahedral elements. Section 4.3 recalls the existing SMS method, then the proposed method is described. A numerical validation is also included in this section. Some numerical applications are presented in Section 4.4, and the conclusions are given in Section 4.5.

4.2 Separation of shear and volumetric eigenmodes

For a linear elastic isotropic material, the constitutive matrix **D** can be written by two independent parameters: K for bulk modulus and G for shear modulus. Then it can be divided into a deviatoric part and a volumetric part as follows:

$$\mathbf{D} = \mathbf{D}_{dev} + \mathbf{D}_{vol} = \begin{bmatrix} G & -G & -G & 0 & 0 & 0 \\ -G & G & -G & 0 & 0 & 0 \\ -G & -G & G & 0 & 0 & 0 \\ 0 & 0 & 0 & G & 0 & 0 \\ 0 & 0 & 0 & 0 & G & 0 \\ 0 & 0 & 0 & 0 & 0 & G \end{bmatrix} + \begin{bmatrix} K+\frac{1}{3}G & K+\frac{1}{3}G & K+\frac{1}{3}G & 0 & 0 & 0 \\ K+\frac{1}{3}G & K+\frac{1}{3}G & K+\frac{1}{3}G & 0 & 0 & 0 \\ K+\frac{1}{3}G & K+\frac{1}{3}G & K+\frac{1}{3}G & 0 & 0 & 0 \\ 0 & 0 & 0 & 0 & 0 & 0 \\ 0 & 0 & 0 & 0 & 0 & 0 \\ 0 & 0 & 0 & 0 & 0 & 0 \end{bmatrix} \tag{4.1}$$

Notice that $\frac{1}{3}G$ appears in $\mathbf{D}_{vol}$ which means that a pure shear deformation also creates pressure even if there is no volume change, this is known as the *Kelvin effect* [BON 97] as mentioned in Section 2.2.2.2.

However, this effect is only significant for large strain and it can be neglected for nearly incompressible materials for which K is much larger than G.

Using the above expression, the elemental stiffness matrix $\mathbf{K}^e$ can also be divided into two parts:

$$\mathbf{K}^e = \mathbf{K}_S^e + \mathbf{K}_L^e \tag{4.2a}$$

$$= \int_{\Omega^e} \mathbf{B}^{\mathbf{T}} \mathbf{D}_{dev} \mathbf{B} \mathrm{d}\Omega^e + \int_{\Omega^e} \mathbf{B}^{\mathbf{T}} \mathbf{D}_{vol} \mathbf{B} \mathrm{d}\Omega^e \tag{4.2b}$$

where **B** is the displacement-strain operator, and Ω^e is the element integration domain. The two parts of stiffness matrix ($\mathbf{K}_S^e$ and $\mathbf{K}_L^e$) may be integrated by different strategies.

$\mathbf{K}^e$ being a symmetric, positive-definite matrix, its spectral expression is:

$$\mathbf{K}^e = \sum_{i=1}^{ndof} \gamma_i^e \Psi^{eT}_{\ i} \Psi^e_{\ i} \tag{4.3}$$

where $ndof$ is the number of degrees of freedom of the element, γ_i^e denotes the eigenvalues sorted in ascending order and Ψ_i^e are the corresponding eigenvectors. In 2D (resp. 3D), there should be 3 (resp. 6) zeros eigenvalues corresponding to the 3 (resp. 6) rigid body eigenmodes. It can be seen that these modes have no contribution on the stiffness. The others eigenmodes ($\gamma_i^e \neq 0$) represent all possible deformations of an element. We

Mode Description	Eigenvector Ψ^e	Eigenvalue γ^e		
		R.I.	S.I.	F.I.
Translation X	$\begin{bmatrix}\frac{1}{2} & 0 & \frac{1}{2} & 0 & \frac{1}{2} & 0 & \frac{1}{2} & 0\end{bmatrix}^T$	0	0	0
Translation Y	$\begin{bmatrix}0 & \frac{1}{2} & 0 & \frac{1}{2} & 0 & \frac{1}{2} & 0 & \frac{1}{2}\end{bmatrix}^T$	0	0	0
Rotation	$\frac{1}{\sqrt{8}}\begin{bmatrix}-1 & 1 & -1 & -1 & 1 & -1 & 1 & 1\end{bmatrix}^T$	0	0	0
Hourglass X	$\begin{bmatrix}\frac{1}{2} & 0 & -\frac{1}{2} & 0 & \frac{1}{2} & 0 & -\frac{1}{2} & 0\end{bmatrix}^T$	0	$\frac{2}{3}G$	$\frac{7}{9}G+\frac{1}{3}K$
*Hourglass*Y	$\begin{bmatrix}0 & \frac{1}{2} & 0 & -\frac{1}{2} & 0 & \frac{1}{2} & 0 & -\frac{1}{2}\end{bmatrix}^T$	0	$\frac{2}{3}G$	$\frac{7}{9}G+\frac{1}{3}K$
Shear X	$\begin{bmatrix}\frac{1}{2} & 0 & 0 & -\frac{1}{2} & -\frac{1}{2} & 0 & 0 & \frac{1}{2}\end{bmatrix}^T$	$2G$	$2G$	$2G$
Shear Y	$\begin{bmatrix}0 & -\frac{1}{2} & -\frac{1}{2} & 0 & 0 & \frac{1}{2} & \frac{1}{2} & 0\end{bmatrix}^T$	$2G$	$2G$	$2G$
Volumetric	$\frac{1}{\sqrt{8}}\begin{bmatrix}-1 & -1 & 1 & -1 & 1 & 1 & -1 & 1\end{bmatrix}^T$	$2(K+\frac{1}{3}G)$	$2(K+\frac{1}{3}G)$	$2(K+\frac{1}{3}G)$

Tableau 4.1: Eigenmodes of an ideal quadrilateral element with different integration strategies. (R.I.: reduced integration; S.I.: selective integration; F.I.: full integration;)

will now show that they can be differentiated when specific integration strategies are employed.

Let us now focus on an ideal four-node square element with unit length side, the eigenvectors Ψ_i^e and eigenvalues γ_i^e can be calculated analytically. We consider the three possible integration strategies: reduced integration (R.I.) which uses one Gauss points for both $\mathbf{K}_S^e$ and $\mathbf{K}_L^e$; selective integration (S.I.) which uses four Gauss points for $\mathbf{K}_S^e$ but one point for $\mathbf{K}_L^e$; and full integration (F.I.) which uses four points for both $\mathbf{K}_S^e$ and $\mathbf{K}_L^e$.

The results are displayed in Tab.4.1, each element has 8 modes (see in Fig.4.1): three rigid motion modes, two *hourglass* modes, two shear deformation modes and one volumetric deformation mode. The eight eigenvectors are all orthogonal to each other. We observe that the eigenvectors are the same for the three integration methods. In fact, they depend only on the shape of the element. Let us now consider the eigenvalues: the three integration methods give the same results for the rigid motions, shear modes and volumetric mode. The shear modes only depend on the shear modulus G, and the volumetric mode depends on both K and G but K is dominant. The difference appears at *hourglass* modes. For reduced integration, the eigenvalues go to zero. It is known that this will lead to spurious deformation in simulations if no stabilization is applied. For selective integration, the eigenvalues depend only on G, consequently, they will be considered as shear modes in the following. For full integration, the eigenvalues are a combination of K and G. They can be neither seen as the volumetric modes nor as the shear modes. For nearly incompressible materials ($K \gg G$), it produces *locking* problems.

To summarize, for reduced or selective integration, the deformation eigenmodes can be gathered in one group depending only on shear modulus and one group depending mainly on volumetric modulus. The conclusion can be extended for irregular elements, but no analytical solution is available. This is the premise to apply selective mass scaling only on the wanted mode, volumetric mode in this work. Similar decomposition can be found in [CHO 13, KOL 15], where decomposition is realized *modally*.

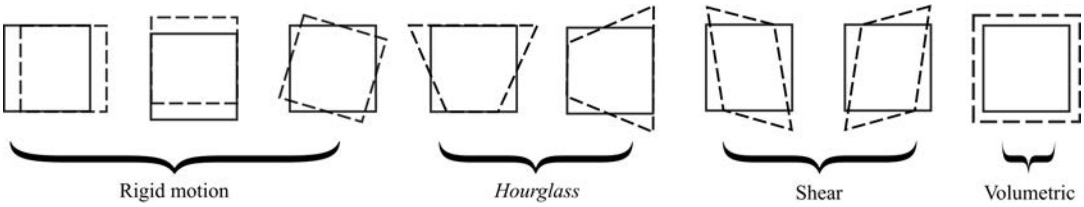

Figure 4.1: All eigenvectors of an ideal quadrilateral element (given by Tab.4.1)

4.3 Selective mass scaling method

In this section, we present the proposed SMS method which is designed to modify only the volumetric eigenmode with no change for shear eigenmodes. The method is then numerically validated by comparing the eigenvalues and eigenvectors between the original system and the scaled system for a model generated randomly.

4.3.1 General form of SMS

Most SMS methods consist of defining the new global mass matrix $\bar{\mathbf{M}}$ by the expression

$$\bar{\mathbf{M}} = \bigcup_e \bar{\mathbf{M}}^e, \quad \bar{\mathbf{M}}^e = \mathbf{M}^e + \boldsymbol{\lambda}^e \tag{4.4}$$

where $\bigcup_e$ is the assembly operator over each element, $\bar{\mathbf{M}}^e$ is the elemental scaled mass matrix, $\mathbf{M}^e$ is the original mass matrix, which is often written in lumped form for the explicit time integration, and $\boldsymbol{\lambda}^e$ is the added artificial mass. The objective of SMS methods is to find an appropriate $\boldsymbol{\lambda}^e$ which reduces the high eigenfrequencies of the system while preserving the eigenmodes in lower frequency range.

Now reconsider the finite element discretized problem with n degrees of freedom, the solution at time $t+\Delta t$ computed with the explicit time integration scheme using the scaled mass matrix $\bar{\mathbf{M}}$ is written:

$$^{t+\Delta t}\mathbf{U} = {}^{t}\mathbf{U} + \Delta t\, {}^{t}\dot{\mathbf{U}} + \frac{1}{2}\Delta t^2\, {}^{t}\ddot{\mathbf{U}} \tag{4.5a}$$

$$\bar{\mathbf{M}}\, {}^{t+\Delta t}\ddot{\mathbf{U}} = {}^{t+\Delta t}\mathbf{F}^{ext} - {}^{t+\Delta t}\mathbf{F}^{int} \tag{4.5b}$$

$$^{t+\Delta t}\dot{\mathbf{U}} = {}^{t}\dot{\mathbf{U}} + \frac{1}{2}\Delta t({}^{t}\ddot{\mathbf{U}} + {}^{t+\Delta t}\ddot{\mathbf{U}}) \tag{4.5c}$$

where $\mathbf{U}, \dot{\mathbf{U}}, \ddot{\mathbf{U}}$ represent the nodal displacements, velocities and accelerations respectively, $\mathbf{F}^{ext}$ and $\mathbf{F}^{int}$ are the external and internal nodal force.

Compared to the conventional explicit method (Eqs.1.46 and 1.48) and SMS methods, the only difference is to use the scaled mass matrix $\bar{\mathbf{M}}$, so it only requires minor modification for an existing explicit code.

The change of solver $\mathbf{M}$ to $\bar{\mathbf{M}}$ leads to a change of stability limit of the time integration scheme. One can apply an amplification factor α to the usual critical time step.

$$\Delta t = \alpha\, \Delta t_{crit} \tag{4.6}$$

We shall see later how α can be estimated. It is important to note that the scaled mass matrix cannot be lumped, this would lead the Eq.4.5b to be computationally costly for large size problems. However, $\bar{\mathbf{M}}$ can be inverted only once at the beginning of simulations for geometrically linear problems. The examples in the next section will show that.

4.3.2 The existing SMS method

Stiffness proportional mass scaling is presented in [OLO 05]: it can be seen as the basic method of SMS family. $\boldsymbol{\lambda}^e$ is chosen to be:

$$\boldsymbol{\lambda}^e = \beta \mathbf{K}^e, \quad \beta \geqslant 0 \tag{4.7}$$

where $\mathbf{K}^e$ is the tangential stiffness matrix, and β is a factor to be determined. The eigenfrequencies of the scaled system can be obtained analytically (see [OLO 05] for details):

$$\bar{\omega}_i^2 = \frac{{\omega_i}^2}{1+\beta{\omega_i}^2}, \quad i \in \{1,...,n\} \tag{4.8}$$

where ω_i represents the eigenfrequencies of the original system sorted in ascending order, and $\bar{\omega}_i$ represents the eigenfrequencies for the scaled system. It can be observed that the high values of the eigenfrequencies decrease much more than the lower ones while the rigid motion modes are not affected (eigenfrequency equals 0) .

By applying the above expression for the maximal frequency ω_{max}, and by considering the Eq.1.49, the following expression is obtained to estimate the factor β:

$$\beta = \frac{\alpha^2 - 1}{\omega_{max}^2} \tag{4.9}$$

Before going into the next section, let us take another way to look the existing method using the conclusion in section 2. The shear eigenmodes and the volumetric eigenmode are totally separated in selective/reduced integration, and the volumetric part has only one eigenmode. Eq.4.7 can be written in spectral form:

$$\boldsymbol{\lambda}^e = \beta(\gamma_L^e {\Psi_L^e}^T \Psi_L^e + \sum_{i=1}^{n_S} \gamma_{Si}^e {\Psi_{Si}^e}^T \Psi_{Si}^e) \tag{4.10}$$

where γ_L^e and Ψ_L^e are the eigenvalue and eigenvector of volumetric mode, γ_S^e and Ψ_S^e are the eigenvalues and eigenvectors of shear modes (n_S is the number of shear modes).

For quadrilateral element, $n_S = 2$ with reduced integration and $n_S = 4$ with selective integration. For hexahedral 3D element, $n_S = 6$ with reduced integration and $n_S = 12$ with selective integration. It should be mentioned that the above form is referred to as the local spectral SMS method in [TKA 14].

The above expression (Eq.4.10) leads us to observe that the existing SMS method “selects” to scale down all the deformation modes (both shear modes and volumetric mode), but not the rigid body modes: this is why it works well for inertia dominant problems. However, for wave propagation problems, the deformation modes have the same importance as the rigid motion modes, this method is not so well suited.

4.3.3 The proposed SMS method

In the simulations of nearly incompressible materials, the volumetric mode contains very little energy but leads to spurious high frequencies. For this reason, it is proposed to scale only the volumetric eigenmode of the stiffness matrix, which is written:

$$\boldsymbol{\lambda}^e = \beta\, \gamma_L^e\, {\Psi_L^e}^T \Psi_L^e \tag{4.11}$$

Using this expression requires calculating the volumetric eigenmode for each element which is time consuming. For implementation simplicity, we use $\boldsymbol{\lambda}^e = \beta \mathbf{K}_L^e$ ($\mathbf{K}_L^e$ should be integrated with one Gauss point).

This method can be regarded as an extension of the existing SMS method, the same equation (Eq.4.9) can be used to determine β. Theoretically, choosing β large enough makes volumetric eigenfrequencies very small. However, as the proposed method does not affect any shear eigenmode, the stable time step is still limited by the maximum frequency of the shear deformation mode, denoted by $\omega_{S,max}$. For this reason, the amplification factor α must verify:

$$1 \leqslant \alpha \leqslant \frac{\omega_{max}}{\omega_{S,max}} \tag{4.12}$$

The above equation (Eq.4.12) requires the knowledge of the whole model eigenfrequencies. This ratio of eigenfrequencies can be simply estimated using the two wave speeds: $\frac{\omega_{max}}{\omega_{S,max}} \simeq \frac{C_L}{C_S}$. By using the maximum admissible value of α, we can say that the time step is no longer limited by the compressional wave speed, but the shear wave speed. For nearly incompressible materials, the two wave speeds have a huge difference, α can be very large. In practice, as usual in pure explicit method, a safety coefficient is used to take account for mesh distortion and approximation of eigenfrequencies, we set therefore $\alpha = 0.9\frac{C_L}{C_S}$

4.3.4 Validation

In this section, we aim to validate the preservation property of proposed SMS method. The characteristic equations for the undamped linear systems are:

- For the original system:

$$(\mathbf{K} - \omega^2 \mathbf{M})\Phi = \mathbf{0} \tag{4.13}$$

- For the scaled system:

$$(\mathbf{K}-\bar{\omega}^2\bar{\mathbf{M}})\bar{\Phi}=\mathbf{0} \tag{4.14}$$

where ω_i and $\bar{\omega}_i$ have been introduced in Section 3.2, Φ_i and $\bar{\Phi}_i$ represent the corresponding eigenvectors.

As pointed out previously [OLO 05, TKA 14], the premises to achieve accurate solutions with SMS method are the preservation or small variation of eigenmode values and vectors. The preservation is not necessarily applying for all eigenmodes, but must be assured for the relevant modes which have high energy content. In real applications, due to the complexity of structures and various types of loads, the important eigenmodes are difficult to know *a priori*. However, nearly incompressible materials have a specific property, because of the huge difference between bulk modulus and shear modulus: the structure deforms barely in the volumetric way, almost all the potential energy is stored in shear deformation modes. This is quite universal for all loading.

In order to examine the preservation property of the proposed method, only the eigenmodes related to shear deformations should be considered. A test model of 50 degrees of freedom is presented in Fig.4.2. Considering a 2D plate with 4 × 4 elements, the nodes position is given in a random way. The material parameters are shown in the figure, they correspond to strong incompressibility, the ratio of the compressional wave speed to the shear wave speed equals 100. Accordingly, the amplification factor α is set to 90 to ensure stability of the explicit time stepping. Hence, $\beta = 1.54 \times 10^{-7}$ (Eq.4.9).

The reasons why an irregular mesh is used are:

- The sensitivity to mesh distortions is checked;
- No symmetric eigenmode will be produced (equal eigenvalue).

The mass matrix **M** is lumped, and the stiffness matrix **K** is formed by using selective integration strategy, with plane strain hypothesis.

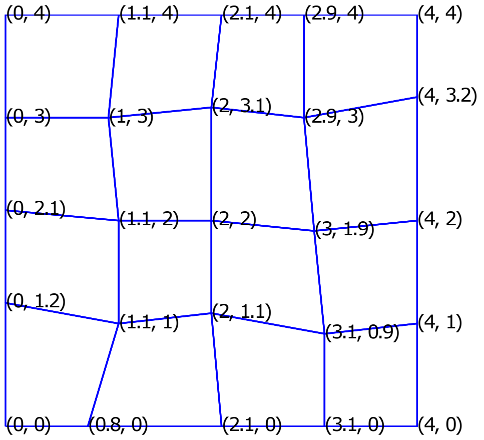

Material properties :
G = 0.001 MPa
ν = 0.49995
ρ = 1000 kg/m³

Figure 4.2: Test model: a square plate with distorted mesh of 50 degrees of freedom.

4.3.4.1 Preservation of eigenvalues

Eigenvalues of the test model are calculated for the original unscaled system, the system scaled by the existing SMS method, and the system scaled by the proposed SMS method. The results are displayed in Fig.4.3. The first three eigenvalues which equal 0 are not shown, they correspond to 3 rigid motion modes.

Fig.4.3(a) shows that an important jump appears at the 35th mode for the original system (red points): the eigenvalues experience a huge increase from this point. Herein, the eigenmodes from 4 to 34 correspond to shear deformation modes, while modes 35 to 50 correspond to volumetric deformation ones. Notice that there are 16 volumetric modes: this is the number of elements of the system.

Remark:

When one replaces $\mathbf{K}$ by $\mathbf{K}_L$(the volumetric stiffness) in equation Eq.4.13, only the high eigenvalues (35 to 50 modes) are found. While $\mathbf{K}_S$ is used, all eigenvalues are small. This observation confirms the deduction above.

More importantly, Fig.4.3(a) shows that the volumetric eigenvalues obtained by both SMS methods decrease significantly (up to the same value of shear eigenvalues), while the shear eigenvalues remain unchanged. A zoom is presented in Fig.4.3(b): the eigenvalues for the original system and for the system scaled by the proposed SMS method are the same. The existing SMS method does not match so well. For instance, the eigenvalues are decreased of about 50% than the original ones. This would introduce notable errors in simulation of shear wave propagations.

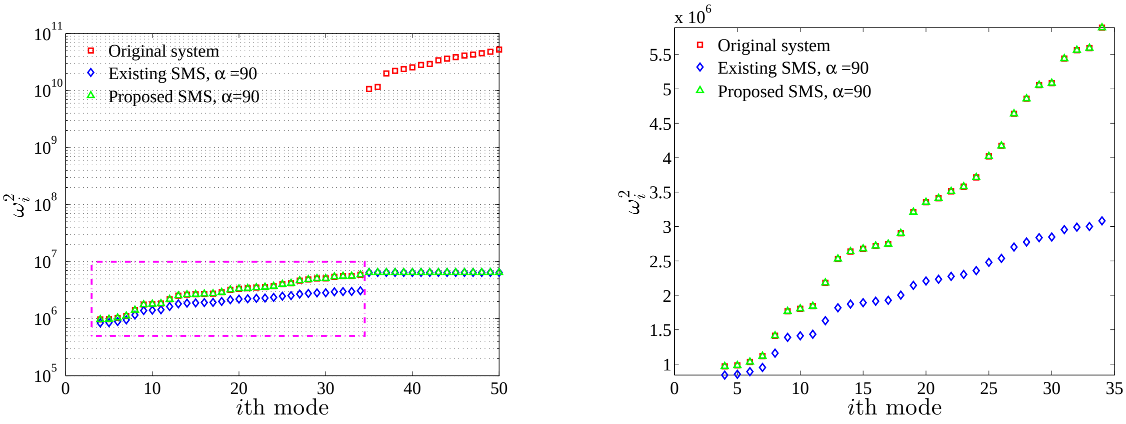

(a) Eigenvalues for all deformation modes

(b) Eigenvalues for shear deformation modes (zoom of left figure)

Figure 4.3: Eigenvalues of test model, first three (rigid motion) modes absent

4.3.4.2 Preservation of eigenvectors

As eigenvectors are also affected, a criterion is needed to quantify the eigenvectors distortion. Thus, φ_i which represents the distortion angle between the original system and the scaled system for the *ith* mode is introduced [TKA 14]:

$$\varphi_i = arccos(\frac{\bar{\Phi}_i \Phi_i}{|\bar{\Phi}_i||\Phi_i|}) \tag{4.15}$$

Fig.4.4 shows the values of distortion angles for all eigenmodes of the test model. For shear eigenmode vectors, the two SMS methods have the same performance, no distortion is observed. For volumetric eigenvectors, the existing SMS keeps the mode shapes while the proposed SMS leads to important distortions. The result about the existing SMS method is consistent with the analytical solution in [OLO 05, MAC 95]. However, it must be mentioned that these distortions have no significant effect in the solutions, because volumetric modes contain very little energy. Examples will emphasize this observation in the next section.

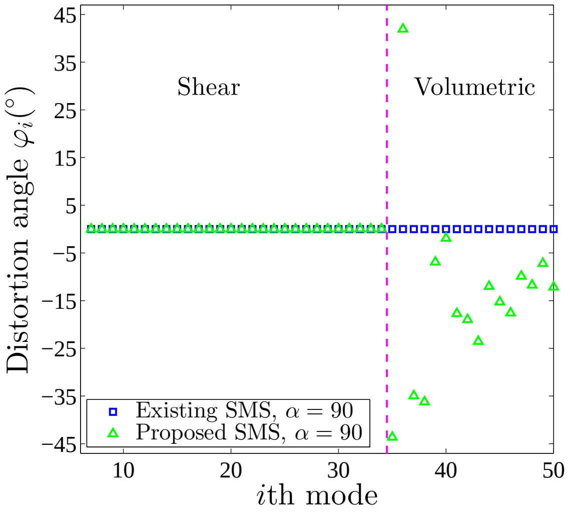

Figure 4.4: Eigenvectors distortion of test model (first three rigid body modes absent)

In Fig.4.5 and 4.6, three shear eigenvectors and three volumetric eigenvectors are chosen to illustrate the distortion. For shear eigenvectors, the eigenvectors for the three systems are identical. For volumetric eigenvectors, the modes of the existing SMS method are the same as those of the original system, while the proposed SMS method leads to distortions.

We can conclude from the presented test model, that both SMS methods decrease high eigenfrequencies, which means that a larger stable time step can be obtained. The proposed SMS method keeps both shear eigenvalues and eigenvectors with a good accuracy, but does not preserve the volumetric eigenvalues and eigenvectors, which barely influences the simulations. However, the existing SMS method will lead to inaccurate results in simulation of shear dominated transient problems because the shear eigenvalues are not well preserved.

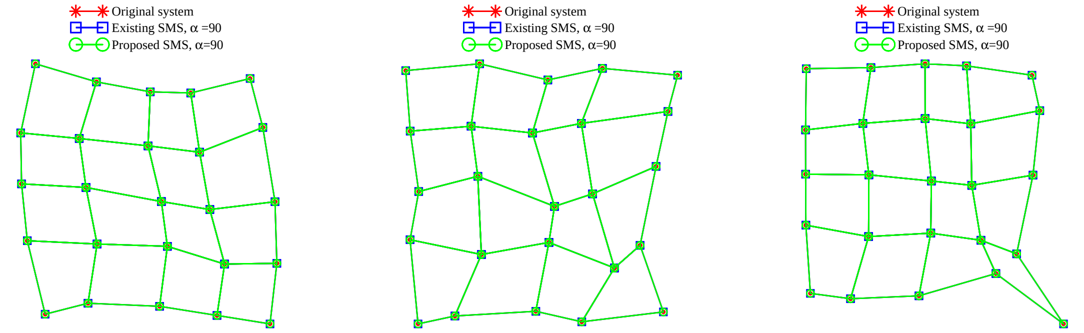

(a) 4th eigenmode: first shear mode

(b) 21th eigenmode, intermediate shear mode

(c) 34th eigenmode, last shear mode

Figure 4.5: Deformations of eigenvectors for 3 shear eigenmode

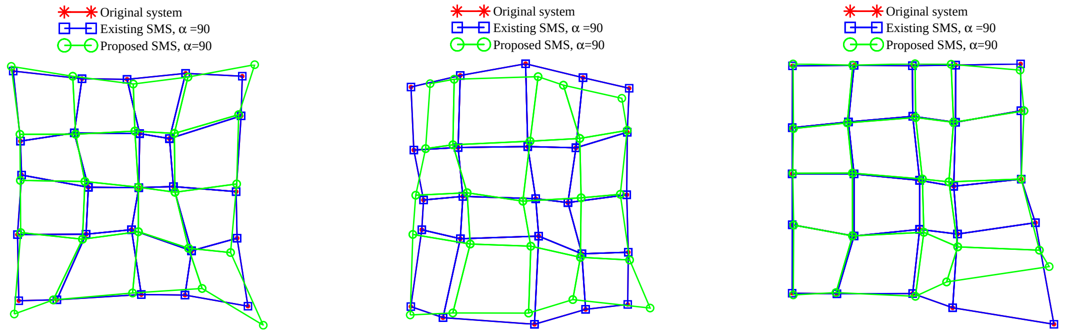

(a) 35th eigenmode, first volumetric mode

(b) 43th eigenmode, intermediate volumetric mode

(c) 50th eigenmode, last volumetric mode

Figure 4.6: Deformations of eigenvectors for 3 volumetric eigenmode

4.4 Numerical examples

To illustrate the performance of the proposed method, six examples related to wave propagation problems for nearly incompressible materials are presented. They are:

-Cantilever beam: to show the influence of the incompressible parameter;

-Circular shear wave propagation: to show the influence of the amplification of time step;

-Planar shear wave propagation in heterogeneous media: to show the numerical performance of the proposed SMS method in heterogeneous media;

-Shear wave propagation in an anisotropic medium: to show the performance in anisotropic media;

-Nonlinear shear wave propagation: to show the performance for finite amplitude waves analysis;

-Shear wave propagation in a pre-stressed medium: to show the performance in pre-stressed media.

In general, these examples contains all situations in elastography simulations. It will be shown that the proposed SMS method improves greatly the computational speed, while accuracy is still guaranteed.

All simulations are carried out by our Finite Element code implemented in Fortran. For the SMS methods, the algorithm *PARDISO* [SCH 04] is used as the inverse matrix solver.

Selective integration is used in all examples. Reduced integration is also available, but the *hourglass* modes should be carefully controlled.

4.4.1 Cantilever beam

The first example is a cantilever beam problem, the model is described in Fig.4.7. The initial velocity $V_0 = 10\ mm/s$ is applied in x direction for all the nodes except the left end. The simulation time is 0.01 s.

The mesh consists of 3072 regular cubic elements with a side length of $l_e = 0.125\ mm$. The time step is estimated by $\Delta t = 0.8\frac{l_e}{C_L}$ for the pure explicit simulations, and $\Delta t = 0.8\frac{l_e}{C_S}$ for the proposed SMS simulations.The material parameters are: the shear modulus $G = 0.001\ MPa$, the density $\rho = 1000\ kg/m^3$, so the shear wave speed is $C_S = 1\ m/s$. Poisson's coefficients are given different values to obtain different levels of incompressibility, see Tab. 4.2. The ratio of the compressional wave speed to the shear wave speed increases while the Poisson's coefficient approaches 0.5. Consequently, the explicit method needs more time steps to complete the simulations. However, for the SMS method, the stable time step is kept constant no matter the value of ν. The CPU cost of the simulation is therefore even more decreased as the ratio C_L/C_S gets higher. The time saving gets remarkable for C_L/C_S reaching 1000, which is a typical value for biological tissues.

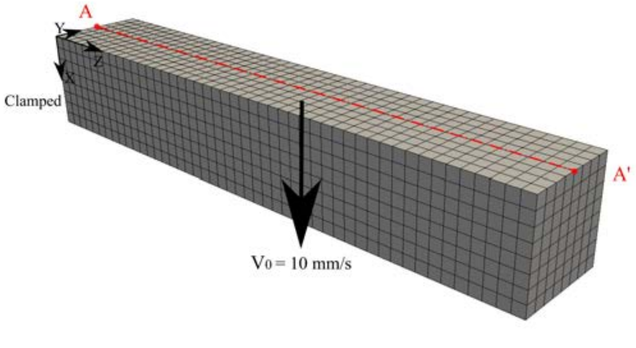

Figure 4.7: Cantilever beam model, dimension: $1 \times 1 \times 6\ mm$.

The displacement results along A-A' point are shown in Fig.4.8, the results obtained by the explicit method are displayed by lines, and the results obtained by the proposed

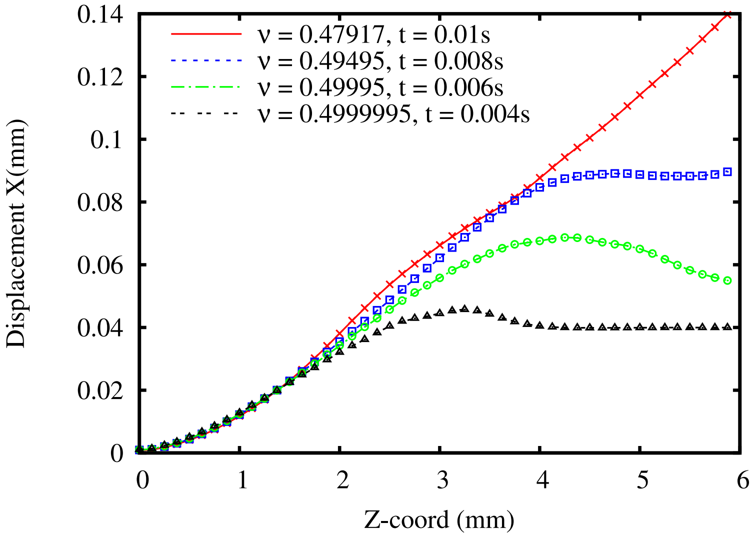

Figure 4.8: Cantilever Beam: displacement along A-A' for different cases. Lines: results by pure explicit simulation; Marks: results by proposed SMS method

ν	C_L/C_S	Pure explicit			Proposed SMS			Gains
		$\Delta t(s)$	Steps	CPU (s)	$\Delta t(s)$	Steps	CPU (s)	
0.47917	5	2×10^{-5}	500	18	1×10^{-4}	100	15.1	1.2
0.49495	10	1×10^{-5}	10^3	36.1	1×10^{-4}	100	15	2.4
0.49995	100	1×10^{-6}	10^4	360	1×10^{-4}	100	15.4	24
0.4999995	1000	1×10^{-7}	10^5	3600	1×10^{-4}	100	15.4	240

Tableau 4.2: Cantilever beam model: summary of simulation parameters

SMS method are displayed by different marks. For different Poisson's coefficients, the results are presented by different colors at different time points. The explicit method and the SMS method give exactly the same results. We would like to point out here that the problem being not in transient dynamic (wave propagation) range, the use of extreme Poisson's coefficient does not have significant effect on simulation results (at the same time point, using different Poisson's coefficients yields almost the same curve). But the objective of this example is to show the computational performance of the proposed SMS method. We experience that the proposed method is much more efficient in applications of highly incompressible materials.

4.4.2 Circular shear wave propagation

The above example shows that in the proposed method, the time step is not controlled by the compressional wave speed anymore, but by the shear wave speed. However, it is also important to consider the influence of the external load frequency.

A shear wave propagation problem is considered in plane strain hypothesis, the model is shown in Fig.4.9(a). The shear modulus is set to $G = 0.001\ MPa$, Poisson's coefficient $\nu = 0.49995$ and density $\rho = 1000\ kg/m^3$. These parameters yield a compressional wave speed $C_L = 100\ m/s$, and a shear wave speed $C_S = 1\ m/s$. Lineic forces are applied at the center zone defined by Ricker wavelet function:

$$f(t) = A(1 - 2\pi^2 f^2 (t - t_0)^2) exp(-\pi^2 f^2 (t - t_0)^2) \tag{4.16}$$

with the amplitude $A = 0.0001\ N$, the frequency $f = 300\ Hz$ and $t_0 = 0.003\ s$. In this example, the critical time step for pure explicit method is limited to $5 \times 10^{-6}\ s$. By applying the selective mass scaling, the maximal amplification of time step can be theoretically $\alpha = 100$, which leads to $\Delta t = 5 \times 10^{-4}\ s$. However, the time step should also be smooth enough to approximate the load function. Finally, we choose to set $\alpha = 30$ and $\alpha = 60$, the time steps are $1.5 \times 10^{-4}\ s$ and $3 \times 10^{-4}\ s$ accordingly. The load function with $\Delta t = 3 \times 10^{-4}\ s$ is plotted in Fig.4.9(b), we note that its shape is well approximated, yet not very accurate. Its effect on the simulation results is presented later.

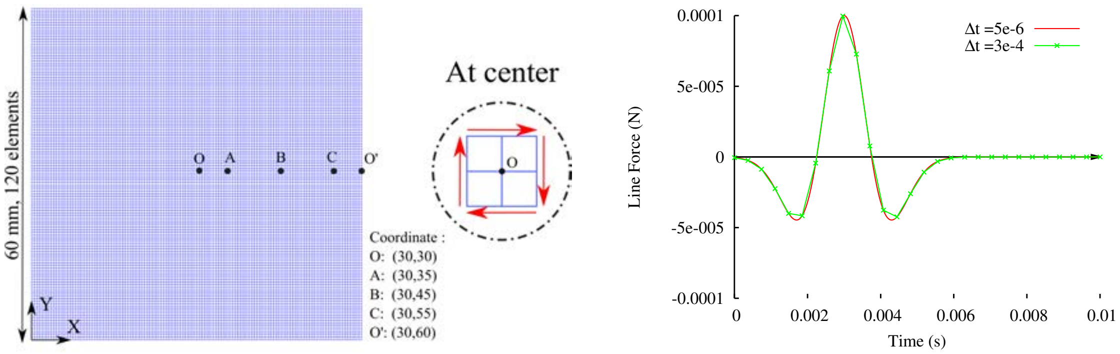

(a) Geometry and measuring points position

(b) Ricker wavelet: Load function plotted with different time step

Figure 4.9: Circular shear wave propagation model

Fig.4.10 shows the velocity and the shear stress field at the end of the simulation ($t = 0.03\ s$). The result is obtained by the proposed SMS method with $\alpha = 30$. We observe the shear wave front in a circular form reaching the edge of the plate. The results obtained by the pure explicit method are not presented here, because they are the same as Fig.4.10. More detailed comparisons are displayed through the measuring points.

Fig.4.11 shows the displacement history for three measuring points A, B and C. Notice that all the results present post oscillations because the used methods are all explicit. Generally, the proposed SMS with $\alpha = 30$ (green) gives a result which is close to the pure explicit method (red). For results obtained by SMS with $\alpha = 60$ (blue), only the shear wave front is well described. For example, at points A and B, the blue curves are strongly dephased compared to the reference (red), while the green ones present a much better coherence. At point C, which is far from the load, we note that the wave front just arrives, and the amplitude of blue curve is superior than the other two.

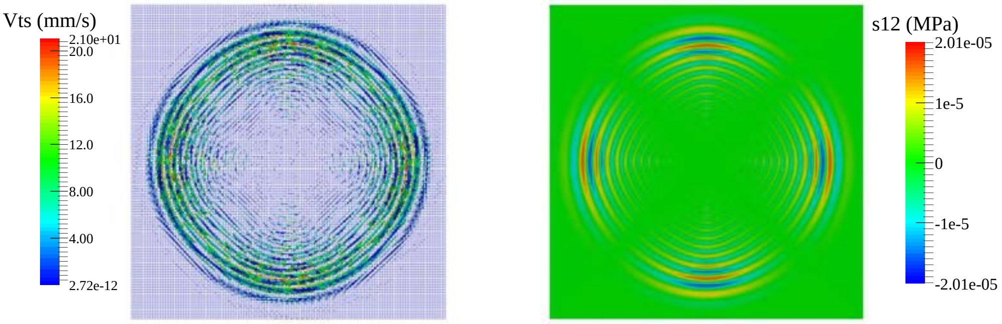

Figure 4.10: Circular shear wave propagation: velocity distribution (left) and shear stress distribution (right) at $t = 0.03\ s$. Results are obtained by the proposed SMS method with $\alpha = 30$.

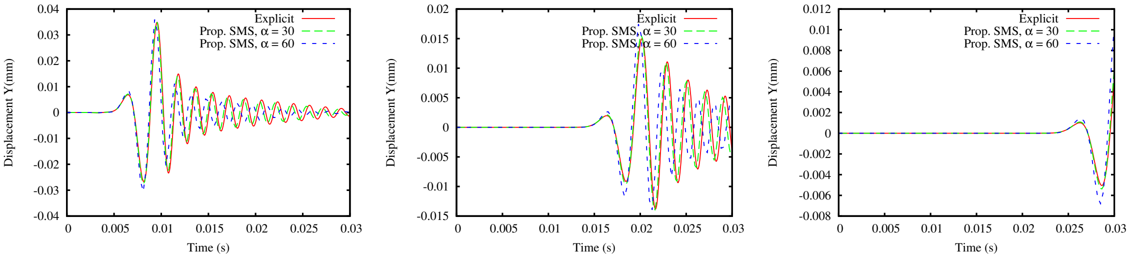

(a) Point A (b) Point B (c) Point C

Figure 4.11: Circular shear wave propagation: vertical displacement at measuring points

Fig.4.12 shows the vertical velocity distribution along O-O' at three different times. We observe that the post oscillations are more serious for the velocities. At the beginning of the simulation ($t = 0.006\ s$), the three results are the same. The result with $\alpha = 60$ (blue) leads to much more distortion as the wave propagates. A similar conclusion can be done: SMS with $\alpha = 30$ yields much better results than $\alpha = 60$.

As presented earlier, choosing a high scaling factor α induces more errors in the results, even though the algorithm is still stable. Moreover, the computational speed is not necessarily improved. In this example, the explicit method takes 189 s, the SMS with $\alpha = 30$ takes 17 s, and the SMS with $\alpha = 60$ takes 13 s. Consequently, when using SMS method, the amplification factor of time step should be well considered in order to improve the computational speed while maintaining the accuracy. In this example, the loading must be described with a sufficient number of points which limits α to 30.

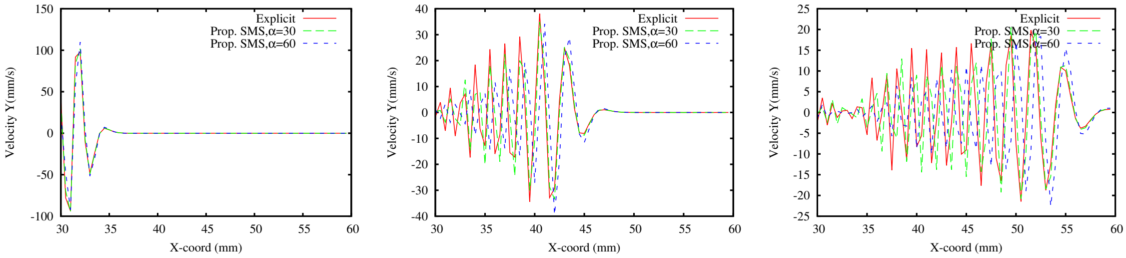

(a) $t = 0.006\ s$ (b) $t = 0.018\ s$ (c) $t = 0.03\ s$

Figure 4.12: Circular shear wave propagation: vertical velocity along O-O' at different time

4.4.3 Planar shear wave propagation in heterogeneous media

The two previous examples can also be performed by the existing SMS method. Its efficiency is the same as the proposed SMS method, however, because of the poor preservation of eigenvalues for shear deformation modes, the accuracy of simulation is not so good. A model of planar shear wave propagation in a heterogeneous medium is now presented to illustrate this point.

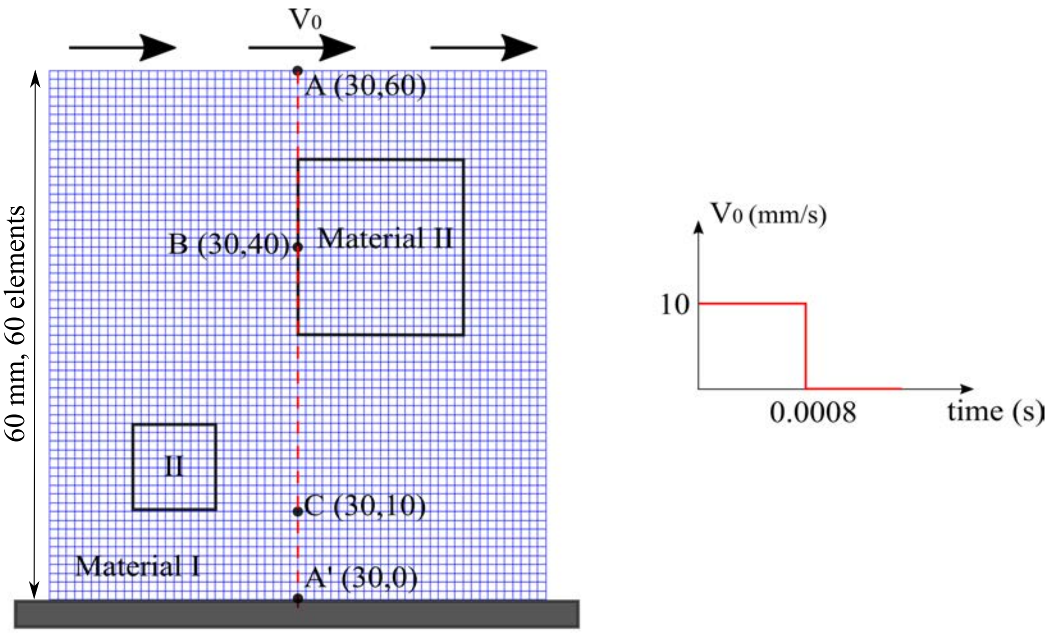

Figure 4.13: Heterogeneous model: geometry and boundary conditions

We consider a square plate in plane strain which is constituted by two linear elastic materials, as shown in Fig.4.13. The mesh has 3600 square elements. The material parameters are summarized in Tab.4.3, in which G is the shear modulus, ν is the Poisson's coefficient and C_L and C_S represent the compressional wave speed and the shear wave

	Material I	Material II
$\rho(kg/m^3)$	1000	1000
$G(MPa)$	10^{-4}	10^{-3}
ν	0.49999	0.4
$C_L(m/s)$	100	2.45
$C_S(m/s)$	0.317	1

Tableau 4.3: Heterogeneous model: Material parameters

speed respectively.

An initial velocity of 10 mm/s is applied at the top side and released after 0.0008 s (see Fig.4.13). The simulation time is set to 0.16 s so that the shear wave travels through the whole model. Note that for the pure explicit method, the time step is controlled by the compressional wave speed of material I, which is 0.8×10^{-5} s. While using the SMS methods (both existing and proposed), the time step raises up to 0.8×10^{-3} s just by considering the faster shear wave speed in the two materials. For computational speed, the pure explicit method costs 221 s, and the two SMS methods cost around 10 s.

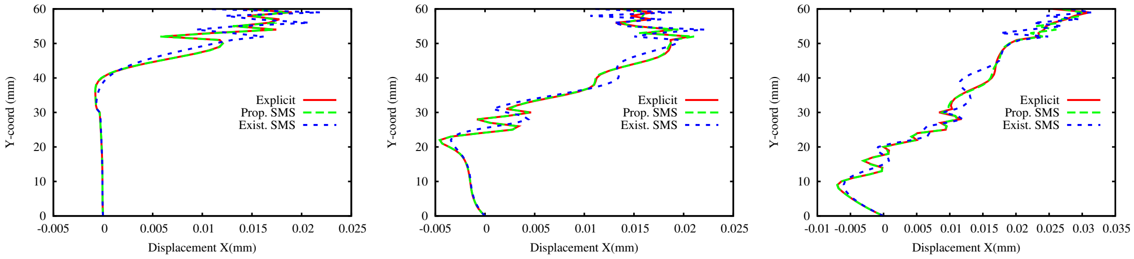

(a) $t = 0.04\ s$ (b) $t = 0.08\ s$ (c) $t = 0.12\ s$

Figure 4.14: Heterogeneous model: horizontal displacement along A-A' at different time

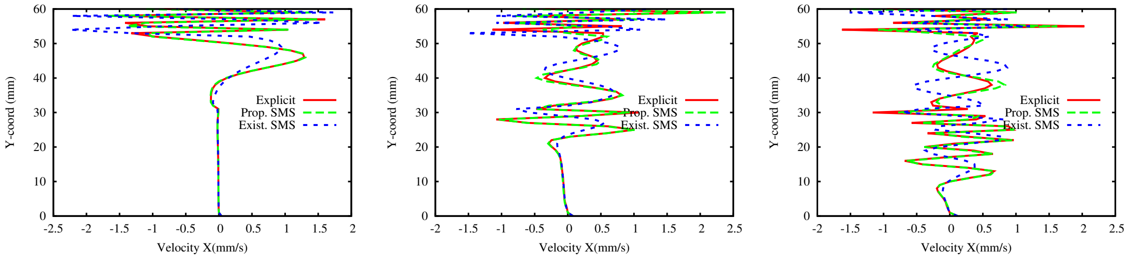

(a) $t = 0.04\ s$ (b) $t = 0.08\ s$ (c) $t = 0.12\ s$

Figure 4.15: Heterogeneous model: horizontal velocity along A-A' at different time

Fig.4.14, 4.15 show the displacement and velocity distribution along A-A'. The advancement of shear wave front is clearly observed at different times. The proposed SMS method (green) presents the results which are very close to the explicit method (red), for both displacements and velocities. On the contrary, the existing SMS results (blue) is not accurate.

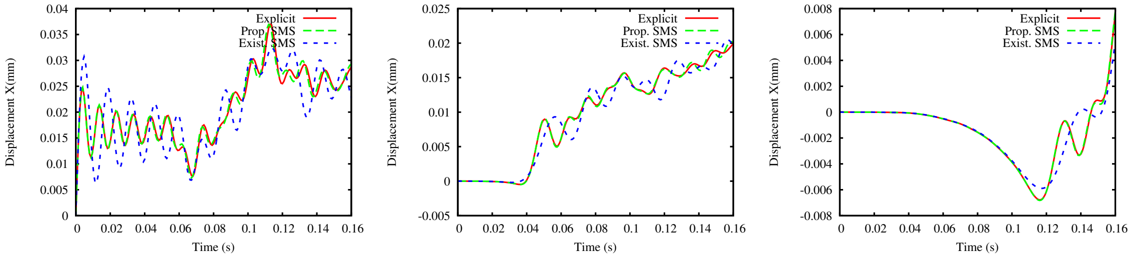

(a) Point A (b) Point B (c) Point C

Figure 4.16: Heterogeneous model: horizontal displacement at measuring points

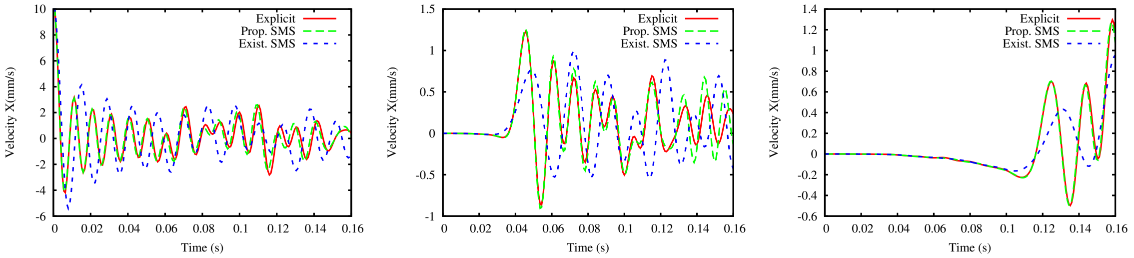

(a) Point A (b) Point B (c) Point C

Figure 4.17: Heterogeneous model: horizontal velocity at measuring points

Fig.4.16 and 4.17 show the displacement and velocity history at three measuring points. The difference between the two SMS methods is quite clear, the proposed method results is more accurate than the existing SMS method.

In Fig.4.18, the shear stress contour plots are compared at times $t = 0.064\ s$ and $t = 0.16\ s$. The time points are chosen so that the shear wave front reaches the heterogeneous part, so one can distinguish the heterogeneity position by stress distribution. The explicit method and the proposed SMS method show the two heterogeneous parts as expected, while the existing SMS method does not make the second heterogeneous block visible in Fig.4.18(b).

4.4.4 Shear wave propagation in an anisotropic medium

The method is proposed for fast dynamic simulations of biological materials which are often anisotropic, it is hoped that the method can be applied directly. As above mentioned

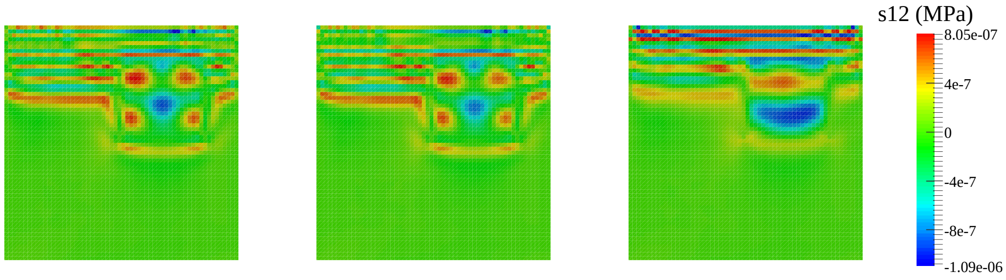

(a) at $t = 0.064\ s$

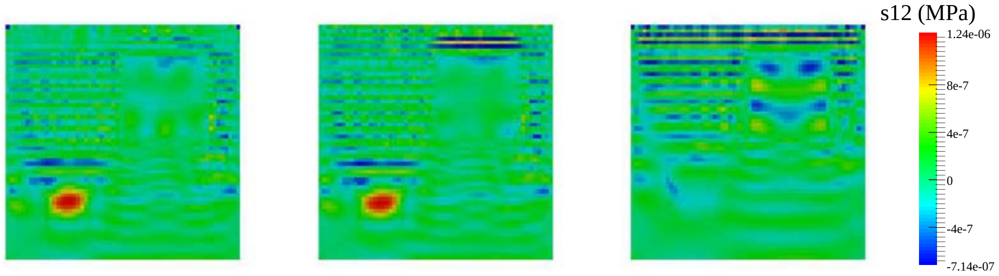

(b) at $t = 0.16\ s$

Figure 4.18: Heterogeneous model: shear stress distribution. Left: Pure explicit; Middle: Proposed SMS; Right: Existing SMS

in Chapter 3, due to high incompressibility, anisotropy in volumetric deformation is trivial and not necessary to be determined, so anisotropy only appears on the deviatoric part [HOL 00]. With a comprehensive understanding, the anisotropy in the deviatoric part results in a different expression of $\mathbf{D}_{dev}$ (Eq.4.1), but nearly no change in $\mathbf{D}_{vol}$ if $G \ll K$. So the proposed SMS method should be applicable just as it is.

Now we consider a transversely isotropic linear elastic material (see Eq.3.2), the parameters are given as follow: $\mu_T = 1\ kPa$, $\mu_L = 2\ kPa$, $\beta = 0.4$, $\nu_{LT} = 0.5$ and $\nu_{TT} = 0.4999$.

The model is described in Fig.4.19, the fibres direction is set along Y-direction. A smoothed sinusoidal velocity is applied at the center, but the applied load keeps small.

The simulations lasts $0.04\ s$. The time step is set to $5 \times 10^{-6}\ s$ for the explicit method, and $2 \times 10^{-4}\ s$ for the SMS method. Fig.4.20(a) displays the shear stress distribution at the end of simulation. As the material is slightly harder in Y-direction than in X-direction, the shear wave front is not a perfect circle. The results of the two simulations are identical.

In Fig.4.20(b), the pressure distributions are shown, but the results are no longer the same. Especially, the SMS method produces spurious high pressure at the load location. The SMS method can not calculate the pressure properly, but the result of pressure is harmless for the whole solution.

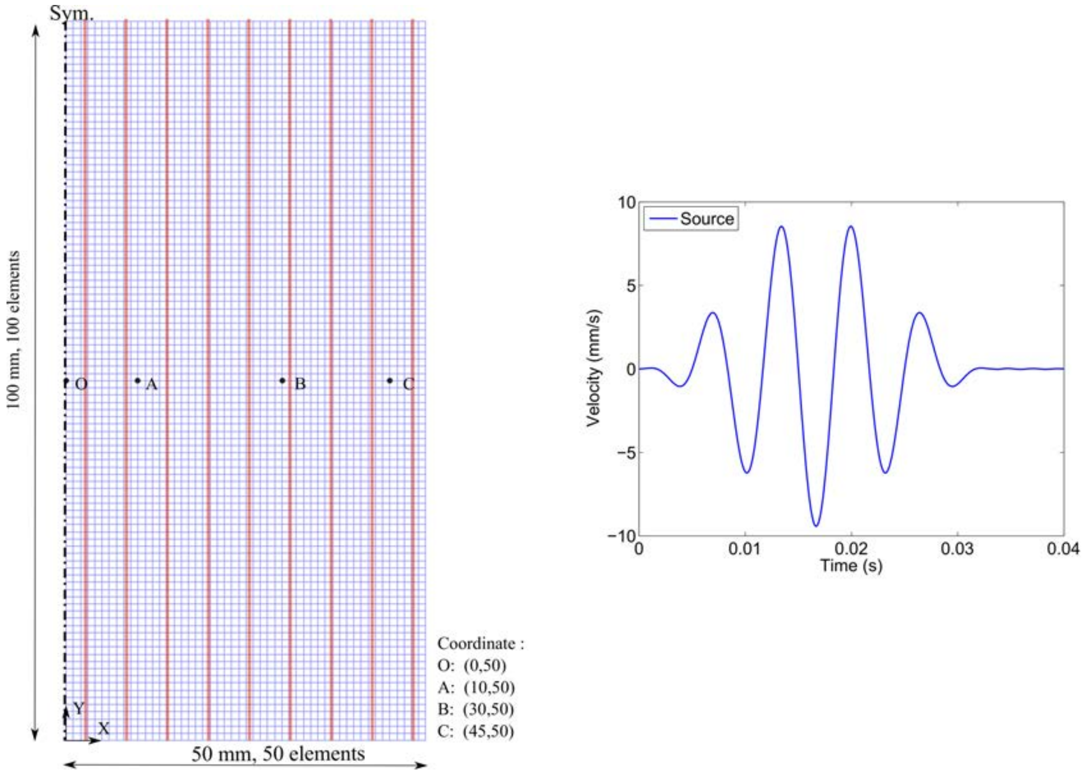

Figure 4.19: Transversely isotropic linear elastic model, the vector of fibre direction is set along Y-direction. The source is applied at point O of the model.

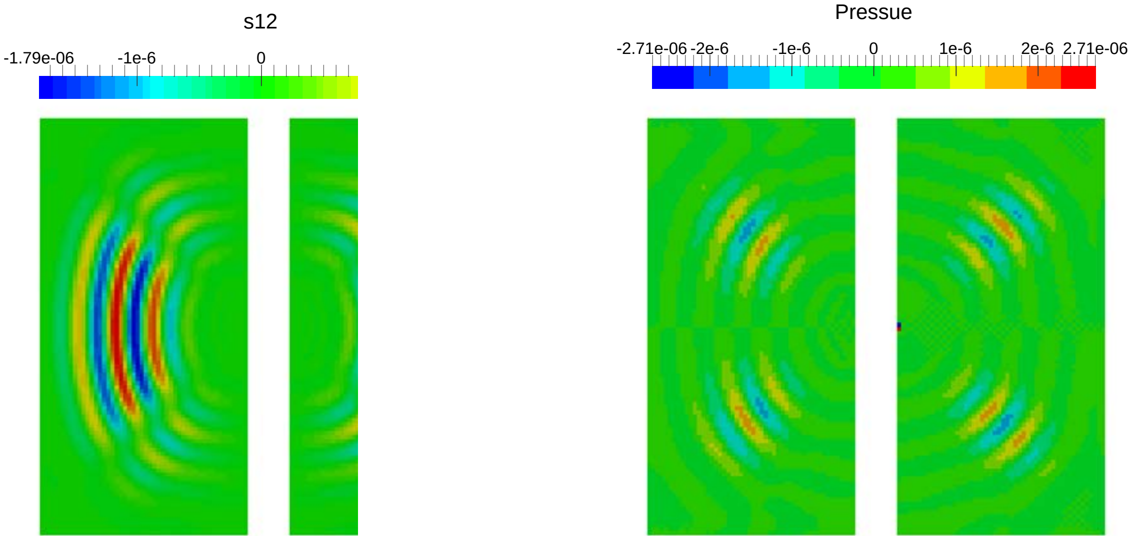

(a) Shear stress. Left: Explicit; F SMS.

(b) Pressure. Left: Explicit; Right: Proposed SMS

Figure 4.20: Anisotropic model: stress distribution at the end of simulation ($t = 0.04\ s$).

For example, in Figs.4.21 and 4.22, the kinematic variables of the point A and C (see in Fig.4.19 for their positions) are shown. The two points are chosen for the reason that one is near the load location, another is far from the load. As a result, point A experienced the whole wave shape from the load and point C only begun vibrating. In general, the two simulations show a good correspondence although the results obtained by the SMS method is slightly larger than the conventional explicit method. In addition, in Fig.4.22, very small oscillations (they are not the compressional wave which should be much faster) can be observed in the explicit method but not in the SMS method. This example shows that the proposed method can be used for the simulation of anisotropic materials without any modification.

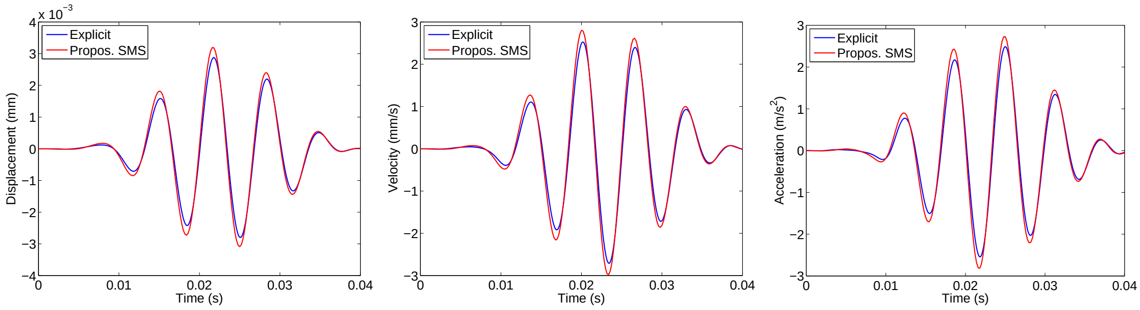

(a) Displacement (b) Velocity (c) Acceleration

Figure 4.21: Anisotropic model: vertical displacement, velocity and acceleration at one point (A) near the load.

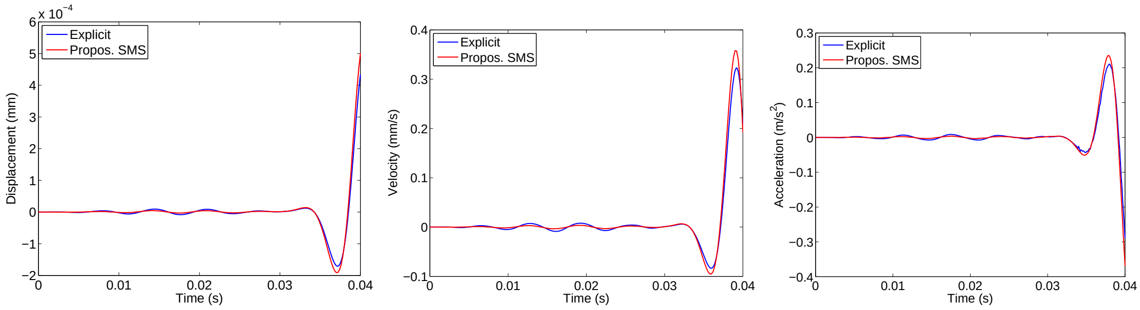

(a) Displacement (b) Velocity (c) Acceleration

Figure 4.22: Anisotropic model: vertical displacement, velocity and acceleration at one point (C) far from the load.

4.4.5 Nonlinear shear wave propagation

In the above examples, the materials are chosen to be linear elastic, the applications for the nonlinear wave propagation are considered in the following.

In solids mechanics without contact, the nonlinearity can be classified as the material nonlinearity and geometrical nonlinearity. The former indicates the nonlinear relationship of strain-stress relationship, and the latter describes the geometrical change due to deformation. Generally, both nonlinearities have been considered for hyperelastic models, this is introduced through the internal force $\mathbf{F}^{int}$ in Eq.4.5b. At time t, it can be expressed by:

$$\mathbf{F}_t^{int} = \int_{\Omega_t} \mathbf{B}_t^T \boldsymbol{\sigma}(\mathbf{u}) d\Omega_t = \int_{\Omega_0} \mathbf{B}_0^T \mathbf{S}(\mathbf{u}) d\Omega_0 \tag{4.17}$$

where $\mathbf{B}$ is the strain-displacement matrix, $\boldsymbol{\sigma}$ or $\mathbf{S}$ as a function of $\mathbf{u}$ is the Cauchy or PK-2 stress, Ω represents the integration domain and the subscript indicates the configuration of which the integration is based on. In the Update Lagrangian (UL) formulation, the integration is based on the actual geometry of time t. And in the Total Lagrangian (TL) formulation, the integration is based on the initial geometry of time 0. For nonlinear problems, the update of geometry is not presented explicitly in TL formulation but it has been implied when evaluating the PK-2 stress $\mathbf{S}$.

Unfortunately, the material nonlinearity only interferes the eigenvalues but the geometrical nonlinearity gives rise to the change of the eigenvectors. In other words, volumetric and shear eigenvectors interact with each other while updating the geometry. In order to apply SMS method properly, one should update the volumetric eigenvectors (or $\mathbf{K}_L$), then assemble and factorize the scaled mass matrix $\bar{\mathbf{M}}$ at every time step. As a consequence, the SMS method would loss its efficiency even using the larger time step.

However, considering the nonlinear shear wave in elastography is finite but still small, the geometrical change induced by nonlinear waves could be neglected. Then, one can choose to approximate the internal nodal force under the initial configuration, at time $t = 0$:

$$\mathbf{F}_t^{int} \simeq \int_{\Omega_0} \mathbf{B}_0^T \boldsymbol{\sigma}(\mathbf{u}) d\Omega_0 \tag{4.18}$$

It should be noted that this approximation is no longer available for simulations of large deformation, for example, in forming processes of metals or auto mobile accident simulations. Nevertheless, with such a simplification, the volumetric eigenmodes do not change during the nonlinear wave simulations, and $\bar{\mathbf{M}}$ remains constant. Consequently, the SMS method can be employed just as in the linear cases.

In the following, we will show that this approximation is valuable for nonlinear elastography simulations, and the proposed SMS method still could be applied efficiently. To this end, the example in Sect.2.3.2 (in Chapter 2) is recalled, we remind that the geometry is presented in Fig.2.5, the material property is included in Tab.2.1 and the load function is described in Eq.2.26. Moreover, we choose two amplitudes loads: $A_0 = 0.4$ *mm* for the small load case (still larger than infinitesimal strain problem) and $A_0 = 0.8$ *mm* for the large load case. These two situations have been used in the parametric study in Sect.2.4.2. The results have been given by the purely explicit method (*i.e.* including the geometrical nonlinearity) and they will be considered as the reference in the following.

4.4.5.1

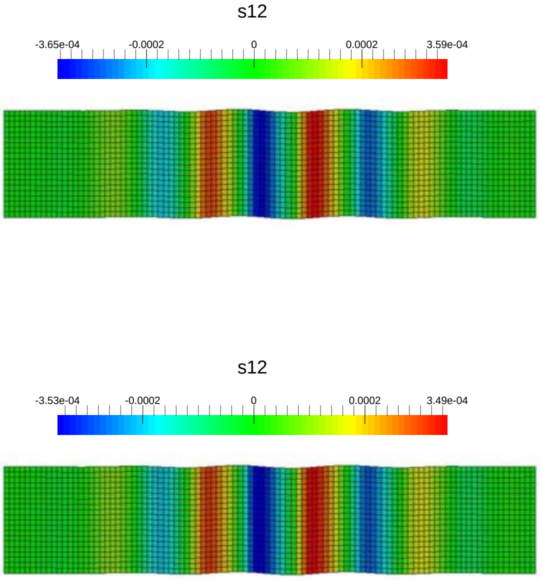

(b) Proposed SMS, $\alpha = 40$

Figure 4.23: Test of small amplitude wave. Shear stress distribution at time $t = 0.05\ s$. The mesh is deformed with the real displacement.

From the material parameters, the ratio of the compressional and the shear wave speed is 50 in infinitesimal strain. Considering this problem is nonlinear, we made the amplification factor $\alpha = 40$. As results, from the comparison of shear stress in Fig.4.23 and kinetic variables in Fig.4.24, the results are very satisfying.

4.4.5.2 Large load case $A_0 = 0.8\ mm$

When $A_0 = 0.8\ mm$, the dimensionless nonlinear parameter Goldberg number is equal to 24.13 (Eq.2.29) , this is the largest number in our parametric study (see Fig.2.21). This case presents the less favorable situation for the application of the SMS method in nonlinear elastography.

Fig.4.25 displays the shear stress at time $t = 0.05\ s$. The mesh deformation is represented with the real amplitude and the geometrical change is visibly larger than in Fig.4.23. However, for the same amplification factor ($\alpha = 40$), the result is highly disturbed, see Fig.4.25(c). We believe that the large mesh distortion makes the maximal time step change during the simulation, so the amplification factor can not simply be estimated by the ratio the wave speeds, and it should be more conservative. Consequently, we reduce α by a half ($\alpha = 20$), and a good result is obtained, see Fig.4.25(b). Further, from the color contour in Fig.4.25(a) and (b), we observe a critical stress discontinuity at the wave front as another evidence of the nonlinearity.

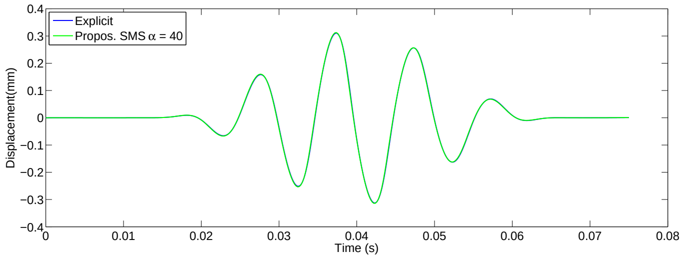

(a) Displacement

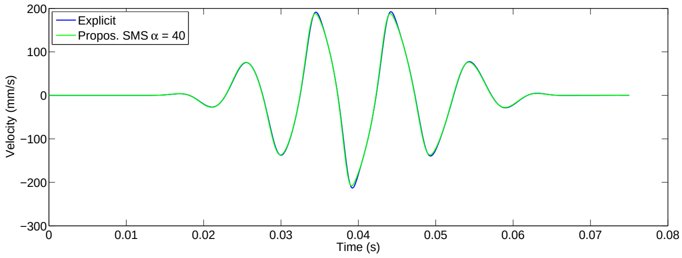

(b) Velocity

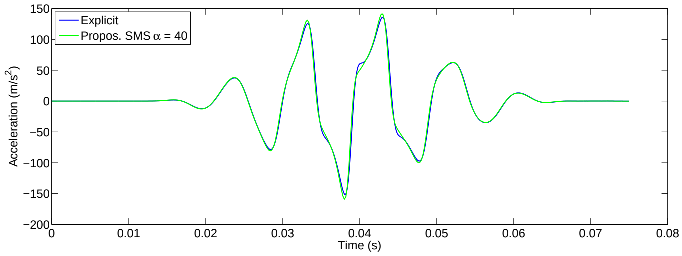

(c) Acceleration

Figure 4.24: Test of small amplitude wave.Vertical displacement, velocity and acceleration at one point 30 *mm* far from the load

Fig.4.26 presents the kinematic variables for simulations. Surprisingly, the simulation with $\alpha = 40$ is not too bad on this aspect. The curves are mainly disrupted by high oscillation of the acceleration after the travel of the wave fronts. Nevertheless, the SMS simulation with $\alpha = 20$ always gives the reliable results.

To sum up, we have shown that, by neglecting the geometrical nonlinearity, the nonlinear wave simulations are satisfying when using appropriate amplify factor α. It can be concluded that the nonlinear phenomena of finite shear waves in elastography is dominated by material nonlinearity, the proposed SMS can be applied for our objective simulations.

4.4.6 Shear wave propagation in a pre-stressed medium

In this example, we consider wave propagation in a pre-stressed medium as an application of nonlinear elastography by acoustoelastic effect (see Chapter 3). Thanks to the flexi-

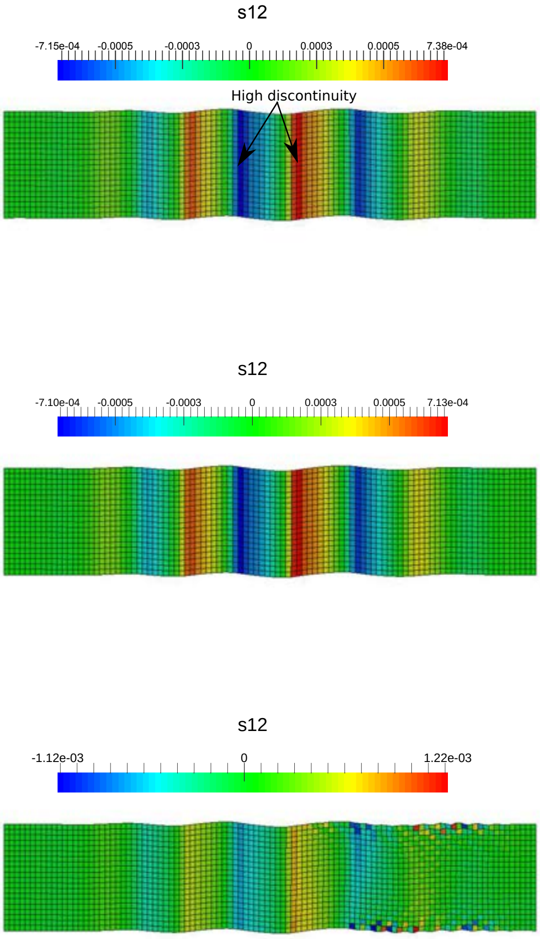

(c) Proposed SMS, $\alpha = 40$

Figure 4.25: Test of large amplitude wave. Shear stress distribution at time $t = 0.05$ s. The mesh is deformed with the real displacement.

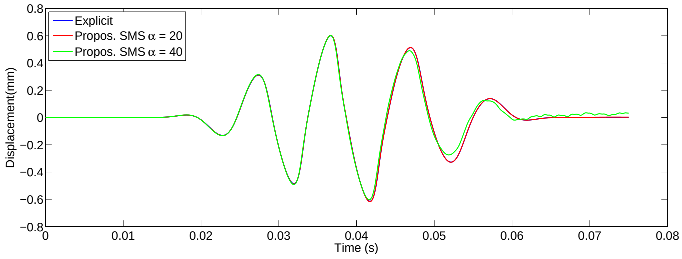

(a) Displacement

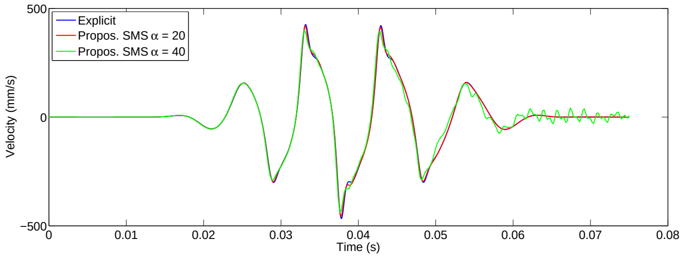

(b) Velocity

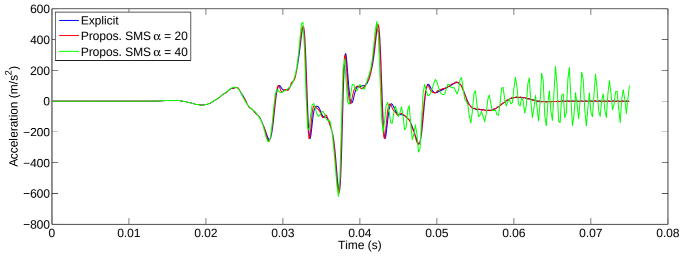

(c) Acceleration

Figure 4.26: Test of large amplitude wave. Vertical displacement, velocity and acceleration at one point 30 *mm* far from the load

bility of FEM, the pre-stressing load could be homogeneous but also inhomogeneous. Besides, the pre-stressing load is much higher than the dynamic load, so the geometrical nonlinearity is considered in the pre-stress step but neglected in the dynamic step, the phenomenon is called *small on big* [DES 09].

The model considered is described in Fig.4.27. As shown, due to symmetry, just a half domain is described. Static pressure is applied at the top with a ramp distribution, the maximum is set to 0.002 N and the minimum is zero. Neo-Hookean hyperelastic law (Eq.1.21) is employed for the material. The properties are chosen in the range of biological tissues, where $\rho = 1000\, kg/m^3$, $\mu = 0.002 MPa$, $K = 10 MPa$. These parameters lead to the speed of compressional wave $C_L = 100\ m/s$, and the shear wave speed $C_s = 1.41\ m/s$ in small deformation.

First, the static simulation is carried out by classical Newton-Raphson algorithm, both material and geometrical nonlinearities are considered. The results are shown in Fig.4.28, we observe that the model deforms in the range of finite strain. Based on this state, a

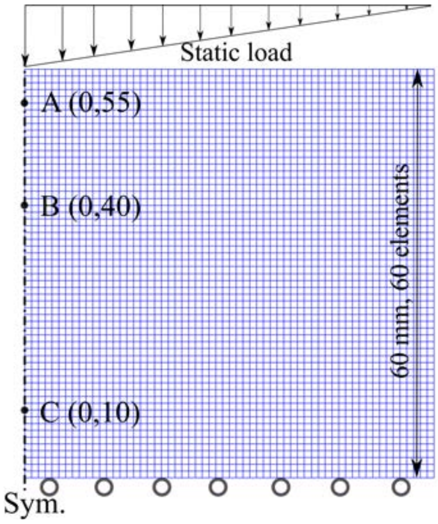

Figure 4.27: Pres-stressed model: Geometry and static load distribution

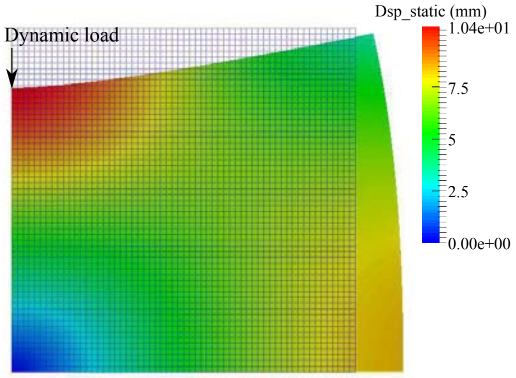

Figure 4.28: Deformed configuration after static load, amplification factor = 1

small sinusoidal load is then added at the top-left corner (see Fig.4.28): the vertical displacement with an amplitude 0.1 mm, and a frequency of 100 Hz is imposed and released at $t = 0.03$ s. Static pressure is still kept to avoid rebound. Dynamic simulation is carried out by both explicit method and proposed SMS method. During this simulation, we treat only material nonlinearity but not geometrical nonlinearity as the dynamic strain remains small.

The dynamic simulation lasts 0.05 s. By considering the deformation of the mesh under static load, the time step for the explicit method is set to 5×10^{-6} s, and for SMS method is 2.5×10^{-4} s which is 50 times larger than previous. For this simulation, explicit method and SMS method cost 110 s and 13 s respectively.

Fig.4.29 shows the dynamic displacement field at the end of the simulation. For both results, shear wave front (in the medium) and Rayleigh wave front (at the superior surface) are clearly distinguishable. No visible difference can be found on the figure. Then, it is important to note that the amplitude is largely smaller than the static displacements field.

Figs.4.30, 4.31 show the displacement and velocity history in time for three measuring points. We can observe that the explicit solution generates high frequency oscillations, especially for velocities. The SMS method has much less oscillations, this is caused by using the larger time step. However, the two results are very close. No significant difference is observed for average values, both for displacements and velocities.

The time evolution of energy is described in Fig.4.32. In Fig.4.32(a), the internal energy is divided into two parts: deviatoric part and volumetric part. We can observe that the deviatoric internal energy curve is the same for the two methods but not the volumetric one. However, it is important to note that the volumetric energy represents less than 3% of the whole internal energy. Fig.4.32(b) shows the two methods give very close kinetic

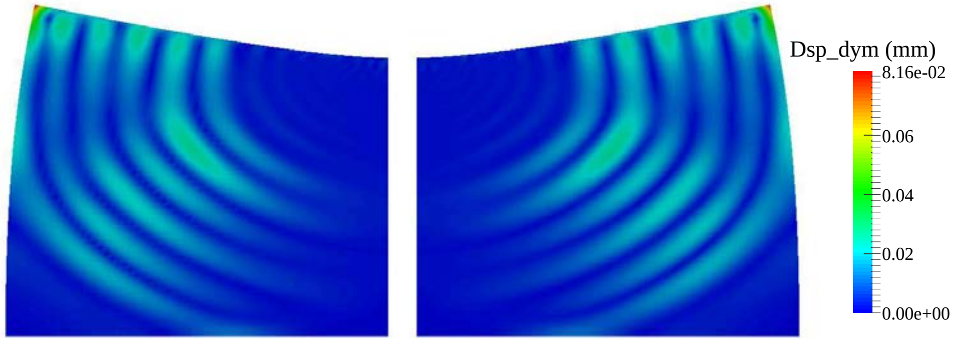

Figure 4.29: Dynamic displacement distribution at $t = 0.05$ s. Left: Explicit; Right: Proposed SMS.

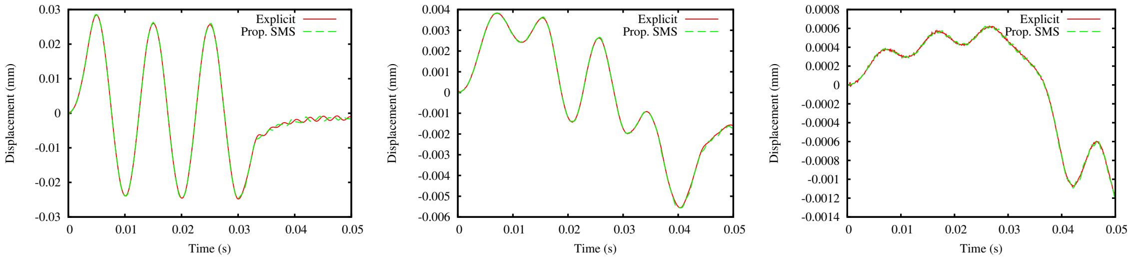

(a) Point A (b) Point B (c) Point C

Figure 4.30: Pre-stressed model: vertical displacement at measuring points

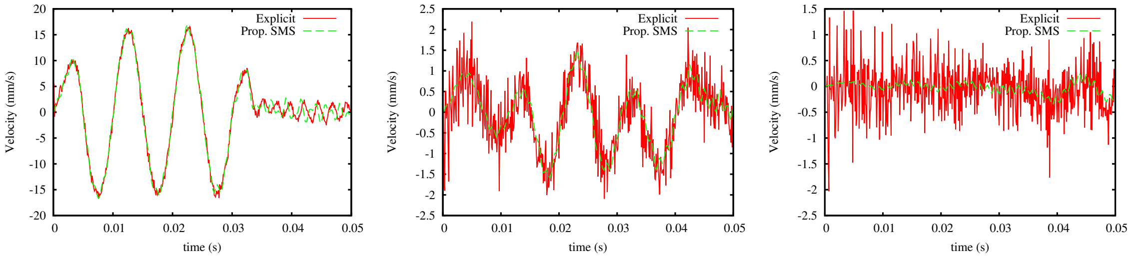

(a) Point A (b) Point B (c) Point C

Figure 4.31: Pre-stressed model: vertical velocity at measuring points

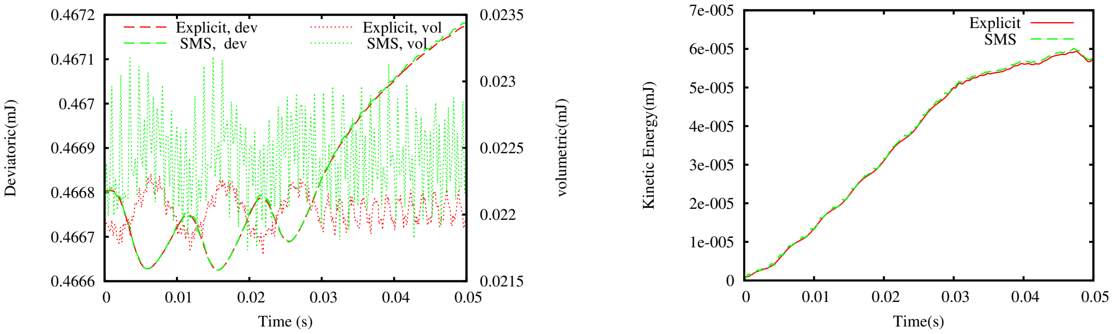

(a) Internal energy, decoupled by deviatoric part and volumetric part

(b) Kinetic energy

Figure 4.32: Pre-stressed model: time history of energy evolution

energy evolution in time.

4.5 Conclusion

A selective mass scaling method based on volumetric and shear mode separation has been presented. The method aims at increasing the stable time step in explicit simulations for nearly incompressible materials. The analysis shows that the proposed method keeps exactly the eigenmodes related to the shear deformation, so the method is accurate for shear dominant problems.

Our objective is to obtain an efficient numerical tool for elastography simulations. The numerical examples show that the proposed SMS method is well suited for simulating shear wave propagation in isotropic and anisotropic linear elastic materials. Moreover, by a reasonable simplification, *i.e.* neglecting the geometrical nonlinearity, the proposed method has a good performance for nonlinear elastography simulations.

The method is based on adding artificial terms to the mass matrix. The added term can not be lumped, which leads to a mass matrix which is no longer diagonal. As shown in examples, for geometrically linear problems, the scaled mass matrix is inverted only once. For nonlinear materials, no iteration is required in the explicit method. Moreover, it is known that the implicit methods lead to pre-shock oscillations and the explicit methods lead to post-shock oscillations, see in [CHO 13, KOL 15]. For wave propagation simulations, the latter case is more interesting. So the explicit time integration is really interesting in this context.

However, we must point out the two limitations of the proposed SMS method. The method might be less interesting for inertia dominant problems, for which one can choose a smaller value of bulk modulus with nearly no effect on the dynamical response. Secondly, for applications where nonlinear geometrical nonlinearity must be considered, the scaled mass matrix has to be updated regularly, the method is no longer efficient. An iterative algorithm is proposed in [OLO 06], but it is still heavy.

Chapter 5

Fractional time-step method

Contents

5.1 Introduction **127**
5.2 Method **127**
5.2.1 Mixed $\mathbf{u} - p$ formulation 128
5.2.2 Pressure stability 128
5.2.3 Fractional step time integration method 129
5.2.4 Discussion 131
5.3 Numerical examples **132**
5.3.1 Spinning model 132
5.3.2 Heterogeneous model 134
5.3.3 Anisotropic model 136
5.3.4 Nonlinear shear wave model 136
5.4 Conclusion **137**

5.1 Introduction

In this chapter, we present another numerical method for fast dynamic simulations of nearly incompressible materials. This method adopts a mixed $\mathbf{u}-p$ formulation in which the pressure appears explicitly. The velocity update over a time step is split into deviatoric and volumetric components. The deviatoric component is computed using explicit time integration, whereas pressure is computed implicitly. Once the pressure is known, the final component of velocity is corrected. Velocity is updated twice over one time step, so the method is referred to as *fractional time-step (FTS) integration method*.

This method was initially proposed by Sudeep K. Lahiri [LAH 06] for triangular or tetrahedral elements. As it treats the shear wave in explicit and the compressional wave in implicit, the maximal time step depends only on the shear wave speed. Consequently, FTS method has a similar performance to the SMS method (see Chapter 4) in dynamic elastography simulations. To enrich our simulation tools, and considering that tetrahedral elements would be more useful for complex 3D models, FTS method has been implemented during this Phd thesis.

In this work, FTS method is also extended to quadrilateral and hexahedral elements. This is based on the following two considerations. Firstly, triangle or tetrahedral mixed elements have serious pressure instability; secondly, a direct comparison can be made for the two numerical methods in this work, *i.e.* SMS *v.s.* FTS.

In this chapter, we present firstly the mixed $\mathbf{u}-p$ formulation and its performance regarding pressure stability. Then, the semi-explicit FTS scheme is described and also its modification for nonlinear wave applications. Several numerical examples are then presented to illustrate its performance compared to pure explicit method and SMS method. A conclusion is given in the end.

5.2 Method

Mixed $\mathbf{u}-p$ formulation was proposed to handle volumetric locking occurring in the simulation of (nearly) incompressible behaviour such as soft tissues and rubbers. Volumetric locking can be explained by the fact that incompressibility constraints are too many compared to the number of degrees of freedom in discrete frame. In the previous chapter, we used reduced (or selective) integration technique to decrease the number of volumetric constraints at the element level. However, this technique is applicable only for quadrilateral or hexahedral elements.

In $\mathbf{u}-p$ formulation, the pressure field p in these elements is interpolated independently of the displacement field. The resulting elements are often called mixed elements and hybrid elements. Hybrid elements could be constructed for all types of mesh, including triangular and tetrahedral elements.

5.2.1 Mixed $\mathbf{u}-p$ formulation

By splitting the stress $\boldsymbol{\sigma}$ into two parts, the balance of momentum equation in Eq.1.40 can be written in the form of

$$\rho\ddot{\mathbf{u}} = div(\bar{\sigma}) + \nabla p + \mathbf{f}_V, \;\; in\; \Omega \times [0,T] \tag{5.1}$$

with $\bar{\sigma}$ the deviatoric stress component and p the pressure (take tension as positive) or mean stress, and we have $\boldsymbol{\sigma} = \bar{\sigma} + p\mathbf{I}$.

The constitutive equation for pressure is written in an independent way

$$\frac{1}{K}p = div(\mathbf{u}) \tag{5.2}$$

Eqs.5.1 and 5.2 are then discretized in space by applying the standard Galerkin method. The field variables $\mathbf{u}$ and p are approximated by

$$\mathbf{u}(t) \approx \mathbf{N}_v\mathbf{U}(t), \quad p(t) \approx \mathbf{N}_p\mathbf{p}(t) \tag{5.3}$$

where $\mathbf{N}_v$ and $\mathbf{N}_p$ are the shape functions for displacement and pressure, and $\mathbf{U}$ and $\mathbf{p}$ are the nodal displacement and pressure vectors of the element. The semi-discretized system can be written as:

$$\begin{bmatrix}\mathbf{M} & \mathbf{0}\\ \mathbf{0} & -\tilde{\mathbf{M}}\end{bmatrix}\begin{bmatrix}\ddot{\mathbf{U}}(t)\\ \mathbf{p}(t)\end{bmatrix} + \begin{bmatrix}\mathbf{K}_{dev} & \mathbf{Q}\\ \mathbf{Q}^{\mathbf{T}} & \mathbf{0}\end{bmatrix}\begin{bmatrix}\mathbf{U}(t)\\ \mathbf{p}(t)\end{bmatrix} = \begin{bmatrix}\mathbf{F}_{ext}\\ \mathbf{0}\end{bmatrix} \tag{5.4}$$

where

$$\begin{aligned}\mathbf{M} &= \int_\Omega \rho\mathbf{N}_v^{\mathbf{T}}\mathbf{N}_v d\Omega, & \tilde{\mathbf{M}} &= \int_\Omega \frac{1}{K}\mathbf{N}_p^{\mathbf{T}}\mathbf{N}_p d\Omega\\ \mathbf{K}_{dev} &= \int_\Omega \mathbf{B}^{\mathbf{T}}\mathbf{D}_{dev}\mathbf{B} d\Omega, & \mathbf{Q} &= \int_\Omega \mathbf{B}^{\mathbf{T}}\mathbf{m}\mathbf{N}_p d\Omega\end{aligned} \tag{5.5}$$

where $\mathbf{B}$ is the stress-strain operator matrix; $\mathbf{D}_{dev}$ is the deviatoric component of constitutive law; and constant vector $\mathbf{m}$ is $[1,1,0]^T$ for 2D problems and $[1,1,1,0,0,0]^T$ for 3D problems.

5.2.2 Pressure stability

Many mixed elements exhibit a spatial instability in the pressure field. As a consequence, the pressure will often be oscillatory or have multiple solutions. As stated by Belytschko *et al.* in [BEL 13a]: “It is an irony of mixed methods that in resolving one difficulty, they introduce another. The removal of volumetric locking leads to pressure instabilities.”

To construct stable mixed elements, the interpolation function of $\mathbf{u}$ and $\mathbf{p}$ have to be carefully chosen to fulfil the LBB (Ladezhvanskaya-Babuska-Brezzi) condition [BAB 73, BRE 74]. Instead of using this sophisticated mathematical condition to test if the elements satisfy the pressure stability requirement, Zienkiewicz-Taylor [ZIE 00] proposed a much simpler method: patch test. In Eq.5.4, the pressure field **p** exists only if the rank of $\mathbf{K}_{dev}$ is greater than or equal to the rank of $\mathbf{Q}$. Since the rank of $\mathbf{K}_{dev}$ is the number of degrees of freedom n_{dof}, then if n_p is the number of pressure nodes in the model, we should have

$$n_{dof} \geq n_p \tag{5.6}$$

This is a necessary but not sufficient condition for the solvability of the pressure field: it is possible that the element are still unstable even if Eq.5.6 is verified. However, Eq.5.6 is a practical guide to ensure that a mixed element provides stable pressure fields.

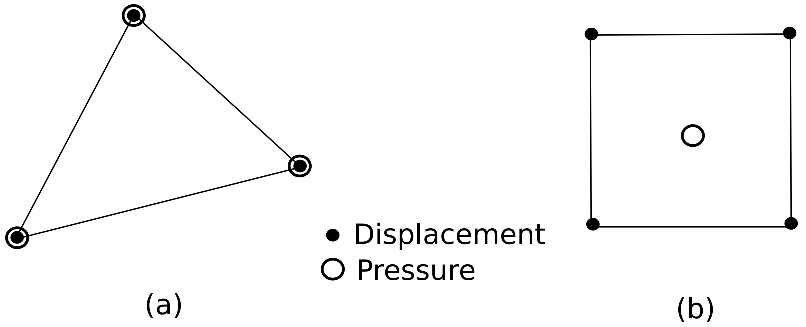

Figure 5.1: Two type of mixed elements. (a) T3P3 element (b) Q4P1 element

Unfortunately, few mixed elements pass this test. For instance, T3P3 element (3-noded linear triangle for displacements and 3-noded linear triangle for pressure, shown in 5.1(a)) which is used in [LAH 06] for the FTS method does not. As a consequence, this element suffers serious pressure oscillations. Even though this effect seems not to be harmful for other variables [BEL 13a], it is still undesirable. In this work, another Q4P1 element is used (4-noded linear quadrilateral for displacements and 1-noded constant pressure, shown in 5.1(b)). This element does not fulfill the LBB condition either (in fact, no linear element can fully pass the patch test, see in [ZIE 00]), but it has a much better pressure stability because pressure is interpolated one order lower than the displacement. This will be shown in the first numerical example in the next section. In addition, it should be mentioned that pressure oscillations can also be eliminated by filtering or by introducing viscosities [BEL 13a].

5.2.3 Fractional step time integration method

In order to introduce the semi-explicit method, it is necessary to present the explicit scheme (Eq.1.46) using a different formalism. Assuming the time step Δt is constant, we have $t = [0, \Delta t, ..., n\Delta t, ..., T]$. The central difference method can be written as follow:

$$\begin{aligned} \dot{\mathbf{U}}^{n+1/2} &= \frac{\mathbf{U}^{n+1} - \mathbf{U}^{n}}{\Delta t} \\ \ddot{\mathbf{U}}^{n} &= \frac{\dot{\mathbf{U}}^{n+1/2} - \dot{\mathbf{U}}^{n-1/2}}{\Delta t} \end{aligned} \tag{5.7}$$

In these equations, velocity is evaluated at the mid-step, *i.e.* $n-1/2$ or $n+1/2$. However, substituting the first equation into the second, Eq.1.46 will be recovered. The two methods of implementation are identical but this version is more convenient for the presentation in the following.

Using these relations, the first line of Eq.5.4 at nth step can be written by

$$\mathbf{M}\frac{\dot{\mathbf{U}}^{n+1/2}-\dot{\mathbf{U}}^{n-1/2}}{\Delta t}=\mathbf{F}^n_{ext}-\mathbf{K}^n_{dev}\mathbf{U}^n-\mathbf{Q}^n\mathbf{p}^n \tag{5.8}$$

For the sake of generality in nonlinear analysis, the superscript n appears in the deviatoric stiffness matrix $\mathbf{K}_{dev}$ and the operator matrix $\mathbf{Q}$. Moreover, pressure $\mathbf{p}^n$ is considered as an unknown and updated by the implicit mid-point method as follow

$$\mathbf{p}^n=\frac{1}{2}(\mathbf{p}^{n-1/2}+\mathbf{p}^{n+1/2}) \tag{5.9}$$

Following this hypothesis and introducing the intermediate velocity $\dot{\mathbf{U}}^*$, Eq.5.8 can be split into two parts:

$$\mathbf{M}\frac{\dot{\mathbf{U}}^{*}-\dot{\mathbf{U}}^{n-1/2}}{\Delta t}=\mathbf{F}^n_{ext}-\mathbf{K}^n_{dev}\mathbf{U}^n-\frac{1}{2}\mathbf{Q}^n\mathbf{p}^{n-1/2} \tag{5.10a}$$

$$\mathbf{M}\frac{\dot{\mathbf{U}}^{n+1/2}-\dot{\mathbf{U}}^{*}}{\Delta t}=-\frac{1}{2}\mathbf{Q}^n\mathbf{p}^{n+1/2} \tag{5.10b}$$

Note that if the mass matrix $\mathbf{M}$ is lumped, these equations can be calculated easily. Before calculating Eq.5.10b, the second line of Eq.5.4 is evaluated at time $n+1/2$ by:

$$\tilde{\mathbf{M}}\mathbf{p}^{n+1/2}=\mathbf{Q}^{n+1/2\ \mathbf{T}}\mathbf{U}^{n+1/2} \tag{5.11}$$

The above expression is indeed a set of nonlinear equations, because the operator matrix $\mathbf{Q}^{n+1/2\ \mathbf{T}}$ depends on the unknown displacement at $n+1$. Lahiri *et al.* [LAH 06] proposed a Newton-Raphson algorithm to solve this equation. However, iteration makes the scheme too heavy so it is no longer interesting. In this work, we assume that the displacement during the increment are small, the operator matrix $\mathbf{Q}^{n+1/2\ \mathbf{T}}$ can be replace by $\mathbf{Q}^{n\ \mathbf{T}}$. The constitutive equation for pressure becomes

$$\tilde{\mathbf{M}}\mathbf{p}^{n+1/2}\simeq\frac{1}{2}\mathbf{Q}^{n\ \mathbf{T}}(\mathbf{U}^n+\mathbf{U}^{n+1})=\mathbf{Q}^{n\ \mathbf{T}}(\mathbf{U}^n+\frac{\Delta t}{2}\dot{\mathbf{U}}^{n+1/2}) \tag{5.12}$$

In the above expression, $\dot{\mathbf{U}}^{n+1/2}$ is still unknown. By substituting into Eq.5.10b, a linear set of equations for the pressure is given as

$$(\tilde{\mathbf{M}}+\frac{\Delta t^2}{4}\mathbf{Q}^{n\ \mathbf{T}}\mathbf{M}^{-1}\mathbf{Q}^n)\mathbf{p}^{n+1/2}=\mathbf{Q}^{n\ \mathbf{T}}(\mathbf{U}^n+\frac{\Delta t}{2}\dot{\mathbf{U}}^*) \tag{5.13}$$

At this stage, the final velocity can be updated by using Eq.5.10b again.

5.2.4 Discussion

In general, FTS time integration scheme contains three steps over one time increment:

1. The intermediate velocity $\dot{\mathbf{U}}^*$ is calculated by Eq.5.10a;
2. The nodal pressure $\mathbf{p}^{n+1/2}$ is updated by Eq.5.13;
3. The velocity $\dot{\mathbf{U}}^{n+1/2}$ is calculated by Eq.5.10b.

The calculation of both Eqs.5.10a and 5.10b is trivial, because the mass matrix **M** can be lumped as in the explicit scheme. However, the matrix in Eq.5.13 can not be lumped, and a linear solver is necessary. For nonlinear applications, the material nonlinearity only affects the deviatoric part in Eq.5.10a, so it has minor effects on the performance of FTS scheme. But the geometrical nonlinearity is still difficult to handle, the operator matrix **Q** should be updated as the geometry changes, then the inverted matrix should be recalculated at every time step.

With the same consideration as in the previous chapter, the geometrical nonlinearity can be neglected for finite but still small displacement problems, especially for nonlinear wave propagation, so the operator **Q** can be always established at initial configuration $t = 0$, the inverse procedure is carried out only once at the beginning of simulations. Finally, the following algorithm is used:

1. Calculate the intermediate velocity $\dot{\mathbf{U}}^*$ by

$$\mathbf{M}\frac{\dot{\mathbf{U}}^* - \dot{\mathbf{U}}^{n-1/2}}{\Delta t} = \mathbf{F}^n_{ext} - \mathbf{F}^n_{dev} - \frac{1}{2}\mathbf{Q}^0\mathbf{p}^{n-1/2} \tag{5.14}$$

where $\mathbf{F}^n_{dev} \simeq \int_{\Omega_0}\mathbf{B}_0^T\boldsymbol{\sigma}^n_{dev}d\Omega_0$ (see Eq.4.18).

2. Calculate the nodal pressure $\mathbf{p}^{n+1/2}$ by

$$(\tilde{\mathbf{M}} + \frac{\Delta t^2}{4}\mathbf{Q}^{0\ \mathbf{T}}\mathbf{M}^{-1}\mathbf{Q}^0)\mathbf{p}^{n+1/2} = \mathbf{Q}^{0\ \mathbf{T}}(\mathbf{U}^n + \frac{\Delta t}{2}\dot{\mathbf{U}}^*) \tag{5.15}$$

3. Calculate the velocity $\dot{\mathbf{U}}^{n+1/2}$ by

$$\mathbf{M}\frac{\dot{\mathbf{U}}^{n+1/2} - \dot{\mathbf{U}}^*}{\Delta t} = -\frac{1}{2}\mathbf{Q}^0\mathbf{p}^{n+1/2} \tag{5.16}$$

In this scheme, pressure is treated implicitly by mid-point method and the deviatoric stress remains explicit. Consequently, the stability condition is determined only by the shear wave speed:

$$\Delta t_{crit} \leq \frac{L^e_{min}}{c_S} \tag{5.17}$$

This condition is the same as SMS method presented in the previous chapter. Besides, both methods require once the inversion procedure at the beginning of simulation.

However, FTS method requires three steps in one time step while SMS method requires only one. On the other hand, the size of the inverted matrix in FTS method is the number of nodes for pressure (see Eq.5.13) which is smaller than the number of degrees of freedom in SMS. Combing these two points, the relative efficiency of the two numerical methods depends on the considered models.

5.3 Numerical examples

During this work, FTS method is implemented in our in-house FE code. In the following, several numerical examples are presented, the first example aims at illustrating the pressure stability issue for different hybrid elements; the other three examples are chosen from the previous chapter, they are considered again to illustrate the performance of FTS in various situations.

5.3.1 Spinning model

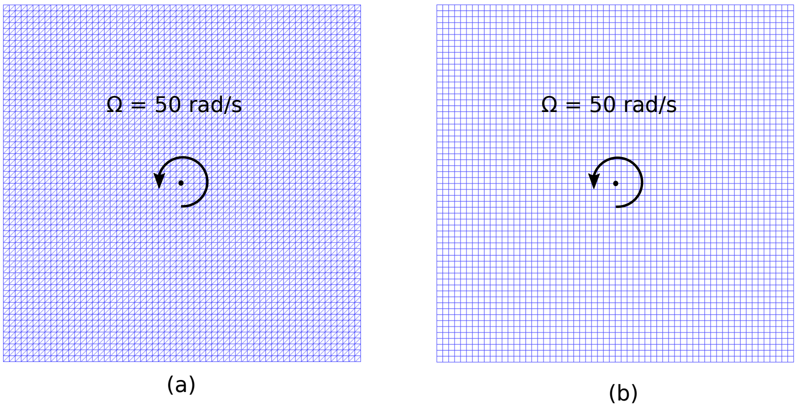

Figure 5.2: Spinning model. (a) T3P3 element (b) Q4P1 element

This example is chosen from [LAH 06] for illustrating pressure instability in triangular elements. As shown in Fig.5.2, the model describes a 60 $mm \times 60$ mm strain plane square rotating around its center without any constraints. The initial angular velocity is set to 50 rad/s and the model is released without initial deformation. Contrary to wave propagation problems, this spinning model is stationary so the stress distribution is more homogeneous, and pressure oscillations in space will be clearly illustrated.

The plate is meshed with 7200 triangular T3P3 elements and 3600 Q4P1 elements. For the material, neo-Hookean model (Eq.1.21) is chosen with $c_1 = 2$ kPa and $K = 10$ MPa. The FTS simulations are carried out for each mesh with a time step of 2×10^{-4} s.

For the two meshes, the pressure distributions at a chosen time are presented in Fig.5.3. In general, they both yield reasonable results: tension (positive pressure) appears around the center because of the centrifugal force, and compression appears at the edge

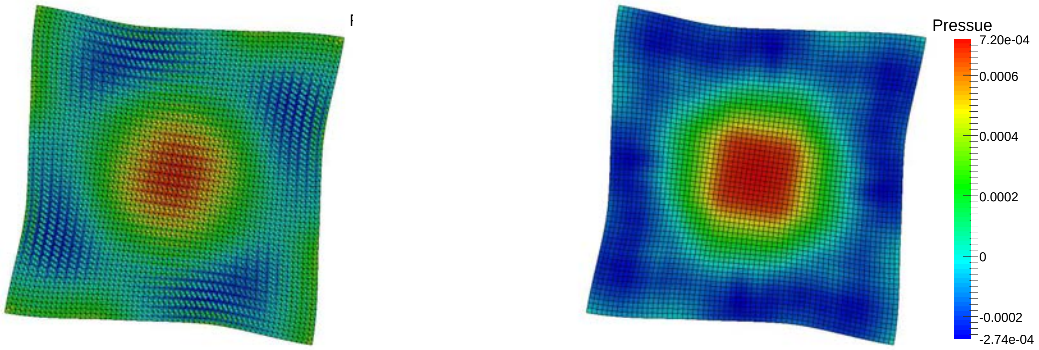

(a) By T3P3 element, serious pressur

(b) By Q4P1 element, no pressure oscillation

Figure 5.3: Spinning model: pressure distribution at time $t = 0.03\ s$

between corners. However, for the mixed triangle elements T3P3 (Fig.5.3(a)), pressure field is clearly oscillatory while Q4P1 elements generate a stable pressure field, which is physically reasonable. The profile of these oscillations in dynamic simulations is unpredictable and it does not happen at every step time. For illustration purpose, the time chosen in Fig.5.3 is when this phenomenon reaches its largest amplitude.

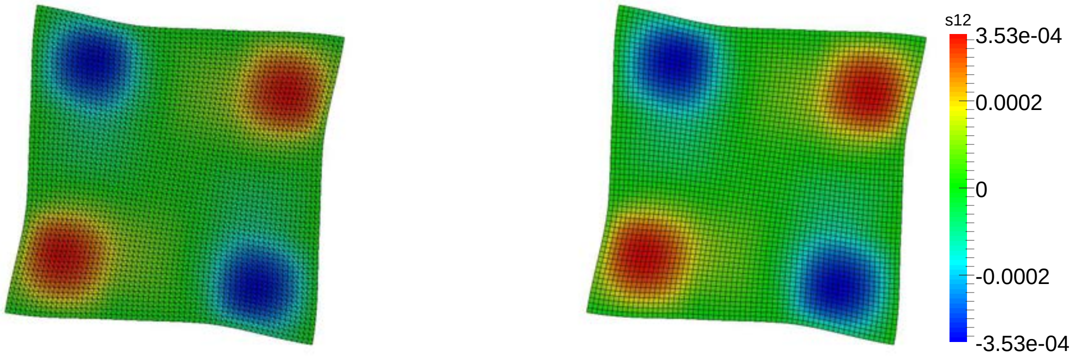

(a) By T3P3 element

(b) By Q4P1 element

Figure 5.4: Spinning model: shear stress distribution at time $t = 0.03\ s$

As mentioned earlier, the oscillations in pressure could be harmless for the whole simulation. For example, Fig.5.4 shows the shear stress distribution at the same time from the two simulations. The results are almost the same, shear stress concentrates at the four corners and the difference of maximal/minimal stress is less than 2% between two models.

5.3.2 Heterogeneous model

This example is chosen from the previous chapter, see Sec.4.4.3. It consists of shear wave propagation in a linear and heterogeneous medium, the detailed description is omitted here. The time step for FTS method is set to be the same as SMS method, so $0.8 \times 10^{-3}\ s$. Velocity distributions are compared at two different times in Fig.5.5, and velocity history curves are compared for two measuring points in Fig.5.6. All three simulations give very similar results.

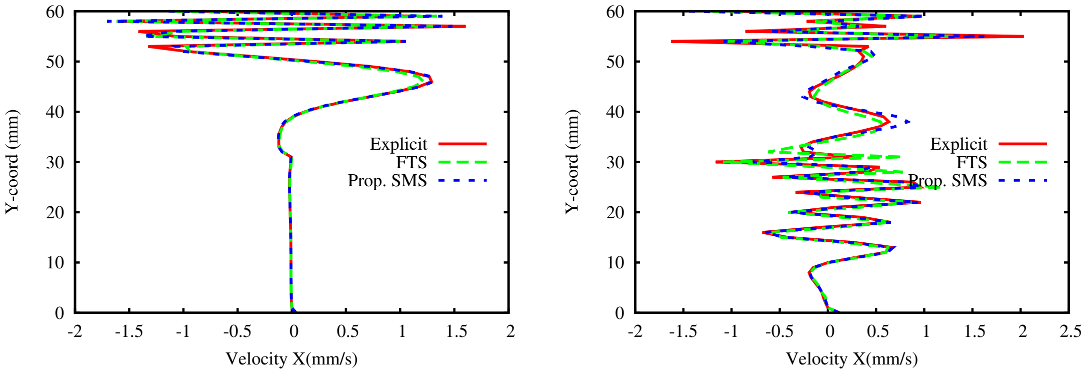

(a) $t = 0.04\ s$ (b) $t = 0.12\ s$

Figure 5.5: Heterogeneous model: Horizontal velocity along A-A' (see Fig.4.13) at different time

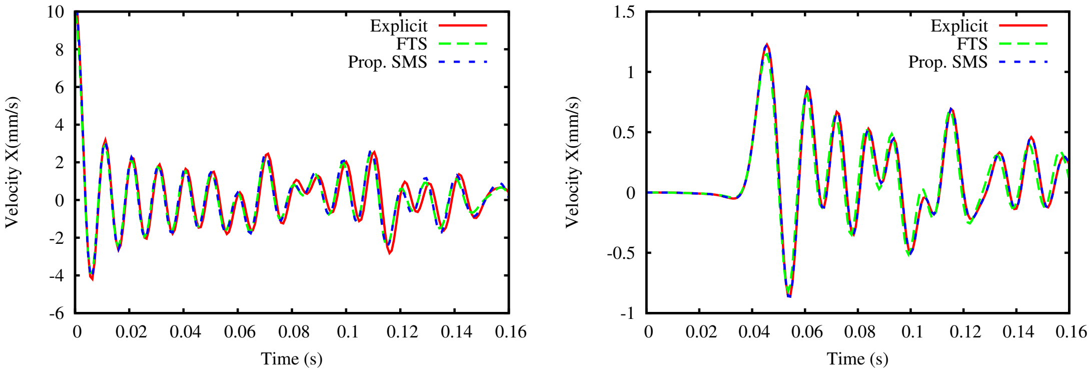

(a) Point A (b) Point B

Figure 5.6: Heterogeneous model: Horizontal velocity at measuring points (see Fig.4.13)

The shear stress distributions are compared in Fig.5.8. A clear stress concentration is observed at the second heterogeneous block, along E-E' line. Both FTS and SMS methods product spurious stress at the top of F-F' line, which is a narrow region between the first heterogeneous block and the boundary, many reflected waves have been generated and interact each other, they cannot be accurately simulated by the large time steps. However, errors remain small compared to the global results.

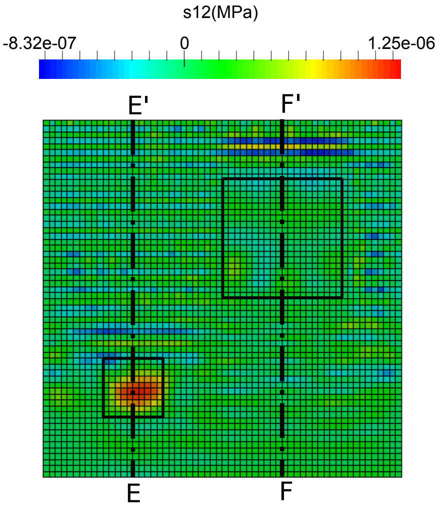

Figure 5.7: Global shear stress distribution obtained by FTS method, the positions of heterogeneous blocks are shown.

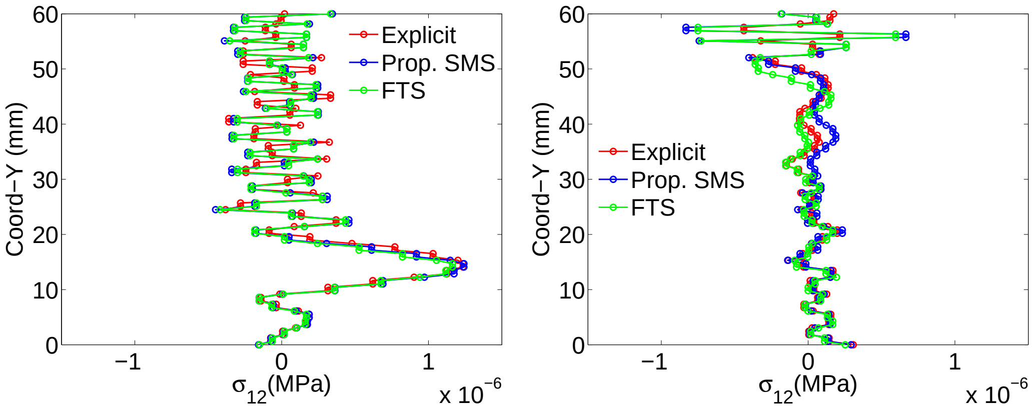

(a) Shear stress along E-E'

(b) Shear stress along F-F'

Figure 5.8: Heterogeneous model: shear stress distribution at $t = 0.16\ s$

In the previous chapter, it has been mentioned that explicit and SMS methods take around 220 s and 10 s respectively. FTS method presented in this chapter costs 22 s which is slower than SMS. The reason has been explained in the above: three times updates for FTS versus one time update for SMS in the same time step. Smaller inverted matrix in FTS does not show advantage for this medium-size model. However, it is still significantly faster than pure explicit method.

5.3.3 Anisotropic model

This example is chosen from Sect.4.4.4. The objective is to illustrate the performance of FTS method for anisotropic applications. As has been mentioned earlier (Chapter 3), the anisotropy of nearly incompressible materials only appears on the deviatoric part (in Eq.5.10a), FTS method can be carried out without any modification.

In these simulations, the time step is set to 5×10^{-6} s for explicit method, and 2×10^{-4} s for both SMS and FTS methods. Finally, the simulations of three methods take 284 s, 52 s and 51 s respectively. It can be seen, for this example, that FTS has the same efficiency as SMS method.

The comparisons are made for the kinetic variables at a measuring point, as shown in Fig.5.9. In all the simulations, the wave fronts are accurately simulated, except that the amplitudes in two new methods (FTS ans SMS) are slightly larger than in pure explicit method, and nearly no difference is observed between FTS and SMS.

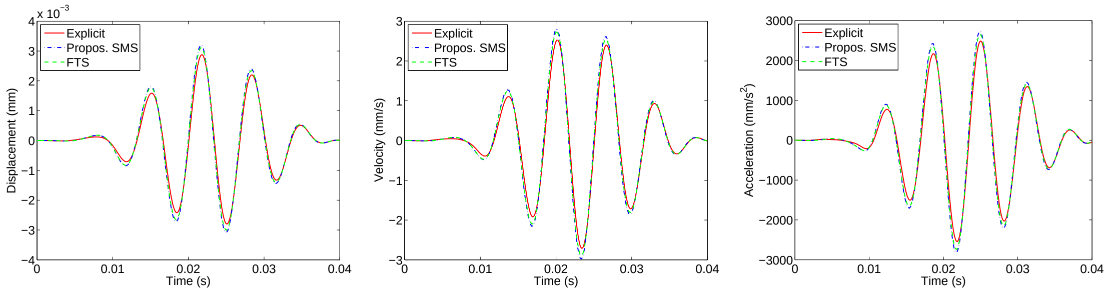

(a) Displacement (b) Velocity (c) Acceleration

Figure 5.9: Anisotropic model: Vertical displacement, velocity and acceleration at point A (see Fig.4.19).

In Fig.5.10, stress distributions are compared quantitatively, the shear stress of elements (for selective integration, it is the average of four Gauss points) is displayed in Fig.5.10(b). Clearly, all three simulations are almost identical.

5.3.4 Nonlinear shear wave model

Finally, nonlinear shear wave propagation is considered for FTS method. The example is chosen from Sec.4.4.5 with $A_0 = 0.8$ mm, *i.e.*, large load case. It is emphasized that the geometrical nonlinearity is neglected as in SMS method.

The time step in FTS is 2×10^{-4} s, it is set to be the same as in SMS and 20 times larger than in pure explicit. As a result, for explicit, SMS and FTS method, the simulation costs 290 s, 50 s and 142 s, respectively.

The kinetic variables are presented at a measuring point, see Fig.5.11. Due to the high nonlinearity of the material, the history curves looks very different for the three variables: the displacement curve is the most smooth, the velocity is more excited and it has been used for characterizing one nonlinear parameter in the Chapter 2; the acceleration history

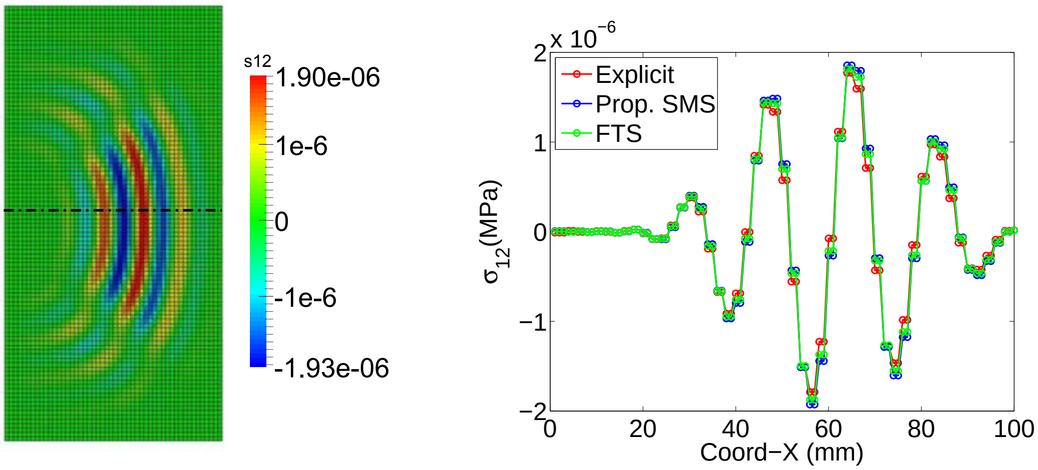

(a) Shear stress along dashed line is displayed at right

(b) Shear stress

Figure 5.10: Anisotropic model: Shear stress distribution at the end of simulation, $t = 0.04\ s$.

is the most discontinuous, its amplitude provides important information in the study of traumatic brain injury [GIA 16b]. Nevertheless, compared to pure explicit method, both new methods obtain reliable numerical results.

Both shear strain and stress are displayed along a chosen line in Fig.5.13. Again, three simulations obtain identical results. It can be seen, in Fig.5.13(b), that the maximal strain reaches up to 8%, however, the geometrical nonlinearity can still be neglected without any negative effect.

5.4 Conclusion

In this last chapter, we revisit the semi-explicit FTS method from the literature. We have shown that triangular/tetrahedral elements suffer serious pressure oscillations but it is not harmful for the whole solution. On the other hand, quadrilateral/hexahedral elements remain stable for pressure.

Quadrilateral elements are then applied into various numerical examples related to shear wave propagation problems, the objective is to compare the performance of FTS method with pure explicit and SMS methods. It has been shown that the accuracy is ensured for both FTS and SMS methods. In efficiency, FTS does not show advantage to SMS but it is still faster than pure explicit method.

At last, we emphasize that FTS method is worth to be considered because it could be applied for tetrahedral elements. This is particularly interesting for *in vivo* applications with complex 3D geometries that cannot be meshed with hexahedral elements only.

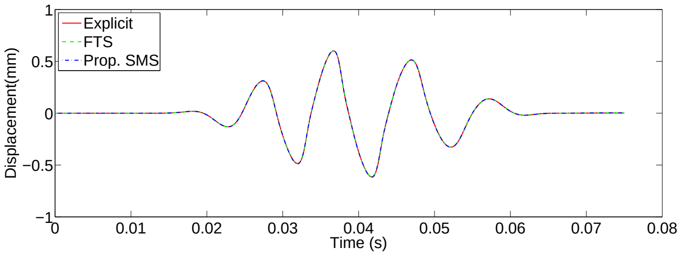

(a) Displacement

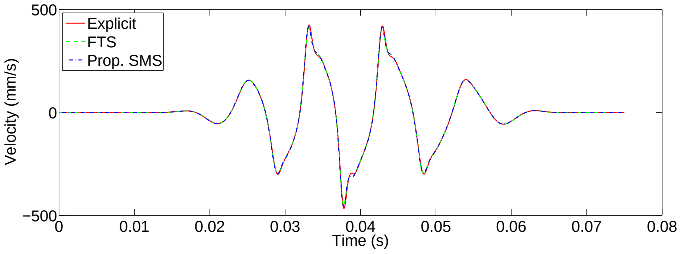

(b) Velocity

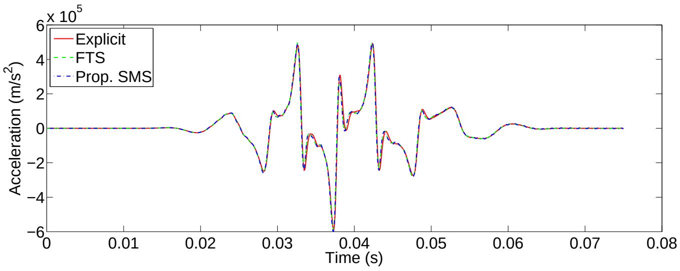

(c) Acceleration

Figure 5.11: Test of large amplitude nonlinear wave.Vertical displacement, velocity and acceleration at one point 30 *mm* far from the load

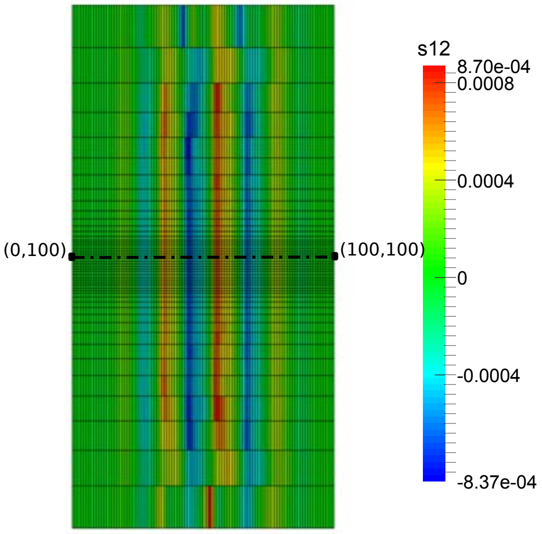

Figure 5.12: Nonlinear wave model: At $t = 0.05\ s$

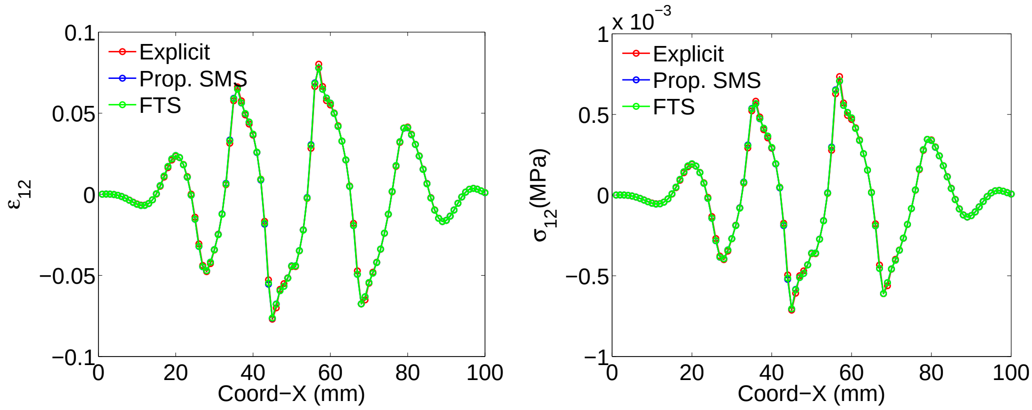

(a) Shear strain (b) Shear stress

Figure 5.13: Nonlinear wave model: Shear strain and stress distributions along dashed line

General conclusions and perspectives

General conclusion

In this thesis, both numerical and analytical models have been developed for characterizing nonlinear elasticity by transient elastography. The nonlinear parameters can be deduced by observing finite amplitude shear waves or small shear waves in pre-deformed states.

To our knowledge, Chapter 2 is the first time that nonlinear shear waves in soft solids are simulated in FEM. Landau's model is implemented in ABAQUS user's subroutine (UMAT & VUMAT) and also in our in-house finite element code. It is shown that the cubic nonlinearity in shear is responsible for the production of harmonics in finite shear wave propagation. On the other hand, some common hyperelastic laws do not have this property, so they should be avoided (modified) in shear dominated nonlinear simulations and characterizations. Besides, viscosity is an important factor which should be considered in finite wave modeling. In this chapter, a new method is proposed to deduce one nonlinear parameter in a homogeneous medium by measuring the first odd harmonic amplitude in plane wave. For applications, the proposed method requires amplifying the intensity of SSI source and adding a spectral analysis in the post-processing, but no extra experimental setup is demanded.

The numerical implementation of linear and nonlinear transverse isotropy was described and validated in Chapter 3. For linear elastic incompressible TI models, except for the two shear moduli, the third parameter is necessary to be identified. Afterwards, the consistency between linear and nonlinear TI models is presented. This work gives a guideline for FE simulations in anisotropic elastography applications.

More importantly, Chapter 3 focuses on the shear wave propagation in pre-deformed homogeneous materials. Nonlinear parameters can be deduced by fitting wave speeds at different pre-deformed states using the proposed analytical expressions. However, this problem is regarded as a inverse process, so stability, uniqueness, reliability are all important issues. They are carefully considered for Landau's model, and a method is proposed to deduce both nonlinear parameters of Landau's solid by incorporating the major results from Chapter 2. Thus, the work has addressed an important improvement of the reliability in the characterization of soft tissues nonlinearity.

In addition, a 3D Finite Element code has been developed. This code is able to perform both nonlinear static and nonlinear dynamic explicit simulations. It has been successfully used into the above mentioned analysis with simple geometries. For fast dynamic (wave propagation) simulations in soft solids, incompressibility leads to an extremely small time step, which largely limits its applications for complex biological systems.

To handle this problem, we proposed a selective mass scaling method in Chapter 4, in which eigenfrequencies related to volumetric deformation modes are selected to be decreased, while the method keeps the shear eigenmodes unchanged. Thus, the time step in the explicit time integration is no longer limited by the fast compressional wave speed but by the slow shear wave speed. Various numerical examples show that the method is available for isotropic/anisotropic materials, linear/finite shear wave propagations in natural/pre-deformed states. This includes almost all the situations that can occur in dynamic elastography simulations, a significant reduction of CPU time is obtained with a good accuracy.

At the same time, an other numerical method from the literature is described in Chapter 5. This method has a similar performance as SMS but using a very different approach. The equilibrium is split into two parts and the compressional wave and shear wave are treated in implicit and in explicit respectively. In the same numerical examples, this method does not show advantages to SMS method. However, this method is available for tetrahedral elements, which will be useful for 3D models with complex geometries.

Perspectives

After this thesis, the future work could be considered in these aspects:

- Experiment validations

  Now that the numerical methods for the simulation of nonlinear shear waves have been developped, it would be an important step to validate them against more complex experiments. For instance the identification of nonlinear constitutive parameters could be performed using the method described in Chapter 2 and 3. Then more and more complex situations could be handled, from controlled experiments on artificial gels to *in vivo* measurements. New identified parameters may offer new possibilities of diagnosis for physicians to better understand organs pathologies. Specifically, nonlinear parameters of soft tissues characterized by elastography may be used to differentiate between benign and malignant tumours.

- Forward numerical simulations

  FEM can be used in more general cases, numerical simulations are expected to handle more complicated cases where the analytical solutions are difficult or impossible to be obtained. For example, focused wave, cylinder wave and circularly polarized wave are idealized models to explore properties of soft solids, they can be realized in numerical models. On the other side, more nonlinear elastic and viscoelastic models, such as Fung's model, generalized Maxwell model could be implemented in the developed FE code, so that a large library of behaviours could be available.

- Inverse numerical simulations

  The inverse FEM is another numerical approach to find optimal values of a set of target parameters by using experimental data as input. It is particularly important for elastography because that the material parameters that require identification often come from heterogeneous media, such as tissues affected by tumours. Linear inverse simulations have been considered in elastography experiments for years [MCL 06a, MCL 06b], but still not for nonlinear problems. Inverse problems are always ill-posed and this will be more serious for nonlinear problems, so this part would require much effort.

- New numerical methods

  In the numerical aspect, two methods have been presented for transient problems of nearly incompressible materials, however, both methods have difficulty in treating geometrical nonlinearity. Even though this might be out of the current objective, this kind of problem has a broad range of applications, for example, drop-impact modelling of rubber-like materials. In recent years, there is already a wealth of numerical techniques in the literature to deal with this problem, for example, the Petrov-Galerkin method in [GIL 14, LEE 14], the component-wise partition method in [CHO 13, KOL 15]. We believe that there is still room to optimise the numerical techniques in this domain.

Bibliography

[ADA 03] ADAMS S. B., ROBERTS M. J., PATEL N. A., PLUMMER S., ROGOWSKA J., STAMPER D. L., FUJIMOTO J. G., BREZINSKI M. E.
The use of polarization sensitive optical coherence tomography and elastography to assess connective tissue. *Lasers and Electro-Optics, 2003. CLEO'03. Conference on* IEEE, 2003, p. 3–pp.

[ALS 01] ALSHAIKH I. A., TURHAN D., MENGI Y.
Two-dimensional transient wave propagation in viscoelastic layered media. *Journal of Sound and vibration*, vol. 244, n^o 5, 2001, p. 837–858, Elsevier.

[ASB 08] ASBACH P., KLATT D., HAMHABER U., BRAUN J., SOMASUNDARAM R., HAMM B., SACK I.
Assessment of liver viscoelasticity using multifrequency MR elastography. *Magnetic Resonance in Medicine*, vol. 60, n^o 2, 2008, p. 373–379, Wiley Online Library.

[BAB 73] BABUŠKA I.
The finite element method with Lagrangian multipliers. *Numerische Mathematik*, vol. 20, n^o 3, 1973, p. 179–192.

[BEL 13a] BELYTSCHKO T., LIU W. K., MORAN B., ELKHODARY K.
Nonlinear finite elements for continua and structures. John Wiley & Sons, 2013.

[BEL 13b] BELYTSCHKO T., LIU W. K., MORAN B., ELKHODARY K.
Nonlinear finite elements for continua and structures. John wiley & sons, 2013.

[BER 04] BERCOFF J., TANTER M., FINK M.
Supersonic shear imaging: a new technique for soft tissue elasticity mapping. *Ultrasonics, Ferroelectrics and Frequency Control, IEEE Transactions on*, vol. 51, n^o 4, 2004, p. 396–409, IEEE.

[BON 97] BONET J., WOOD R. D.
Nonlinear continuum mechanics for finite element analysis. Cambridge university press, 1997.

[BOW 11] BOWER A. F.
Applied mechanics of solids. CRC press, 2011.

[BRE 74] BREZZI F.
On the existence, uniqueness and approximation of saddle-point problems arising from Lagrangian multipliers. *Revue française d'automatique, informatique, recherche opérationnelle. Analyse numérique*, vol. 8, n° 2, 1974, p. 129–151.

[BRU 12] BRUM J.
Elastographie et retournement temporel des ondes de cisaillement: application à l'imagerie des solides mous. Thèse de doctorat, Université de Grenoble, 2012.

[BUR 12] BUREL A., IMPÉRIALE S., JOLY P.
Solving the homogeneous isotropic linear elastodynamics equations using potentials and finite elements. The case of the rigid boundary condition. *Numerical Analysis and Applications*, vol. 5, n° 2, 2012, p. 136–143, Springer.

[CAT 98] CATHELINE S.
Interférométrie-Speckle ultrasonore: Application à la mesure d'élasticité. Thèse de doctorat, Université Paris-Diderot-Paris VII, 1998.

[CAT 99a] CATHELINE S., THOMAS J.-L., WU F., FINK M. A.
Diffraction field of a low frequency vibrator in soft tissues using transient elastography. *IEEE transactions on ultrasonics, ferroelectrics, and frequency control*, vol. 46, n° 4, 1999, p. 1013–1019, IEEE.

[CAT 99b] CATHELINE S., WU F., FINK M.
A solution to diffraction biases in sonoelasticity: the acoustic impulse technique. *The Journal of the Acoustical Society of America*, vol. 105, n° 5, 1999, p. 2941–2950, Acoustical Society of America.

[CAT 03a] CATHELINE S., GENNISSON J.-L., FINK M.
Measurement of elastic nonlinearity of soft solid with transient elastography. *The Journal of the Acoustical Society of America*, vol. 114, n° 6, 2003, p. 3087–3091, Acoustical Society of America.

[CAT 03b] CATHELINE S., GENNISSON J.-L., TANTER M., FINK M.
Observation of shock transverse waves in elastic media. *Physical review letters*, vol. 91, n° 16, 2003, p. 164301, APS.

[CAT 04] CATHELINE S., GENNISSON J.-L., DELON G., FINK M., SINKUS R., ABOUELKARAM S., CULIOLI J.
Measurement of viscoelastic properties of homogeneous soft solid using transient elastography: an inverse problem approach. *The Journal of the Acoustical Society of America*, vol. 116, n° 6, 2004, p. 3734–3741, Acoustical Society of America.

[CAT 15] CATHELINE S., BENECH N.
Longitudinal shear wave and transverse dilatational wave in solids. *The Journal of the Acoustical Society of America*, vol. 137, n° 2, 2015, p. EL200–EL205, Acoustical Society of America.

[CHE 05] CHEN Q., RINGLEB S. I., MANDUCA A., EHMAN R. L., AN K.-N.
A finite element model for analyzing shear wave propagation observed in magnetic resonance elastography. *Journal of Biomechanics*, vol. 38, n^{o} 11, 2005, p. 2198 - 2203.

[CHE 06] CHEN Q., RINGLEB S. I., MANDUCA A., EHMAN R. L., AN K.-N.
Differential effects of pre-tension on shear wave propagation in elastic media with different boundary conditions as measured by magnetic resonance elastography and finite element modeling. *Journal of biomechanics*, vol. 39, n^{o} 8, 2006, p. 1428–1434, Elsevier.

[CHO 13] CHO S., PARK K., HUH H.
A method for multidimensional wave propagation analysis via component-wise partition of longitudinal and shear waves. *International Journal for Numerical Methods in Engineering*, vol. 95, n^{o} 3, 2013, p. 212–237, Wiley Online Library.

[COC 13] COCCHETTI G., PAGANI M., PEREGO U.
Selective mass scaling and critical time-step estimate for explicit dynamics analyses with solid-shell elements. *Computers & Structures*, vol. 127, 2013, p. 39 - 52. Special Issue IASS-IACM-2012.

[COC 15] COCCHETTI G., PAGANI M., PEREGO U.
Selective mass scaling for distorted solid-shell elements in explicit dynamics: optimal scaling factor and stable time step estimate. *International Journal for Numerical Methods in Engineering*, vol. 101, n^{o} 9, 2015, p. 700–731, Wiley Online Library.

[DEF 09] DEFFIEUX T., MONTALDO G., TANTER M., FINK M.
Shear wave spectroscopy for in vivo quantification of human soft tissues visco-elasticity. *IEEE transactions on medical imaging*, vol. 28, n^{o} 3, 2009, p. 313–322, IEEE.

[DES 05] DESTRADE M., OTTÉNIO M., PICHUGIN A. V., ROGERSON G. A.
Non-principal surface waves in deformed incompressible materials. *International Journal of Engineering Science*, vol. 43, n^{o} 13, 2005, p. 1092–1106, Elsevier.

[DES 09] DESTRADE M., OGDEN R. W., SACCOMANDI G.
Small amplitude waves and stability for a pre-stressed viscoelastic solid. *Zeitschrift für angewandte Mathematik und Physik*, vol. 60, n^{o} 3, 2009, p. 511–528, Springer.

[DES 10a] DESTRADE M., GILCHRIST M. D., MURPHY J. G.
Onset of nonlinearity in the elastic bending of blocks. *Journal of Applied Mechanics*, vol. 77, n^{o} 6, 2010, p. 061015, American Society of Mechanical Engineers.

[DES 10b] DESTRADE M., GILCHRIST M. D., SACCOMANDI G.
Third-and fourth-order constants of incompressible soft solids and the acousto-elastic effect. *The Journal of the Acoustical Society of America*, vol. 127, n^{o} 5, 2010, p. 2759–2763, Acoustical Society of America.

[DES 13a] DESTRADE M., MAC DONALD B., MURPHY J., SACCOMANDI G.
At least three invariants are necessary to model the mechanical response of incompressible, transversely isotropic materials. *Computational Mechanics*, vol. 52, n^{o} 4, 2013, p. 959–969, Springer.

[DES 13b] DESTRADE M., SACCOMANDI G., VIANELLO M.
Proper formulation of viscous dissipation for nonlinear waves in solids. *arXiv preprint arXiv:1303.1617*, , 2013.

[DOW 90] DOWAIKH M., OGDEN R.
On surface waves and deformations in a pre-stressed incompressible elastic solid. *IMA Journal of Applied Mathematics*, vol. 44, n^{o} 3, 1990, p. 261–284, IMA.

[FRÍ 14] FRÍAS G., AQUINO W., PIERSON K., HEINSTEIN M., SPENCER B.
A multiscale mass scaling approach for explicit time integration using proper orthogonal decomposition. *International Journal for Numerical Methods in Engineering*, vol. 97, n^{o} 11, 2014, p. 799–818, Wiley Online Library.

[FUN 90] FUNG Y.-C.
Biomechanical aspects of growth and tissue engineering. *Biomechanics*, p. 499–546 Springer, 1990.

[GAL 11] GALLOT T., CATHELINE S., ROUX P., BRUM J., BENECH N., NEGREIRA C.
Passive elastography: shear-wave tomography from physiological-noise correlation in soft tissues. *IEEE transactions on ultrasonics, ferroelectrics, and frequency control*, vol. 58, n^{o} 6, 2011, p. 1122–1126, IEEE.

[GEN 03] GENNISSON J.-L., CATHELINE S., CHAFFAI S., FINK M.
Transient elastography in anisotropic medium: application to the measurement of slow and fast shear wave speeds in muscles. *The Journal of the Acoustical Society of America*, vol. 114, n^{o} 1, 2003, p. 536–541, Acoustical Society of America.

[GEN 04] GENNISSON J.-L., BALDEWECK T., TANTER M., CATHELINE S., FINK M., SANDRIN L., CORNILLON C., QUERLEUX B.
Assessment of elastic parameters of human skin using dynamic elastography. *IEEE transactions on ultrasonics, ferroelectrics, and frequency control*, vol. 51, n^{o} 8, 2004, p. 980–989, IEEE.

[GEN 05] GENNISSON J. L., CORNU C., CATHELINE S., FINK M., PORTERO P.
Human muscle hardness assessment during incremental isometric contraction using transient elastography. *Journal of biomechanics*, vol. 38, n^{o} 7, 2005, p. 1543–1550, Elsevier.

[GEN 07] GENNISSON J.-L., RÉNIER M., CATHELINE S., BARRIÈRE C., BERCOFF J., TANTER M., FINK M.
Acoustoelasticity in soft solids: Assessment of the nonlinear shear modulus with the

acoustic radiation force. *The Journal of the Acoustical Society of America*, vol. 122, n° 6, 2007, p. 3211–3219, Acoustical Society of America.

[GIA 16a] GIAMMARINARO B.
Focalisation non linéaire des ondes de choc de cisaillement dans les solides incompressibles. Thèse de doctorat, Université Pierre et Marie Curie-Paris VI, 2016.

[GIA 16b] GIAMMARINARO B., COULOUVRAT F., PINTON G.
Numerical Simulation of Focused Shock Shear Waves in Soft Solids and a Two-Dimensional Nonlinear Homogeneous Model of the Brain. *Journal of biomechanical engineering*, vol. 138, n° 4, 2016, p. 041003, American Society of Mechanical Engineers.

[GIL 14] GIL A. J., LEE C. H., BONET J., AGUIRRE M.
A stabilised Petrov–Galerkin formulation for linear tetrahedral elements in compressible, nearly incompressible and truly incompressible fast dynamics. *Computer Methods in Applied Mechanics and Engineering*, vol. 276, 2014, p. 659–690, Elsevier.

[HAM 04] HAMILTON M. F., ILINSKII Y. A., ZABOLOTSKAYA E. A.
Separation of compressibility and shear deformation in the elastic energy density (L). *Acoustical Society of America Journal*, vol. 116, 2004, p. 41–44.

[HIB 02] HIBBITT K., SORENSEN
ABAQUS/CAE User's Manual. Hibbitt, Karlsson & Sorensen, Incorporated, 2002.

[HOL 00] HOLZAPFEL G. A.
Nonlinear solid mechanics, vol. 24. Wiley Chichester, 2000.

[HON 16] HONARVAR M., ROHLING R., SALCUDEAN S.
A comparison of direct and iterative finite element inversion techniques in dynamic elastography. *Physics in medicine and biology*, vol. 61, n° 8, 2016, p. 3026, IOP Publishing.

[HUG 53] HUGHES D. S., KELLY J.
Second-order elastic deformation of solids. *Physical review*, vol. 92, n° 5, 1953, p. 1145, APS.

[HUG 12] HUGHES T. J.
The finite element method: linear static and dynamic finite element analysis. Courier Corporation, 2012.

[JAC 07] JACOB X., CATHELINE S., GENNISSON J.-L., BARRIÈRE C., ROYER D., FINK M.
Nonlinear shear wave interaction in soft solids. *The Journal of the Acoustical Society of America*, vol. 122, n° 4, 2007, p. 1917–1926, Acoustical Society of America.

[JIA 15a] JIANG Y., LI G.-Y., QIAN L.-X., HU X.-D., LIU D., LIANG S., CAO Y.
Characterization of the nonlinear elastic properties of soft tissues using the supersonic shear imaging (SSI) technique: inverse method, ex vivo and in vivo experiments. *Medical image analysis*, vol. 20, n^o 1, 2015, p. 97–111, Elsevier.

[JIA 15b] JIANG Y., LI G., QIAN L.-X., LIANG S., DESTRADE M., CAO Y.
Measuring the linear and nonlinear elastic properties of brain tissue with shear waves and inverse analysis. *Biomechanics and modeling in mechanobiology*, vol. 14, n^o 5, 2015, p. 1119–1128, Springer.

[KHE 12] KHELLADI H.
Goldberg's Number Influence on the Validity Domain of the Quasi-Linear Approximation of Finite Amplitude Acoustic Waves. INTECH Open Access Publisher, 2012.

[KOL 15] KOLMAN R., CHO S., PARK K.
Efficient implementation of an explicit partitioned shear and longitudinal wave propagation algorithm. *International Journal for Numerical Methods in Engineering*, , 2015.

[KOO 14] KOO T. K., GUO J.-Y., COHEN J. H., PARKER K. J.
Quantifying the passive stretching response of human tibialis anterior muscle using shear wave elastography. *Clinical Biomechanics*, vol. 29, n^o 1, 2014, p. 33–39, Elsevier.

[KRO 98] KROUSKOP T. A., WHEELER T. M., KALLEL F., GARRA B. S., HALL T.
Elastic moduli of breast and prostate tissues under compression. *Ultrasonic imaging*, vol. 20, n^o 4, 1998, p. 260–274, SAGE Publications.

[LAH 05] LAHIRI S. K., BONET J., PERAIRE J., CASALS L.
A variationally consistent fractional time-step integration method for incompressible and nearly incompressible Lagrangian dynamics. *International journal for numerical methods in engineering*, vol. 63, n^o 10, 2005, p. 1371–1395, Wiley Online Library.

[LAH 06] LAHIRI S. K.
Variationally consistent methods for Lagrangian dynamics in continuum mechanics. Thèse de doctorat, Massachusetts Institute of Technology, 2006.

[LAN 86] LANDAU L. D., LIFSHITZ E. M.
Theory of Elasiticy. Pergamon, New York, 1986.

[LEE 12] LEE K. H., SZAJEWSKI B. A., HAH Z., PARKER K. J., MANIATTY A. M.
Modeling shear waves through a viscoelastic medium induced by acoustic radiation force. *International journal for numerical methods in biomedical engineering*, vol. 28, n^o 6-7, 2012, p. 678–696, Wiley Online Library.

[LEE 14] LEE C. H., GIL A. J., BONET J.
Development of a stabilised Petrov–Galerkin formulation for conservation laws in Lagrangian fast solid dynamics. *Computer Methods in Applied Mechanics and Engineering*, vol. 268, 2014, p. 40–64, Elsevier.

[LI 16] LI G.-Y., ZHENG Y., LIU Y., DESTRADE M., CAO Y.
Elastic Cherenkov effects in transversely isotropic soft materials-I: Theoretical analysis, simulations and inverse method. *Journal of the Mechanics and Physics of Solids*, vol. 96, 2016, p. 388–410, Elsevier.

[LOM 13] LOMBARDO M., ASKES H.
Lumped mass finite element implementation of continuum theories with micro-inertia. *International Journal for Numerical Methods in Engineering*, vol. 96, n° 7, 2013, p. 448–466, Wiley Online Library.

[MAC 95] MACEK R. W., AUBERT B. H.
A mass penalty technique to control the critical time increment in explicit dynamic finite element analyses. *Earthquake engineering & structural dynamics*, vol. 24, n° 10, 1995, p. 1315–1331, Wiley Online Library.

[MCL 06a] MCLAUGHLIN J., RENZI D.
Shear wave speed recovery in transient elastography and supersonic imaging using propagating fronts. *Inverse Problems*, vol. 22, n° 2, 2006, p. 681, IOP Publishing.

[MCL 06b] MCLAUGHLIN J., RENZI D.
Using level set based inversion of arrival times to recover shear wave speed in transient elastography and supersonic imaging. *Inverse Problems*, vol. 22, n° 2, 2006, p. 707, IOP Publishing.

[MCL 11] MCLAUGHLIN J., THOMAS A., YOON J.-R.
Basic theory for generalized linear solid viscoelastic models. *AMS Contemporary Mathematics Volume: Tomography and Inverse Transport Theory, edited by G. Bal, D. Finch, P. Kuchment, J. Schotland, P. Stefanov, and G. Uhlmann. Providence: American Mathematical Society*, , 2011, p. 101–134.

[MER 05] MERODIO J., OGDEN R.
Mechanical response of fiber-reinforced incompressible non-linearly elastic solids. *International Journal of Non-Linear Mechanics*, vol. 40, n° 2, 2005, p. 213–227, Elsevier.

[MIC 10] MICHEL DESTRADE R. W. O.
On the third- and fourth-order constants of incompressible isotropic elasticity. *The Journal of the Acoustical Society of America*, , 2010.

[MIL 10] MILLONIG G., FRIEDRICH S., ADOLF S., FONOUNI H., GOLRIZ M., MEHRABI A., STIEFEL P., PÖSCHL G., BÜCHLER M. W., SEITZ H. K. et al.

Liver stiffness is directly influenced by central venous pressure. *Journal of hepatology*, vol. 52, n° 2, 2010, p. 206–210, Elsevier.

[MOC 05] MOCZO P., KRISTEK J.
On the rheological models used for time-domain methods of seismic wave propagation. *Geophysical Research Letters*, vol. 32, n° 1, 2005, Wiley Online Library.

[MUR 13] MURPHY J.
Transversely isotropic biological, soft tissue must be modelled using both anisotropic invariants. *European Journal of Mechanics-A/Solids*, vol. 42, 2013, p. 90–96, Elsevier.

[NIG 01] NIGHTINGALE K. R., PALMERI M. L., NIGHTINGALE R. W., TRAHEY G. E.
On the feasibility of remote palpation using acoustic radiation force. *The Journal of the Acoustical Society of America*, vol. 110, n° 1, 2001, p. 625–634, Acoustical Society of America.

[NOL 14] NOLAN D., GOWER A., DESTRADE M., OGDEN R., MCGARRY J.
A robust anisotropic hyperelastic formulation for the modelling of soft tissue. *Journal of the mechanical behavior of biomedical materials*, vol. 39, 2014, p. 48–60, Elsevier.

[OGD 97] OGDEN R. W.
Non-linear elastic deformations. Courier Corporation, 1997.

[OGD 07] OGDEN R. W.
Incremental statics and dynamics of pre-stressed elastic materials. *Waves in nonlinear pre-stressed materials*, p. 1–26 Springer, 2007.

[OLO 04] OLOVSSON L., UNOSSON M., SIMONSSON K.
Selective mass scaling for thin walled structures modeled with tri-linear solid elements. *Computational Mechanics*, vol. 34, n° 2, 2004, p. 134–136, Springer.

[OLO 05] OLOVSSON L., SIMONSSON K., UNOSSON M.
Selective mass scaling for explicit finite element analyses. *International Journal for Numerical Methods in Engineering*, vol. 63, n° 10, 2005, p. 1436–1445, Wiley Online Library.

[OLO 06] OLOVSSON L., SIMONSSON K.
Iterative solution technique in selective mass scaling. *Communications in numerical methods in engineering*, vol. 22, n° 1, 2006, p. 77–82, Wiley Online Library.

[OPH 91] OPHIR J., CESPEDES I., PONNEKANTI H., YAZDI Y., LI X.
Elastography: a quantitative method for imaging the elasticity of biological tissues. *Ultrasonic imaging*, vol. 13, n° 2, 1991, p. 111–134, Elsevier.

[PAL 05] PALMERI M. L., SHARMA A. C., BOUCHARD R. R., NIGHTINGALE R. W., NIGHTINGALE K. R.
A finite-element method model of soft tissue response to impulsive acoustic radiation force. *Ultrasonics, Ferroelectrics and Frequency Control, IEEE Transactions on*, vol. 52, n^{o} 10, 2005, p. 1699–1712, IEEE.

[PAP 06] PAPAZOGLOU S., RUMP J., BRAUN J., SACK I.
Shear wave group velocity inversion in MR elastography of human skeletal muscle. *Magnetic resonance in medicine*, vol. 56, n^{o} 3, 2006, p. 489–497, Wiley Online Library.

[PAR 92] PARKER K. J., LERNER R.
Sonoelasticity of organs: shear waves ring a bell. *Journal of ultrasound in medicine*, vol. 11, n^{o} 8, 1992, p. 387–392, Am inst Ulrrasound Med.

[PAR 09] PARK 1 E., MANIATTY A. M.
Finite element formulation for shear modulus reconstruction in transient elastography. *Inverse Problems in Science and Engineering*, vol. 17, n^{o} 5, 2009, p. 605–626, Taylor & Francis.

[PEE 14] PEET Y., FISCHER P.
Legendre spectral element method with nearly incompressible materials. *European Journal of Mechanics-A/Solids*, vol. 44, 2014, p. 91–103, Elsevier.

[QIA 15] QIANG B., BRIGHAM J. C., ARISTIZABAL S., GREENLEAF J. F., ZHANG X., URBAN M. W.
Modeling transversely isotropic, viscoelastic, incompressible tissue-like materials with application in ultrasound shear wave elastography. *Physics in medicine and biology*, vol. 60, n^{o} 3, 2015, p. 1289, IOP Publishing.

[RÉN 08] RÉNIER M., GENNISSON J.-L., BARRIÈRE C., ROYER D., FINK M.
Fourth-order shear elastic constant assessment in quasi-incompressible soft solids. *Appl. Phys. Lett*, vol. 93, n^{o} 10, 2008, p. 101912–101912.

[RIV 48] RIVLIN R.
Large elastic deformations of isotropic materials. IV. Further developments of the general theory. *Philosophical Transactions of the Royal Society of London A: Mathematical, Physical and Engineering Sciences*, vol. 241, n^{o} 835, 1948, p. 379–397, The Royal Society.

[ROU 13] ROUZE N. C., WANG M. H., PALMERI M. L., NIGHTINGALE K. R.
Finite element modeling of impulsive excitation and shear wave propagation in an incompressible, transversely isotropic medium. *Journal of biomechanics*, vol. 46, n^{o} 16, 2013, p. 2761–2768, Elsevier.

[ROY 11] ROYER D., GENNISSON J.-L., DEFFIEUX T., TANTER M.
On the elasticity of transverse isotropic soft tissues (L). *The Journal of the Acoustical Society of America*, vol. 129, n° 5, 2011, p. 2757–2760, Acoustical Society of America.

[SAE 04] SAENGER E. H., BOHLEN T.
Finite-difference modeling of viscoelastic and anisotropic wave propagation using the rotated staggered grid. *Geophysics*, vol. 69, n° 2, 2004, p. 583–591, Society of Exploration Geophysicists.

[SAN 02a] SANDRIN L., TANTER M., CATHELINE S., FINK M.
Shear modulus imaging with 2-D transient elastography. *Ultrasonics, Ferroelectrics and Frequency Control, IEEE Transactions on*, vol. 49, n° 4, 2002, p. 426–435, IEEE.

[SAN 02b] SANDRIN L., TANTER M., GENNISSON J.-L., CATHELINE S., FINK M.
Shear elasticity probe for soft tissues with 1-D transient elastography. *Ultrasonics, Ferroelectrics and Frequency Control, IEEE Transactions on*, vol. 49, n° 4, 2002, p. 436–446, IEEE.

[SAR 98] SARVAZYAN A. P., RUDENKO O. V., SWANSON S. D., FOWLKES J. B., EMELIANOV S. Y.
Shear wave elasticity imaging: a new ultrasonic technology of medical diagnostics. *Ultrasound in medicine & biology*, vol. 24, n° 9, 1998, p. 1419–1435, Elsevier.

[SAR 11] SARVAZYAN A., J HALL T., W URBAN M., FATEMI M., R AGLYAMOV S., S GARRA B.
An overview of elastography-an emerging branch of medical imaging. *Current medical imaging reviews*, vol. 7, n° 4, 2011, p. 255–282, Bentham Science Publishers.

[SCH 04] SCHENK O., GÄRTNER K.
Solving unsymmetric sparse systems of linear equations with PARDISO. *Future Generation Computer Systems*, vol. 20, n° 3, 2004, p. 475–487, Elsevier.

[SHE 12] SHEARER T.
Waves in nonlinear elastic media with inhomogeneous pre-stress. Thèse de doctorat, University of Manchester, 2012.

[SIN 05a] SINKUS R., TANTER M., CATHELINE S., LORENZEN J., KUHL C., SONDERMANN E., FINK M.
Imaging anisotropic and viscous properties of breast tissue by magnetic resonance-elastography. *Magnetic resonance in medicine*, vol. 53, n° 2, 2005, p. 372–387, Wiley Online Library.

[SIN 05b] SINKUS R., TANTER M., XYDEAS T., CATHELINE S., BERCOFF J., FINK M.
Viscoelastic shear properties of in vivo breast lesions measured by MR elastography. *Magnetic resonance imaging*, vol. 23, n° 2, 2005, p. 159–165, Elsevier.

[SUS 09] SUSSMAN T., BATHE K.-J.
A model of incompressible isotropic hyperelastic material behavior using spline interpolations of tension–compression test data. *International Journal for Numerical Methods in Biomedical Engineering*, vol. 25, n^{o} 1, 2009, p. 53–63, Wiley Online Library.

[TKA 14] TKACHUK A., BISCHOFF M.
Local and global strategies for optimal selective mass scaling. *Computational Mechanics*, vol. 53, n^{o} 6, 2014, p. 1197–1207, Springer.

[TKA 15] TKACHUK A., BISCHOFF M.
Direct and sparse construction of consistent inverse mass matrices: general variational formulation and application to selective mass scaling. *International Journal for Numerical Methods in Engineering*, vol. 101, n^{o} 6, 2015, p. 435–469, Wiley Online Library.

[TWE 15] TWETEN D. J., OKAMOTO R. J., SCHMIDT J. L., GARBOW J. R., BAYLY P. V.
Estimation of material parameters from slow and fast shear waves in an incompressible, transversely isotropic material. *Journal of biomechanics*, vol. 48, n^{o} 15, 2015, p. 4002–4009, Elsevier.

[WEI 96] WEISS J. A., MAKER B. N., GOVINDJEE S.
Finite element implementation of incompressible, transversely isotropic hyperelasticity. *Computer methods in applied mechanics and engineering*, vol. 135, n^{o} 1-2, 1996, p. 107–128, Elsevier.

[WOC 08] WOCHNER M. S., HAMILTON M. F., ILINSKII Y. A., ZABOLOTSKAYA E. A.
Cubic nonlinearity in shear wave beams with different polarizations. *The Journal of the Acoustical Society of America*, vol. 123, n^{o} 5, 2008, p. 2488–2495, Acoustical Society of America.

[YE 17] YE W., BEL-BRUNON A., CATHELINE S., ROCHETTE M., COMBESCURE A.
A selective mass scaling method for shear wave propagation analyses in nearly incompressible materials. *International Journal for Numerical Methods in Engineering*, vol. 109, n^{o} 2, 2017, p. 155–173.

[YE ew] YE W., BEL-BRUNON A., CATHELINE S., ROCHETTE M., COMBESCURE A.
Simulation of non linear transient elastography: finite element model for the propagation of shear waves in soft tissue. *International Journal for Numerical Methods in Biomedical Engineering*, , (Under review).

[ZAB 04] ZABOLOTSKAYA E. A., HAMILTON M. F., ILINSKII Y. A., MEEGAN G. D.
Modeling of nonlinear shear waves in soft solids. *The Journal of the Acoustical Society of America*, vol. 116, n^{o} 5, 2004, p. 2807–2813, Acoustical Society of America.

[ZHA 15] ZHAO X., PELEGRI A. A.
A Bayesian approach for characterization of soft tissue viscoelasticity in acoustic radiation force imaging. *International journal for numerical methods in biomedical engineering*, , 2015, Wiley Online Library.

[ZHO 96] ZHOU Z., JOOS B.
Stability criteria for homogeneously stressed materials and the calculation of elastic constants. *Physical Review B*, vol. 54, n^o 6, 1996, p. 3841, APS.

[ZIE 00] ZIENKIEWICZ O. C., TAYLOR R. L.
The finite element method: solid mechanics, vol. 2. Butterworth-heinemann, 2000.

[ZOR 15] ZORGANI A., SOUCHON R., DINH A.-H., CHAPELON J.-Y., MÉNAGER J.-M., LOUNIS S., ROUVIÈRE O., CATHELINE S.
Brain palpation from physiological vibrations using MRI. *Proceedings of the National Academy of Sciences*, vol. 112, n^o 42, 2015, p. 12917–12921, National Acad Sciences.

FOLIO ADMINISTRATIF

THESE DE L'UNIVERSITE DE LYON OPEREE AU SEIN DE L'INSA LYON

NOM : YE DATE de SOUTENANCE : 2 Juin 2017

Prénoms : Wenfeng

TITRE : Numerical methods for the simulation of shear wave propagation in nearly incompressible medium --- Application in elastography

NATURE : Doctorat Numéro d'ordre : 2017LYSEI046

Ecole doctorale : Mécanique, Énergétique, Génie Civil, Acoustique (ED 162 MEGA)

Spécialité : MÉCANIQUE – GÉNIE MÉCANIQUE – GÉNIE CIVIL

RESUME : L'élastographie transitoire est une technologie médicale de caractérisation qui permet d'estimer la rigidité des tissus mous biologiques. En visualisant la propagation de l'onde de cisaillement dans le tissu, on peut déduire le module de cisaillement μ. Au cours de la dernière décennie, cette technique a été utilisée avec succès pour étudier diverses pathologie, en particulier la fibrose, le cancer. Cependant, de nombreux facteurs, comme par exemple, la réflexion des ondes, les conditions aux limites et la précontrainte perturbent les mesures en élastographie, la qualité de la caractérisation mécanique du tissu peut alors être altérée. De plus, les tissus présentent des propriétés mécaniques plus complexes, dont la viscosité, la nonlinéarité et l'anisotropie, dont la caractérisation peut améliorer la valeur diagnostique de l'élastographie. Les simulations de propagation d'onde par Eléments Finis (EF) apparaissent alors prometteuses puisqu'elles permettent d'étudier l'influence des paramètres mécaniques intrinsèques et extrinsèques sur les vitesses de propagation et ainsi, de permettre l'identification de propriétés mécaniques complexes dans les cas de mesure réels.

Dans ce travail, nous développons un modèle d'éléments finis pour la propagation d'ondes non-linéaires dans les tissus mous. Les modèles numériques ont été validés à partir d'expériences d'élastographie issues de la littérature et ensuite utilisés pour évaluer l'identifiabilité des paramètres d'un modèle de comportement non-linéaire dans l'élastographie: la loi de Landau. En mesurant les ondes d'amplitude finie et les ondes de faible amplitude autour d'un état pré-déformé, une méthode pratique et robuste proposée pour identifier la nonlinéarité des tissus homogènes en utilisant l'expérience d'élastographie.

La problématique du coût de calcul est également étudiée dans ce travail. En effet, la quasi-incompressibilité des tissus biologiques rend la vitesse de l'onde de pression extrêmement élevée, ce qui limite le pas de temps d'un calcul formulé en dynamique explicite.

Pour faire face à cette difficulté, différentes méthodes numériques sont présentées, dans lesquelles l'incrément de temps est limité par la vitesse d'onde de cisaillement au lieu de la vitesse d'onde de compression. Divers exemples numériques sont testés dans le cadre de l'élastographie dynamique, il a été montré que les méthodes sont précises pour ces problèmes et une réduction significative du temps CPU est obtenue.

MOTS-CLÉS : Élastographie, Élément fini, Onde de cisaillement, Intégration temporelle, Hyperélasticité, Incompressibilité, *Selective mass scaling*, Pas de temps fractionné, Modèle de Landau, Identification des paramètres.

Laboratoire (s) de recherche : Laboratoire de Mécanique des Contacts et des Structures, UMR CNRS 5259 – INSA de Lyon

Directeur de thèse : Alain COMBESCURE

Président de jury : Claire PRADA-JULIA

Composition du jury :

A S. BONNET-BENDHIA	Directeur de Recherche (ENSTA ParisTech)	Rapporteur
D. KOMATITSCH	Directeur de Recherche (Aix-Marseille Université)	Rapporteur
A. COMBESCURE	Professeur (INSA de Lyon)	Directeur de thèse
A. BEL-BRUNON	Maître de Conférences (INSA de Lyon)	Co-Directeur
S. CATHELINE	Directeur de Recherche (Université Lyon 1)	Examinateur
M. ROCHETTE	Ph.D. (ANSYS, France)	Examinateur
C. PRADA-JULIA	Directeur de Recherche (Institut Langevin)	Présidente du jury
R. KOLMAN	Ph.D. (Institute of thermomechanics, Czech)	Examinateur